

**INVESTIGATIONS ON HIGH  
TEMPERATURE CORROSION AND  
EROSION BEHAVIOUR OF PLASMA  
SPRAYED Co-BASED COMPOSITE  
COATINGS**

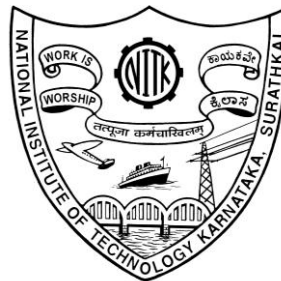
Thesis

Submitted in partial fulfilment of the requirements for the degree of

**DOCTOR OF PHILOSOPHY**

By

**NITHIN H S**



**DEPARTMENT OF MECHANICAL ENGINEERING  
NATIONAL INSTITUTE OF TECHNOLOGY, KARNATAKA,  
SURATHKAL, MANGALORE - 575 025**

**JUNE 2018**

## **DECLARATION**

I hereby declare that the research thesis entitled “**INVESTIGATIONS ON HIGH TEMPERATURE CORROSION AND EROSION BEHAVIOUR OF PLASMA SPRAYED Co-BASED COMPOSITE COATINGS**” which is being submitted to the **National Institute of Technology Karnataka, Surathkal** in partial fulfilment of the requirements for the award of the Degree of **Doctor of Philosophy in Mechanical Engineering** is a *bonafide report of the research work carried out by me*. The material contained in this research thesis has not been submitted to any University or Institution for the award of any degree.

Register Number: **138028ME13F16**

Name of the Research Scholar: **NITHIN H S**

Signature of the Research Scholar:

**Department of Mechanical Engineering**

Place: NITK-Surathkal

Date:

## **CERTIFICATE**

This is to certify that the research thesis entitled “**INVESTIGATIONS ON HIGH TEMPERATURE CORROSION AND EROSION BEHAVIOUR OF PLASMA SPRAYED Co-BASED COMPOSITE COATINGS**” submitted by **Mr. NITHIN H S (Register No. 138028ME13F16)** as the record of the research work carried out by him, *is accepted as the Research Thesis submission* in partial fulfillment of the requirements for the award of the degree of **Doctor of Philosophy**.

### **Research Guides**

**Dr. Vijay Desai**

Professor

Department of Mechanical  
Engineering, NITK, Surathkal

**Dr. Ramesh M R**

Associate Professor

Department of Mechanical  
Engineering, NITK, Surathkal

**Chairman-DRPC**

**Date:**

## ACKNOWLEDGEMENTS

*It is with great and profound sense of gratitude I thank my guide **Dr. Vijay Desai**, Professor, Department of Mechanical Engineering, NITK, Surathkal for his inspiring guidance, excellent research supervision and valuable discussions throughout the course of this research work.*

*I have great privilege and indebtedness to my co-guide **Dr. Ramesh M R**, Associate Professor, Department of Mechanical Engineering, NITK, Surathkal who spent enormous time in guiding me throughout the course of the research work on the analysis and integration of the variety of experimental test results that we had obtained. It is very hard to forget his enormous patience in routing the thesis work to a level that it stands today.*

*I am especially indebted to **Dr. Narendranath S**, Professor and Head, Department of Mechanical Engineering, and **Dr. Prasad Krishna** and **Dr. Gangadharan K V**, Former Head, Department of Mechanical Engineering, NITK, Surathkal for their constant encouragement, help and suggestions from time to time.*

*I express my gratitude to **Dr. Udaya Bhat K**, RPAC member, Department of Metallurgical and Materials Engineering and **Dr. Mrityunjay R Doddamani**, RPAC member, Department of Mechanical Engineering, NITK, Surathkal, for their valuable suggestions and support during the research work.*

*I wish to record deep sense of gratitude to **Dr. K. Rajendra Udupa**, Department of Metallurgical and Materials Engineering, Surathkal for providing facilities to carry out SEM/EDAX analysis and XRD.*

*I wish to register sincere thanks to **Dr. N. D. Prasanna**, Professor and **Girish V. Kulkarni**, Assistant Professor, Department of Materials Engineering, MSRIT, Bengaluru for providing facilities and support to carry out Erosion studies. Also I would like express my thankfulness to **Dr. Ramesh Singh**, Associate Professor, Mechanical Engineering Department, IIT Bombay for extending the permission to utilize Optical Profiler.*

*I would like to thank the teaching, non-teaching staff and research scholars of the Mechanical Engineering department, NITK for their direct and indirect help during the course work.*

*I also express my gratitude to my parents **Shive Gowda H S** and **Prabhamani S**, my most supportive spouse **Nishchitha K M**, my brother **Ashrith H S** and my family members for their support and help during the course of the research work. Finally, I acknowledge the encouragement and help received from all of my friends and well-wishers.*

**NITHIN H S**

## ABSTRACT

The components of the gas turbines such as combustor and transition duct, exit blades, vanes, and disks operate between the temperatures of 600-800°C. These components also work typically under higher cyclic loads in association with oxidising, corrosive and erosive environment. Providing surface coating through thermal spray process is one of the promising techniques to protect against such surface degradations and maintain the mechanical stability of underlying components. Plasma spray coating process is one of the most versatile and widely used cost-effective technique to deposit metals and ceramic materials on materials used in structural applications and machine parts to improve their oxidation, hot corrosion, and tribological resistance. The MCrAlY are promising coatings (M=Ni, Co and Fe) for the protection of components such as in the hot sections of gas turbines, aero engines, land-based gas turbines and naval diesel engine manufactured out of superalloys, particularly while operating at high temperatures. In the present study, oxides and carbides reinforced CoCrAlY feedstock powders such as CoCrAlY+28%Al<sub>2</sub>O<sub>3</sub>+2%YSZ, CoCrAlY+2%CeO<sub>2</sub>, CoCrAlY+30%WC-Co and CoCrAlY+30%Cr<sub>3</sub>C<sub>2</sub>-NiCr are coated on MDN 321 and Superni 76 superalloys by plasma spray technique. The microstructure, composition, phases and mechanical properties of coatings are characterized to evaluate and investigate their potential under high-temperature erosion, corrosion and oxidation conditions.

The high-temperature solid particle erosion experiments were carried out using air jet erosion test rig. Two impact angles; 90° and 30° of the jet are investigated and alumina sand is used as erodent at a temperature of 600°C. The thermo cyclic oxidation and hot corrosion behaviour of coated and uncoated alloys are investigated in both static air and molten salt (Na<sub>2</sub>SO<sub>4</sub>-60% V<sub>2</sub>O<sub>5</sub>) environment at 700°C for 50 cycles. Each cycle consisted of heating at 700°C for 1 hour, followed by 20 minutes of cooling in static air. The thermogravimetric technique is used to approximate the kinetics of oxidation. The corrosion products and eroded surface are analysed using X-ray diffraction (XRD) and Scanning electron microscopy/Energy dispersive X-ray analysis (SEM/EDAX).

The characterization studies have revealed that CoCrAlY+WC-Co coating has achieved comparatively higher hardness (384 Hv) and fracture toughness ( $14.3 \pm 3.2 \text{ MPa m}^{1/2}$ ), whereas CoCrAlY+CeO<sub>2</sub> coating exhibited the least porosity and higher bond strength ( $15.6 \pm 2.2 \text{ MPa}$ ). All the coatings have undergone adhesive fracture during bond strength test indicating better cohesive strength between the splats.

CoCrAlY+WC-Co coating has shown superior erosion resistance at 600°C temperature among the coatings with a volume loss of 0.9 mm<sup>3</sup> and 2.1 mm<sup>3</sup> at 90° and 30° impact angle respectively for 5 cycles. This is mainly attributed to its higher hardness and fracture toughness with lower porosity. CoCrAlY+WC-Co coating has experienced both ductile and brittle mode of erosion mechanism with the coating showing features of indentations, ridges, cracks, ploughing marks, lips and minor carbide pull. WC splats resist the erodent impact with minimal deformation thereby providing the shielding effect to Co matrix. The better erosion resistance of CoCrAlY+CeO<sub>2</sub> coatings is owing to its least porosity, higher fracture toughness and microstructure refinement by CeO<sub>2</sub> reinforcement. The coating has experienced ductile erosion mechanism with the absence of cracks and craters. CoCrAlY+Al<sub>2</sub>O<sub>3</sub>+YSZ coating exhibited brittle fracture and hard phase pull out due to repetitive erodent impact. The CoCrAlY+Cr<sub>3</sub>C<sub>2</sub>-NiCr coating showed least erosion resistance and has undergone severe brittle fracture at both impact angle and this mainly due to carbide dissolution at elevated temperature. From the XRD studies of eroded surface and observation of crack formation and oxide fragments, it very strongly indicates that all the coatings have undergone oxidation modified erosion.

The hot corrosion tests were conducted under molten salt environment and at 700°C. CoCrAlY+Cr<sub>3</sub>C<sub>2</sub>-NiCr coating showed at least of 23% higher hot corrosion resistance than other coatings and also the substrates. This coating has shown dense, thin, continuous Cr rich oxide layer on the surface which contributes to its better performance. The presence of dominant Cr<sub>2</sub>O<sub>3</sub> and CoCr<sub>2</sub>O<sub>4</sub> oxide layer having lower solubility for corrosive melts and oxygen. The presence of stable metal oxide reinforcement of  $\alpha$ -Al<sub>2</sub>O<sub>3</sub> with surface oxide scale of Cr<sub>2</sub>O<sub>3</sub>, CoCr<sub>2</sub>O<sub>4</sub> and CoAl<sub>2</sub>O<sub>4</sub> results in slow-scale growth kinetics during

hot corrosion of CoCrAlY+Al<sub>2</sub>O<sub>3</sub>+YSZ coating. In the case of CoCrAlY+WC-Co coating the formation of CoWO<sub>4</sub>, CoCr<sub>2</sub>O<sub>4</sub> and Cr<sub>2</sub>O<sub>3</sub> as strong phases with stable CoSO<sub>4</sub> provides hot corrosion resistance by developing dense non porous well adhered oxide scale. The growth of CeVO<sub>4</sub> as a result of acidic fluxing develops stresses on surrounding splats/oxide scale leads to the development of cracks. The infiltration of molten salt through the cracks results in higher corrosion rate and oxide scale delamination. Thus CoCrAlY+CeO<sub>2</sub> coating has shown the least hot corrosion resistance. All the coatings have shown the parabolic weight gain kinetics during hot corrosion studies. The MDN 321 and Superni 76 have shown higher corrosion rate with linear weight gain nature. In oxidation condition, CoCrAlY+Al<sub>2</sub>O<sub>3</sub>+YSZ coating has exhibited higher oxidation resistance than other coatings and substrates by showing least weight gain. The coatings experienced parabolic weight gain nature indicating all the possibilities of the formation of protective oxide layer. The uncoated alloys showed para-linear weight gain with a change from steady state to linear condition.

The coatings under study have been found to be successful in protecting the given substrate alloys tested under laboratory conditions against erosion, hot corrosion and oxidation. In addition to applications in gas turbine, these coatings can be applied to other applications like superheater zone of coal fired boilers, fluidized bed combustors, industrial waste incinerators and internal combustion engines etc.

**Keywords:** Plasma spray coatings, mechanical properties, solid particle erosion, optical profilometer, hot corrosion, oxidation.

## CONTENTS

Declaration	
Certificate	
Acknowledgement	
Abstract	
Contents	i
List of Figures	v
List of Tables	xi
Nomenclature	xii
<b>1 INTRODUCTION</b>	<b>1</b>
<b>2 LITERATURE REVIEW</b>	<b>7</b>
2.1 Solid particle erosion	7
2.2 High temperature oxidation	11
2.3 Hot Corrosion	13
2.3.1 High temperature (Type I) hot corrosion (HTHC)	14
2.3.2 Low temperature (Type II) hot corrosion (LTHC)	15
2.3.3 Hot corrosion mechanism	15
2.4 Protective coating	19
2.4.1 Plasma spraying	20
2.4.2 Plasma Spray Processing and Coating Formation	21
2.4.3 Process variants of plasma spray techniques	22
2.4.4 Role of spray coating	23
2.4.6 Literature based on carbide reinforced coatings	31
<b>3 EXPERIMENTAL PROCEDURE</b>	<b>37</b>
3.1 Substrate material	37
3.2 Coating powders	37
3.3 Deposition of coatings	38
3.4 High temperature solid particle erosion studies	38
3.4.1 Experimental setup	38

3.4.2	Erosion test	40
3.5	High temperature oxidation and hot corrosion studies	42
3.5.1	Experimental setup	42
3.5.2	Oxidation studies in air	42
3.5.3	Hot corrosion studies in molten salt ( $\text{Na}_2\text{SO}_4$ -60% $\text{V}_2\text{O}_5$ ) environment	42
3.6	Characterisation of coatings, analysis of corrosion and erosion products	43
3.6.1	Preparation of samples for cross sectional analysis	43
3.6.2	Measurement of as-sprayed coating thickness	43
3.6.3	Porosity and density measurement	43
3.6.4	Microhardness measurement	44
3.6.5	Fracture toughness measurement	44
3.6.6	Bond strength test	45
3.6.7	X-ray diffraction (XRD) analysis	46
<b>4</b>	<b>CHARACTERISATION OF COATINGS</b>	<b>47</b>
4.1	Morphology of coating powders	47
4.2	Coating thickness and metallographic studies	48
4.3	Porosity and density of coatings	51
4.4	Evaluation of microhardness	52
4.5	Evaluation of fracture toughness of coatings	53
4.6	Evaluation of bond strength of coating	54
<b>5</b>	<b>SOLID PARTICLE EROSION STUDIES</b>	<b>57</b>
5.1	Visual examination of erosion samples	57
5.2	Erosion rate based on weight loss method	58
5.3	Erosion of CoCrAlY+ $\text{Al}_2\text{O}_3$ +YSZ coating	61
5.4	Erosion of CoCrAlY+ $\text{CeO}_2$ coating	67
5.5	Erosion of CoCrAlY+WC-Co coating	70
5.6	Erosion of CoCrAlY+ $\text{Cr}_3\text{C}_2$ -NiCr coating	74
5.7	Erosion of uncoated SUPERNI 76 alloys	77
5.8	Comparative discussion of erosion of coatings	80
<b>6</b>	<b>HOT CORROSION</b>	<b>85</b>
6.1	CoCrAlY+ $\text{Al}_2\text{O}_3$ +YSZ coating	85
6.1.1	Thermogravimetric studies	85

6.1.2	X-RAY diffraction analysis	86
6.1.3	Surface SEM and EDS analysis	87
6.1.4	Cross sectional and elemental mapping	89
6.1.5	Discussion	91
6.2	CoCrAlY+CeO <sub>2</sub> coating	93
6.2.1	Thermogravimetric studies	93
6.2.2	X-ray diffraction analysis	94
6.2.3	Surface SEM and EDS analysis	95
6.2.4	Cross sectional and elemental mapping	97
6.2.5	Discussion	98
6.3	CoCrAlY+WC-Co coating	100
6.3.1	Thermogravimetric studies	100
6.3.2	X-Ray diffraction analysis	101
6.3.3	Surface SEM and EDS analysis	102
6.3.4	Cross sectional and elemental mapping	103
6.3.5	Discussion	105
6.4	CoCrAlY+Cr <sub>3</sub> C <sub>2</sub> -NiCr coating	107
6.4.1	Thermogravimetric studies	107
6.4.2	X-Ray diffraction analysis	109
6.4.3	Surface SEM and EDS analysis	109
6.4.4	Cross section and elemental mapping	111
6.4.5	Discussion	113
6.5	Uncoated alloys	114
6.5.1	Thermogravimetric studies	114
6.6	Comparative discussion	116
<b>7</b>	<b>OXIDATION STUDIES</b>	<b>121</b>
7.1	CoCrAlY+Al <sub>2</sub> O <sub>3</sub> +YSZ coating	121
7.1.1	Thermogravimetric studies	121
7.1.2	X-ray Diffraction Analysis	123
7.1.3	Surface SEM and EDS analysis	123
7.1.4	Cross sectional and elemental mapping	124
7.1.5	Discussion	126

7.2	CoCrAlY+CeO <sub>2</sub> coating	128
7.2.1	Thermogravimetric studies	128
7.2.2	X-ray diffraction analysis	129
7.2.3	Surface SEM and EDS analysis	130
7.2.4	Cross Section and Elemental mapping	131
7.2.5	Discussion	133
7.3	CoCrAlY+WC-Co coating	134
7.3.1	Thermogravimetric studies	134
7.3.2	X-ray diffraction analysis	135
7.3.3	Surface SEM and EDS analysis	136
7.3.4	Cross Section and Elemental mapping	137
7.3.5	Discussion	139
7.4	CoCrAlY+Cr <sub>3</sub> C <sub>2</sub> -NiCr Coating	140
7.4.1	Thermogravimetric studies	140
7.4.2	X-ray Diffraction Analysis	141
7.4.3	Surface SEM and EDS analysis	142
7.4.4	Cross Section and Elemental mapping	143
7.4.5	Discussion	145
7.5	Uncoated alloys	146
7.5.1	Thermo gravimetric studies	146
7.6	Comparative Discussion	148
	<b>CONCLUSIONS</b>	<b>151</b>
	References	157
	List of Publications and Conferences based on PhD Research Work	169
	Biodata	

## LIST OF FIGURES

Figure 2.1 Schematic showing crack formation due to erodent particle impact (Wensink and Elwenspoek, 2002).	9
Figure 2.2 Schematic showing erosion mechanisms at (a) 30° and (b) 90° impact angle (Islam and Farhat 2014).	10
Figure 2.3 Diagram showing initiation stage and propagation stages of hot corrosion.	14
Figure 2.4 Phase Diagram for Na <sub>2</sub> SO <sub>4</sub> -V <sub>2</sub> O <sub>5</sub> System (Otero et al, 1987).	17
Figure 2.5 Plasma Spray schematic (Tucker 1994).	21
Figure 2.6 High-temperature attack of metallic coatings (aluminide, chromide, MCrAlY) at different temperature ranges (National Materials Advisory Board, 1996).	25
Figure 2.7 High temperature oxidation and corrosion resistance of different coating systems (Nicholls et al. 2002).	26
Figure 3.1 (a) Air jet erosion test rig (b) Fixture, sample holder and heating element (c) heated specimen under test.	39
Figure 3.2 Schematic of erosion test rig.	40
Figure 3.3 Schematic of erosion volume loss measurement (Ivosevic et al. 2006).	41
Figure 3.4 Tubular furnace for oxidation and hot corrosion test.	43
Figure 3.5 Pycnometer.	44
Figure 3.6 Adhesion strength test using ultimate tensile test.	45
Figure 4.1 SEM morphology of (a) CoCrAlY+Al <sub>2</sub> O <sub>3</sub> +YSZ, (b) CoCrAlY+CeO <sub>2</sub> , (c) CoCrAlY+WC-Co and (d) CoCrAlY+Cr <sub>3</sub> C <sub>2</sub> -NiCr coating powders.	47
Figure 4.2 SEM morphology of (a, b) CoCrAlY+Al <sub>2</sub> O <sub>3</sub> +YSZ, (c, d) CoCrAlY+CeO <sub>2</sub> , (e, f) CoCrAlY+WC-Co and (g, h) CoCrAlY+Cr <sub>3</sub> C <sub>2</sub> -NiCr coating cross section.	49
Figure 4.3 XRD patterns of coating powders and as-coated samples of (a) CoCrAlY+Al <sub>2</sub> O <sub>3</sub> +YSZ, (b) CoCrAlY+CeO <sub>2</sub> , (c) CoCrAlY+WC-Co and (d) CoCrAlY+Cr <sub>3</sub> C <sub>2</sub> -NiCr coatings.	51
Figure 4.4 Bar chart for average microhardness of substrates and coatings.	53
Figure 4.5 Micrographs of cracks produced by indentation on (a) CoCrAlY+Al <sub>2</sub> O <sub>3</sub> +YSZ, (b) CoCrAlY+CeO <sub>2</sub> , (c) CoCrAlY+WC-Co and (d) CoCrAlY+Cr <sub>3</sub> C <sub>2</sub> -NiCr coatings.	54

Figure 4.6 Fractured surface of adhesion test sample of (a) CoCrAlY+Al <sub>2</sub> O <sub>3</sub> +YSZ, (b) CoCrAlY+CeO <sub>2</sub> , (c) CoCrAlY+ WC-Co and (d) CoCrAlY+ Cr <sub>3</sub> C <sub>2</sub> -NiCr coating.	55
Figure 5.1 Erosion scar produced on target surface at different impact angle.	57
Figure 5.2 Erosion scar produced at different impact angle.	58
Figure 5.3 Variation of erosion rate for uncoated samples at impact angle of (a) 90° and (b) 30°.	59
Figure 5.4 Variation of erosion rate for all coatings at 90° (a) and 30° (b) impact angle.	60
Figure 5.5 X-ray diffraction patterns of eroded CoCrAlY+Al <sub>2</sub> O <sub>3</sub> +YSZ coating at 600°C.	62
Figure 5.6 3-D profile of erosion scar of CoCrAlY+Al <sub>2</sub> O <sub>3</sub> +YSZ coating at (a) 90° and (b) 30° impact angles.	63
Figure 5.7 Erosion depth profile of CoCrAlY+Al <sub>2</sub> O <sub>3</sub> +YSZ coating at (a) 90° and (b) 30° impact angles.	64
Figure 5.8 Example showing screen shot of results from zeta optical profiler, (a) volume of eroded sample at 30° impact angle and (b) volume of uneroded CoCrAlY+Al <sub>2</sub> O <sub>3</sub> +YSZ coating.	64
Figure 5.9 Erosion surface morphology and EDS analysis of CoCrAlY+Al <sub>2</sub> O <sub>3</sub> +YSZ coating at (a, b, e) 90° and (c, d, f) 30° impact angle.	66
Figure 5.10 X-ray diffraction patterns of eroded CoCrAlY+CeO <sub>2</sub> coating at 600°C.	67
Figure 5.11 3-D profile of erosion scar of CoCrAlY+CeO <sub>2</sub> coating at (a) 90° and (b) 30° impact angles.	68
Figure 5.12 Erosion depth profile of CoCrAlY+CeO <sub>2</sub> coating at (a) 90° and (b) 30° impact angles.	68
Figure 5.13 Erosion surface morphology and EDS analysis of CoCrAlY+CeO <sub>2</sub> coating at (a, b, e) 90° and (c, d) 30° impact angle.	69
Figure 5.14 X-ray diffraction patterns of eroded CoCrAlY+WC-Co coating at 600°C.	70
Figure 5.15 3-D profile of erosion scar of CoCrAlY+WC-Co coating at (a) 90° and (b) 30° impact angles.	71
Figure 5.16 Erosion depth profile of CoCrAlY+WC-Co coating at (a) 90° and (b) 30° impact angles.	72

Figure 5.17 Erosion surface morphology and EDS analysis of CoCrAlY+WC-Co coating at (a, b, e) 90° and (c, d) 30° impact angle.	73
Figure 5.18 X-ray diffraction patterns of eroded CoCrAlY+Cr <sub>3</sub> C <sub>2</sub> -NiCr coating at 600°C.	74
Figure 5.19 3-D profile of erosion scar of CoCrAlY+Cr <sub>3</sub> C <sub>2</sub> -NiCr coating at (a) 90° and (b) 30° impact angles.	75
Figure 5.20 Erosion depth profile of CoCrAlY+Cr <sub>3</sub> C <sub>2</sub> -NiCr coating at (a) 90° and (b) 30° impact angles.	75
Figure 5.21 Erosion surface morphology and EDS analysis of CoCrAlY+Cr <sub>3</sub> C <sub>2</sub> -NiCr coating at 90° (a, b) and 30° (c, d, e) impact angle.	76
Figure 5.22 3-D profile of erosion scar of CoCrAlY+Cr <sub>3</sub> C <sub>2</sub> -NiCr coating at (a) 90° and (b) 30° impact angles.	78
Figure 5.23 Erosion depth profile of CoCrAlY+Cr <sub>3</sub> C <sub>2</sub> -NiCr coating at (a) 90° and (b) 30° impact angles.	79
Figure 5.24 Erosion surface morphology of Superni 76 at (a, b) 90° and (c, d) 30° impact angle.	79
Figure 5.25 Bar chart illustrating erosion volume loss of substrate and coatings at 90° and 30° impact angles.	81
Figure 6.1 Weight gain vs. number of cycles plot of CoCrAlY+Al <sub>2</sub> O <sub>3</sub> +YSZ coated alloy subjected to hot corrosion.	86
Figure 6.2 (Weight gain/area) <sup>2</sup> vs. number of cycles plot of CoCrAlY+Al <sub>2</sub> O <sub>3</sub> +YSZ coated alloys subjected to hot corrosion.	86
Figure 6.3 XRD patterns for CoCrAlY+Al <sub>2</sub> O <sub>3</sub> +YSZ coated alloys subjected to hot corrosion.	87
Figure 6.4 Surface morphology of hot corroded CoCrAlY+Al <sub>2</sub> O <sub>3</sub> +YSZ coatings on MDN 321(a, b) and Superni76 (c).	88
Figure 6.5 Corroded coating cross section and EDS point analysis (wt. %) of the CoCrAlY+Al <sub>2</sub> O <sub>3</sub> +YSZ coating.	89
Figure 6.6 BSEI and elemental X-ray mapping along the cross-section of the CoCrAlY+Al <sub>2</sub> O <sub>3</sub> +YSZ coating subjected to hot corrosion.	90
Figure 6.7 Weight gain vs. number of cycles plot of CoCrAlY+CeO <sub>2</sub> coated alloys subjected to hot corrosion.	93
Figure 6.8 (Weight gain/area) <sup>2</sup> vs. number of cycles plot of CoCrAlY+CeO <sub>2</sub> coated alloys subjected to hot corrosion.	94

Figure 6.9 XRD patterns for CoCrAlY+CeO <sub>2</sub> coated alloys subjected to hot corrosion.	94
Figure 6.10 Surface morphology of hot corroded CoCrAlY+CeO <sub>2</sub> coatings on (a) MDN 321 and (b) Superni76.	96
Figure 6.11 Corroded coating cross section and EDS point analysis (wt. %) of the CoCrAlY+CeO <sub>2</sub> coating.	97
Figure 6.12 BSEI and elemental X-ray mapping along the cross-section of the CoCrAlY+CeO <sub>2</sub> coating subjected to hot corrosion.	98
Figure 6.13 Weight gain vs. number of cycles plot of CoCrAlY+WC-Co coated alloys subjected to hot corrosion.	101
Figure 6.14 (Weight gain/area) <sup>2</sup> vs. number of cycles plot of CoCrAlY+WC-Co coated alloys subjected to hot corrosion.	101
Figure 6.15 XRD patterns for CoCrAlY+WC-Co coated alloys subjected to hot corrosion.	102
Figure 6.16 Surface morphology of hot corroded CoCrAlY+WC-Co coatings on (a) MDN 321 and (b) Superni76.	103
Figure 6.17 Corroded coating cross section and EDS point analysis (wt. %) of the CoCrAlY+WC-Co coating.	104
Figure 6.18 BSEI and elemental X-ray mapping along the cross-section of the CoCrAlY+WC-Co coating subjected to hot corrosion.	105
Figure 6.19 Weight gain vs. number of cycles plot of CoCrAlY+Cr <sub>3</sub> C <sub>2</sub> -NiCr coated alloys subjected to hot corrosion.	108
Figure 6.20 (Weight gain/area) <sup>2</sup> vs. number of cycles plot of CoCrAlY+Cr <sub>3</sub> C <sub>2</sub> -NiCr coated alloys subjected to hot corrosion.	108
Figure 6.21 XRD patterns for CoCrAlY+Cr <sub>3</sub> C <sub>2</sub> -NiCr coated alloys subjected to hot corrosion.	109
Figure 6.22 Surface morphology of corroded CoCrAlY+Cr <sub>3</sub> C <sub>2</sub> -NiCr coating on (a) MDN 321 and (b) Superni76.	110
Figure 6.23 Cross section and EDS point analysis of the CoCrAlY+Cr <sub>3</sub> C <sub>2</sub> -NiCr coating subjected to hot corrosion.	111
Figure 6.24 BSEI and elemental X-ray mapping along the cross-section of the CoCrAlY+Cr <sub>3</sub> C <sub>2</sub> -NiCr coating subjected to hot corrosion.	112
Figure 6.25 Weight gain vs. number of cycles plot of uncoated alloys subjected to hot corrosion.	115

Figure 6.26 (Weight gain/area) <sup>2</sup> Vs. number of cycles plot of uncoated alloys subjected to hot corrosion.	115
Figure 6.27 Total weight gain (mg/cm <sup>2</sup> ) of uncoated and Plasma coated alloys subjected to hot corrosion.	116
Figure 7.1 Weight gain vs. number of cycles plot of CoCrAlY+Al <sub>2</sub> O <sub>3</sub> +YSZ coated alloys subjected to oxidation.	122
Figure 7.2 (Weight gain/area) <sup>2</sup> vs. number of cycles plot of CoCrAlY+Al <sub>2</sub> O <sub>3</sub> +YSZ coated alloys subjected to oxidation.	122
Figure 7.3 XRD patterns for CoCrAlY+Al <sub>2</sub> O <sub>3</sub> +YSZ coated alloys subjected to oxidation.	123
Figure 7.4 Surface morphology of oxidised CoCrAlY+Al <sub>2</sub> O <sub>3</sub> +YSZ coatings on (a) MDN 321 and (b) Superni76.	124
Figure 7.5 Oxidised coating cross section and EDS point analysis (wt. %) of the CoCrAlY+Al <sub>2</sub> O <sub>3</sub> +YSZ coating.	125
Figure 7.6 BSEI and elemental X-ray mapping along the cross-section of the CoCrAlY+Al <sub>2</sub> O <sub>3</sub> +YSZ coating subjected to oxidation.	126
Figure 7.7 Weight gain vs. number of cycles plot of CoCrAlY+CeO <sub>2</sub> coated alloys subjected to oxidation.	128
Figure 7.8 (Weight gain/area) <sup>2</sup> vs. number of cycles plot of CoCrAlY+CeO <sub>2</sub> coated alloys subjected to oxidation.	129
Figure 7.9 XRD patterns for CoCrAlY+CeO <sub>2</sub> coated alloys subjected to oxidation.	129
Figure 7.10 Surface morphology of oxidised CoCrAlY+CeO <sub>2</sub> coatings on (a) MDN 321 and (b) Superni76.	130
Figure 7.11 Oxidised coating cross section and EDS point analysis (wt. %) of the CoCrAlY+CeO <sub>2</sub> coating.	132
Figure 7.12 BSEI and elemental X-ray mapping along the cross-section of the CoCrAlY+CeO <sub>2</sub> coating subjected to oxidation.	132
Figure 7.13 Weight gain vs. number of cycles plot of CoCrAlY+WC-Co coated alloys subjected to oxidation.	134
Figure 7.14 (Weight gain/area) <sup>2</sup> vs. number of cycles plot of CoCrAlY+WC-Co coated alloys subjected to oxidation.	135
Figure 7.15 XRD patterns for CoCrAlY+WC-Co coated alloys subjected to oxidation.	135

Figure 7.16 Surface morphology of oxidised CoCrAlY+WC-Co coatings on (a) MDN 321 and (b) Superni76.	136
Figure 7.17 Oxidised coating cross section and EDS point analysis (wt. %) of the CoCrAlY+WC-Co coating.	138
Figure 7.18 BSEI and elemental X-ray mapping along the cross-section of the CoCrAlY+WC-Co coating subjected to oxidation.	139
Figure 7.19 Weight gain vs. number of cycles plot of CoCrAlY+Cr <sub>3</sub> C <sub>2</sub> -NiCr coated alloys subjected to oxidation.	140
Figure 7.20 (Weight gain/area) <sup>2</sup> vs. number of cycles plot of CoCrAlY+Cr <sub>3</sub> C <sub>2</sub> -NiCr coated alloys subjected to oxidation.	141
Figure 7.21 XRD patterns for CoCrAlY+Cr <sub>3</sub> C <sub>2</sub> -NiCr coated alloys subjected to oxidation.	141
Figure 7.22 Surface morphology of oxidised CoCrAlY+Cr <sub>3</sub> C <sub>2</sub> -NiCr coating on (a) MDN 321 and (b) Superni 76.	142
Figure 7.23 Oxidised coating cross section and EDS point analysis (wt. %) of the CoCrAlY+Cr <sub>3</sub> C <sub>2</sub> -NiCr coating.	143
Figure 7.24 BSEI and elemental X-ray mapping along the cross-section of the CoCrAlY+Cr <sub>3</sub> C <sub>2</sub> -NiCr coating subjected to oxidation.	144
Figure 7.25 Weight gain vs. number of cycles plot of uncoated alloys subjected to oxidation for 50 cycles in air environment at 700°C.	147
Figure 7.26 (Weight gain/area) <sup>2</sup> vs. number of cycles plot of uncoated alloys subjected to oxidation for 50 cycles in air environment at 700°C.	147
Figure 7.27 Total weight gain (mg/cm <sup>2</sup> ) of uncoated and Plasma coated alloys subjected to oxidation.	148

## LIST OF TABLES

Table 3.1 Chemical composition (wt. %) of substrate alloys.	37
Table 3.2 Composition and particle size of powders.	37
Table 3.3 Spray parameters of Plasma Spray process.	38
Table 3.4 Air jet erosion test parameters.	40
Table 4.1 Particles size ( $\mu\text{m}$ ) distribution of coating powders.	48
Table 4.2 Thickness, porosity and density of the coatings.	52
Table 6.1 Point EDS of CoCrAlY+Al <sub>2</sub> O <sub>3</sub> +YSZ coating along the cross section in wt. %.	89
Table 6.2 Point EDS of CoCrAlY+CeO <sub>2</sub> coating along the cross section in wt. %.	97
Table 6.3 Point EDS of CoCrAlY+WC-Co coating along the cross section in wt. %.	104
Table 6.4 Point EDS of CoCrAlY+Cr <sub>3</sub> C <sub>2</sub> -NiCr coating cross section in wt. %.	111
Table 7.1 Point EDS of CoCrAlY+ Al <sub>2</sub> O <sub>3</sub> +YSZ coating along the cross section in wt. %.	125
Table 7.2 Point EDS of CoCrAlY+CeO <sub>2</sub> coating along the cross section in wt. %.	132
Table 7.3 Point EDS of CoCrAlY+WC-Co coating along the cross section in wt. %.	138
Table 7.4 Point EDS of CoCrAlY+Cr <sub>3</sub> C <sub>2</sub> -NiCr coating cross section in wt. %.	144

## NOMENCLATURES

$p$  = weight of the stoppered pycnometer in g.

$W$  = weight of the stoppered pycnometer and sample in g.

$w_1$  = weight of the stoppered pycnometer filled with water in g.

$w_2$  = weight of the stoppered pycnometer, sample, and water in g.

$H_v$  = Vickers hardness.

$E$  = Young's modulus.

$d$  = half-diagonal of the Vickers indentation.

$a$  = radial crack length.

$c$  = indentation crack length.

$d$  = half diagonal of the Vickers indentation.

$K_{IC}$  = Fracture toughness.

$K_p$  = Parabolic rate constant.

## 1 INTRODUCTION

Worldwide, the demand for energy is ever increasing. According to the survey on world energy resource published by world energy council (2016), India is the third largest country in the world to use coal for power production and also usage of fuel oil has increased by about 5.2% as compared to 2015 survey report. India is one among the countries using natural gas as energy source. Gas turbines are the major prime movers used in power generation and also there is an increased usage of gas turbines for applications in jet engines, marine propulsion, automotive, chemical, pharmaceuticals and fertilizer sectors. The reason for increasing demand is primarily due to the efficiency of these turbines and also they are reliable power producers, especially under base load operating conditions. An important aspect concerned to the gas turbines is development of materials for their components in order to minimize degradation and improve efficiencies, life cycle and reduce emissions (Wright and Gibbons 2007).

The components of land based gas turbines and air craft engines operate under high temperature and aggressive environment and are prone to degradation. The aerodynamic components such as compressor, turbine blades, and air foils are more prone to degradation. Corrosion is one among the degradation processes that occurs by wet deposits of salts and acids (chlorine and sulfides). The corrosion is typically more predominant with heavy fuel oils than with natural gas because of impurities and additives in the liquid fuels that deposits aggressive combustion derivatives (Kurz et al. 2014) (Wilcox et al. 2010). The depletion of high-grade fuel and cost effectiveness of heavy oils are the major reasons for using heavy oils as energy source. Oxidation is the chemical reaction between metal surface and atmosphere oxygen. The surface oxide layer can either be beneficial as a protective barrier or detrimental on account of spallation/crack. Erosion in gas turbines is a process of material removal by impact of solid/liquid particles on the surface of rotating or stationary surfaces. The solid particles are produced during the combustion of heavy oils and pulverized coal (Mishra et al. 2006). Syngas produced from coal gasification contains traces of fly-ash ranging in size from 1 to 10  $\mu\text{m}$ . These particles are the cause for erosion (Lawson and Thole 2012). The removal of material eventually changes the surface geometry of parts resulting in

deviations in the air flow path, roughening of surfaces, changes in clearances, and reduction of cross-sectional areas (Kurz and Brun 2007).

Multiple failure mechanisms are observed in the failure of turbine components. Particularly for disk failure by fatigue, corrosion and erosion are referred as the initiation points. Corrosion can reduce blade section size while erosion will reduce cross-section of metal components (Wilcox et al. 2012)

Some of the examples of surface damage in the gas turbine components as suggested by (Kurz et al. 2014) and (Wilcox et al. 2012) include:

- Fouling on compressor section is caused by the adhesion of particles such as salts, heavy hydrocarbons (oils and waxes), carbon and other dirt.
- Engine fouling is caused by the deposition of contaminants on the internal components. Both these fouling alter the profiles of the components and cause change in the air flow direction which results in reduction of turbine efficiency.
- Sulfidation and vanadium stimulated hot corrosion results in cracking of turbine blades and further, the growth of subsurface cracks due to mechanical stress leads to failure. This is recognized as a principal cause for aircraft and land based gas turbine engine failure.
- Corrosion Pitting is a localized corrosion mechanism that promotes the development of small deep holes on the metal surface and into it and is also not easily detectable. Pitting cause significant danger and unexpected failures of compressor blade.
- Crevice corrosion occurs at highly stressed surfaces between rotor blade base and disk slots which cannot be detected until the blades are disassembled for maintenance. Crevice corrosion leads to the risk of catastrophic failure.
- Erosion results in permanent damage eventually requiring refurbishment or replacement of parts. Formation of skirt at the leading edge of the turbine blade is a typical example.
- Erosion is a more serious problem in aircraft engines. The state of the art filtration systems used for industrial applications will typically eliminate the bulk of the larger particles. The source for erosion in case of aircraft compressor is desert sand, volcanic ashes, sea salts and atmospheric dust.

High-temperature corrosion in heavy oils and gas fired base turbine systems varies widely depending on the grade of fuel and turbine operating conditions. Many studies are conducted to understand the mechanism of corrosion of a particular system and to provide the solution. The species of hot corrosion degradation are those containing sulfur, chlorine, vanadium, alkali metals (Na and K) and other trace metals (Pb and Zn). The levels of these contaminants are significantly different in the various potential solid fuels (Simms et al. 2008). Severe hot corrosion occurs when these contaminants or eutectic sulfides melt or vaporize during gasification and combustion and eventually condense on metal surfaces removing the protective layer from those surfaces by chemical reactions, fluxing, or fracturing. The important contribution related to fluxing model was made by Rapp and Goto (1981) who proposed that if the solubility gradient of the protective oxide with distance into the salt layer becomes negative at the oxide/salt interface, accelerated attack could be sustained. The rate of corrosion depends on the rate of deposition factor, metal temperature and the surrounding environment.

The presence of volcanic ashes, desert sands, mining dust and traces of fly ash from low grade fuel (syngas) in the pressurised gaseous stream results in the removal of material in gas turbine compressor and in turbine blade. The coupling effect of oxidation and corrosion environments at higher temperatures make the erosion process quite complicated. The presence of SiO<sub>2</sub> traces in fly ash and volcanic ash can embed on the target surface due to high impact resulting in chemical reaction between the erodent containing SiO<sub>2</sub> and oxide scale on the surface. Hidalgo et al. (2001) detailed that erosion rate depends on the oxidation kinetics and erodent reactivity towards the oxidised surface. Similar types of materials degradations (corrosion and erosion) can be anticipated in steam turbines using solid fuel coal, as some of the degradation species are same as for the coal fired systems.

The use of stainless steel for blades and vanes of gas turbines during the initial stages of their applications and observations of catastrophic failure or degradations influenced the development of Ni and Co based alloys (alloying elements as Cr, Al, Ti, Mo, Ta, C,

B etc) both with respect to composition and processing (Sims et al. 1987). Since the alloying alone cannot provide both the mechanical and chemical stability, only the development of alloy is not sufficient to protect against degradation, (Harb and Smith 1990). Consequently, it is essential for the materials researchers to develop a new material to provide resistance against the degradations such as oxidation, corrosion and erosion. Material has to provide better corrosion, wear and erosion resistance at high temperatures in addition to excellent high temperature mechanical properties such as good strength, creep resistance and microstructure stability. However, these requirements sometimes cannot be accomplished simultaneously by alloy development alone. In order to achieve mechanical strengthening alloy development is the better approach, while surface coating is now widely accepted industrial practice to resist against surface degradations such as corrosion or erosion. Coating can provide necessary resistance to surface degradation by maintaining the mechanical stability of the underneath substrate. Coatings can add value to component up to 10 times the cost of the coating (Matthews et al. 1998). Coatings can provide a way to extend the component life limits in higher temperature applications (Sidky and Hocking 1999).

The protective coatings on structural alloys are used in aircraft and energy conversion systems to protect the surface against oxidation, corrosion, erosion and abrasion under extreme reactive environment (Rajendran 2012). On exposure to higher temperatures, the coating forms an oxide scale which is expected to provide long term corrosion resistance stability and also good resistance to spallation or cracking under mechanical and cyclic thermal stress induced during operating condition (Gurrappa 2003). One of the feasible solutions is development of new coating material compositions which can contribute these features. Among the coating techniques, the thermal spray coatings are particularly interesting for investigation as they are reported to offer the advantage of higher performance / cost ratio. Unique compositions and microstructures can be obtained with thermal spraying. These processes have no limitation in terms of the material to be coated and also the processes have the ability to deposit coatings of thicknesses ranging from several micrometers to millimeters. Additionally, it is suitable for a great variety of shapes and sizes and has the advantage of maintaining the substrate temperature relatively low (Rodriguez et al. 2003).

Formation of close, compact and dense splats is the major criteria to develop a faultless coating with better properties. Plasma spraying is a well-accepted and versatile coating technique for producing coatings using both metals and ceramics powders. It is referred to as one of the reliable and cost-effective solution for many industrial problems and also contributes the advantages of the rapid solidification process (Steffens and Mack 1990) (Pfender 1988).

The present research deals with the development of novel coating materials, specifically the combination of metals and ceramics (oxides/carbides) composite to dispense the combined corrosion and erosion resistance at elevated temperature. Cobalt-based coatings with reinforced with oxides ( $\text{Al}_2\text{O}_3$  and  $\text{CeO}_2$ ) and carbides ( $\text{WC}$  and  $\text{Cr}_3\text{C}_2$ ) are developed through plasma spray process. The performance of coatings with respect to oxidation, hot corrosion resistance and solid particle erosion at higher temperature is evaluated.

**THIS PAGE IS LEFT BLANK.**

## 2 LITERATURE REVIEW

The literature review is presented to get an understanding of mechanisms of erosion, oxidation and hot corrosion. The types of thermal spray coatings, process details of Plasma spray coating and role of metallic and composite coatings in restricting the degradation is highlighted.

### 2.1 Solid particle erosion

Erosion is the progressive loss of material from a solid surface as a result of mechanical interaction between the solid surface and a multi-component fluid or impinging solid particles or liquid. Erosion occurs when the solid particles entrained in a fluid stream (gaseous or liquid) strikes the surface (Westergard et al. 2000). Manifestations of solid particle erosion in actual service conditions are usually in the form of thinning of components, macroscopic scooping in the direction of gas or particle flow, surface roughening and in some cases, the formation of ripple patterns on metal surface (Davis 2001).

Solid particle erosion is a principal material degradation mechanism encountered in many systems such as thermal power plants, aircraft gas turbine engines, pneumatic bulk transport systems, coal liquefaction/gasification plants and ore or coal slurry pipelines. The worst case scenarios of degradation normally occur where there is a combination of both erosion and oxidation, particularly the case of erosion and high-temperature oxidation (Wellman and Nicholls 2004) (Sundararajan and Roy 1997). In industrial applications and power generation, solid particles are formed during the combustion of pulverized coal, heavy oils and synthetic fuels (Tabakoff 1999).

In general, erosion mechanisms are distinguished as two types or modes often called as brittle and ductile erosion. The brittle erosion occurs with formation of crack, while cutting and ploughing effects are observed in ductile erosion. The erosion rate is mainly governed by three factors (Finnie 1960):

- Flow of erosive media and environmental conditions- Impingement angle, particle velocity, temperature, impingement rate and presence of corrosive agents.
- Impacting particles properties- Size, shape, density and hardness.

- Surface conditions- Topology, stress level and roughness.

The erosion rate of ductile and brittle material varies with respect to the impact angle (Suckling and Allen 1997). Investigations of the erosion rate at different impact angles provide an idea of the maximum erosion rate occurring under particular test conditions. During ductile mode of erosion, impacting particles cause localized plastic strain that ultimately exceeds the strain values that can cause failure of the deformed material (Levy and Sa 1995). During the brittle erosion mode, impacting particle cause high compressive and shear stresses forming radial cracks. Further the plastic deformation results in lateral cracks and chipping leading to the material removal (Finnie 1960). The extent of erosion damage is allied to the ability of the material to elastically recover and hence it is imperative to understand the mechanical properties of target material. The brittle materials experience higher erosion rate at higher impact angles and the ductile material has higher erosion rate at lower impact angles (Ramesh et al. 2010).

Many erosion mechanisms have been proposed by various researchers indicating the way the material is worn away from the surface. In the case of ductile surfaces, elastic and plastic strains may occur, depending on whether the yield strength of materials is exceeded or not during impact whereas for brittle materials, different modes of crack formation contributes to the loss of material by erosion (Hutchings 1974). The collision of hard solid particles on brittle material surface at normal angle of impact leads to the growth of radial cracks around damaged areas on the surface (Finnie et al. 1979).

(Wensink and Elwenspoek 2002) explained the erosion of brittle material and the schematic is represented in Figure 2.1. When angular hard particles impinge on the brittle material, the contact area experiences high compressive and shear stresses resulting in the formation of radial crack. Subsequent to the impact, the plastic deformation leads to large tensile stresses that result in lateral cracks causing the material removal. He has also concluded that when the particle velocity and size is reduced, the impact energy of particles is sufficient only to produce plastic deformation. This change in erosion mode is called the ductile–brittle transition (Sheldon and Finnie 1966).

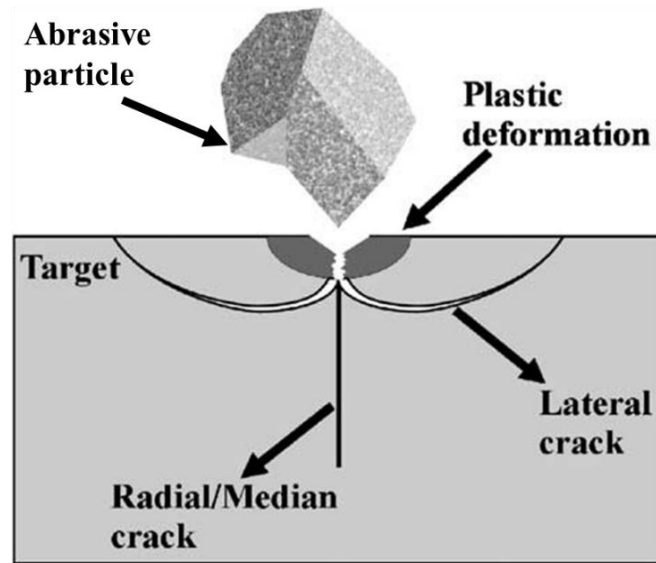


Figure 2.1 Schematic showing crack formation due to erodent particle impact (Wensink and Elwenspoek, 2002).

Levy (1986) described the “platelet erosion mechanism” of ductile materials in three distinct phases, which occur sequentially in the steady state condition. In the first phase, an impinging particle forms a crater and material is extruded from the crater to form a raised lip. In the second phase the displaced material is deformed by subsequent impacts and can be accompanied by ductile fracture in heavily strained regions. Finally, severely strained material gets detached from the surface by ductile fracture in the form of platelet.

Studies on erosion mechanism were conducted by Liebhard and Levy (1991) to investigate the effect of abrasive particle feed rate, particle size and shape on the sensitivity of erosion rate. The increase in spherical erodent particle feed rate by an order of magnitude decreased the material loss of about 50%. At higher feed rate of these spherical particles the erodent particle interference reduced the particles effectiveness to erode the surface. The particles rebounding from the target surface after impact were reported to be deflecting the preceding particles in the downward moving stream away from their path. However, in case of angular shape erodent particles, with similar increase in feed rate, the material loss is reported to be 14%. This implies that the angular erodent particles can remove material more effectively than spherical particles and tend to reduce the particle interference effect. Finally it observed that as

the abrasive particle size increases, the sensitivity of erosion rate to particle feed rate significantly drops.

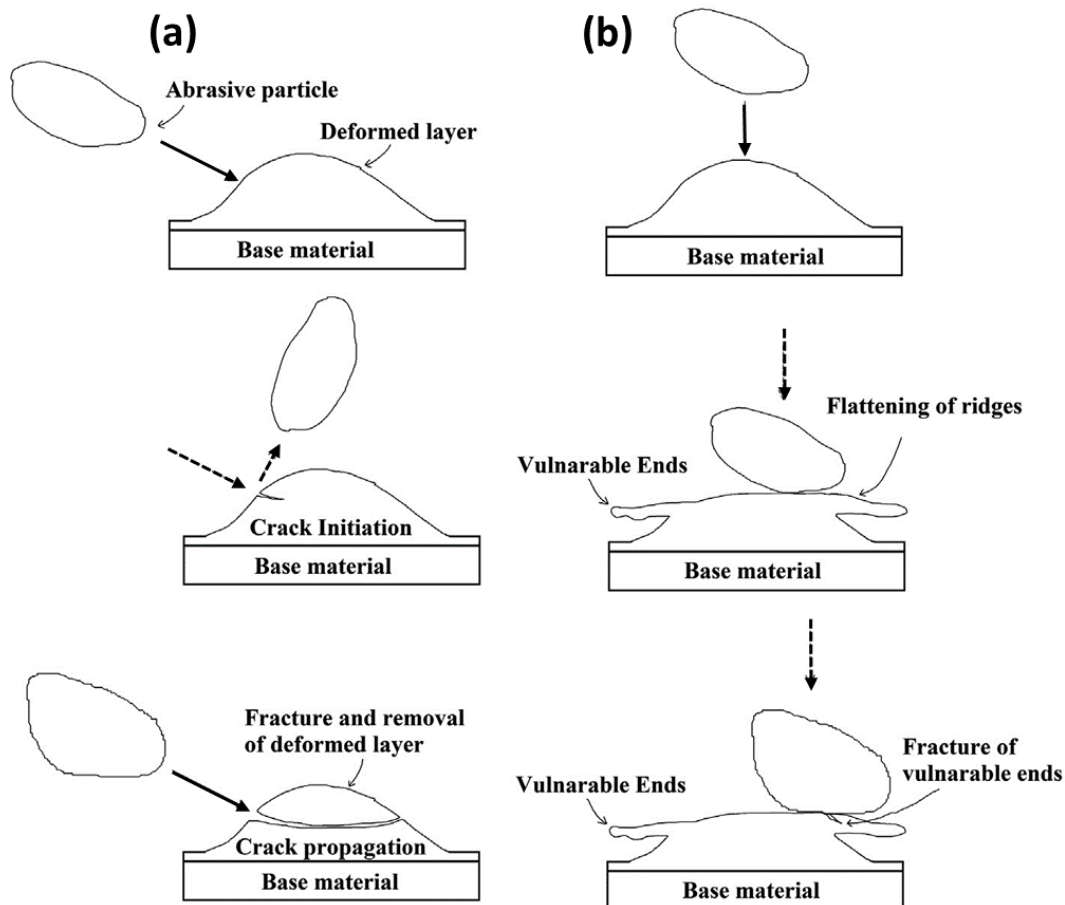


Figure 2.2 Schematic showing erosion mechanisms at (a) 30° and (b) 90° impact angle (Islam and Farhat 2014).

Islam and Farhat (2014) studied the effect of impact angle and velocity of erodent on erosion of API X42 pipeline steel. The authors observed that at lower impact angle of 30° and particle velocity of 36 m/s, the alumina erodent particles strike the target surface resulting in formation of dimples (indents) by localised micro-forging and ploughing and ploughing was dominant erosion mechanism. It is also reported that, at low impact angle and high particle velocity of 86 m/s, the particles strike the surface with higher kinetic energy and cut the target in the form of small chips. This process was emphasised as “low angle metal cutting”. At this condition metal removal takes place by low angle metal cutting and removal of ridges around dimples. At higher impact angle of 90°, with lower particle velocity 36 m/s, the impact of alumina particles

resulted in squeezing of the metal resulted in formation of dimples surrounded by ridges and embedment of particles. These ridges further fractured due to flattening and plastic deformation due to the subsequent particle impacts, while at higher particle velocity the high kinetic energy resulted in extensive embedment of erodent on the surface. Ridges around the dimples were flattened by erodent impact resulting in formation of extended vulnerable lips which further underwent brittle fracture. Authors also observed occurrence of secondary metal cutting due to the deflected erodent by pre embedded particle. All the erosion mechanisms are represented in Figure 2.2.

## **2.2 High temperature oxidation**

Metals and alloys get oxidised when they are heated to elevated temperatures in air or highly oxidising environments. It has long been established that most metals and alloys would react with oxygen to oxidize to some extent in gaseous atmosphere. Oxides are generally more thermodynamically stable than reaction products from other species (like N and S) which may be present in the environment. It is therefore common for oxides to be formed at the gas-metal interface (Pettit 1977).

Oxidation of metals seems to be the simplest of chemical reactions. However, according to Kofstad and Hed (1969), the reaction path and oxidation behaviour of a metal may depend on a variety of factors and as a result the reaction mechanisms may prove to be complex. The initial step in the metal-oxygen reaction involves the adsorption of gas on the metal surface. As the reaction proceeds, oxygen may dissolve in the metal resulting in the formation of oxide on the surface either as a film or as separate oxide nuclei. Both the adsorption and the initial oxide formation are functions of surface orientation, crystal defects at the surface, surface preparation and impurities in both the metal and the gas. Thermodynamically, an oxide is likely to form on a metal surface when the oxygen potential in the environment is greater than the oxygen partial pressure in the equilibrium with the oxide.

Stott (1998) has explained that the establishment of an oxide layer on an alloy takes place by a nucleation and growth process. According to him, when a clean component is exposed to an oxygen rich gas, small impinging nuclei of all the thermodynamically stable oxides develop on the surface. These initial nuclei of oxide coalesce rapidly to

give a complete layer. During the initial or transient stage, the rate of oxidation is rapid, all the elements in the alloy oxidise and the amounts of various oxides in the layer are approximately proportional to the concentration of the elements in the alloy.

When the oxidation process involves an alloy instead of a pure metal, many factors described for the oxidation of pure metals may be applied to the oxidation of the alloy. However, for oxidation in alloys is generally much more complex as a result of some, or all, of the following (Kofstad and Hed 1969) (Birks et al. 1983)

- The elements of the alloy will have different affinities for oxygen reflected by the different free energies of formation of the oxides.
- Ternary and higher oxides may be formed.
- A degree of solid solubility between the oxides may exist.
- The various metal ions will have different mobility in the oxide phases.
- The various metals will have different diffusivities in the alloy.
- Dissolution of oxygen into the alloy may result in sub-surface precipitation of oxides of one or more alloying elements (internal oxidation).

As the equilibrium partial pressure of oxygen for oxides is generally very small, initially all the elements on the surface of the alloy will form their respective oxides. However, with time, the formation of the oxides on the surface of an alloy depends upon the individual activities of the elements and their relative affinities for oxygen (Li et al. 1998).

Further, the requirement of a protective oxide scale is to have a slow growth rate. Oxidation reactions of protective oxide generally follow a parabolic rate equation given by:

$$x^2 = K_p t \quad (2.1)$$

where  $x$  is the scale thickness in dimensions of length,  $t$  is the time and  $K_p$  the parabolic-growth rate constant in dimensions of length<sup>2</sup>/time. However minor deviations from the parabolic behaviour are often observed (Doychak, 1995).

### 2.3 Hot Corrosion

Hot corrosion is defined as the accelerated oxidation of materials at elevated temperature induced by salt contaminants such as  $\text{Na}_2\text{SO}_4$ ,  $\text{NaCl}$  and  $\text{V}_2\text{O}_5$  that form molten deposits resulting in the damage of protective surface or surface oxides (Rapp and Zhang 1994) (Khajavi and Shariat 2004).

During hot corrosion, the degradation of metals and alloys occurs at higher rate than in oxidation due to porous non-protective oxide scale formed at the surface and sulfides in the substrate (Sidhu and Prakash 2006A). The kinetics and the characteristics of the reaction products is critically dependent on the oxygen partial pressure, metal temperature, salt composition and salt deposition rate (Simms et al. 2008).

The hot corrosion occurs in two stages, as initiation stage and propagation stage as shown in Figure 2.3. The initiation stage of hot corrosion can be attributed to failure of the protective oxide scale and repair of oxide scale by itself. When the salt mixture deposits on a surface previously covered with a protective oxide, it can cause accelerated oxidation if the protective oxide is damaged. The oxide scale damage can take place in four different ways (Khajavi and Shariat 2004).

- The mechanical disruption of the oxide scale by thermal cycling, erosion, wear and by elastic straining of the substrate resulting in setting up tensile stresses in the oxide.
- In case of salts containing sulfur, diffusion of sulfur through the oxide layer until chromium-rich sulfides form within the metal; later development of the external oxide or its restoration is inhibited.
- Fluxing of the protective oxide layer by the salts.
- A local reducing environment may form due to incomplete burning of fuel, which can damage the surface oxide scale, particularly in the presence of contaminants such as  $\text{Na}_2\text{SO}_4$ .

# HOT CORROSION CHRONOLOGY

## Initiation Stage

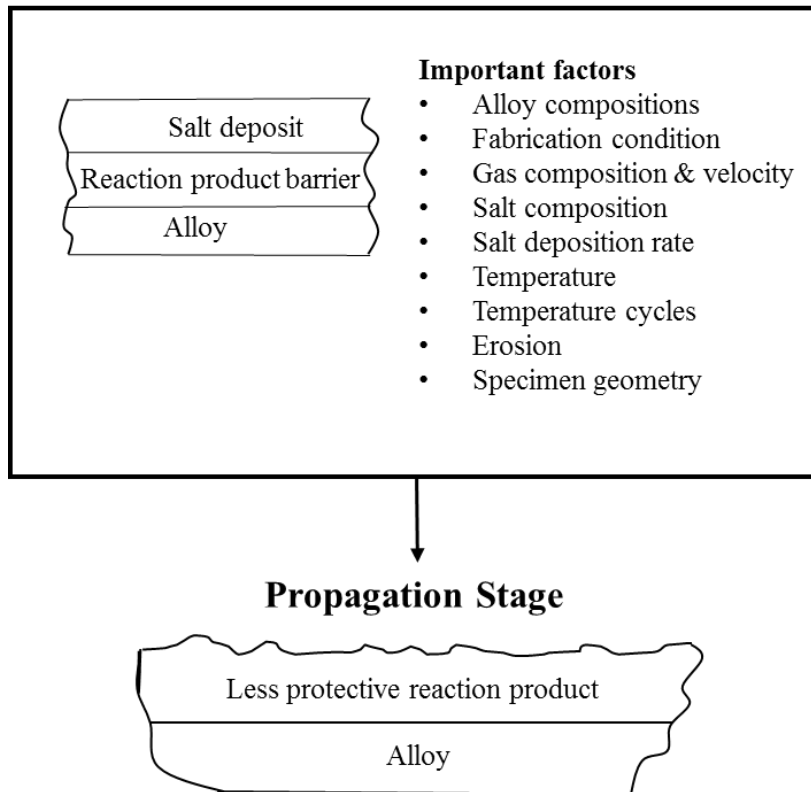


Figure 2.3 Diagram showing initiation stage and propagation stages of hot corrosion.

### 2.3.1 High temperature (Type I) hot corrosion (HTHC)

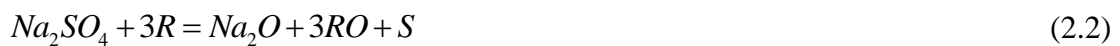
High temperature (Type I) hot corrosion (HTHC) is normally observed in the temperature range of about 825-950°C where the condensed salt film is completely in molten state. The typical microstructure for HTHC shows the formation of sulfides and a corresponding depletion of the reactive component in the alloy substrate. The external corrosion products frequently comprise of oxide precipitates dispersed in the salt film (Rapp and Zhang 1994). The major source of corrosion in HTHC is  $\text{Na}_2\text{SO}_4$  due to its high thermodynamic stability. The presence of  $\text{Na}_2\text{SO}_4$  salt is more prominent in marine atmosphere, but also found in industrial pollutants, volcanic discharges and as a combustion product of fuels. The macroscopic observation in HTHC process is severe peeling of the metal surface and significant color changes in the area of the accelerated attack. While microscopic observation reveals sulfidation and depletion regions under the porous oxide scale (Eliaz et al. 2002).

### 2.3.2 Low temperature (Type II) hot corrosion (LTHC)

Low temperature (Type II) hot corrosion (LTHC) occurs well below the melting point of salt. The reaction product morphology for this type of corrosion can be characterized by a non-uniform attack in the form of pits, with only little sulfide formation close to the alloy/scale interface and little depletion of elements in the alloy substrate. This form of corrosion is observed mainly within the temperature range 650-800°C (Nicholls 2000). The reaction of salt and metals forming low melting point eutectics causes typical LTHC pitting. Wright (1987) suggested that a high partial pressure of SO<sub>3</sub> in the gaseous phase is vital for LTHC reactions, in contrary to HTHC. Localized nature of attack is more dominant due to localized molten salt attack, thermal cycling and erosion which results in crevice corrosion. Crevice corrosion is responsible for substantial risk of catastrophic failure, since it cannot be inspected without disassembling (Kurz et al. 2014).

### 2.3.3 Hot corrosion mechanism

Simens et al (1955) were among the first to study the chemical reaction between the salt and the metal or scale. They examined the oxidation of alloys involving Na<sub>2</sub>SO<sub>4</sub> and found protective scale was ineffective and sulfide was observed at the oxidation front. They concluded that the hot corrosion process is triggered by the initial reduction of the salt through an unspecified reducing agent R (equation 2.2 and 2.3).



Where M represents metallic component in the alloy. The metallic sulfides could then react with more Na<sub>2</sub>SO<sub>4</sub> to liberate sulphur (equation 2.4 and 2.5).



The above equation indicates autocatalytic destruction.

Fluxing is known as dissolution of molten salt in oxide scale and this action in hot corrosion at the propagation stage was first explained by Bomstein et al. (1975). They

have suggested that hot corrosion associated with sulfidation is due to the reaction between  $\text{Na}_2\text{O}$  and the elements of the alloy. The characteristic of hot corrosion is the lowering of oxygen activity on alloy surface by the salt deposit. This occurs because of the elements present in the alloys have high affinities for oxygen. If the salt is  $\text{Na}_2\text{SO}_4$  the reaction is sulfidation or if the salt is  $\text{NaCl}$ , the reaction is chlorination.

The protection efficiency of the surface oxide layer reduces significantly as a result of fluxing. This fluxing may be either due to combination of oxides with  $\text{O}^{2-}$  to form anions (basic fluxing) or by decomposition of the oxides into the corresponding cations and  $\text{O}^{2-}$  (acidic fluxing). As compared to basic fluxing, acidic fluxing causes more severe oxidation. The acidic fluxing takes place when the  $\text{O}^{2-}$  activity in the molten salt is markedly lower and sulfur activity is higher. In contrast to this, basic fluxing take place when the oxide ion activity in molten salt is high due to the separation of sulfur and oxygen from  $\text{Na}_2\text{SO}_4$  (Goebel and Pettit 1970).

Otero et al. (1988) investigated the presence of  $\text{Na}_2\text{SO}_4$ -60% $\text{V}_2\text{O}_5$  ratio mixture on a variety of in service component surfaces exposed to high-temperature gases formed by the burning of fuels containing impurities like sodium, vanadium, sulfur etc. The presence of sulfur and its oxidized compounds were reported to favor the formation of isolated lobes with radial morphology which will allow access to the oxygen resulting in reduction of protective nature of oxide scale. The presence of vanadium and its oxidized products were observed to generate compounds with aciculate morphology, identified to look like alkaline vanadate complexes. These aciculate shapes reduce the protective nature of the scale. The equilibrium diagram for varying composition of  $\text{Na}_2\text{SO}_4$  is shown in Figure 2.4. The mixture of  $\text{Na}_2\text{SO}_4$ -60% $\text{V}_2\text{O}_5$  is seen to be the lowest eutectic temperature. Kolta et al. (1972) proposed that  $\text{Na}_2\text{SO}_4$  can react with  $\text{V}_2\text{O}_5$  to increase the acidity of melt through the formation of sodium vanadates  $\text{NaVO}_3$ . Similarly during combustion, the vanadium contaminants are oxidized to the higher valence vanadium oxides ( $\text{V}_2\text{O}_4$  and  $\text{V}_2\text{O}_5$ ) and sodium vanadates are formed by the reaction of vanadium oxides and sodium salts as reported by Kofstad (1988).

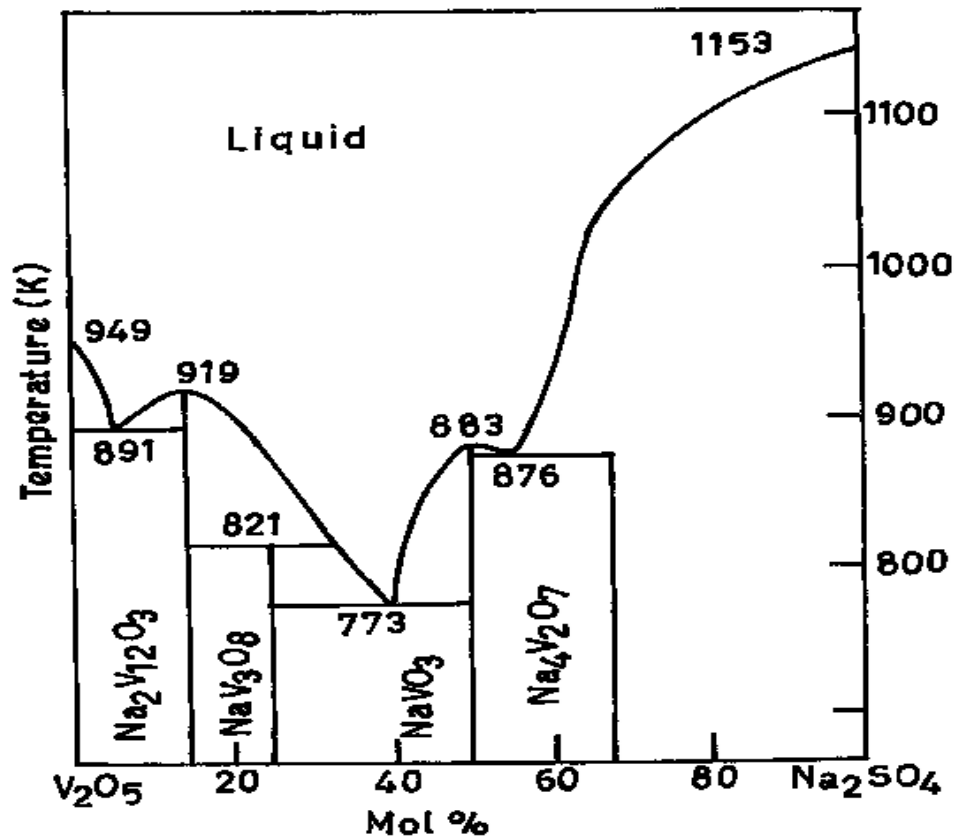


Figure 2.4 Phase Diagram for Na<sub>2</sub>SO<sub>4</sub>-V<sub>2</sub>O<sub>5</sub> System (Otero et al, 1987).

Tiwari and Prakash (1997) have studied hot corrosion behaviour of few superalloys exposed to corrosive environments comprising of Na<sub>2</sub>SO<sub>4</sub>, Na<sub>2</sub>SO<sub>4</sub>-15% V<sub>2</sub>O<sub>5</sub> and Na<sub>2</sub>SO<sub>4</sub>-60% V<sub>2</sub>O<sub>5</sub> at the temperatures between 700°C and 900°C. Corrosion rates were observed to be very high in case of Na<sub>2</sub>SO<sub>4</sub>-60% V<sub>2</sub>O<sub>5</sub> composition due to its low melting point of about 500°C. Tiwari (1997) further reported that in Na<sub>2</sub>SO<sub>4</sub>-60% V<sub>2</sub>O<sub>5</sub> melt, the degradation features showed the cracking of the oxide scale under the influence of the fluxing action of the melt for both Fe-base alloy Superfer 800H and Cobalt base alloy Superco 605.

Many researchers have studied hot corrosion and oxidation behaviour of iron based and nickel based superalloy. Hot corrosion of Ni based alloys at 600-700°C experience accelerated oxidation due to formation of spongy structured oxide scale of Ni(VO<sub>3</sub>)<sub>2</sub>. In case of Fe based alloy the formation of Cr<sub>2</sub>O<sub>3</sub> is observed at the earlier stage of hot corrosion due to high affinity of Cr towards oxygen. But with time oxide scale spalling is reported and attributed to severe strain due to Fe<sub>2</sub>O<sub>3</sub> precipitation from the liquid

phase. The presence of different elemental phases would also impose severe strain on oxide scale resulting in cracking and exfoliation of the scale (Singh et al. 2005).

The corrosion resistance of superalloy is correlated with the chemical composition of the alloy particularly at high temperature. Unfortunately, many alloying elements show an adverse effect on the mechanical properties of the superalloy at high temperatures and on its resistance to hot corrosion. For examples, elements such as tungsten, vanadium and molybdenum are excellent in terms of improving the mechanical properties, but their presence makes the alloys highly susceptible to hot corrosion (Stringer 1987) while, Cr is most effective alloying element for improving the hot corrosion resistance of superalloy. The positive effect of Cr and Al on hot corrosion of IN657 alloy is observed by the formation of protective  $\text{Cr}_2\text{O}_3$  and  $\text{Al}_2\text{O}_3$  protective oxide scale inhibiting dissolution. It is also reported that higher Cr content in the alloy would decrease the strength and ductility of the alloy at high temperature (Otsuka and Rapp 1990).

The addition of alloying elements tantalum and titanium are influential for hot corrosion resistance, while small additions of manganese, silicon, boron and zirconium do not provide makeable hot corrosion resistance of superalloys (Pettit and Meier 1984). He also suggested that addition of carbon is detrimental to hot corrosion. For example, addition of molybdenum and iron made to Inconel 718 reduced the hot corrosion resistant. The addition of 9.5% tungsten and minor additions of other alloying elements rendered CM247LC highly susceptible to hot corrosion. Increase in chromium and a small amount of titanium in Nimonic 75 is responsible for hot corrosion resistance (Gurrappa 2003).

From the discussed literature, it appears that developing an alloy having both high temperature strength and high temperature corrosion resistance simultaneously is not easy, since some alloying elements improve high temperature strength while some improve high temperature corrosion resistance. Components of gas turbines working under elevated operating temperatures experience high cyclic fatigue, thermal stress, and are also exposed to salt environment. Better performance with greater efficiency in

gas turbines can be achieved by surface coatings that can endure environmental degradations thereby ensuring the mechanical stability of the component life.

#### **2.4 Protective coating**

Coating can be defined as a layer of material, developed or deposited on the surface of an object known as substrate with the aim of obtaining required surface properties (Burakowski and Wierzchon 1999). Coatings provide a way of extending the limits of use of materials at the upper end of their performance capabilities, by allowing the mechanical properties of the substrate materials to be maintained while protecting them against wear or corrosion (Sidky and Hocking 1999).

Thermal spray coating techniques are widely practiced in many industrial applications for surface engineering. Various properties such as wear and corrosion resistance, thermal or electrical insulation can be achieved using thermal spray coating techniques using suitable coating materials (Yamada et al. 2002). The term thermal spray designates a family of processes that use chemical or electrical energy to melt/soften and accelerate coating particles on to the surface for deposition. The quality of coating is determined by the nature of the thermal spray process and the processing parameters. Thermal spray coatings are a good option to repair components and prevent excessive degradation because of the fact that during the deposition process no significant changes occur in the microstructure of substrates (Santa et al. 2009). The principle of thermal spray is to melt material feedstock (wire or powder) and accelerate the melt in high velocity stream to impact on a substrate where rapid solidification followed by deposit build up occurs (Miguel et al. 2003).

The thermal spray processes that are used to deposit the coatings for protection against high-temperature corrosion and wear are listed below as summarised by Heath et al. (1997):

- Flame spraying
- Plasma spraying
- High Velocity Oxy-fuel (HVOF) spraying
- Detonation Gun

These thermal spray processes are basically differentiated from each other on the basis of particle speed, flame temperature and spray atmosphere. In spray processes the coating adhesion is very sensitive to surface preparation and it depends upon the mechanical anchorage to the surface of the substrate. Therefore contaminants such as rust, scale grease, moisture, etc. must be removed from the surface. After cleaning, roughening of the substrate surface dry sand grit blasting is necessary (Heath et al. 1997).

Among the thermal spray coating processes, plasma spraying is reported to be versatile technology that has been successful as a reliable cost-effective solution for many industrial problems. Plasma spraying is the most flexible thermal spray process with respect to the sprayed materials. The high temperatures of plasma spray processes permit the deposition of coatings useful for applications requiring protection against high temperature corrosion, oxidation and wear and also special applications for thermal, electrical and biomedical purposes (Sidhu and Prakash 2006A).

#### **2.4.1 Plasma spraying**

Plasma spraying is family of thermal spray group, which utilises electrical energy to deposited finely divided metallic and non-metallic materials in molten or semi-molten state on a prepared substrate (Fauchais et al. 2001).

Plasma techniques are used to produce thick coatings of several micrometres at high production rates with greater coating efficiency without affecting the mechanical properties of the substrate alloy. But major drawback of these processes is poor adhesion, specifically in case of ceramics on metals. This can be overcome by the use of bond coat interlayer between substrate and top coat (Yoshida 1993). The key features of plasma spraying are formation of microstructures with fine elongated splats, ability to produce coatings that do not show change in composition with thickness, ability to process materials in virtually any environment.

Plasma spray coatings find applications which demand prevention of corrosion and wear of materials, heat resistant properties and production of monolithic and near net shape profiles. Powder of glassy metals can be plasma sprayed without changing their amorphous characteristics. High temperature superconductive materials have also been

deposited by the plasma spray process. The plasma spray also finds application in reclamation of worn or corroded components, production of aerospace and nuclear power components (Pfender 1988).

#### 2.4.2 Plasma Spray Processing and Coating Formation

A plasma torch or gun consists of a water cooled copper anode and cylindrical tungsten cathode as shown in Figure 2.5. Argon gas flows around the cathode and through the anode. The shape of the anode is made in the form of a radial concentric nozzle. The inert gases, usually argon (Ar), helium (He), or nitrogen (N<sub>2</sub>) or mixtures of these flow around the cathode and exits through the anode (Sidky and Hocking 1999). The material used for anode is usually high purity oxygen free copper (Fauchais 2001).

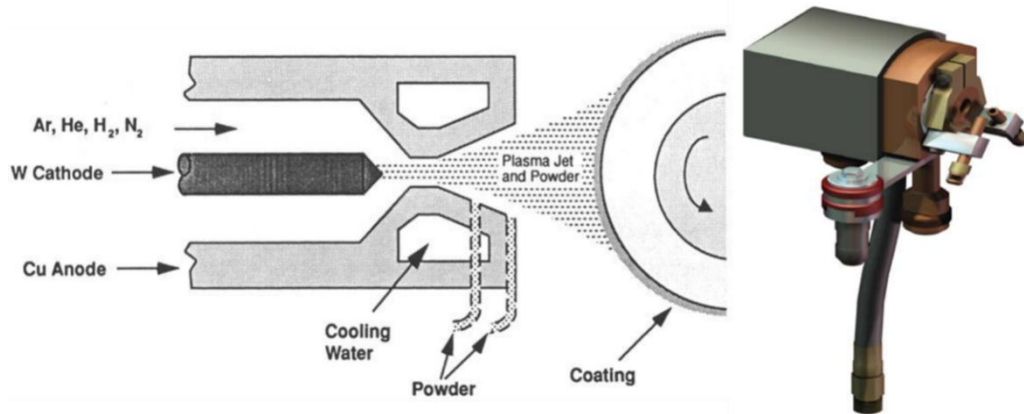


Figure 2.5 Plasma Spray schematic (Tucker 1994).

A high energy dc arc is maintained between the electrodes. As the inert gases pass through the arc, reaction between the electrons from cathode source and the gas molecules results in dissociation or ionization of the gas, and thus creating plasma state. The gases are heated as they pass through high energy arc, expand radially and axially and accelerate through the nozzle forming high velocity stream (Sidky and Hocking 1999). The gas plasma generated by the arc consists of free electrons, ionised atoms and some neutral atoms as reported by Tucker (1994). The plasma emerges at a temperature of 6,000 - 12,000°C at a distance of 1 cm from the nozzle, decreasing rapidly to 3000°C at a distance of 10 cm from the nozzle. The point of entry of the powder into the plasma jet is usually in the diverging portion of the nozzle or sometimes the powder is fed externally. In some applications RF (Radio frequency) discharges are

used as heat sources instead of dc arc and main difference between them is torch internal diameter which influences on particle flow velocity i.e. below 100 m/s for RF torch (Fauchais 2004).

Plasma gas velocities with most conventional torches are subsonic, but supersonic velocities can be generated by using converging-diverging nozzles with critical exit angles. The most important parameters relative to the powder particles at impact on the surface are their temperature, velocity and extent of reaction with the gaseous environment (Tucker 1994). The particle velocity is in the range of 120 to 600 m/s. The high impingement speeds of the molten particles during spraying are intended to ensure that the molten droplets disintegrate on contact surface instead of remaining as discrete droplets and this process is known as splat formation. The structure of the plasma sprayed coatings is envisaged as a series of interlocking splats (Batchelor et al. 2003). Further a rapid quenching of the sprayed particles takes place due to the radial spreading and increase in surface area of rather small mass of the spray particles. The time necessary for solidification is about  $10^{-8}$ -  $10^{-6}$  seconds (Knotek 2001). The solidification of a impinging splat is generally achieved before the next particle impacts at the same location (Fauchais 2004).

In plasma spraying the bonding is suggested to be obtained from the mechanical interlock and solid state adhesion between the atoms in the coatings and substrate. Mechanical interlocking is physical keying between a deliberately roughened substrate and a coating that is in very close contact with the substrate (Batchelor et al. 2003). The quenching stresses within the spray particles increase the interlocking effects (Knotek 2001).

### **2.4.3 Process variants of plasma spray techniques**

The plasma spray process can be performed under different environments and various process variants (Knotek 2001). Different plasma spray techniques are listed below:

1. Atmospheric Plasma Spray (APS)
2. Vacuum (VPS) or Low Pressure Plasma Spray (LPPS)
3. Shrouded Plasma Spray (SPS)
4. Controlled Atmosphere Plasma Spray (CAPS)

APS, due to its relatively high deposition efficiency, flexibility, and easy automation has become a commercial coating process for producing wear and corrosion resistance coatings (Dong et al. 2012). It is the most economical process variant which is carried out in air. The powder particles can interact with the air limiting the choice of the spray material leading to oxides built into the coating. The major fields for APS-applications are coatings for wear and corrosion protection, often based on oxide ceramic materials. Other typical coating materials are metals and some alloys especially insensitive to oxidation (Susila et al. 2015).

VPS takes place in a closed chamber with reduced pressure and the coating process started after the chamber is evacuated to pressures  $< 10^{-1}$  mbar and refilled with an inert gas atmosphere. In order working chamber pressure the pump has to be employed in order to remove the steadily injected plasma gases. These methods are used for the metals that are too reactive to be sprayed in air (Sidky and Hocking 1999). The main drawback of the system is high technical effort/expense for achieving the vacuum conditions and also it cannot be used for insight repair. For some application where the low melting point material as substrates, there is insufficient convective heat transfer within the chamber.

SPS has been developed to reduce the effort for chamber and pumping system for less expensive applications. Similar to shrouded welding processes, envelope of an inert gas, which is not ionized, protects the plasma jet from the surrounding oxygen containing atmosphere and also improves substrate cooling (Tucker 1994). CAPS is the combination of vacuum plasma spraying and inert-gas plasma spraying system.

#### **2.4.4 Role of spray coating**

Coatings are expected to provide protection against high temperature oxidation by forming a dense, adherent oxide scale comprising of oxides of active elements of coating that provides a barrier between the high-temperature gases and the underlying metal (National Materials Advisory Board, 1996). Bluni and Marder (1996) have suggested that in order to protect the base alloy against high-temperature corrosion, thermal spray coatings must possess the chemical composition that promotes the formation of continuous, dense and thick enough oxide scale to significantly delay the

diffusion of corrosive species to the substrate and also to form the protective oxides at splat boundaries and thus fill voids or pores.

The plasma sprayed MCrAlY coatings are commonly deposited as thick coatings on large industrial components to lengthen service life under oxidising atmosphere (Wu et al. 2001). Under high temperature oxidising environment, MCrAlY coatings are referred as secondary aluminium and chromium oxide formers. Initially they form chromium oxide on the surface followed by aluminium oxide under the chromium oxide layer (Warnes 2003). Also the NiCrAlY coatings are used as bond coats in many applications for providing a rough surface for mechanical bonding of the top coat. The bond coat protect the underlying substrate against high temperature corrosion and minimize the effect of coefficient of thermal expansion mismatch between the substrate and the top coat materials (Evans and Taylor 2001). Many studies reported on the high temperature oxidation/corrosion behaviour of MCrAlY (M= Ni, Co, Fe) coatings by varying the Cr from 18-40% and Al from 8-16% indicate that high Cr and low Al MCrAlY resist typically LTHC, while low Cr and high Al MCrAlY resist HTHC (Eliaz et al. 2002). The severity of high temperature corrosion attack on metallic coatings such as aluminide, chromide and MCrAlY coatings on nickel base superalloys is estimated with respect to large temperature range and described in Figure 2.6 (National Materials Advisory Board, 1996).

In general, alloy coatings based on iron, nickel and cobalt have been developed to form protective oxide scales of either  $\text{Cr}_2\text{O}_3$ ,  $\text{Al}_2\text{O}_3$  or  $\text{SiO}_2$  under high temperature oxidizing conditions. At temperatures above 900 °C,  $\text{Cr}_2\text{O}_3$  react with oxygen to form volatile  $\text{CrO}_3$  reducing the lifetime of coating.  $\text{Al}_2\text{O}_3$  and  $\text{SiO}_2$  can withstand higher temperature up to 1200-1300°C,  $\text{SiO}_2$  formation is limited to environments with adequate oxygen activity due to the tendency of forming volatile  $\text{SiO}$  at low oxygen activities (Puetz et al. 2010).

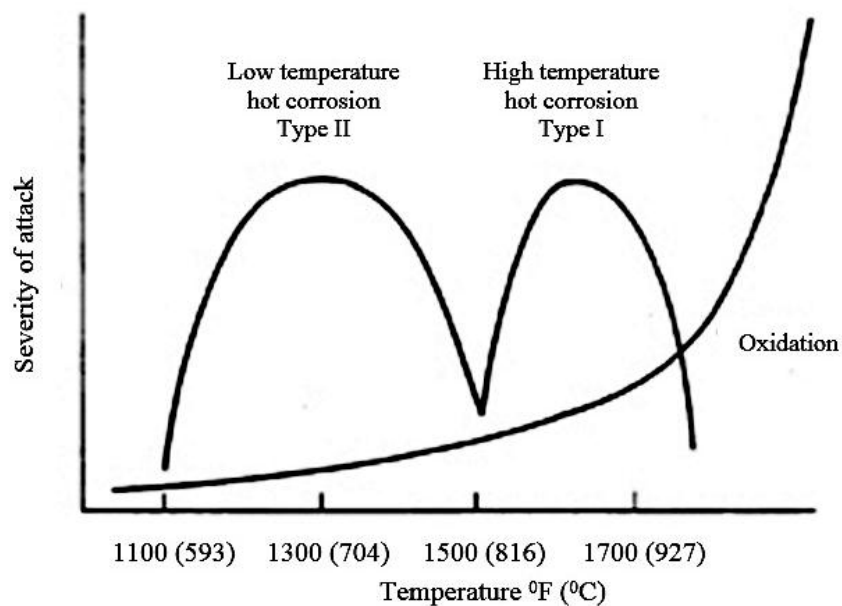


Figure 2.6 High-temperature attack of metallic coatings (aluminide, chromide, MCrAlY) at different temperature ranges (National Materials Advisory Board, 1996).

MCrAlY coating is known for its higher temperature oxidation and hot corrosion resistance. It is suggested that presence of minimum chromium of about 20% in the alloys results in the formation of protective oxide layer which reduces hot corrosion (Stringer 1987). NiCrAlY coatings are undergone lesser degradation by providing most oxidation resistant, while CoCrAlY systems provide good hot corrosion resistance. Under high-temperature oxidation and type I hot-corrosion resistance, NiCrAlY coatings that form a stable alumina scale offer the best performance. Whereas, under type II hot-corrosion conditions, high chromium (25-30%) containing CoCrAlY coatings exhibit least corrosion attack (Nicholls et al. 2002) (Rajendran 2012). Cobalt enhances hot corrosion resistance as the diffusivity of sulfur in cobalt is nearly one hundredth of that in nickel and the melting temperature of  $\text{Co}_4\text{S}_3$ -Co eutectic ( $876^\circ\text{C}$ ) is higher than  $\text{Ni}_3\text{S}_2$ -Ni ( $644^\circ\text{C}$ ) eutectic (Jena and Chaturvedi 1984).

It is reported that Ni<sub>23</sub>Co<sub>15</sub>Cr<sub>12.5</sub>Al<sub>0.5</sub>Y (wt. %) coating had satisfactory oxidation and hot corrosion properties for blade airfoils. Brittle to ductile transition temperature of MCrAlY coating can be shortened from  $700^\circ\text{C}$  to  $300^\circ\text{C}$  by addition of Co to NiCrAlY combination i.e NiCoCrAlY (Goward 1998). The isothermal oxidation behaviour of plasma sprayed CoNiCrAlY, CoCrAlY, NiCoCrAlY and NiCrAlY

coating at 1000°C for 1000 h was investigated by D Seo et al. (2008). Interestingly CoCrAlY exhibits highest oxidation resistance with 50 times lesser parabolic rate constant ( $K_p$ ) value than NiCrAlY, since Ni element diffused from the substrate may help the CoCrAlY to be more stable. Because, CoNiCrAlY and NiCoCrAlY are the coatings which mean that they are more stable in interdiffusion than CoCrAlY and NiCrAlY. High temperature oxidation and corrosion resistance of different coating systems are illustrated in Figure 2.7.

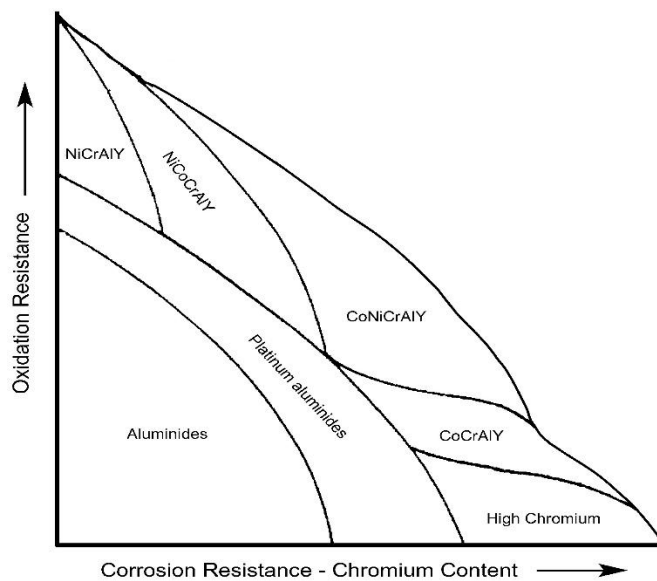


Figure 2.7 High temperature oxidation and corrosion resistance of different coating systems (Nicholls et al. 2002).

The addition of different reactive elements (Y, Si, Ti, Zr and Hf) to CoCrAl coating on Ti substrate for erosion resistance was investigated by Nicholls et al. (2002). All the coatings are heat treated in 1000°C for 100h before subjected to erosion. The author has reported that existence of pegging between the coating and scale interface increases the erosion resistance of the scale, particularly for coating with Hf and Y. Coating with Si and Ti resulted in smooth coating-scale interface and accordingly higher erosion rate. Even though Zr contributed pegging interface, it still resulted in higher erosion rate due to porous non protective layer. Interestingly coating without addition of active elements having smooth interface also provides better erosion resistance than Zr, Si and Ti. This is due to greater integrity of the scale morphology and/or due to the presence of minor amounts of titanium oxide at the interface diffused from the substrate material.

In recent years attempts have been made to improve the traditional MCrAlY coatings by addition of reactive elements such as Ti, Zr, Hf, Si, Ta, Ce, Ru, Ir, and Mo (Yuan et al. 2015). Reactive element Y enhances the adhesion of alumina scale and lower Y-oxide in the alumina scale can decrease the grain-boundary diffusion resulting in slower oxidation rate. While segregation of Hf in alumina grain boundaries accelerates the inter diffusion of oxygen. Ru and Ir oxides have no direct influence on the oxidation of the coating. Thus it is evident that under both oxidising and erosive environment the presence of Y as a reactive element in MCrAl coating is more feasible.

MCrAlY coatings (M=Co, Ni or both) is generally employed to prevent oxidation and hot corrosion up to 1100°C. However, these coatings are reported to be undesirable for the applications in wear conditions, since its lower hardness leads to severe material loss (Bolelli et al. 2015). Oxide coatings individually used for high temperature thermal cycling, corrosion and thermal barrier purpose, but more prone to severe erosion loss by brittle cracking (Amaya et al. 2009).

Carbides such as WC and Cr<sub>3</sub>C<sub>2</sub> coatings with minor amount of metallic binder are used for high temperature wear resistant applications. Although these coatings have excellent wear behaviour, they are not good for applications in hot corrosion environments (Zhang et al. 2016). There are many high temperature applications such as compressor outlet blades, vanes and disks, turbine exit blades, vanes and disks and turbine inlet disks and outer casing where both corrosion and wear problems predominate (James and Rajagopalan 2014).

The addition of oxide particles to high temperature coating materials strengthens the coating and eventually increases the hardness and wear resistance. (Bobzin et al. 2008) studied wear behaviour of 10 wt. % YSZ oxide of reinforced in NiCoCrAlY coating at 700 °C. It is reported that reinforced refractory oxides act as hard phases and provide greater resistance to wear and these oxides also have shown greater chemical stability. Similarly, the reinforcement of refractory carbides such as WC, WC-Co, TiC, and CrC to the metallic matrix will greatly increase the wear resistance of the coating. Wang et al. (1996) studied that the wear behaviour of plasma sprayed NiCrSiB coating reinforced with WC coating and he reported that addition WC reinforcements increases

hardness and wear resistance as compared to NiCrSiB coating. Therefore development of composite coating by reinforced with hard phases (oxides and carbides) appears as a possible solution in order to couple the accelerated oxidation resistance of the metal matrix to the hardness of the ceramic phase (Bobzin et al. 2008) (Zhao et al. 2004).

#### **2.4.5 Literature based on oxide reinforced coatings**

The percentage of hard phase reinforcement in the metal matrix and its effect on wear behaviour has been studied by many researchers. NiCoCrAlY coated using HVOF technique provides better fracture toughness when reinforced with 40%  $Al_2O_3$  compared to 60%  $Al_2O_3$  which shows excellent hardness. Also it is mentioned that scratch test results showed that for Ni+20%  $Al_2O_3$  the coating could resist up to 6.9 N the critical load which is 3-4 times higher than Ni+40% and Ni+60% coating composition (Grewal et al. 2013). Hence we can presume that Ni+40% is good composition for impact erosion applications. (Zhao et al. 2004) reported that 50%  $Al_2O_3$  reinforcement with NiCoCrAlY provided observed 5% improvement in sliding wear resistance at room temperature. The erosion was observed to be severe with presence of brittle cracking features. The author has reported that higher  $Al_2O_3$  has reduced the cohesion between the splats thus loosening overall coating structure. Recently Bolelli et al. (2015) studied the wear behaviour of NiCrAlY+ $Al_2O_3$  coatings with  $Al_2O_3$  addition ranging from 0, 3, 6, 12, 18 wt.% at both room and high temperature. At room temperature, the wear resistance increased gradually with increase in reinforcement and 18% $Al_2O_3$ +NiCrAlY exhibits 3 times higher wear resistance than NiCrAlY coating. Wear proceeds by local cracking and spallation of the tribo-layer, allowing for the occasional occurrence of adhesive wear. At the temperatures of 400°C and 700°C, no much difference is observed between all the coatings with respect to wear resistance. Hence the effect of the added  $Al_2O_3$  therefore becomes irrelevant. The dominant wear mechanism is tribo-oxidation, due to the formation of dense “glaze” layer by direct oxidation of coating surface. Tribo oxidation is a phenomenon in which major oxides are formed on the surface and the counter body. Studies by Susila et al. (2015) reported that NiCrSiB coating with 40%  $Al_2O_3$  reinforcement shows 60% and 20% higher erosion resistance at 30° and 90° impact angle as compared to the substrate AISI 304. The better resistance at 30° than 90° impact angle is attributed to the pinning and shielding effect of the  $Al_2O_3$

reinforcement thus restricting the erodent impact. Coating experienced combined ductile and brittle erosion with respect to matrix and reinforcement. From the above literature it is observed that reinforcement of  $\text{Al}_2\text{O}_3$  as hard phase is used particularly for improving mechanical and tribological properties. Most of the literatures available on hot corrosion and oxidation behaviour of  $\text{Al}_2\text{O}_3$  reinforced YSZ,  $\text{TiO}_2$  and  $\text{Y}_2\text{O}_3$  coatings are for the purpose of thermal barrier applications (Afrasiabi et al. 2008) (Mishra and Mishra 2014). Only limited literature is available on the hot corrosion and oxidation studies of  $\text{Al}_2\text{O}_3$  reinforced metal matrix composite coating.

The CoNiCrAlY is reinforced with variable YSZ oxide (0, 5, 10 and 15 wt. %) was coated by HVOF technique on IN 617 to investigate the strength improvement. The ball milled composite powders are annealed for 10 h at  $1000^\circ\text{C}$  and then coated by plasma spray to study the grain growth. The coating with reinforcement of 10% YSZ, milled for 24 h and annealed for 10 h showed delay in the grain growth due to the uniform distribution of a large amount reinforcements in the matrix (Tahari 2015).

Wear and hot corrosion behaviour of  $\text{Cr}_2\text{O}_3$  reinforced Ni and Co based coating at  $800^\circ\text{C}$  was investigated by Zhang et al. (2016). He suggested that NiCoCrAlY- $\text{Cr}_2\text{O}_3$  coating experience severe brittle fracture and undergone two times the wear rate of CoNiCrAlY- $\text{Cr}_2\text{O}_3$  coating at temperatures below  $400^\circ\text{C}$ . Above this temperature, the oxide formed behaves like a lubrication film and exhibits lower wear rates for both the coatings up to  $800^\circ\text{C}$ . NiCoCrAlY- $\text{Cr}_2\text{O}_3$  coating experience lesser weight gain as compared to CoNiCrAlY- $\text{Cr}_2\text{O}_3$  due to presence of spinel oxide  $\text{NiCr}_2\text{O}_4$  and  $\text{CoCr}_2\text{O}_4$  formed in the upper scales showed better oxidation resistance at  $800^\circ\text{C}$  for 140 h. The oxidation rate for CoNiCrAlY- $\text{Cr}_2\text{O}_3$  coating was  $1.36 \times 10^{-2} \text{ mg/cm}^2\text{h}$  and NiCoCrAlY- $\text{Cr}_2\text{O}_3$  coating showed a value of  $1.03 \times 10^{-2} \text{ mg/cm}^2\text{h}$ . In hot corrosion condition CoNiCrAlY- $\text{Cr}_2\text{O}_3$  coating exhibited higher resistance with corrosion rate of 0.25 times of the NiCoCrAlY- $\text{Cr}_2\text{O}_3$ . The higher hot corrosion resistance is attributed to the formation of more stable  $\text{Co}_3\text{S}_2$  eutectic having higher melting point than  $\text{Ni}_3\text{S}_2$ .

The use of rare earth elements to improve wear and corrosion resistance of thermal sprayed coatings was initially attempted by (Wang et al. 1996). Various alloy coatings, intermetallic coatings and ceramic coatings were modified by reinforcing rare earth

elements to investigate improvement in hardness, toughness, bond strength and thermal shock resistance of the coating materials. Accordingly, he investigated the mechanical and erosion properties of NiAl intermetallic coating with reinforcement of Ceria ( $\text{CeO}_2$ ) in varying wt. % of 0, 2, 5 and 8. The NiAl intermetallic coatings containing ceria showed features of less porosity, higher hardness, and higher elastic modulus than the NiAl coatings. However coating with 2%  $\text{CeO}_2$  showed higher hardness (765 HV) and higher young's modulus (178 Gpa). Due to the improvement in mechanical properties and physical integrity, the NiAl intermetallic coatings containing 2%  $\text{CeO}_2$  exhibited significant increase in their erosion resistance of 7 times as compared to NiAl coatings. Also coating contains 2%  $\text{CeO}_2$  possesses higher resistance as compared to reaming composition. Erosion rate of the coating containing 5%  $\text{CeO}_2$  is very close to that of the coating containing 2%  $\text{CeO}_2$ . From this it is suggested that the optimal content of  $\text{CeO}_2$  in the NiAl intermetallic coatings should be less than 5% (Wang and Chen 2003)(Wang et al. 2007). Ogawa et al. (2006) also reported that the addition of Ce to bond coat can effectively resist crack propagation of the thermal barrier coating up to 1000°C.

Cerium being a surface-active element reduces the surface tension and the interfacial energy between the crystal nucleus and the melt during the process of coating solidification, which results in improving the wetting properties and decreasing the contact angle between the melt and a substrate (Tian et al. 2006). Grain refinement and purification of the grain boundaries was seen in case of FeNiCr coatings containing  $\text{CeO}_2$  leading to 30% increase in micro hardness and 15% higher wear resistance than FeNiCr coatings (Zhang et al. 2006). Some studies were reported on tribological behaviour of  $\text{CeO}_2$  reinforced (0, 0.3, 0.6, 0.9, 1.2 and 1.5 wt. %) Ni-WC composite coating. Lowest porosity of 3.2% was observed for 0.6%  $\text{CeO}_2$ , while coating having 0.9%  $\text{CeO}_2$  obtained highest hardness of 1300 HV. Coating contains 0.9%  $\text{CeO}_2$  exhibits higher wear resistance and coating contains 0.6%  $\text{CeO}_2$  exhibits higher solid particle erosion resistance. Coating contains 1.5%  $\text{CeO}_2$  shows lower wear and erosion resistance due to higher porosity (Purkayastha and Dwivedi 2013) (He et al. 2014).

Higher microhardness of about 697-920 HV and lower average porosity of 0.58% are reported by Kamal et al. (2010) while investigating the mechanical characteristics of detonation sprayed  $0.4\text{CeO}_2+\text{MCrAlY}$ . Zhou and Ouyang (2017) recently published

that electrodeposited Ni-CeO<sub>2</sub> nanocrystalline coating has better interfacial adhesion and dense structure of oxides as compared to pure Ni coating.

#### **2.4.6 Literature based on carbide reinforced coatings**

Thermal sprayed cemented carbide composite coatings are extensively used to resist wear and erosion. WC-Co is the most commonly used composite coating for tribological applications, but its corrosion and oxidation performance limits the application below 450°C (Berger and Livshitz 1996).

Cr<sub>3</sub>C<sub>2</sub>-NiCr based coatings are principally used under corrosive and moderate wear environments at temperatures up to 850°C (Staia et al. 2001) (Matthews et al. 2009). In the following paragraphs literature concerning tribological aspects of WC and Cr<sub>3</sub>C<sub>2</sub> based coatings are explained followed by the oxidation and corrosion studies.

Some publications report about the high temperature erosion, corrosion, and wear behaviour of thermal sprayed carbide based cermet coatings (Chatha et al. 2012) (Sidhu et al. 2007A). Limited studies done to compare their hot corrosion resistance as a specific function of the metal matrix composition are explained below.

Among all types of reinforcing particles, refractory carbide (WC) is one of the popular reinforcement in alloy coatings for its extremely high hardness and excellent wear resistance. The mechanical properties and wear resistance of self-fluxing alloys (NiCrFeSiB) coatings can be increased by the reinforcement of refractory carbides such as WC, VC, WC-Co, TiC, and CrC (Kulu and Phil 2002). Kim et al. (2003) investigated the effect of WC (15, 25, 35, 40, 45 wt. %) reinforced NiCrBSiC coating on physical and mechanical properties of coating. The 35% WC+NiCrBSiC coating showed better hardness of 950 HV and porosity of 1.5%. Also, 35% WC+NiCrBSiC coatings exhibited almost 3 times higher wear resistance than coatings having 15 and 45% WC. There is a toughening effect and hardness increase without significant increase in brittleness up to 35% WC. Further increase of WC decreased the hardness which is attributed to sharp increase of the porosity and pore size that generates high stress concentration. Referring to above literature Ramesh et al. (2010) studied solid particle erosion behaviour of NiCrFeSiB coatings reinforced with 35% WC-Co. The coating experienced both

ductile and brittle erosion mechanism. WC hard phase in the matrix provides shielding effect on erodent impact which is attributed to greater erosion response.

Bolelli et al. (2014A) studied wear performance of WC reinforced Fe alloys. The wear resistance of WC-FeCrAl coating at room temperature is compared to WC-CoCr coating. Results indicate that the coating exhibits a wear mechanism showing plastic deformation and pull-out of individual carbide particles. At 400°C, WC-FeCrAl coatings oxidise more extensively than WC-CoCr by developing an oxide layer based on FeO+WO<sub>3</sub>. Wear occurred by plastic smearing and structural modification of the oxide layer and its abrasion and delamination. The wear rates are higher than that of the WC-CoCr reference which does not develop a complete oxide layer and undergoes limited abrasive grooving. Similarly he studied the wear behaviour of Fe-Cr-Ni-Si-B-C alloy coatings and also alloy strengthened with 20 wt. % and 40 wt. % WC-Co. Considerable reinforcing effect of the WC-Co phase was observed at room temperature as a result of decrease of the wear rate of composite coatings by more than one order of magnitude compared to Fe-based coatings. While at higher temperatures, the strengthening effect of WC-Co became less significant due to thermal softening and to WC-Co being more reactive to high temperature oxidation than the Fe alloy (Bolelli et al. 2014B). From the above literature it is understood that both wear and solid particle erosion properties can be improved by WC reinforced composite coating at room temperature as well as at higher temperature.

Cr<sub>3</sub>C<sub>2</sub> is a hard phase known for its good tribological response. Stein et al. (1999) studied the solid particle erosion performance by varying the percentage reinforcement of Cr<sub>3</sub>C<sub>2</sub> in NiCr and FeCrAlY metal matrix. FeCrAlY reinforced composite provided higher erosion resistance than NiCr based coating in the full range of reinforcement percentage (20-80). The author suggested that the optimum hard phase carbide percentage for maximum erosion resistance is preferable around 40%. Later Wang and Verstak (1999) studied the influence of impact angle and reported that the Cr<sub>3</sub>C<sub>2</sub>/TiC–NiCrMo coating presented good thermal shock resistance and high temperature erosion resistance at both high and low impact angles with 2-3 times less thickness loss than the blended Cr<sub>3</sub>C<sub>2</sub>–NiCr coating. Then (Wang and Shui 2002) studied the erosion behaviour of Cr<sub>3</sub>C<sub>2</sub> reinforced with 25 wt.% metallic binders such as NiCr, NiCSi,

NiCrMoNb. These coating powders are produced as a blended and sintered composite. Cr<sub>3</sub>C<sub>2</sub>/25%NiCr coating contributes superior bond strength (39 MPa), hardness (704 HV) and lower porosity (<1%) which is confirmed by greater erosion resistance by lowest thickness loss. Matthews et al. (2009) studied the role of phase microstructure on high temperature erosion of Cr<sub>3</sub>C<sub>2</sub>-NiCr coatings. At ambient temperature this coating exhibited a brittle response wherein it transferred high loads to a greater volume of material without plastic deformation. As the temperature increased ductility increased and the coating showed plastic deformation and toughening at the carbide-matrix interface thus localised brittle fracture was not seen. The increased NiCr matrix ductility also reduced the impact loading on the splat boundaries leading to a generalised transition in erosion response from splat based to microstructure based erosion mechanisms. Later Murthy et al. (2010) studied the influence of binder property and effect of heat treatment on Cr<sub>3</sub>C<sub>2</sub>-50(Ni20Cr) coating while investigating the solid particle erosion response. The erosion rate decreased with increasing annealing temperature up to 600°C and then increased marginally. An improvement of erosion resistance of nearly 40% was seen in the coating annealed at 600°C compared to the as-sprayed coating. Annealing of coating leads to microstructural changes in binder due to occurrence of recrystallization at 400°C and the precipitation of Cr<sub>23</sub>C<sub>6</sub> carbides within nanocrystalline binder phase. With increase in annealing temperature to about 800°C the carbide volume fraction increases and the metallic binder becomes only Ni. The secondary precipitates are mainly Cr<sub>3</sub>C<sub>2</sub> carbides. The formation of nanocrystalline binder with ultra-fine precipitates results in peak hardness that gradually decreases with further annealing as the binder softens.

Recently, Vashishtha et al. (2017) studied solid particle erosion behaviour of WC-12Co, WC-10Co-4Cr and Cr<sub>3</sub>C<sub>2</sub>-25NiCr coatings using particle velocity as 30, 60, 90 m/s at 30° and 90° impact angle. WC-12Co coatings exhibited relatively higher hardness of 1270±100 HV and WC-10Co-4Cr coatings have higher fracture toughness of 5.1 MPa m<sup>1/2</sup>. For all the coatings, higher erosion rate was observed for high particle velocity 90 m/s. At both impact angles WC-12Co coating experienced higher erosion resistance than other coatings at all the particle velocities. It is also reported that addition of Cr to WC-Co did not provide improvement for erosion resistance. For all

the coatings the transition of erosion mechanism is observed from ductile to mixed (ductile and brittle) with the increased erodent velocity.

Some limited studies are available on oxidation and hot corrosion behaviour of carbide reinforced composite coatings. Sidhu et al. (2006B) compared the hot corrosion behaviour of HVOF sprayed WC-Co, Cr<sub>3</sub>C<sub>2</sub>-NiCr, NiCr and Stellite-6 coatings in molten salt environment at 900°C. He found that among the coatings NiCr is most resistant to hot corrosion followed by Cr<sub>3</sub>C<sub>2</sub>-NiCr coating. WC-Co coating is least resistant to hot corrosion with the coating showing peeling off, spalling and cracking. Studies on the oxidation and hot corrosion behaviour of WC-NiCrFeSiB are conducted by Sidhu et al. (2007A). He has reported that coating is more resistant to oxidation (1.1 mg/cm<sup>3</sup>) than hot corrosion (2.5 mg/cm<sup>3</sup>). Under the molten salt environment chlorine generated by the dissociation of NaCl reacts with alloying elements such as chromium, nickel, and iron forms highly volatile metal chlorides, further diffuse out releasing chlorine resulting in discontinuous loose oxide scale. Whereas, Somasundaram et al. (2014) reported that in case of 35%WC+NiCrAlY coating acidic fluxing is initiated at the tungsten rich particles in the coating, since the activity of WO<sub>3</sub> in molten salt condition is much higher in this area. This resulted in failure of protective oxides on the surface. The author has reported that for the same coating in air environment the presence of tungsten in the coating does not necessarily result in catastrophic oxidation.

Chromium carbide-based cermet (Cr<sub>3</sub>C<sub>2</sub>-NiCr) coatings obtained by thermal spraying are known to exhibit good tribological and oxidation properties in severe operative conditions. Chatha et al. (2012) reported that at 750°C the 80Ni-20Cr coating shows 2.5 times higher hot corrosion resistance than the 75Cr<sub>3</sub>C<sub>2</sub>-25(Ni-20Cr) coating. The presence of oxides of nickel and chromium, and their spinels might have contributed to the hot corrosion resistance of HVOF sprayed coatings. Baiamonte et al. (2016) studied hot corrosion protection of exhaust valves in naval diesel engines by using different metallic binder with Cr<sub>3</sub>C<sub>2</sub>. The coatings used are Cr<sub>3</sub>C<sub>2</sub>-CoNiCrAlY, Cr<sub>3</sub>C<sub>2</sub>-self fluxing alloy, Cr<sub>3</sub>C<sub>2</sub>-NiCrAlY, Cr<sub>3</sub>C<sub>2</sub>-NiCr, SiO<sub>2</sub>-Mullite-NiCr. Cr<sub>3</sub>C<sub>2</sub>-NiCr coatings show better hot corrosion resistance with the oxide scale of 20 µm than the other coatings. While the Cr<sub>3</sub>C<sub>2</sub> having self-fluxing alloy shows the least hot corrosion performance with high corrosion rate. The coatings consisting of Cr approximately 70

wt. % resists hot corrosion by forming protective chromium oxide up to 700°C. But many of the recent articles reported that the presence of spinels such as  $\text{CoCr}_2\text{O}_4$  and  $\text{NiCr}_2\text{O}_4$  could also provide resistant to hot corrosion degradation (Yuan et al. 2015) (Singh et al. 2016).

From the literature review it can be inferred that the addition of optimum amount of reinforcements such as oxides and carbides will certainly influence the mechanical properties and wear properties of the coatings. Therefore, composite coatings reinforced with such oxides and carbides are projected to offer good resistance to both hot corrosion and erosion at elevated temperatures.

**THIS PAGE IS LEFT BLANK.**

### 3 EXPERIMENTAL PROCEDURE

#### 3.1 Substrate material

Ni based Super alloy-Superni 76 [ASTM equivalent-Hastelloy X] and special steel-MDN 321 [AISI equivalent-321], which are the currently used materials for blades and other components of land based gas turbines and aero engines are selected as substrate materials (Nkhoma et al. 2014) (Matsukawa et al. 2011). The substrate materials are procured in the form of plates from M/s MIDHANI, Hyderabad-India. The plates are cut using shear cutting machine to the dimensions of 25mm x 25mm x 4mm. The composition of as supplied substrate materials are determined by spectroscopy (Table 3.1).

Table 3.1 Chemical composition (wt. %) of substrate alloys.

Type of substrate	Equivalent standard	C	Mn	Si	P	Cr	Mo	Fe	Co	W	Ti	Ni
Superni 76	Hastelloy x	0.08	0.44	0.3	0.004	21.87	9.08	20	1.39	0.52	0.14	Bal
MDN 321	AISI 321	0.1	1.46	0.55	0.013	18.13	-	Bal	-	-	0.62	10.36

#### 3.2 Coating powders

The CoCrAlY powder is mechanically blended with oxides and carbides to develop composite feedstock. The powders are procured from Praxair India Private Limited, Bangalore. The specific chemical composition (wt. %) of CoCrAlY is Co23Cr13Al0.62Y, Al<sub>2</sub>O<sub>3</sub> is 99.9% pure, CeO<sub>2</sub> is 99.9% pure, WC-Co is W5.5C-12Co and Cr<sub>3</sub>C<sub>2</sub>-25NiCr is Cr10C21Ni. The chemical composition of the coating powders is reported in Table 3.2.

Table 3.2 Composition and particle size of powders.

No	Coating powder	Chemical composition (wt. %)
1	CoCrAlY+Al <sub>2</sub> O <sub>3</sub> +YSZ	70 % (CoCrAlY)+28% (Al <sub>2</sub> O <sub>3</sub> )+2% (YSZ)
2	CoCrAlY+CeO <sub>2</sub>	98 % (CoCrAlY)+2% (CeO <sub>2</sub> )
3	CoCrAlY+WC-Co	70 % (CoCrAlY)+30% (WC-Co)
4	CoCrAlY+Cr <sub>3</sub> C <sub>2</sub> -NiCr	70 % (CoCrAlY)+30% (Cr <sub>3</sub> C <sub>2</sub> -NiCr)

### 3.3 Deposition of coatings

Coatings are developed through plasma spray process using METCO USA 3 MB equipment (M/S Spraymet Surface Technologies Pvt. Ltd. Bengaluru, India). The plasma spraying process parameters adopted for deposition are listed in Table 3.3. These spray parameters were kept constant throughout all coating processes. Substrate alloys were grit-blasted using  $\text{Al}_2\text{O}_3$  (approximately 150  $\mu\text{m}$ ) prior to the plasma spraying for better adhesion between the coating and the substrate.

Table 3.3 Spray parameters of Plasma Spray process.

Argon	Pressure	0.7 MPa
	Flow	40 L/min
Hydrogen	Pressure	0.35 MPa
	Flow	7 L/min
Current		490 A
Voltage		60 V
Powder feed		60 g/min
Stand of Distance		100-125 mm

### 3.4 High temperature solid particle erosion studies

#### 3.4.1 Experimental setup

Solid particle Erosion test was carried out as per ASTM G76-13 standard using Air Jet Erosion Tester TR-471-800 shown in Figure 3.1 (Ducom instruments Pvt Ltd, Bangalore, India) at an operating temperature of 600°C. Figure 3.1 shows the fixture equipped with movable heating furnace unit and Figure 3.1c shows the fixture in heated condition. The schematic diagram of erosion machine is shown in Figure 3.2 which represents the components and its working cycle. The test rig consists of an air compressor, particle feeder, an air-particle mixing chamber, nozzle and heating furnace. The pneumatic system drives the furnace unit in upward and downward direction. This helped in reducing the heat loss during the testing condition. Conveyor belt is used as feeder which carries the erodent particles to mixing chamber and then accelerated by passing the air and erodent mixture through a nozzle of diameter 1.5 mm. The distance from the specimen surface to the nozzle end was 10 mm. The erosion studies were

performed both on substrate and coating at 600°C. The erosion testing parameters are listed in Table 3.4.

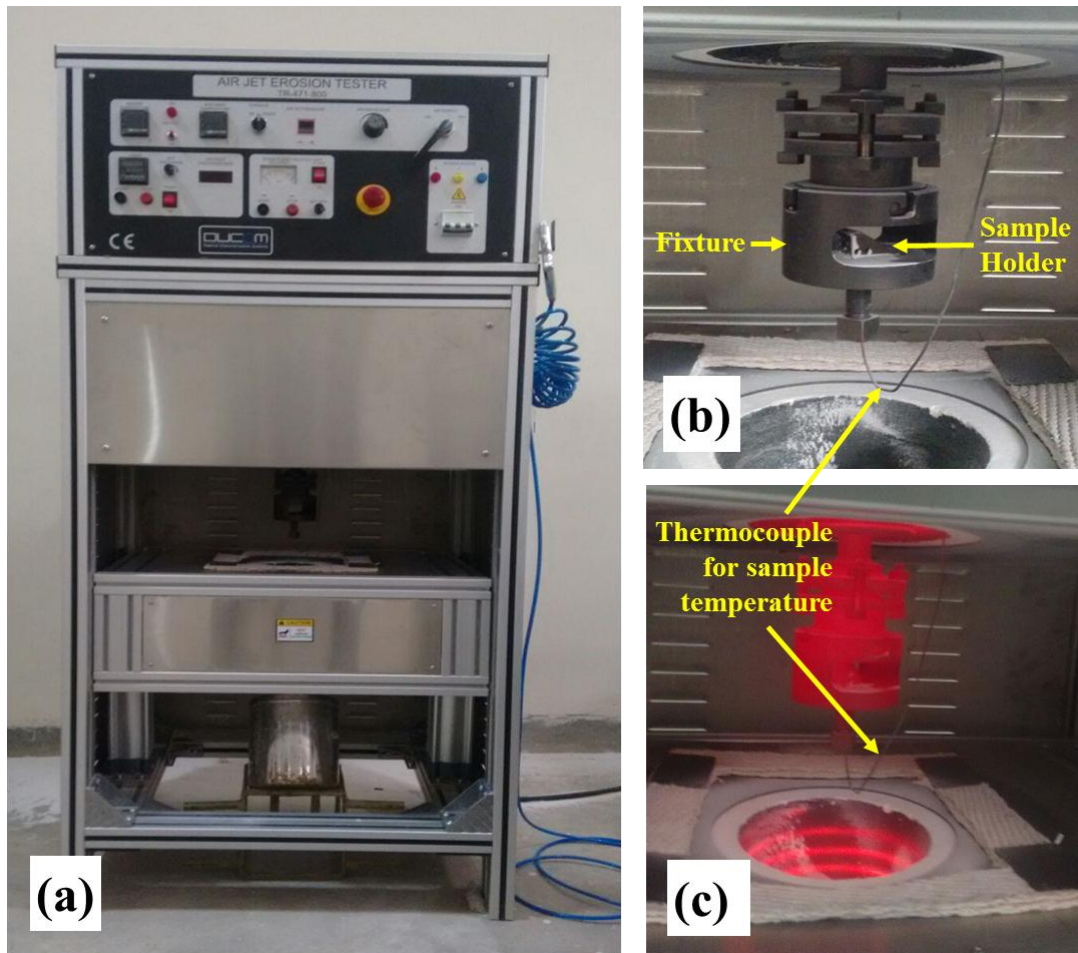


Figure 3.1 (a) Air jet erosion test rig (b) Fixture, sample holder and heating element (c) heated specimen under test.

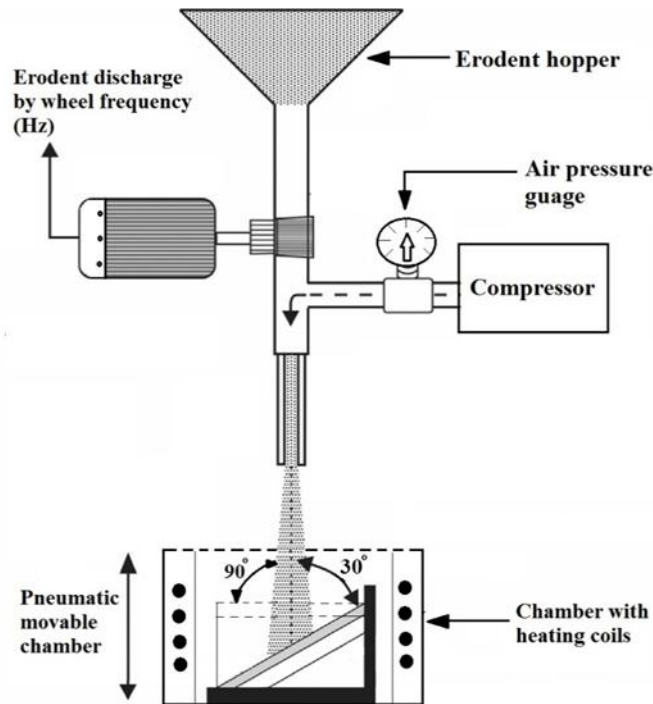


Figure 3.2 Schematic of erosion test rig.

Table 3.4 Air jet erosion test parameters.

Erodent material	Alumina
Erodent average size	30-50 $\mu\text{m}$
Particle velocity	35 m/s
Erodent feed rate	2 g/min
Impact angle	30° and 90°
Temperature	600 °C
Cycle test time	10 min
Standoff distance	10 mm
Nozzle diameter	1.5 mm

### 3.4.2 Erosion test

Erosion tests are conducted on both uncoated and coated alloys at 600°C. The erosion parameters are listed in Table 3.4. Initially the samples are cleaned using acetone and weighed in electronic weighing balance having a least count of 0.001g. The SPE process is carried out for 5 cycles with a cycle duration is 10 minutes each. After each

erosion cycle, the eroded sample is cleaned in acetone using ultrasonicator and weighed to determine the weight loss. The weight loss normalized by the mass of the alumina particles causing the weight loss (i.e., testing time x particle feed rate) was then computed as the dimensionless incremental erosion rate. The above procedure was repeated for all the cycles. The constant value of the incremental erosion rate was defined as the steady-state erosion rate.

Erosion volume loss was measured using non-contact optical profilometer (Zeta-20). Non-contact optical profiler provides three dimensional profiler patterns with excellent accuracy (Ivosevic et al. 2006) (Wiecinski et al. 2014). The scanned surface is profiled by computer generated map by extracting the data from three-dimensional interferogram of scanned surface. Erosion Volume loss is measured by taking difference of volumes obtained before and after erosion. Schematic representation of volume loss measurement is shown in Figure 3.3 where,  $V_1$  is volume measured prior to the erosion which is considered as reference and  $V_2$  is the volume measured after erosion with the same scanning area (field of view). The difference between  $V_1$  and  $V_2$  gives the total erosion volume loss.

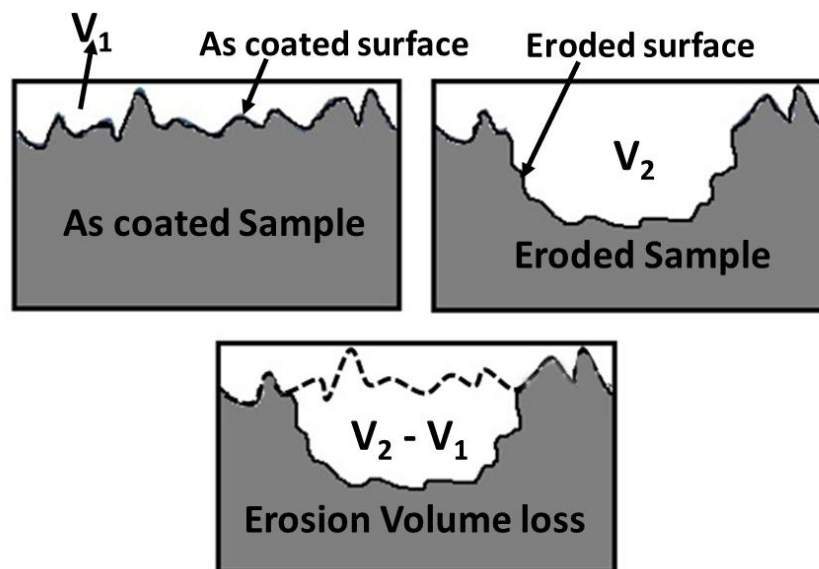


Figure 3.3 Schematic of erosion volume loss measurement (Ivosevic et al. 2006).

### **3.5 High temperature oxidation and hot corrosion studies**

#### **3.5.1 Experimental setup**

Oxidation and hot corrosion studies are conducted at 700°C in silicon carbide tube furnace supplied by Heatron Pvt. Ltd, India. The furnace is calibrated to an accuracy of  $\pm 5^\circ\text{C}$  using an external thermocouple fitted with a temperature indicator in order to determine the difference between set value and hot zone temperature value. Dimensions of the samples were noted carefully with digital Vernier caliper to calculate the total surface area. Consequently, the samples are cleaned with acetone and dried in hot air to remove any moisture. The prepared specimen is kept in an alumina boat and the weight of boat and specimen is measured. The boat containing the specimen is introduced to hot zone of the furnace at a temperature of 700°C. Heating time in the furnace is one hour in still air after which the boat with specimen is taken out and cooled at the ambient temperature for 20 minutes (Ramesh et al. 2011) (Sidhu et al. 2007C). If any spalled scale in the boat that can occur due to thermal stresses is also taken into consideration during weight measurements. Electronic weighing balance (Sartorius BSA223S) with the least count 0.001mg is used. The weight change in samples is measured after each cycle to understand the kinetics of oxidation and corrosion. After every cycle visual examination is made to inspect any scale damage or spallation and color. All oxidation and hot corrosion studies are carried out for 50 cycles. The reproducibility in the experiments is established by repeating some of the experiments.

#### **3.5.2 Oxidation studies in air**

The oxidation test is conducted at 700°C on uncoated and coated alloys in tubular furnace up to 50 cycles as discussed in section 3.5.1.

#### **3.5.3 Hot corrosion studies in molten salt ( $\text{Na}_2\text{SO}_4$ -60% $\text{V}_2\text{O}_5$ ) environment**

The salt mixture of  $\text{Na}_2\text{SO}_4$ -60% $\text{V}_2\text{O}_5$  dissolved in distilled water was coated on the warm samples with the help of camel hair brush. The amount of the salt coating varies from 3.0 -5.0  $\text{mg}/\text{cm}^2$  (Somasundaram et al. 2014). The salt coated specimen is dried in the furnace for 3 h at 150°C and weighed before being exposed to hot corrosion tests. The uncoated as well as coated samples after application of salt were subjected to hot corrosion in the tube furnace at 700°C for 50 cycles as discussed in section 3.5.1. The tubular furnace used for oxidation and hot corrosion test is shown in Figure 3.4.

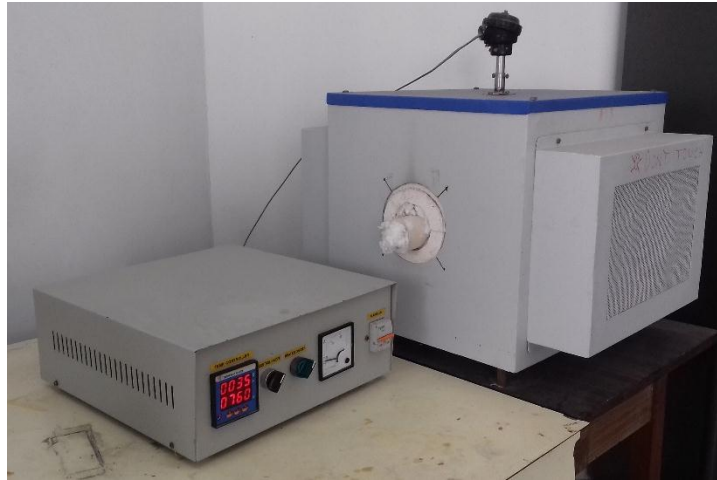


Figure 3.4 Tubular furnace for oxidation and hot corrosion test.

### **3.6 Characterisation of coatings, analysis of corrosion and erosion products**

#### **3.6.1 Preparation of samples for cross sectional analysis**

The samples were cut along the cross-sections using metallurgical sample saw-MS-10 (DUCOM Instruments Pvt. Ltd., Bangalore, India) at slow speed of 200 rpm. The sectioned samples were cold mounted and then polished up to 2000 grad SiC emery paper. Finally cloth polishing was carried out using ultrafine (0.25  $\mu\text{m}$ ) diamond paste to obtain mirror finish.

#### **3.6.2 Measurement of as-sprayed coating thickness**

The thickness of the as-sprayed coatings was continuously monitored during the process of plasma spraying with the help of Minitest-2000 thin film thickness gauge (Elektro-Physik Koln Company, Germany, precision  $\pm 1 \mu\text{m}$ ). Further, the back scattered images obtained by SEM along the coating cross section were used to validate the average coatings thickness.

#### **3.6.3 Porosity and density measurement**

BIOVIS Materials Plus optical microscope, interfaced with image analysing software (version-4.58) was used to obtain optical image along the cross-section of as-sprayed coatings and to determine the porosity percentage. Fifteen fields of view were taken in each sample at 250X magnification.

The densities of the coatings was measured by water immersion method using pycnometer in accordance with standard ASTM test method C-135-03. Pycnometer is

used in the study to measure sample weight in air and water is shown in Figure 3.5.

Density of the coating is calculated using following equation

$$\rho = \frac{(W - p)}{(w_1 - p) - (w_2 - w)} \quad (3.1)$$

$p$  = weight of the stoppered pycnometer in g.

$W$  = weight of the stoppered pycnometer and sample in g.

$w_1$  = weight of the stoppered pycnometer filled with water in g.

$w_2$  = weight of the stoppered pycnometer, sample, and water in g.



Figure 3.5 Pycnometer.

#### 3.6.4 Microhardness measurement

The micro hardness was measured using Omni-tech Vickers tester (MVH-S-AUTO) under 300 g load and a dwell time of 10 s. The indentations were taken along the coating cross section of the coating and the indentations were done at 20 random points with in the coating to obtain the average hardness value.

#### 3.6.5 Fracture toughness measurement

Fracture toughness is one of the significant property responsible for the erosion resistance of the coatings. The fracture toughness of coatings is measured by indentation crack technique (Movahedi 2013) (Macwan et al. 2015). The indentations were done along the cross section with the load of 1 kg. The radial crack is produced using a square pyramid indenter along the diagonal of indentation. The fracture

toughness was calculated using crack length by the following equations (Ramanujam and Nakamura 2009).

$$K_{IC} = 0.0193 (H_V d)(E/H_V)^{2/5} (a)^{-1/2} \dots\dots\dots (c/d \leq 2.5) \text{ Palmqvist Crack} \quad (3.2)$$

$$K_{IC} = 0.0711 (H_V d^{1/2})(E/H_V)^{2/5} (c/d)^{-3/2} \dots\dots\dots (c/d \geq 2.5) \text{ Half penny Crack} \quad (3.3)$$

Where  $H_V$  is the Vickers hardness,  $E$  is the Young's modulus,  $d$  is the half-diagonal of the Vickers indentation. The radial crack length ( $a$ ) is equal to the indentation crack length ( $c$ ) minus the half diagonal of the Vickers indentation ( $d$ ). Values of  $a$ ,  $c$  and  $d$  were measured using SEM images.

### 3.6.6 Bond strength test

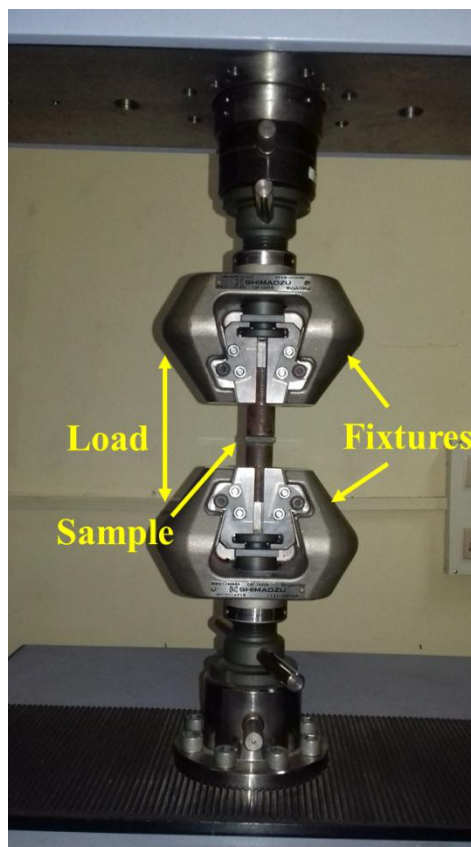


Figure 3.6 Adhesion strength test using ultimate tensile test.

The bond strength (Adhesion strength) test was carried out using Shimadzu hydraulic tensile testing machine, with a crosshead speed of 0.5 mm/min in accordance with ASTM C633-13 standard. The coated specimens were bonded to a 25 mm diameter rod

using HTK ultra-bond adhesive glue and thermal curing is carried in furnace at 150°C. Curing enhances the adhesion between coating and glue. The adhesion strength was calculated as ratio of maximum load to the cross-sectional area of sample. The loading of the glued joint is shown in Figure 3.6.

### **3.6.7 X-ray diffraction (XRD) analysis**

X-ray diffraction analysis was conducted for feedstock powders, as-sprayed coatings and after erosion, oxidation and corrosion samples. Diffraction patterns were obtained by RIGAKU MINIFLEX-600 with  $\text{CuK}_\alpha$  radiation and cooper filter at 20 mA under a voltage of 35 kV. The specimens were scanned with a scanning speed of 2 degrees per minute. The  $2\theta$  range of 20° to 90° is used and the intensities were recorded at a chart speed of 1 cm/min with 1°/min as Goniometer speed. Scanning electron microscopy (SEM) and Energy dispersive X-ray (EDAX) analysis

Surface morphology of the coating powder, as-sprayed coating, eroded coating, oxidized coating and corroded coating were examined using scanning electron microscopy. Back scattered images were taken along the cross-section of the polished samples. The elemental compositions of different phases observed on the surface as well as along the cross-section have been obtained using energy dispersive X-ray analysis. SEM/EDAX analysis was performed using JOEL-JSM-6380LA Scanning Electron Microscope (SEM with EDAX Genesis software attachment, JEOL scanning microscope (JSM-840A and JSM-5800) with Link ISIS(UK) EDAX attachment, and Scanning Electron Microscope (LEO 435VP, UK).

## 4 CHARACTERISATION OF COATINGS

In this chapter the results of Coating characterisation are presented. The CoCrAlY+Al<sub>2</sub>O<sub>3</sub>+YSZ, CoCrAlY+CeO<sub>2</sub>, CoCrAlY+WC-Co and CoCrAlY+Cr<sub>3</sub>C<sub>2</sub>-NiCr systems have been characterized in powder form and in as-coated conditions.

### 4.1 Morphology of coating powders

The morphology of the coating powders is examined using scanning electron microscopy as shown in Figure 4.1. In the four composite coatings Co-based alloy powder particles appeared as spherical shapes. Al<sub>2</sub>O<sub>3</sub> appeared as irregular shape particles with angular edges (Figure 4.1a), CeO<sub>2</sub> particles having dimension of 15-35 μm appeared as cluster (Figure 4.1b). Agglomerated spherical carbide particles such as WC and Cr<sub>3</sub>C<sub>2</sub>. The spherical powder increases the flowability and minimize surface tensions (Ruzic et al. 2012). The nominal particle size distribution of the coating powders are measured by laser diffraction technique (Cilas 1064, France) as per ASTM C1070 and reported in Table 4.1. The average particle size for all the composite coatings ranges between 49-59 μm.

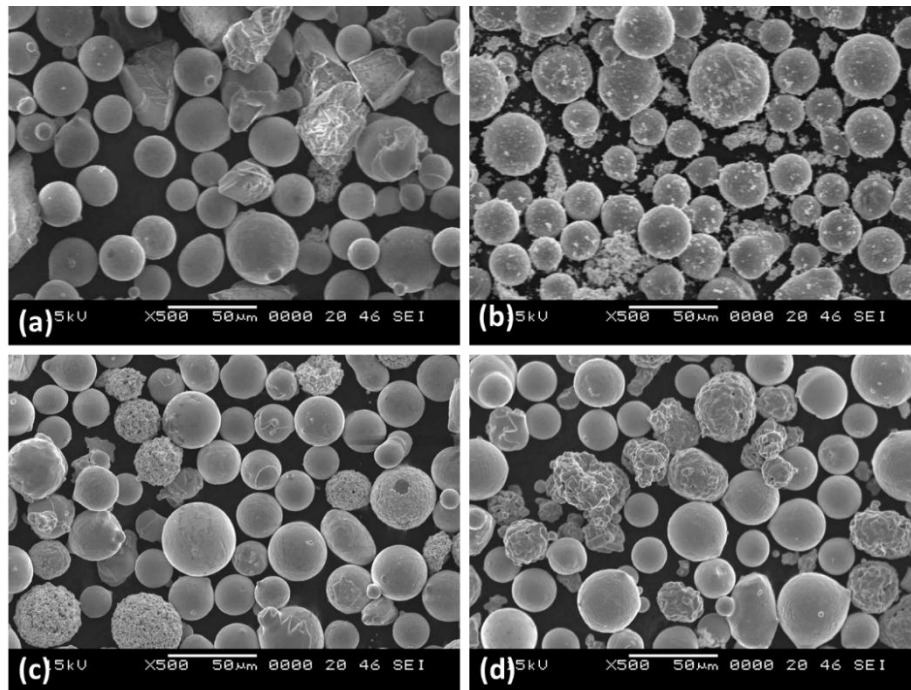


Figure 4.1 SEM morphology of (a) CoCrAlY+Al<sub>2</sub>O<sub>3</sub>+YSZ, (b) CoCrAlY+CeO<sub>2</sub>, (c) CoCrAlY+WC-Co and (d) CoCrAlY+Cr<sub>3</sub>C<sub>2</sub>-NiCr coating powders.

Table 4.1 Particles size ( $\mu\text{m}$ ) distribution of coating powders.

Particle Size	CoCrAlY+Al <sub>2</sub> O <sub>3</sub> +YSZ	CoCrAlY+CeO <sub>2</sub>	CoCrAlY+WC-Co	CoCrAlY+Cr <sub>3</sub> C <sub>2</sub> -NiCr
D (0.1)	23.92	16.79	19.35	21.77
D (0.5)	55.24	45.36	48.62	54.89
D (0.9)	99.78	91.32	89.30	104.43
Mean Diameter	58.19	49.97	51.42	59.00

#### 4.2 Coating thickness and metallographic studies

The accelerated melted/semi melted powder particles impacting on the substrate forming rapidly solidified splats. The building up of these series of layers of splats forms coating of required dimension. The Figure 4.2 shows the cross section of CoCrAlY+Al<sub>2</sub>O<sub>3</sub>+YSZ, CoCrAlY+CeO<sub>2</sub>, CoCrAlY+WC-Co and CoCrAlY+Cr<sub>3</sub>C<sub>2</sub>-NiCr coatings using back scattered electron image. The thickness of the coatings was measured by scanning electron microscope image taken along the cross section of the coatings. The total thickness of the coatings are observed to be in the range of 273-298  $\mu\text{m}$  with the top coat ranges between 142-162  $\mu\text{m}$ . The back scattered electron images in Figure 4.2 shows the different contrast for every element with respect to their atomic number i.e elements having lower atomic number appear dark and elements having higher atomic number appears bright. The Figure 4.2a, c, e and g shows the lower magnified image where top coat, bond coat and substrate which can be easily differentiated and it marked as particulars. The magnified image of coatings cross section is shown in Figure 4.2b, d, f and h. It is observed that the higher operating temperature of plasma spray process makes the particle to molten or semi molten state which resulting in the formation of well flattened lamellar structure. This result in forming the dense compact coating structure. The presence of thin dark line is observed along the splat boundaries of completely flattened splat which are called as oxide stringer. These are formed due to the oxidation of coating particle occurred during coating process due to high in-flight time and temperature of plasma spray process. The Al is observed to be dark grey splat, whereas Co and Cr are the major elements appeared as two different light grey contrast and distributed throughout the coatings (Figure 4.2b,

d, f and h). This observation is same for all the coatings, since the major coating composition or matrix for the coatings is CoCrAlY.

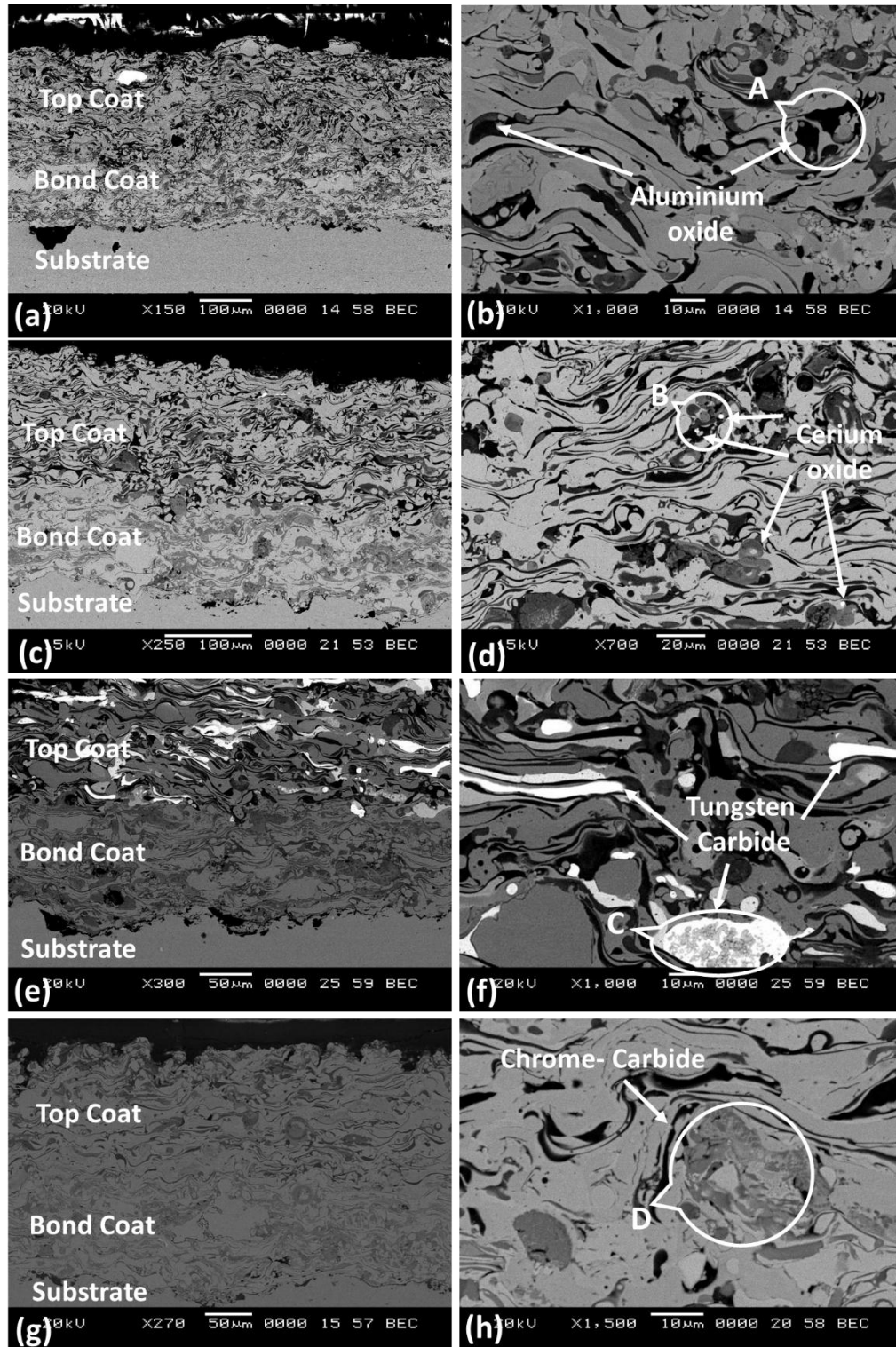


Figure 4.2 SEM morphology of (a, b) CoCrAlY+Al<sub>2</sub>O<sub>3</sub>+YSZ, (c, d) CoCrAlY+CeO<sub>2</sub>, (e, f) CoCrAlY+WC-Co and (g, h) CoCrAlY+Cr<sub>3</sub>C<sub>2</sub>-NiCr coating cross section.

Figure 4.2b shows the completely dark irregular shape splats in CoCrAlY+Al<sub>2</sub>O<sub>3</sub>+YSZ are assumed to be Al<sub>2</sub>O<sub>3</sub> because of its lower atomic and it is also evident from the EDS analysis at region 'A' showing rich O and Al. In case of CoCrAlY+CeO<sub>2</sub> coating, Figure 4.2d shows the presence of CeO<sub>2</sub> particles as bright white small particles distributed along the splat boundaries in and the EDS analysis at region 'B' shows dominant O and Ce elements.

The presence bright white tungsten partially melted splat with black carbides particles inside at region 'C' is observed in magnified cross sectional image of CoCrAlY+WC-Co coating in Figure 4.2f and it is evident from EDS analysis. Also the bright white splats with unusual black carbide spots are observed this may be due to the decarburization of WC at high processing temperature. In case of CoCrAlY+Cr<sub>3</sub>C<sub>2</sub>-NiC coating, from the magnified image in Figure 4.2h it is observed that the all the splat appeared of similar colour with small contrast difference. From the EDS analysis at region 'D' it is observed as constituents of Cr, C and Ni which implies the presence of Cr<sub>2</sub>C<sub>2</sub> splat.

X-ray diffraction pattern of the powder and as-coated samples of all coatings is shown in Figure 4.3. The major peaks of all the powder and as-coated patterns are indexed Co, Cr, and Al<sub>5</sub>Co<sub>2</sub> phases, since in the all the composite coating systems comprises CoCrAlY as a matrix. In all the as-coated patterns metal oxides of Al<sub>2</sub>O<sub>3</sub> is observed which are due to occurrence of oxidation during in flight time, and it is reported that plasma spray process has longer in flight time compared to other thermal spray process (Sharma 2012). Since, Al having higher affinity to oxygen responsible for oxidation during coating process. Also, AlCo and Al<sub>5</sub>Co<sub>2</sub> are the phases indexed in the powder and coated patterns, since these phases shows its presence in wide range of temperatures ranging from 200-1600°C and this phase is observed to be present in Co rich regions. The Al<sub>2</sub>O<sub>3</sub> and CeO<sub>2</sub> are reinforcement phases remain unchanged and same are observed in as-coated patterns of CoCrAlY+Al<sub>2</sub>O<sub>3</sub>+YSZ and CoCrAlY+CeO<sub>2</sub> coating (Figure 4.3a and b).

W<sub>2</sub>C and Cr<sub>7</sub>C<sub>3</sub> are the two phase observed in the as-coated XRD analysis of CoCrAlY+WC-Co and CoCrAlY+Cr<sub>3</sub>C<sub>2</sub>-NiCr coatings, however these are not found in powder XRD analysis (Figure 4.3c and d). This is due to the decarburization of

carbides in WC and  $\text{Cr}_3\text{C}_2$  reinforcements due to high temperature exposure during plasma coating process. The diffraction peak broadening is observed in carbides reinforced as-coated XRD pattern, which be attributed to differential dissolution of carbides in the Co-based matrix and the presence of partly amorphous/fine crystalline phases (Murthy et al. 2010). More peak broadening is observed in case of  $\text{CoCrAlY}+\text{Cr}_3\text{C}_2\text{-NiCr}$  as-coated pattern, indicating more dissolution of  $\text{Cr}_3\text{C}_2$  carbides.

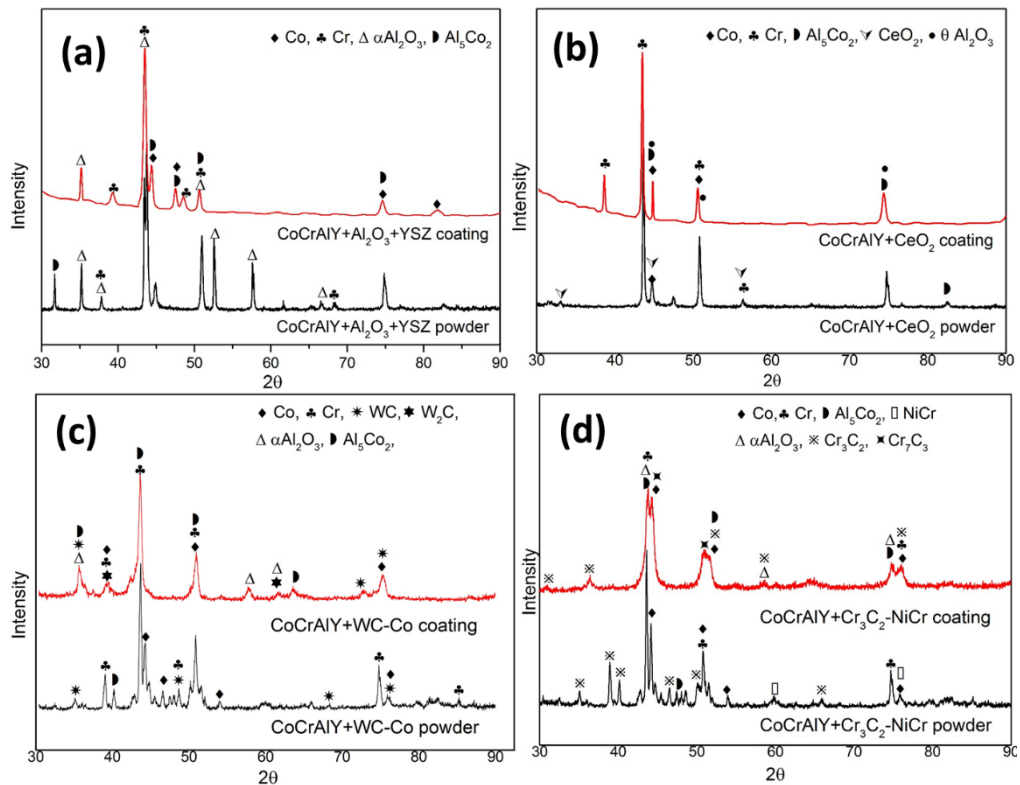


Figure 4.3 XRD patterns of coating powders and as-coated samples of (a)  $\text{CoCrAlY}+\text{Al}_2\text{O}_3+\text{YSZ}$ , (b)  $\text{CoCrAlY}+\text{CeO}_2$ , (c)  $\text{CoCrAlY}+\text{WC-Co}$  and (d)  $\text{CoCrAlY}+\text{Cr}_3\text{C}_2\text{-NiCr}$  coatings.

### 4.3 Porosity and density of coatings

Porosity is one of the prime physical properties of coating which influence the mechanical properties of coating and consequently its resistance to the erosion and corrosion degradation. BIOVIS Materials Plus optical microscope, interfaced with image analysing software version 4.58, was used to obtain optical image along the cross section of as-sprayed coatings and to determine the porosity content. To determine the

porosity fifteen fields of view were taken in each coated samples at 250x magnification. The porosity values of coatings are presented in Table 4.2. CoCrAlY+CeO<sub>2</sub> coating having lowest reinforcement percentage (2 wt. %) leads to better compaction between the metallic splats attributed to the least porosity value. CoCrAlY+Al<sub>2</sub>O<sub>3</sub>+YSZ coating having 30 wt. % of oxides shown the highest porosity value. Whereas CoCrAlY+WC-Co and CoCrAlY+Cr<sub>3</sub>C<sub>2</sub>-NiCr coatings having 30 wt.% of carbides reinforcement show lower porosity values than CoCrAlY+Al<sub>2</sub>O<sub>3</sub>+YSZ coating attributed to the presence of Co and NiCr as binders in carbides. Kim et al. (2003) reported that the porosity and pore size increases with increase in the hard phase reinforcement content in the coating and also responsible to generate high stress concentration.

The densities of the coatings were measured by water immersion method as per ASTM test method designation C-135-03. The density of the coatings are reported in Table 4.2.

Table 4.2 Thickness, porosity and density of the coatings.

Coating type	Coating thickness (μm)	Porosity (%)	Density (g/cm <sup>3</sup> )
CoCrAlY+Al <sub>2</sub> O <sub>3</sub> +YSZ	286	6.2±0.6	5.0±0.3
CoCrAlY+CeO <sub>2</sub>	279	4.6±0.3	6.6±0.3
CoCrAlY+WC-Co	288	5.2±0.5	7.5±0.5
CoCrAlY+Cr <sub>3</sub> C <sub>2</sub> -NiCr	293	5.3±0.5	5.9±0.2

#### 4.4 Evaluation of microhardness

The microhardness values are measured at more than 20 random points along the cross section of the coating and the average values are reported. The average hardness values of coatings as well as substrates are represented by bar chart along with error bar to show standard deviation in Figure 4.4. CoCrAlY+WC-Co coating shows the highest hardness of 384 Hv, whereas other coatings CoCrAlY+Al<sub>2</sub>O<sub>3</sub>+YSZ, CoCrAlY+CeO<sub>2</sub> and CoCrAlY+Cr<sub>3</sub>C<sub>2</sub>-NiCr exhibited the hardness values of 306, 273 and 336 Hv respectively. The standard deviation of coatings are high as compared to the substrate due to its heterogeneous nature. The deformation in coating by indentation purely depends on the resistance offered by the respective and surrounding splats.

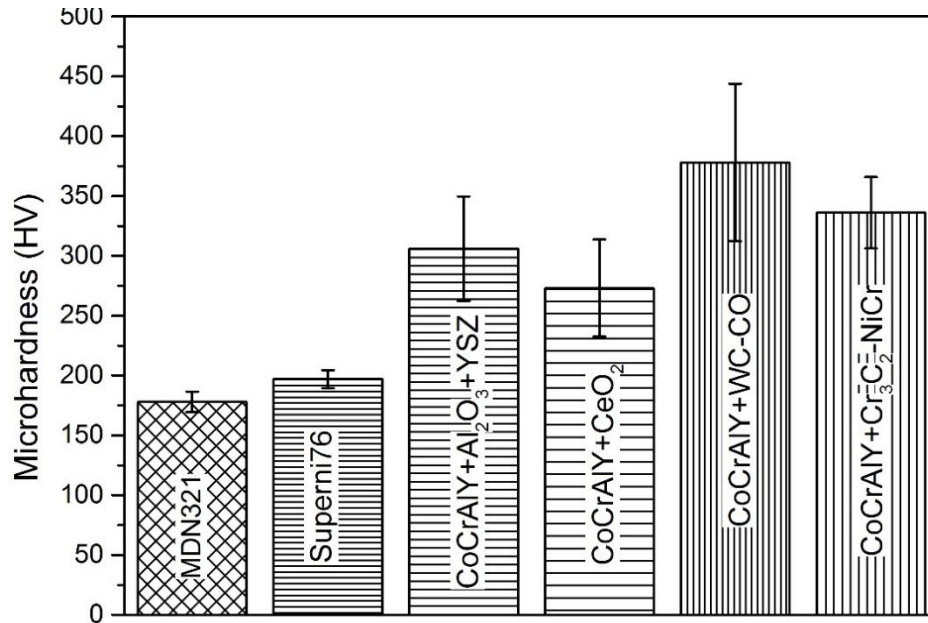


Figure 4.4 Bar chart for average microhardness of substrates and coatings.

#### 4.5 Evaluation of fracture toughness of coatings

The fracture toughness of the coating was measured by indentation crack method considering only those cracks in which crack has propagated along the diagonal of the indentation. Indentations were done under the load of 1 kg and dwell time of 15 seconds in order to produce cracks along the diagonal of the indentations. The ratio of the indentation crack length (c) and the half diagonal of the Vickers indentation (d) is less than 2.5 for all coatings. Hence formed crack is known as Palmqvist cracks and (3.1) is used to calculate fracture toughness. The average toughness value is obtained by five readings measured along the cross section of the coatings. The indentations and cracks produced on coatings cross section are shown in Figure 4.5. CoCrAlY+WC-Co coating displays the highest toughness of  $14.3 \pm 3.5 \text{ MPa m}^{1/2}$  and other coatings CoCrAlY+Al<sub>2</sub>O<sub>3</sub>+YSZ, CoCrAlY+CeO<sub>2</sub> and CoCrAlY+Cr<sub>3</sub>C<sub>2</sub>-NiCr exhibited the toughness of  $9.5 \pm 3.2$ ,  $10.8 \pm 2.1$  and  $11.5 \pm 2.8 \text{ MPa m}^{1/2}$  respectively.

CoCrAlY+Al<sub>2</sub>O<sub>3</sub>+YSZ coating shows long cracks propagated along the weak inter splat boundaries with porous structure leading to lower fracture toughness. Al<sub>2</sub>O<sub>3</sub> reinforcement is likely to develop residual stresses during the coating process which cause lower toughness values (Movahedi 2013). Also cracks propagating from the side of the square indenter is observed in Figure 4.5(a). This types of cracks is also observed in case of CoCrAlY+Cr<sub>3</sub>C<sub>2</sub>-NiCr coatings due to the embrittlement effect of coating by

carbide dissolution in the metal matrix (Mathapati et al. 2017) and shown in Figure 4.5(c).

CoCrAlY+WC-Co coating having lesser porosity with better carbide retention due to higher melting point of tungsten results in higher fracture toughness. CoCrAlY+CeO<sub>2</sub> coating having reinforcement of only 2 wt. % with highest metal matrix experience ductile nature resulting in better fracture toughness.

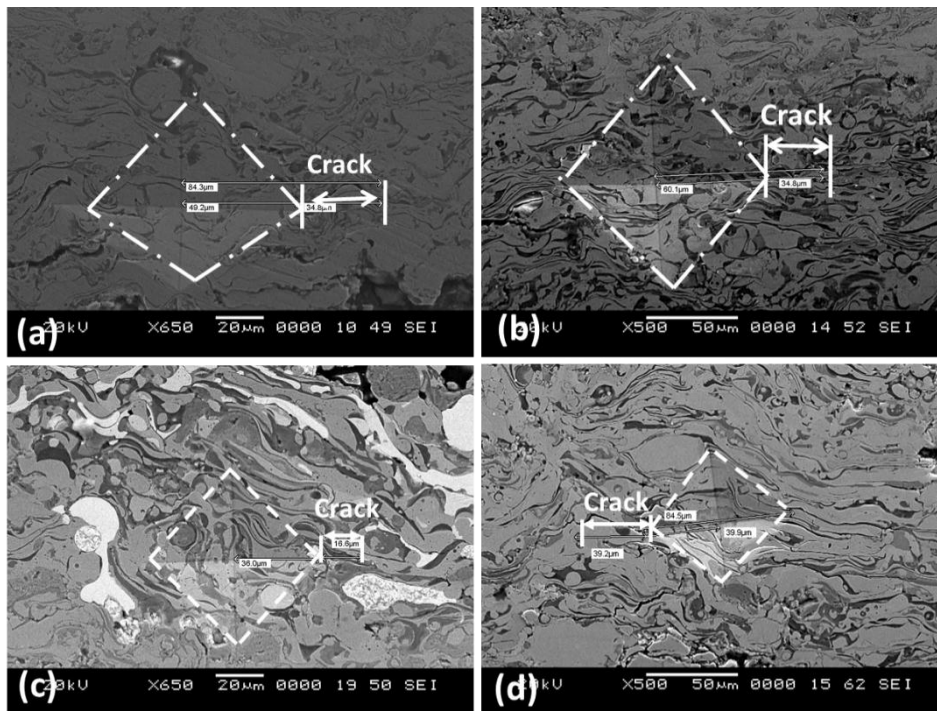


Figure 4.5 Micrographs of cracks produced by indentation on (a) CoCrAlY+Al<sub>2</sub>O<sub>3</sub>+YSZ, (b) CoCrAlY+CeO<sub>2</sub>, (c) CoCrAlY+WC-Co and (d) CoCrAlY+Cr<sub>3</sub>C<sub>2</sub>-NiCr coatings.

#### 4.6 Evaluation of bond strength of coating

Adhesion strength of the coating has good correlation with coating thickness; ASTM-C633-13 standard recommends the top coat to be less than 300µm. Better adhesion of the coating is expected at lower thicknesses as the effect of internal stress will be lower for smaller thickness. Figure 4.6 shows the typical fracture surface between coating and the substrate interface. CoCrAlY+CeO<sub>2</sub> coating obtained the highest bond strength of 15.6±2.2 MPa and other coatings CoCrAlY+Al<sub>2</sub>O<sub>3</sub>+YSZ, CoCrAlY+WC-Co and CoCrAlY+Cr<sub>3</sub>C<sub>2</sub>-NiCr coating exhibited the bond strength of 9.2±3.5, 12.4±3 and 11.5±2.5 MPa respectively.

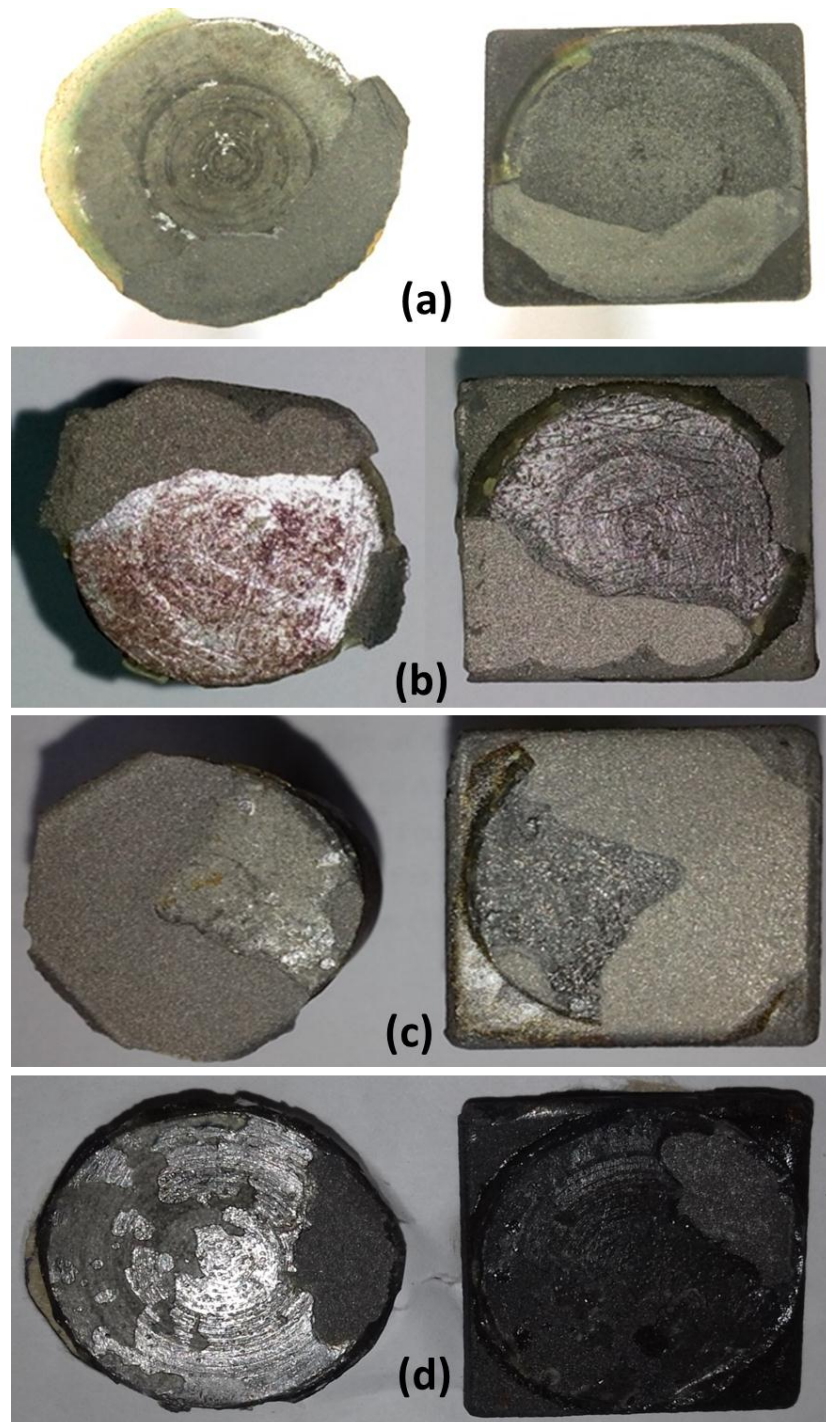


Figure 4.6 Fractured surface of adhesion test sample of (a) CoCrAlY+Al<sub>2</sub>O<sub>3</sub>+YSZ, (b) CoCrAlY+CeO<sub>2</sub>, (c) CoCrAlY+ WC-Co and (d) CoCrAlY+ Cr<sub>3</sub>C<sub>2</sub>-NiCr coating.

Figure 4.6 shows a clear picture of adhesive failure i.e. fracture occurring between coating and substrate which reflects better cohesive strength between the splats in coatings (Irisawa and Matsumoto 2006). Coating adhesion is influenced by

microstructural aspects such as pores and cracks formed during spray process (Sadeghi-Fadaki et al. 2010). In case of CoCrAlY+CeO<sub>2</sub> coating, CeO<sub>2</sub> being a rare earth oxide acts as surface active element refines the microstructure by segregating along the splat boundaries resulting in finer splats and better bonding between splats attributed to higher bond strength as compared to other coatings (He et al. 2014b). CoCrAlY+Al<sub>2</sub>O<sub>3</sub>+YSZ coating shows the least adhesion strength value attributed to higher porosity of the coating.

## 5 SOLID PARTICLE EROSION STUDIES

The solid particle erosion behaviour of uncoated MDN 321 and Superni 76 alloys and the plasma spray coated CoCrAlY+Al<sub>2</sub>O<sub>3</sub>+YSZ, CoCrAlY+CeO<sub>2</sub>, CoCrAlY+WC-Co and CoCrAlY+Cr<sub>3</sub>C<sub>2</sub>-NiCr coatings at elevated temperature of 600°C is described in this chapter. The impingement angles of erodent of 30° and 90° are provided to study the extreme erosion conditions using angular alumina sand as erodent. The erosion performance is almost similar for coating on both Ni and Fe based alloys under same coating parameters, substrate temperature and roughness (Nithin et al. 2017A). Similar observations have also been reported by Sidhu et al. (2007B) for the erosion performance of NiCr coating on GrAl, T-11 and T-22 substrates. This is attributed to the phenomenon of splat morphology of coating which remains common for both metals and ceramics substrates unless its roughness and temperature changed. The mechanical and physical properties of coating depends on splat morphology (Sampath et al. 1999) which is a characteristic features of particle velocity, size, shape, flattening and solidification of the splats. In the present study erosion performance of all the four coatings on Superni 76 are done and presented.

### 5.1 Visual examination of erosion samples

The macrograph and schematic diagram of erosion scar produced on the target surface at an impact angles of 90° and 30° are shown in Figure 5.1 and Figure 5.2 respectively. The schematic representation referring to Figure 5.2 differentiates the center as localized region of material loss (A) and surrounded area as region of elastically loaded material (B).

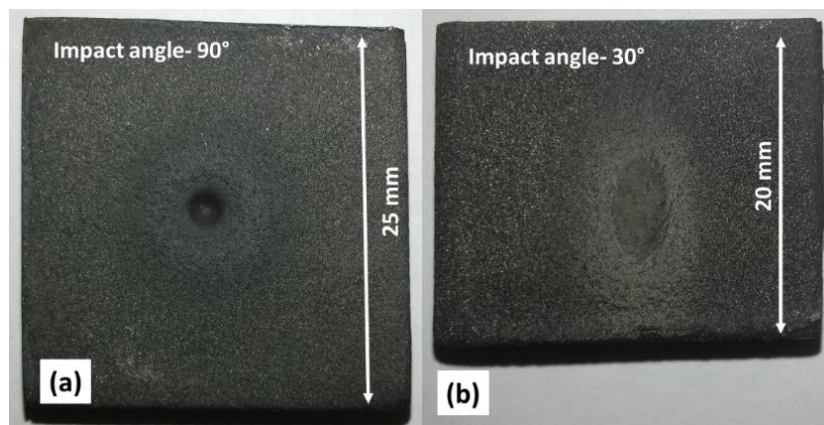


Figure 5.1 Erosion scar produced on target surface at different impact angle.

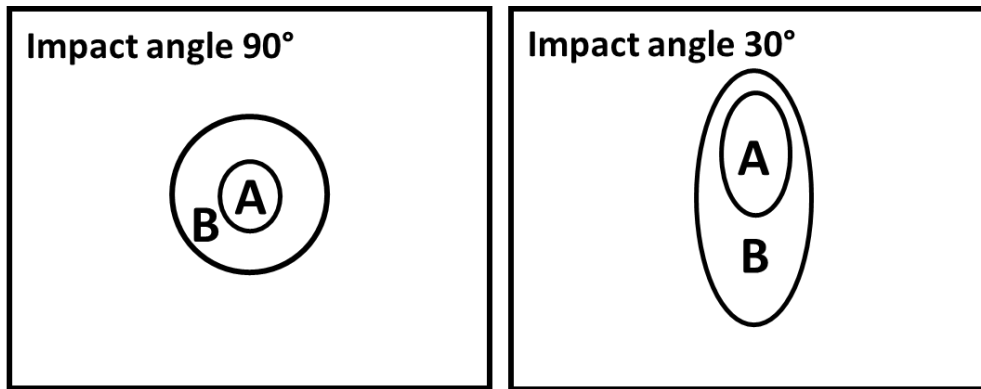


Figure 5.2 Erosion scar produced at different impact angle.

### 5.2 Erosion rate based on weight loss method

The weight loss of the sample after each cycle (of 10 minutes duration) is recorded and the erosion rate is measured as the ratio of cumulative weight loss to the mass of the erodent as (Mishra et al. 2006) (Ramesh et al. 2010).

$$\text{Erosion rate (g/g)} = \frac{\text{Cumulative weight loss of sample}}{\text{Mass of erodent}} \quad (5.1)$$

The erosion rate curve is drawn as a plot of erosion rate Vs. cumulative mass of the erodent, for both the impact angles. The erosion rate of uncoated alloys and coatings are shown in Figure 5.3 and Figure 5.4 respectively. It is assumed that, all the mass of erodent impacted the target since the erosion scar produced is within the sample dimension.

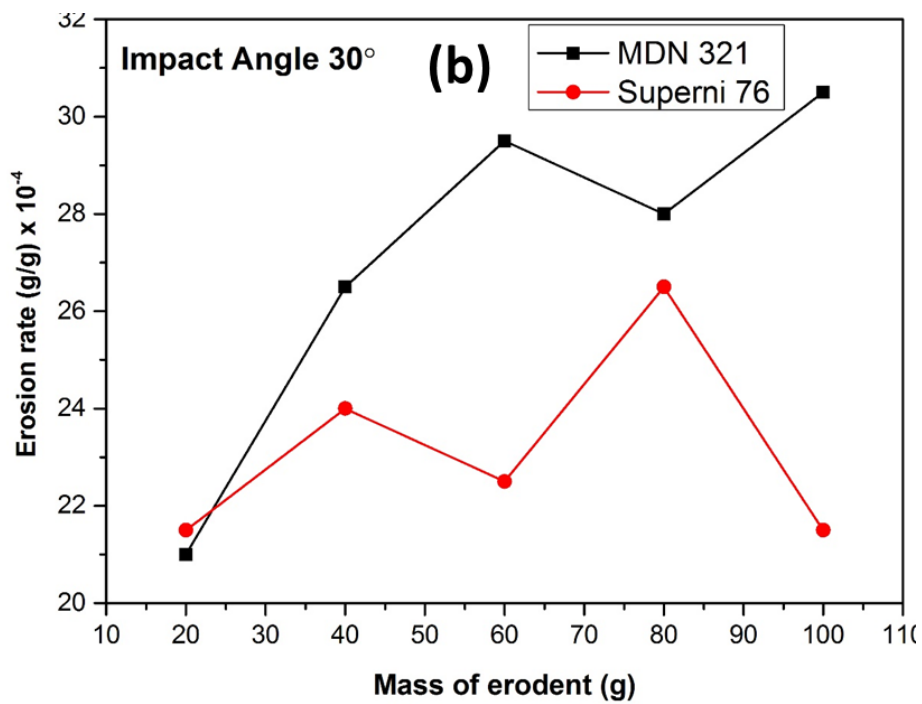
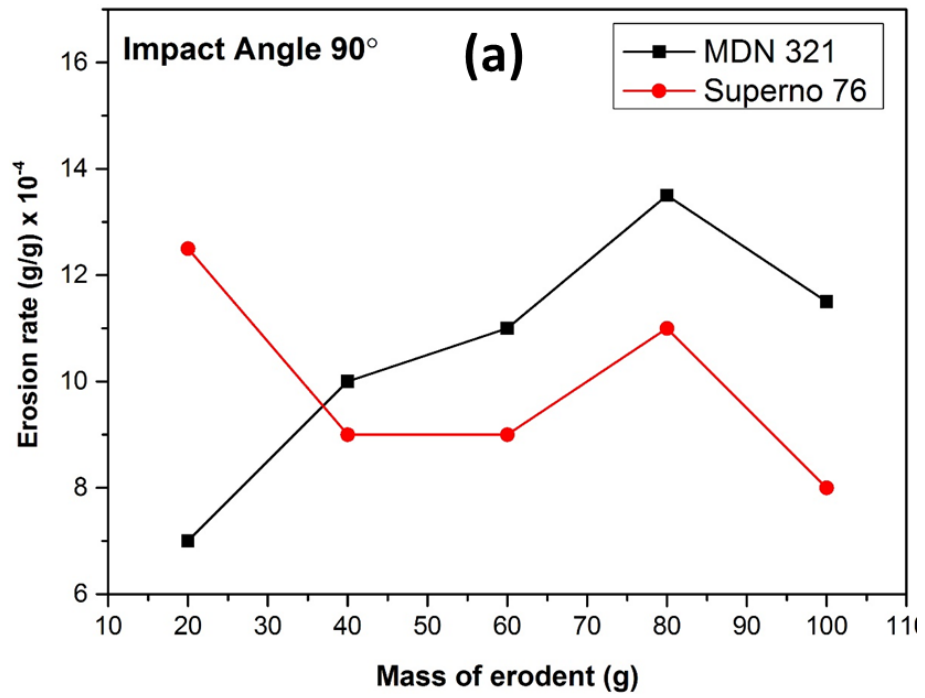


Figure 5.3 Variation of erosion rate for uncoated samples at impact angle of (a) 90° and (b) 30°.

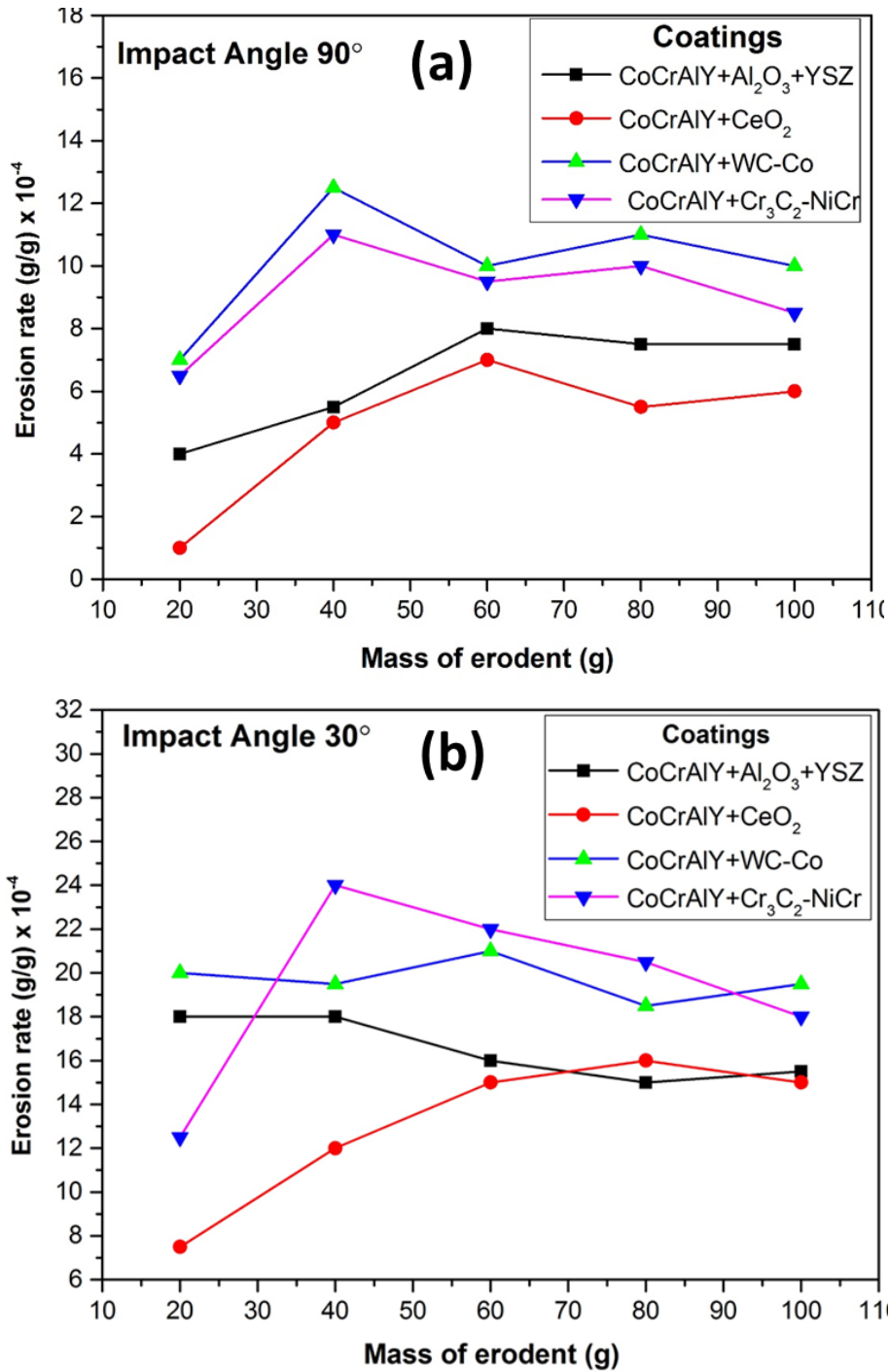


Figure 5.4 Variation of erosion rate for all coatings at 90° (a) and 30° (b) impact angle.

The graphs clearly indicate variations in erosion rate after each cycle. The uncoated alloys and the coatings show lower erosion rate during the initial cycles. This is due to rapid oxidation of the active elements of target surface which resulting in addition of

weight in the form of oxide. In contrast to this, due to thermal stresses sputtering of surface oxides may cause higher weight loss.

Uncoated alloys and coatings show immense variation in the erosion rate in each cycle due to embedding and detaching of alumina erodent. At higher temperature material tends to be more ductile which aids easy embedment and detachment of erodent particles causing weight gain and weight loss respectively during the erosion cycles. Due to these unpredictable variations in erosion rate, it is very complex to grade the erosion resistance of the coatings and uncoated alloys.

The conventional method for the evaluation of erosive volume loss by normalising weight loss with density may not provide accurate measurement in multilayer coatings in terms of top coat and bond coat with different densities. The evaluation of erosion performance by weight loss method is not considered as promising technique. Based on some of the research articles available in the literature on grading of erosion performance using optical profiler (Ivosevic et al. 2006) (Wiecinski et al. 2014) (Yang et al. 2016). In the present study 3D-optical profiler (Zeta-20) is used to evaluate the erosion performance by estimating erosion volume loss and erosion depth after the erosion cycles. The erosion behaviour of uncoated alloys and coatings are described individually in the following sections.

### **5.3 Erosion of CoCrAlY+Al<sub>2</sub>O<sub>3</sub>+YSZ coating**

The phase changes in the coatings after subjecting to erosion at 600°C is evaluated by XRD analysis and shown in Figure 5.5. CoO,  $\alpha$ -Al<sub>2</sub>O<sub>3</sub> and AlYO<sub>3</sub> as the major oxide phases observed and minor peaks corresponding to Cr<sub>2</sub>O<sub>3</sub>.

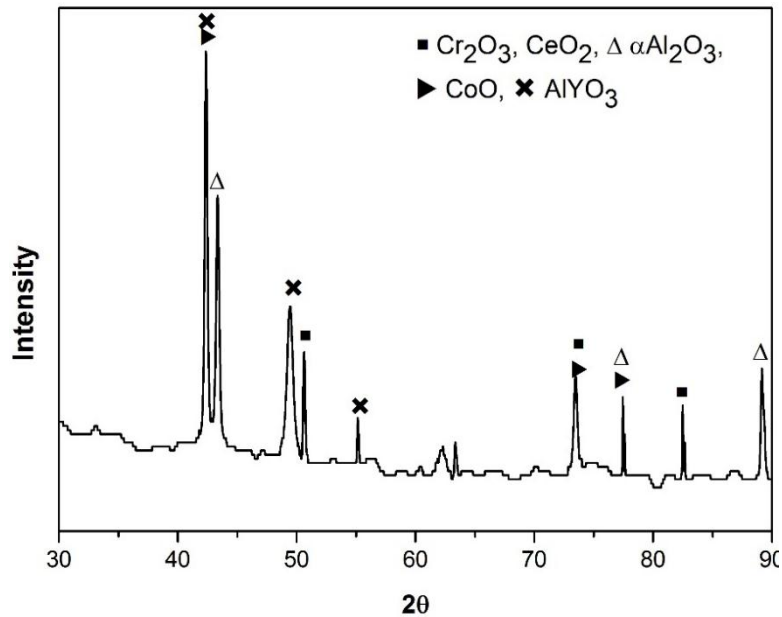


Figure 5.5 X-ray diffraction patterns of eroded CoCrAlY+Al<sub>2</sub>O<sub>3</sub>+YSZ coating at 600°C.

Volumetric material losses from the eroded region are also determined through three dimensional profile patterns generated using non-contact optical profilometer. All the measurements were done on effective magnification of 5x with field view of 4.98×3.74 mm, so that the area of erosion scar is always within the analyzed area (field of view).

3D profile of eroded scar region and the plot of erosion depth graph at 90° and 30° impact angles are shown in Figure 5.6 and Figure 5.7. Figure 5.6 shows the 3D profile of erosion scar with different colors, black region shows the deepest point and white as top point of scar.

CoCrAlY+Al<sub>2</sub>O<sub>3</sub>+YSZ coating shows volume loss of 2.1 mm<sup>3</sup> and 2.9 mm<sup>3</sup> at 90° and 30° impact angles respectively. Figure 5.8 shows the screen shots of optical profiler results obtained when erosion loss of CoCrAlY+Al<sub>2</sub>O<sub>3</sub>+YSZ coating is measured at 30°. The volume measured before and after erosion is shown in Figure 5.8a and b respectively. All the data given in the screen shot are in micrometres. The erosion depth of the coating is observed to be 125±5 μm at 90° and 73±5 μm at 30° impact angle. From erosion depth results it can be inferred that the coating have shown resistance to the erodent impact at both impact angles without allowing the erodent to penetrate into the bond coat of 150 μm thickness at testing temperature of 600 °C. Erosion volume

loss is more at 30° impact angle as compared 90° impact angle which is a characteristic feature of ductile material indicating dominant ductile erosion mechanism (Sidhu et al. 2007A). Erosion mechanism of the coating is described in the following section.

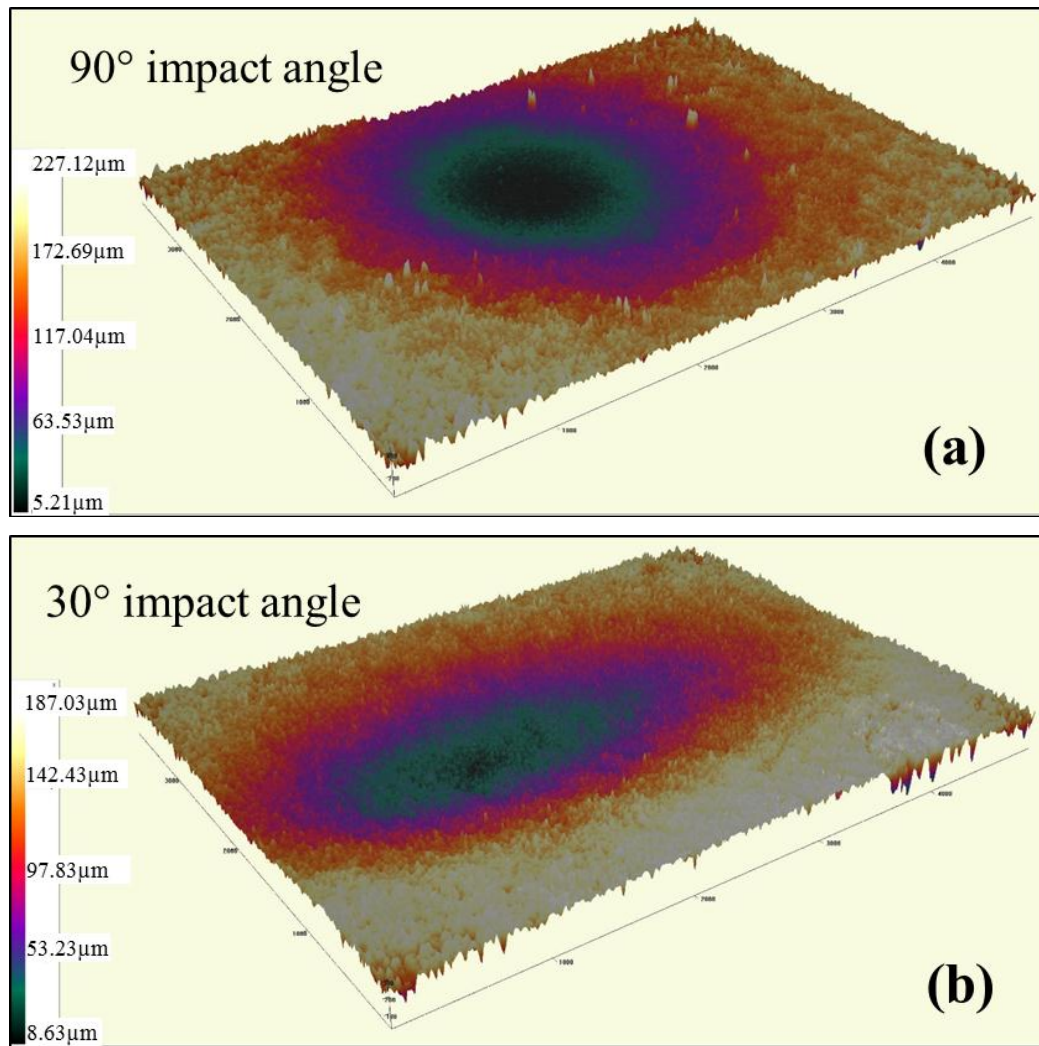


Figure 5.6 3-D profile of erosion scar of CoCrAlY+Al<sub>2</sub>O<sub>3</sub>+YSZ coating at (a) 90° and (b) 30° impact angles.

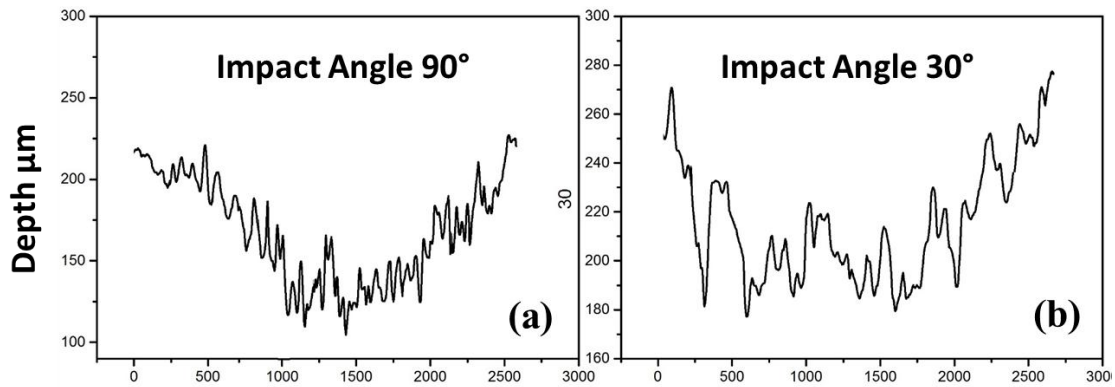


Figure 5.7 Erosion depth profile of CoCrAlY+Al<sub>2</sub>O<sub>3</sub>+YSZ coating at (a) 90° and (b) 30° impact angles.

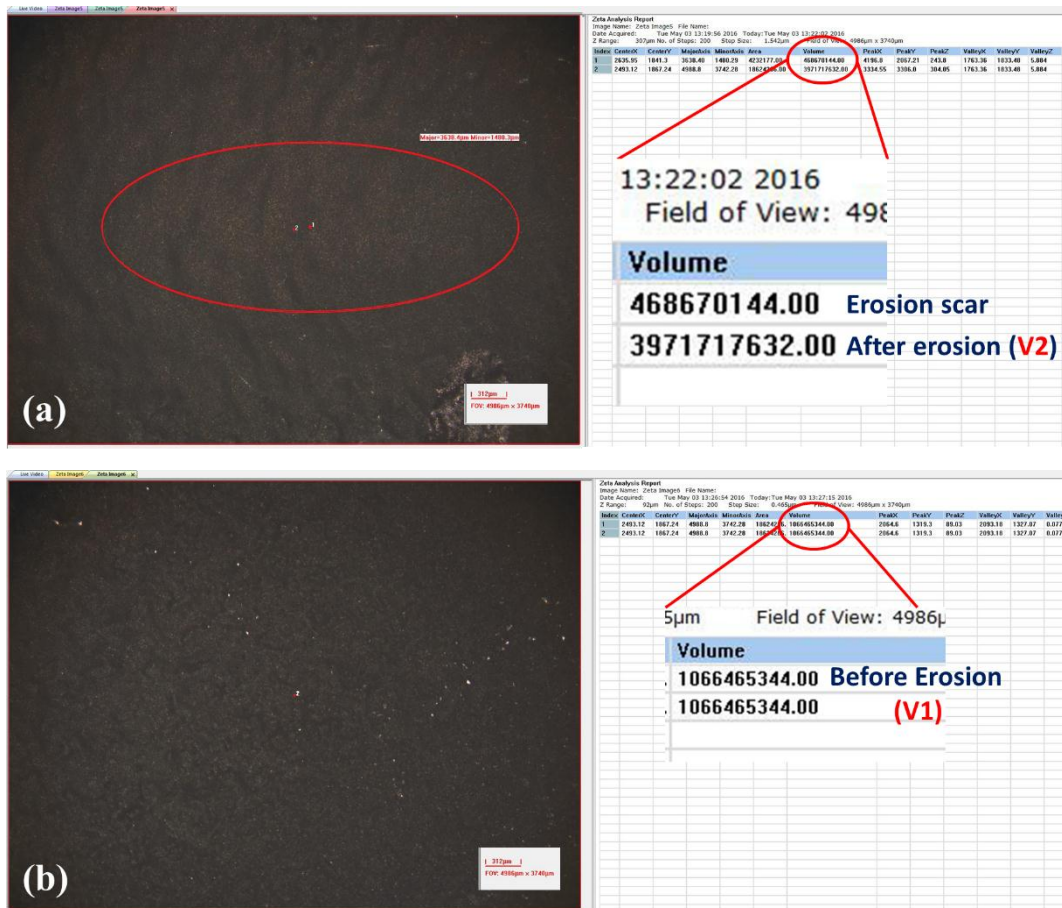


Figure 5.8 Example showing screen shot of results from zeta optical profiler, (a) volume of eroded sample at 30° impact angle and (b) volume of uneroded CoCrAlY+Al<sub>2</sub>O<sub>3</sub>+YSZ coating.

Surface morphology of erosion damage of CoCrAlY+Al<sub>2</sub>O<sub>3</sub>+YSZ coating at 90° and 30° impact angles are shown in Figure 5.9. At 90° impact angle, the erodent impinges and produces indentations by plastically straining the material resulting in the formation of raised lips (ridges) at the periphery of indentation (Figure 5.9). The continuous impact of erodent particles on the deformed material leads to high strain and material removal takes place in the form of platelets pointing the ductile behavior of coating material at elevated temperature. The Al<sub>2</sub>O<sub>3</sub> reinforcements within the matrix (coating) offers counter action for erodent impact. The series of repetitive impact on Al<sub>2</sub>O<sub>3</sub> hard phase results in hard phase detachment/brittle fracture leaving as craters (Figure 5.9a). This is due to the reduction in the bonding energy of Al<sub>2</sub>O<sub>3</sub> with the surrounding splats. Brittle fracture of Al<sub>2</sub>O<sub>3</sub> hard phase in the form of crack is observed in Figure 5.9b. The surface oxide layer formed due to oxidation at higher temperature resulted in brittle fracture by erodent impact and the material removal is in the form of fragments marked as 'A' in Figure 5.9a. The EDS analysis of detached fragment reveals the composition to be the combination of oxides of Cr and Co. The presence of metal oxides is also evident from surface XRD analysis of eroded coating surface (Figure 5.5).

At 30° impact angle, the erodent particles impinge with higher tangential force resulting in the formation of severe ploughing, micro cutting, craters, cracks and lip formation on the eroded surface of coating (Figure 5.9c and d). Ploughing marks present more predominantly on the eroded surface confirms the ductile nature of coating. Ploughing of material end up by forming lips and these lips which are further eroded from the surface in the form of platelets. The angular erodent containing higher particle sizes form large groves on the surface by ploughing mechanism. Ploughing occurs mostly in the softer Co-based matrix region whereas micro cutting is due to the impact of tiny angular erodent particle. Al<sub>2</sub>O<sub>3</sub> reinforcement in the Co-based matrix provides the shielding effect by taking impact load of the erodent. Further, material removal around Al<sub>2</sub>O<sub>3</sub> particle (Figure 5.9c) is due to repeated impact of erodent that weakens the splat boundary resulting in hard phase (Al<sub>2</sub>O<sub>3</sub>) pull out leaving the craters (Ramesh et al. 2010). This accounts for the higher material loss at lower impact angle. The exposed hard phase Al<sub>2</sub>O<sub>3</sub> is evident in the EDS analysis and is marked as region 'B'. The eroded coating shows presence of indentations and craters at 90° and ploughing, micro cutting

and lips at 30° impact angle indicating ductile mode of erosion and in addition cracks visible on the coating implies brittle mode of erosion. Hence, it can be inferred as coating undergoes combination of ductile and brittle mode of erosion mechanism.

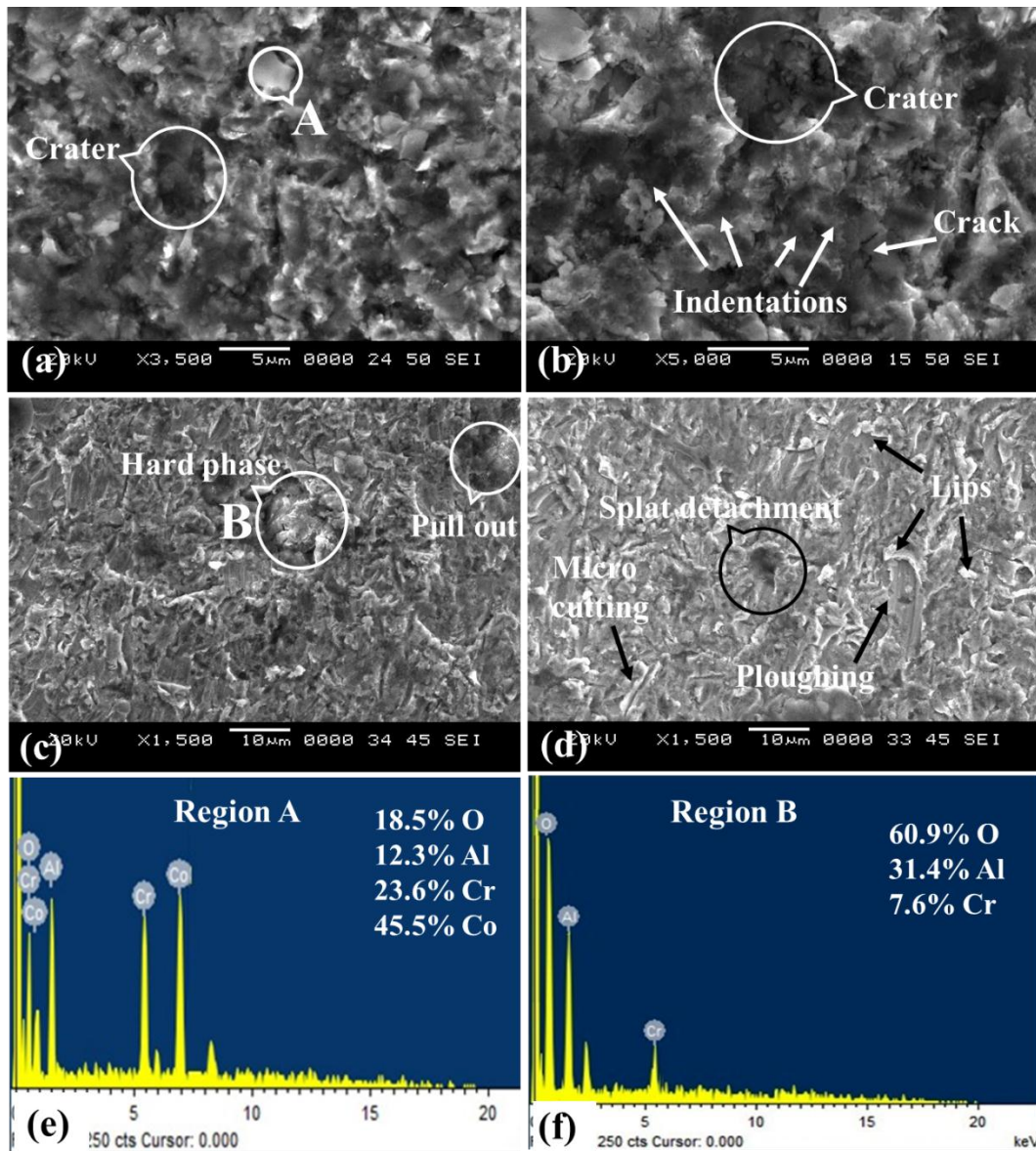


Figure 5.9 Erosion surface morphology and EDS analysis of CoCrAlY+Al<sub>2</sub>O<sub>3</sub>+YSZ coating at (a, b, e) 90° and (c, d, f) 30° impact angle.

#### 5.4 Erosion of CoCrAlY+CeO<sub>2</sub> coating

The phase analysis of coatings subjected to erosion at 600°C is evaluated by XRD analysis and shown in Figure 5.10. Elements of the coating have undergone oxidation due to high temperature exposure and the XRD pattern shows CoO and  $\alpha$ -Al<sub>2</sub>O<sub>3</sub> as major phases while the minor peaks are indexed to CeO<sub>2</sub> and Cr<sub>2</sub>O<sub>3</sub>.

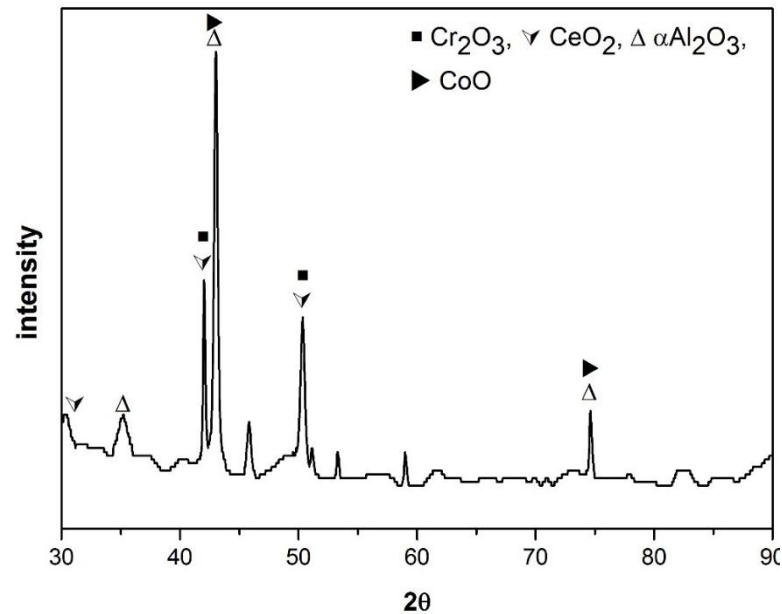


Figure 5.10 X-ray diffraction patterns of eroded CoCrAlY+CeO<sub>2</sub> coating at 600°C.

3D profile of eroded scar region and the plot of erosion depth graph of CoCrAlY+CeO<sub>2</sub> coating at 90° and 30° impact angles are shown in Figure 5.11 and Figure 5.12. CoCrAlY+CeO<sub>2</sub> coating shows volume loss of 1.9 mm<sup>3</sup> and 2.2 mm<sup>3</sup> at 90° and 30° impact angles respectively. The erosion depth of the coating is 103±7 μm at 90° and 69±6 μm at 30° impact angle. The erosion volume loss is more at 30° as compared 90° impact angle indicating ductile erosion is predominant.

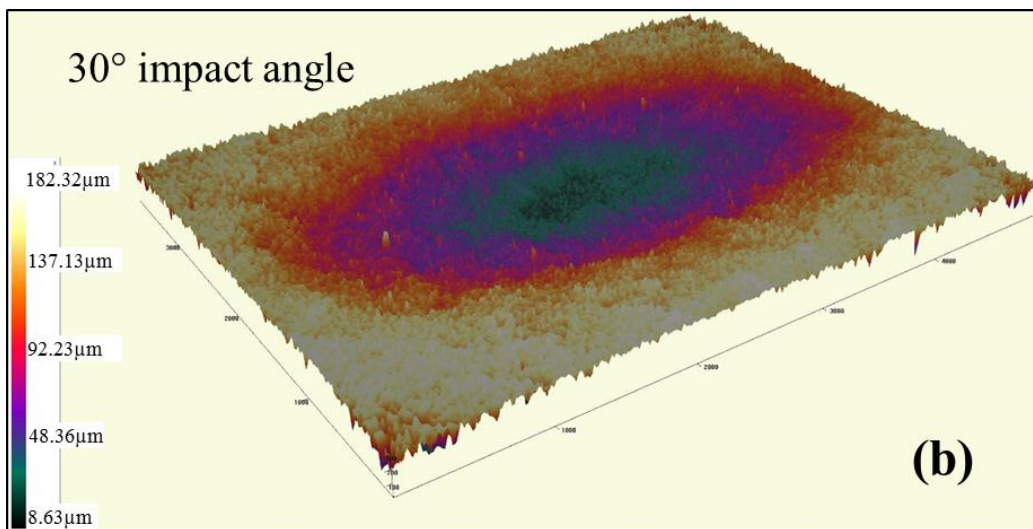
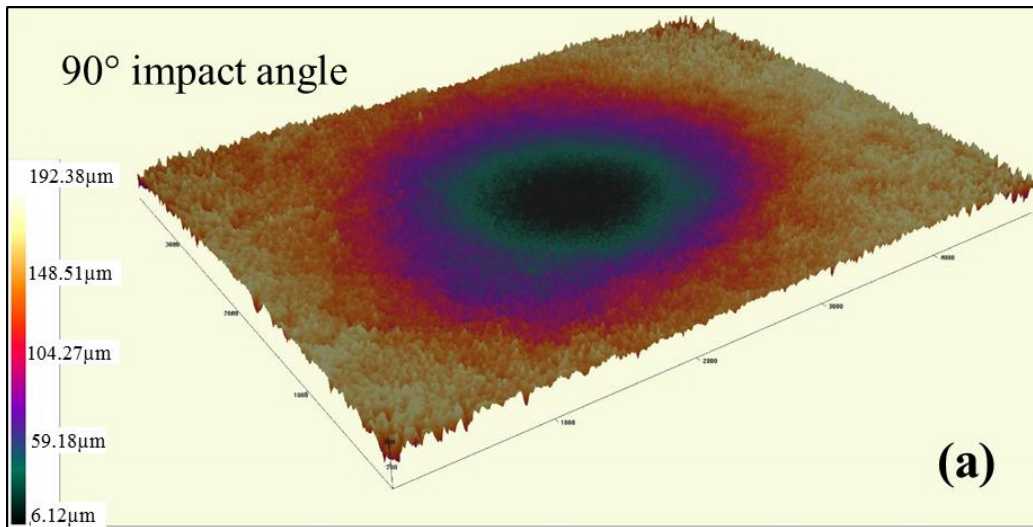


Figure 5.11 3-D profile of erosion scar of CoCrAlY+CeO<sub>2</sub> coating at (a) 90° and (b) 30° impact angles.

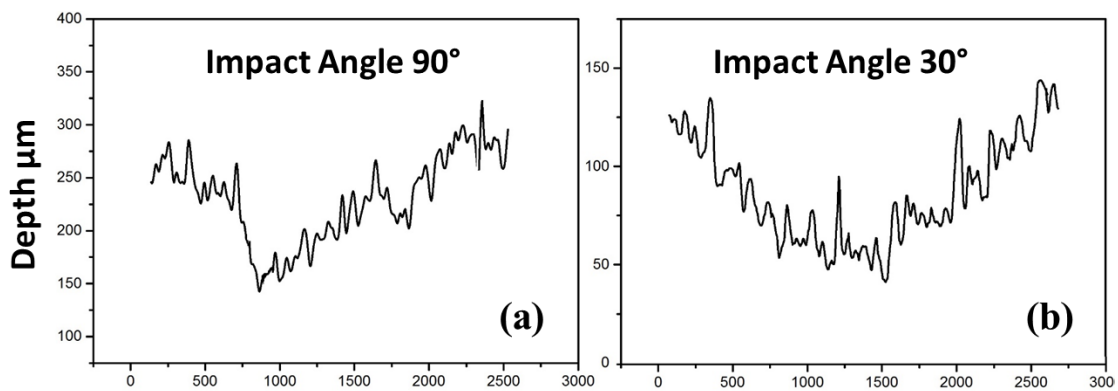


Figure 5.12 Erosion depth profile of CoCrAlY+CeO<sub>2</sub> coating at (a) 90° and (b) 30° impact angles.

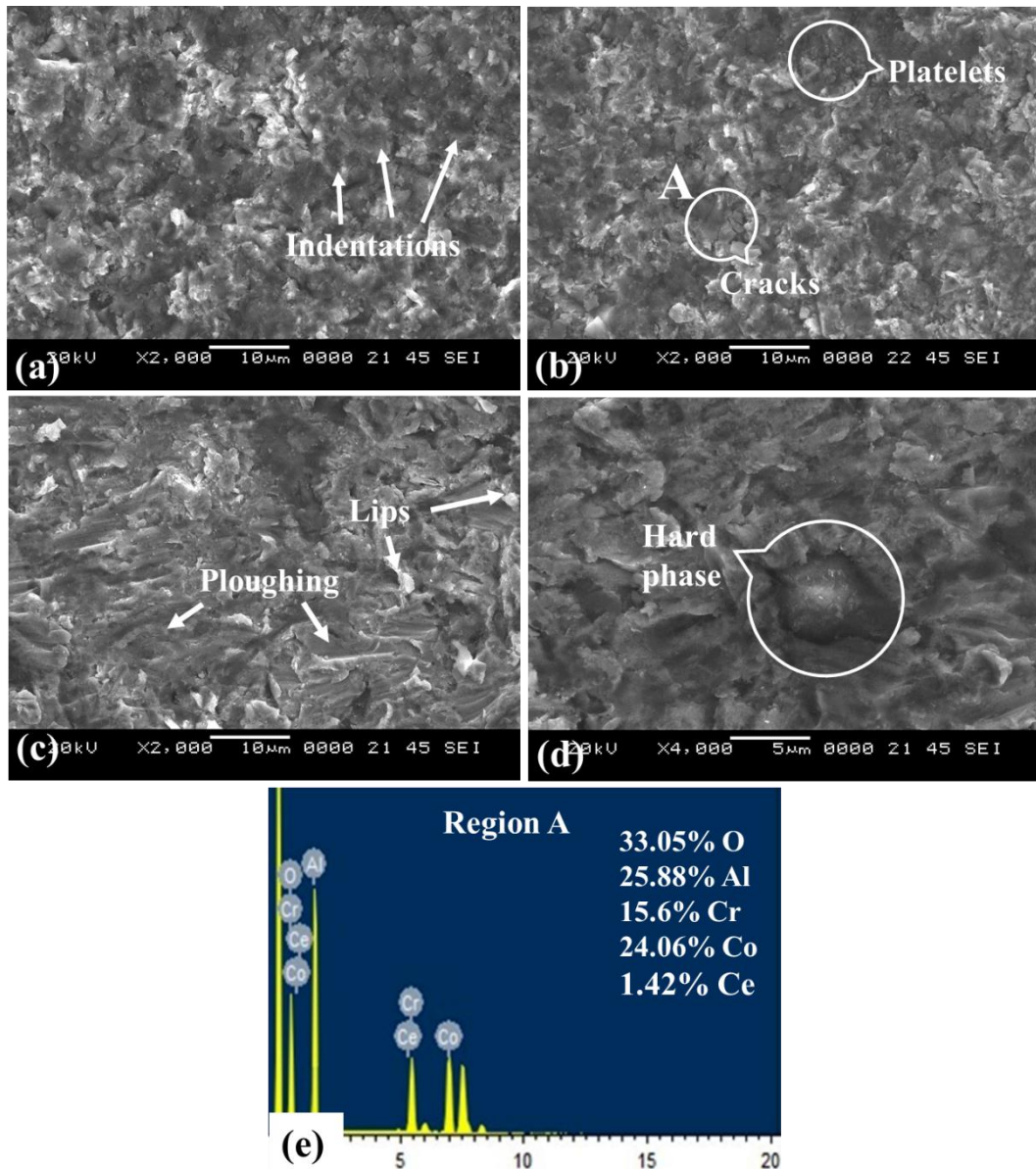


Figure 5.13 Erosion surface morphology and EDS analysis of CoCrAlY+CeO<sub>2</sub> coating at (a, b, e) 90° and (c, d) 30° impact angle.

Surface morphology of erosion damage of CoCrAlY+CeO<sub>2</sub> coating at 90° and 30° impact angles are shown in Figure 5.13. Referring to Figure 5.13a presence of indentations are observed significantly throughout surface for 90° impact angle. The ridges around the indentations are removed due to series of impact and the removed material is has appeared as platelets. The EDS analysis of region 'A' reveals that the presence of oxides of Al, Co and Cr. These oxides are formed due to the oxidation of active elements of the coating material. At 30° impact angle the material removal is due

to significant ploughing. Figure 5.13d shows that deformation of material around the  $\text{CeO}_2$  particle is significant and  $\text{CeO}_2$  particle does not show any deformation emphasizing the resistance offered by it to erodent impact. The observations such as indentation, ridges, ploughing marks, lips and micro cutting indicate that coating has experienced dominant ductile erosion mechanism at both impact angles. The features such as craters and hard phase detachments and pull outs have not appeared in the coating. This is attributed to the following reasons (i) lower particle size of the  $\text{CeO}_2$  reinforcement and (ii) Surface active nature of  $\text{CeO}_2$  acts as coating refiner. This is due to characteristic feature of  $\text{CeO}_2$ , where  $\text{CeO}_2$  being a surface active element which reduces the surface tension of other melted particles and minimizes the unification of similar melted particles.  $\text{CeO}_2$  dispersing along the splat boundaries of coating material on solidification resulting to grain refinement effect. This influences the mechanical properties and erosion resistance of the coating (Nithin et al. 2017B) (Kamal et al. 2010) (Long et al. 2014).

### 5.5 Erosion of CoCrAlY+WC-Co coating

Figure 5.14 shows the XRD analysis of CoCrAlY+WC-Co coating subjected to erosion at  $600^\circ\text{C}$ . The metal oxide phases of CoO,  $\text{Al}_2\text{O}_3$  and  $\text{Cr}_2\text{O}_3$  are dominant metal oxides phases formed due to oxidation at high temperature exposure. The presence WC reinforcement and its decarburised phase  $\text{W}_2\text{C}$  are also observed.

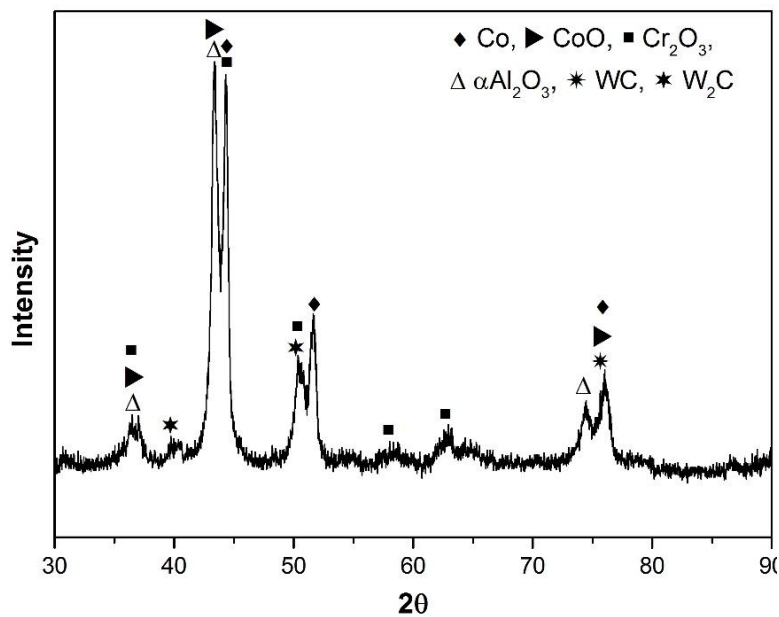


Figure 5.14 X-ray diffraction patterns of eroded CoCrAlY+WC-Co coating at  $600^\circ\text{C}$ .

3D profile of eroded scar region and the plot of erosion depth graph of CoCrAlY+WC-Co coating at 90° and 30° impact angles are shown in Figure 5.15 and Figure 5.16. CoCrAlY+WC-Co coating shows a volume loss of 0.9 mm<sup>3</sup> and 2.1 mm<sup>3</sup> at 90° and 30° impact angles respectively. The erosion depth of the coating is 125±5 μm at 90° and 61±9 μm at 30° impact angle. It is observed that the erosion volume loss at 30° is more as compared to 90° impact angle indicating that ductile erosion is predominant.

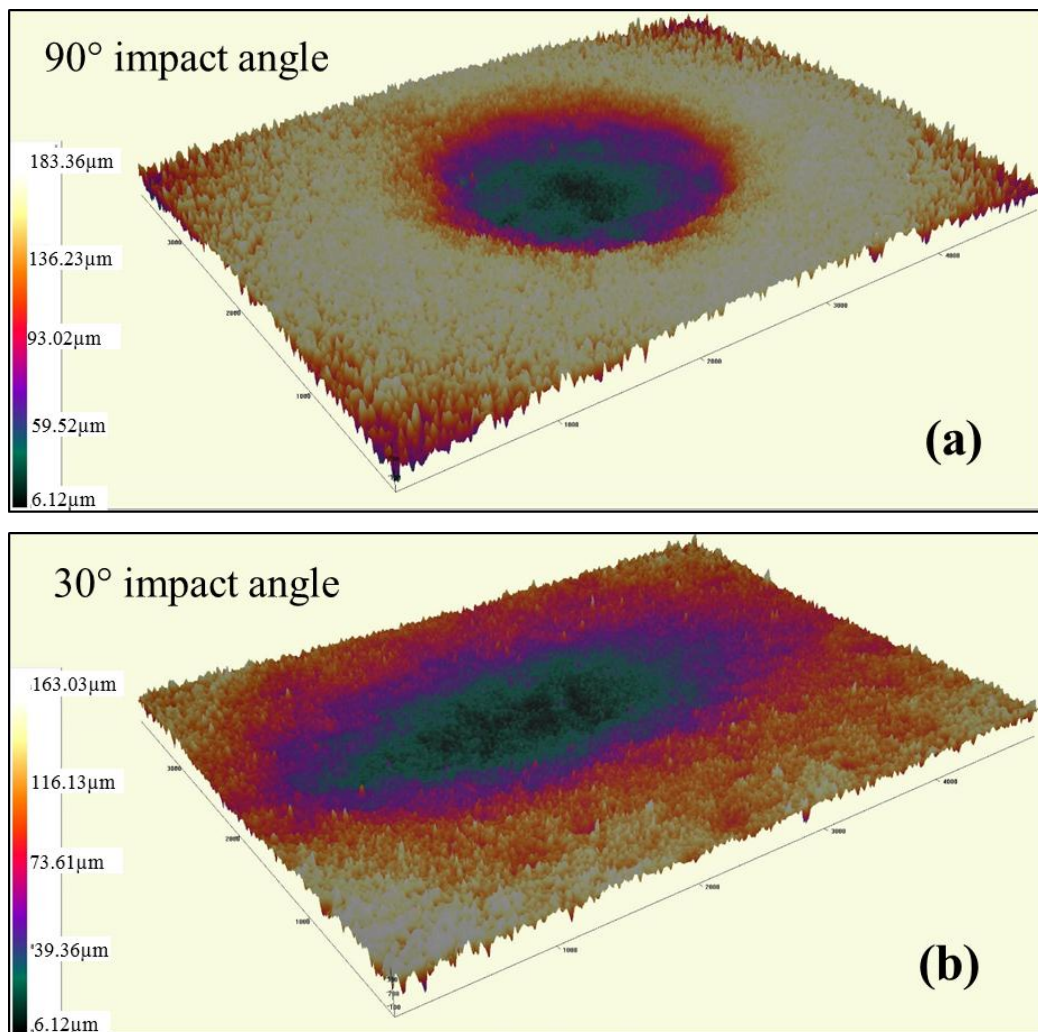


Figure 5.15 3-D profile of erosion scar of CoCrAlY+WC-Co coating at (a) 90° and (b) 30° impact angles.

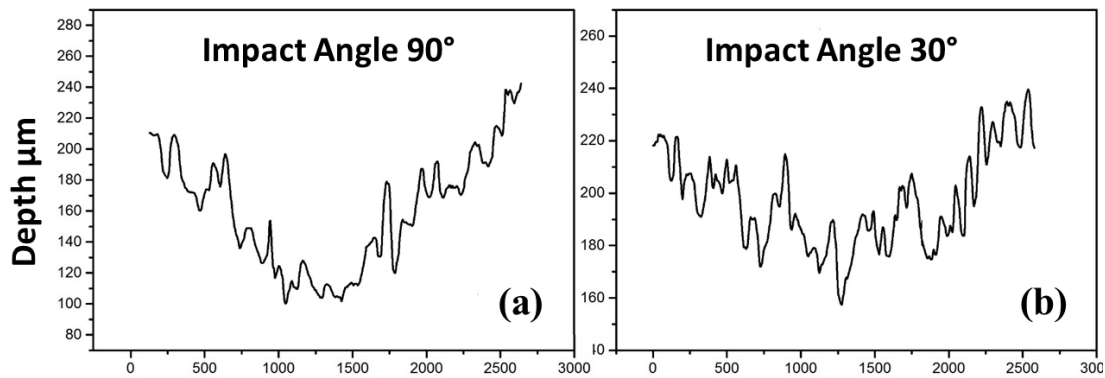


Figure 5.16 Erosion depth profile of CoCrAlY+WC-Co coating at (a) 90° and (b) 30° impact angles.

Erosion surface morphology of CoCrAlY+WC-Co coating at 90° and 30° impact angles are shown in Figure 5.17. At 90° impact angle (Figure 5.17a and b) indentations are seen and ridges at the periphery of indentation which are plastically strained material. These ridges are further removed from the surface in the form of platelets due to high strain rate produced by repetitive impact of erodent particles. Unusual micro cracks are also observed on the coating surface. This is attributed to the brittle fracture of W<sub>2</sub>C particle (Sharma and Goel 2016). This crack initiation in the regime containing carbide further ends up as craters with material removed in the form of chips/flakes. The embedment of angular erodent particles to ductile metallic region of the coating surface is observed in Figure 5.17a.

Erosion at 30° impact angle shows ploughing and micro cutting as the dominant erosion mechanism depicted in Figure 5.17c and d. Ploughing has occurred mainly at softer matrix region and is caused by larger size erodent particles and micro cutting is caused by small erodent particle impact both these confirm the ductile behavior of the coating. During ploughing the erodent particles having enough energy removes the material and the particles having lower energy resulting the formation of lips as Figure 5.17c. Further due to repetitive erodent impact the lips will remove in the form of platelets. The WC reinforcements restrict the deformation of metallic matrix occurring by erodent impact thereby extending the erosion resistance of coating. This is due to shielding effect provided by WC. This is evident from EDS analysis of least deformed region 'A' which revealed W as a major element with C and Co. Further the carbide removal from coating may occur for different reasons: (i) repetitive impact of erodent leading the carbide to

brittle fracture (ii) the significant removal of metal matrix at high rate around the carbide resulting in its pull out and (iii) chipping of brittle  $W_2C$ . Craters are formed by carbide pull out and carbide fracture which occurs more at lower impact angle due to the action of high shear force on coating. The indentations represent the ductile nature and cracks represents the brittle nature, hence it can be inferred that coating has undergone combined ductile and brittle erosion mechanism. Due to high operating temperature of plasma spray technique the carbides within the metallic binder may dissolve in it resulting in the embrittlement of coating. The decarburization of WC to  $W_2C$  and dissolution of carbides are responsible for brittle fracture in the coating.

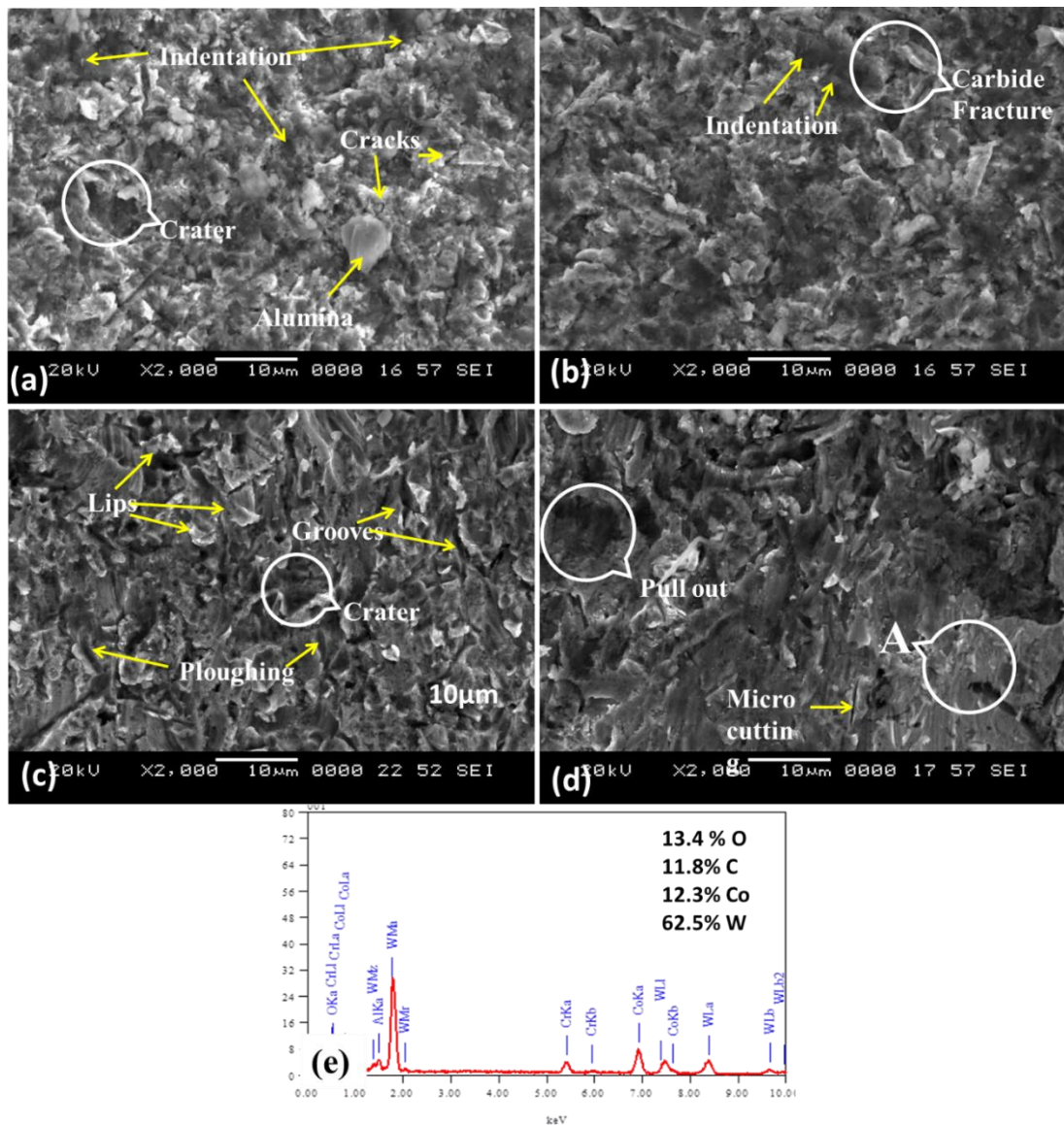


Figure 5.17 Erosion surface morphology and EDS analysis of CoCrAlY+WC-Co coating at (a, b, e) 90° and (c, d) 30° impact angle.

## 5.6 Erosion of CoCrAlY+Cr<sub>3</sub>C<sub>2</sub>-NiCr coating

The phase analysis of CoCrAlY+Cr<sub>3</sub>C<sub>2</sub>-NiCr coating subjected to erosion at 600°C is assessed by XRD analysis as shown in Figure 5.18. Dominant phases indexed are metal oxides such as CoO, Al<sub>2</sub>O<sub>3</sub> and Cr<sub>2</sub>O<sub>3</sub> which are formed due to oxidation occurring at high temperature exposure. Minor peaks are indexed to Co, Cr<sub>3</sub>C<sub>2</sub> and decarburised phase Cr<sub>7</sub>C<sub>3</sub>.

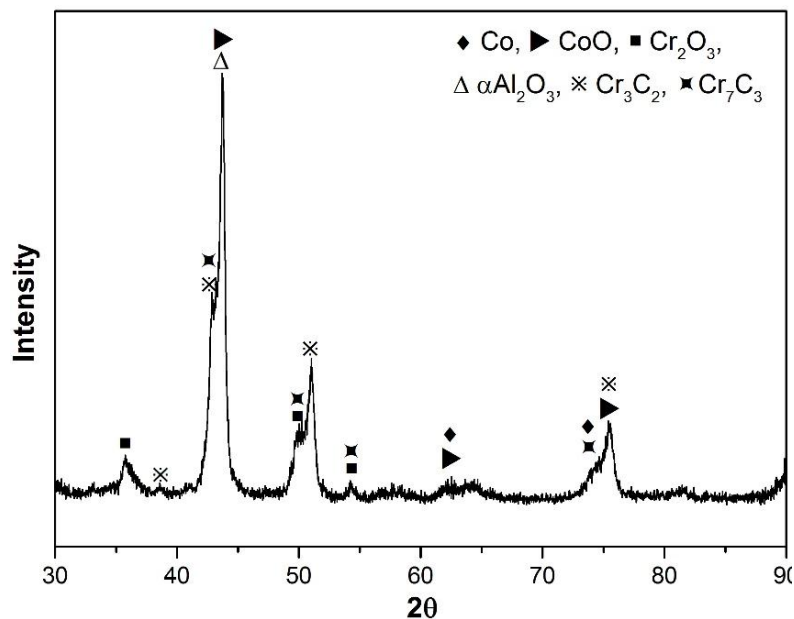


Figure 5.18 X-ray diffraction patterns of eroded CoCrAlY+Cr<sub>3</sub>C<sub>2</sub>-NiCr coating at 600°C.

3D profile of eroded scar and the plot of erosion depth of CoCrAlY+Cr<sub>3</sub>C<sub>2</sub>-NiCr coating at 90° and 30° impact angles are shown in Figure 5.19 and Figure 5.20. CoCrAlY+Cr<sub>3</sub>C<sub>2</sub>-NiCr coating shows volume loss of 2.9 mm<sup>3</sup> and 3.7 mm<sup>3</sup> at 90° and 30° impact angles respectively. The erosion depth of the coating is 200±6 μm at 90° and 130±5 μm at 30° impact angle. The erosion depth at 90° is more than 150 μm indicating that the top coat is eroded completely and reached the bond coat. It is observed that the erosion volume loss at 30° is more as compared to 90° impact angle indicating ductile erosion is predominant. Under erosion conditions larger area of the target surface experienced material removal at 30° impact angle than at 90° impact angle.

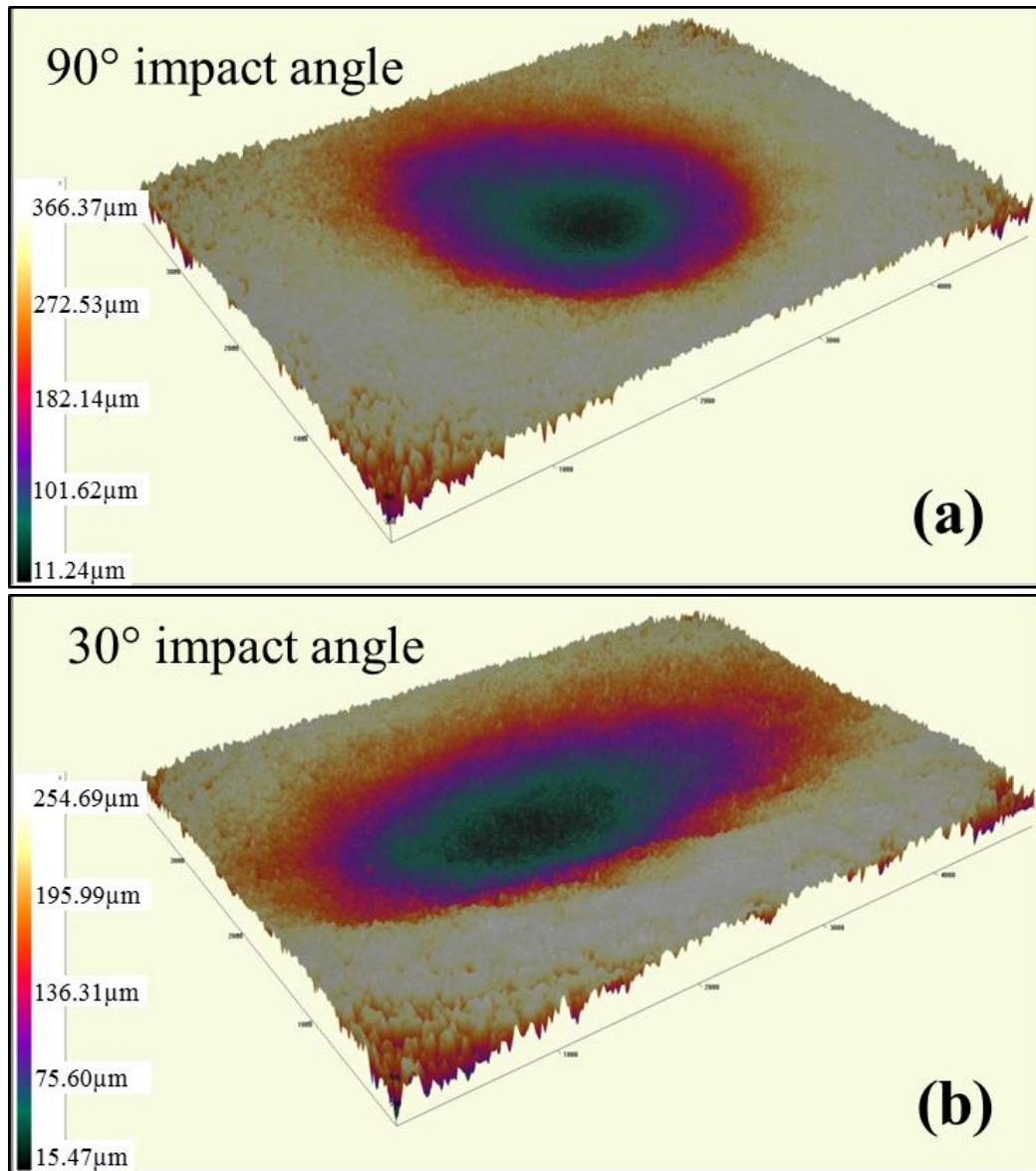


Figure 5.19 3-D profile of erosion scar of CoCrAlY+Cr<sub>3</sub>C<sub>2</sub>-NiCr coating at (a) 90° and (b) 30° impact angles.

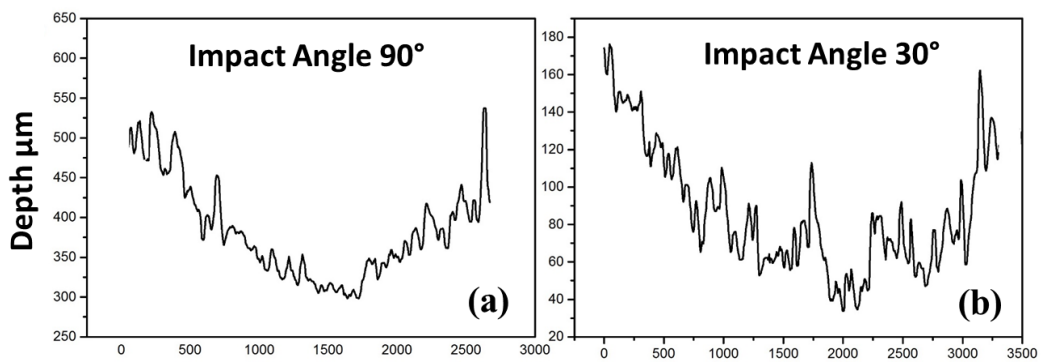


Figure 5.20 Erosion depth profile of CoCrAlY+Cr<sub>3</sub>C<sub>2</sub>-NiCr coating at (a) 90° and (b) 30° impact angles.

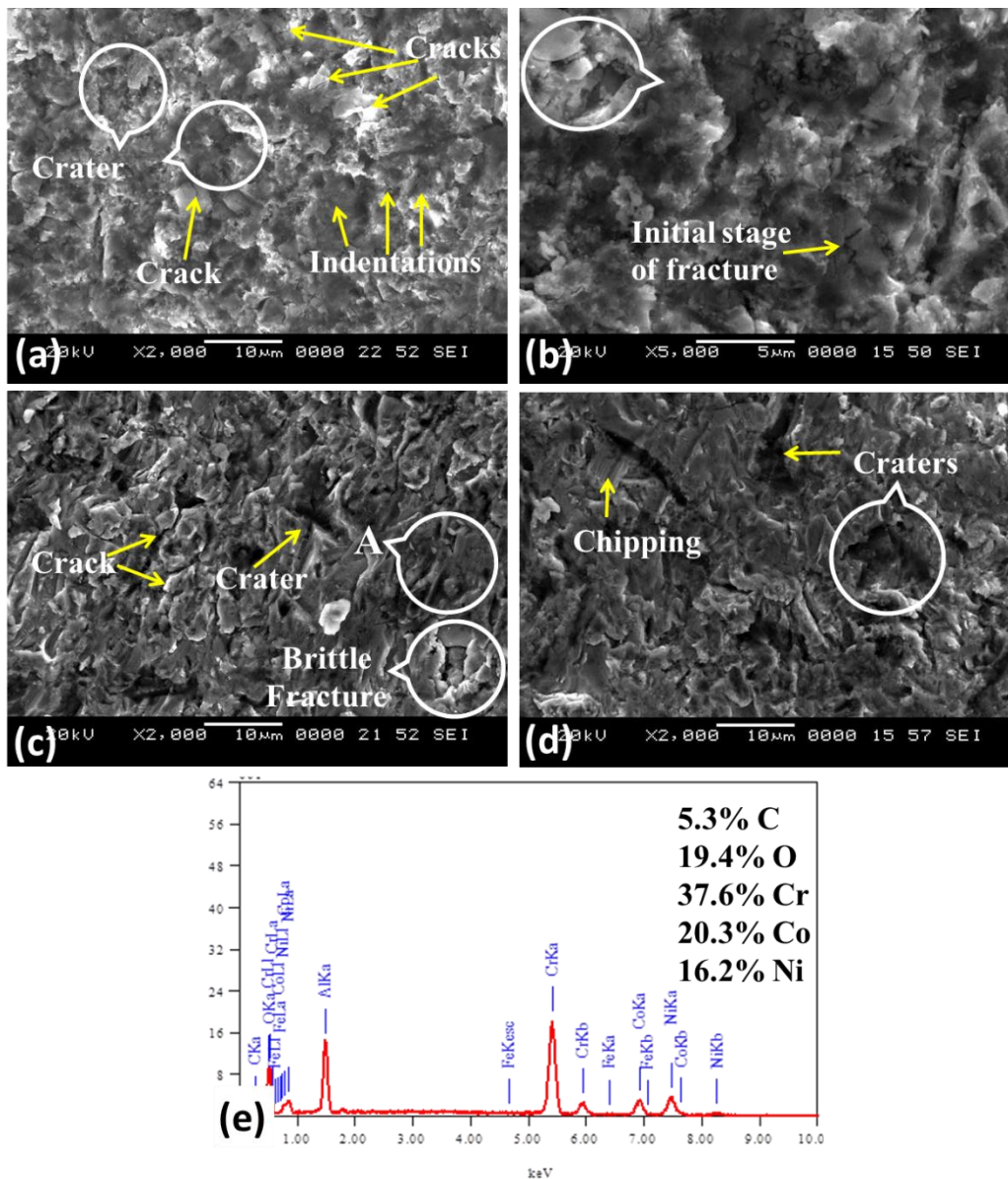


Figure 5.21 Erosion surface morphology and EDS analysis of CoCrAlY+Cr<sub>3</sub>C<sub>2</sub>-NiCr coating at 90° (a, b) and 30° (c, d, e) impact angle.

The erosion morphology of CoCrAlY+Cr<sub>3</sub>C<sub>2</sub>-NiCr coating at 90° and 30° impact angles is shown in Figure 5.21. At 90° impact angle, the indentations are observed in softer matrix region with ridges around the indentations. Dominant cracks and craters are observed due to the brittle fracture of decarburized Cr<sub>7</sub>C<sub>3</sub> particles and cracks are the initiation stage of brittle fracture. At 30° impact angle ploughing and micro cutting are observed at the softer matrix region. Cracks, craters and chipping are also significant throughout the eroded surface and it is observed in Figure 5.21a and b. Interestingly,

considerable cracks and craters are also observed in lower impact angle, where craters are formed due to carbide pull out and splat delamination.

The less deformed region under erosion is marked as 'A' in Figure 5.21c and EDS of this region reveals the presence of combination of Co, Cr, C, Ni and O. The lesser deformation is attributed to the presence of favourable C percentage and it is evident from the EDS analysis. The dissolution of carbide in metallic binder takes place due to high temperature exposure of feedstock during coating process. The dissolution leads to the embrittlement of coating material during rapid solidification and coating results in significantly brittle. This leads to brittle fracture during erodent impact and resulted in the appearance of considerable cracks in CoCrAlY+Cr<sub>3</sub>C<sub>2</sub>-NiCr coating at both impact angle. Similar observations have been made by Mathapati et al. (2017) while investigating the erosion behaviour of carbide reinforced Ni based plasma coating at 600°C. From the above discussion it is observed that indentation, crack, ploughing and chipping are appeared at 90° and at 30° impact angle indicating coating experience combination of ductile and brittle erosion mechanism.

### **5.7 Erosion of uncoated SUPERNI 76 alloys**

3D profile of eroded scar and the plot of erosion depth of Superni 76 alloy at 90° and 30° impact angles are shown in Figure 5.22 and Figure 5.23. Superni 76 exhibits the total volume loss of 3.5 mm<sup>3</sup> and 4.8 mm<sup>3</sup> at 90° and 30° impact angles respectively. The erosion depth of the coating is 285±3 µm at 90° and 172±4 µm at 30° impact angle. The erosion depth at both the impact angles is higher as compared to all the coatings. It is observed that the erosion volume loss at 30° is more as compared to 90° impact angle indicating ductile erosion is predominant. Under erosion conditions larger area of the target surface experienced material removal at 30° impact angle than at 90° impact angle.

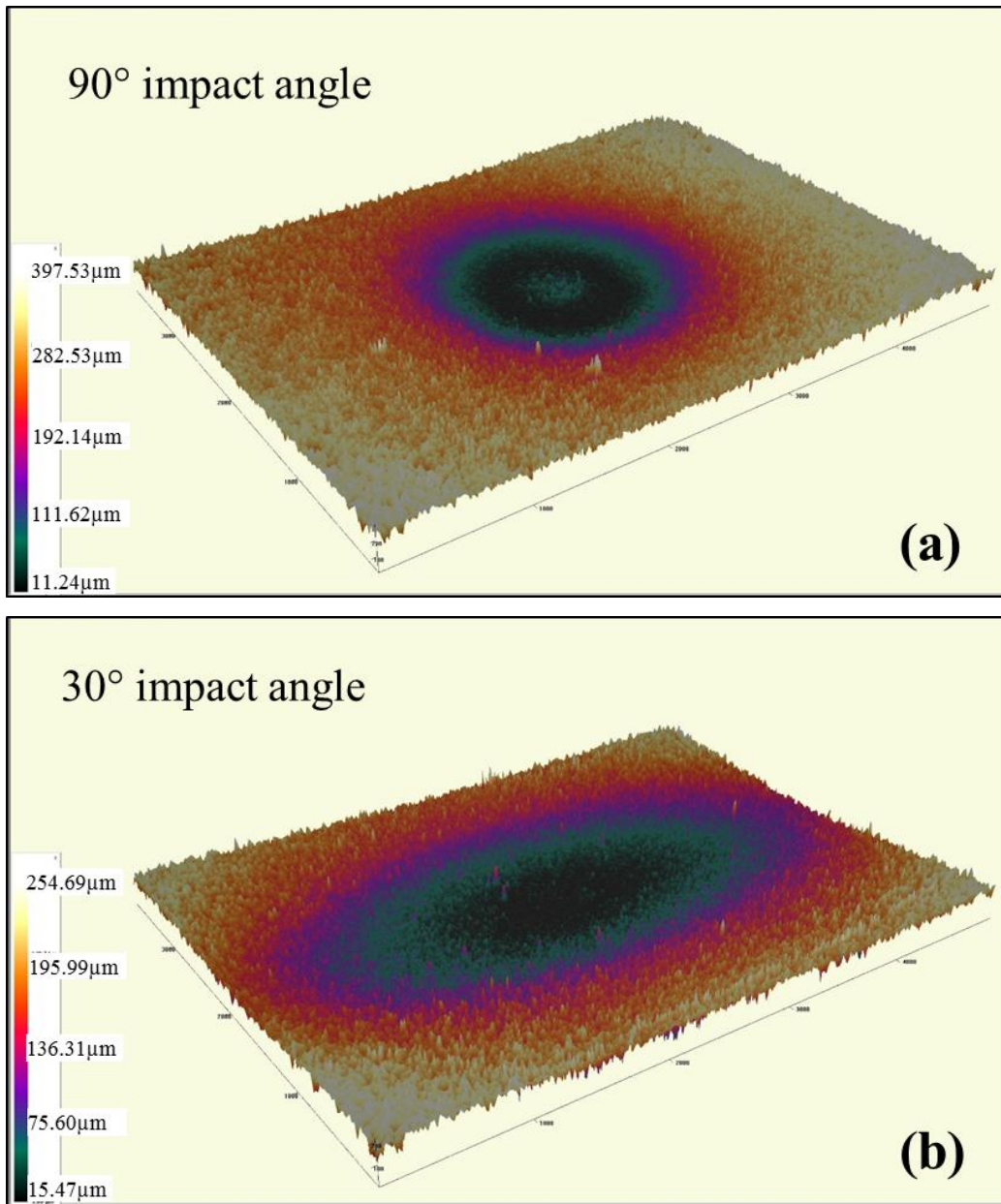


Figure 5.22 3-D profile of erosion scar of CoCrAlY+Cr<sub>3</sub>C<sub>2</sub>-NiCr coating at (a) 90° and (b) 30° impact angles.

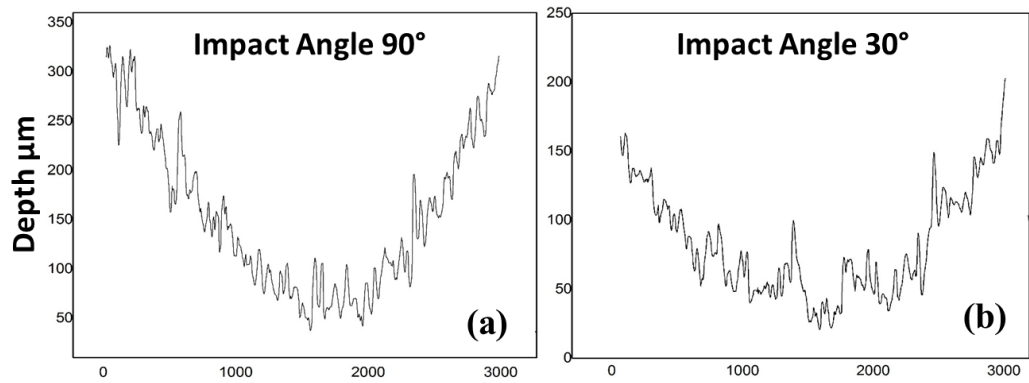


Figure 5.23 Erosion depth profile of CoCrAlY+Cr<sub>3</sub>C<sub>2</sub>-NiCr coating at (a) 90° and (b) 30° impact angles.

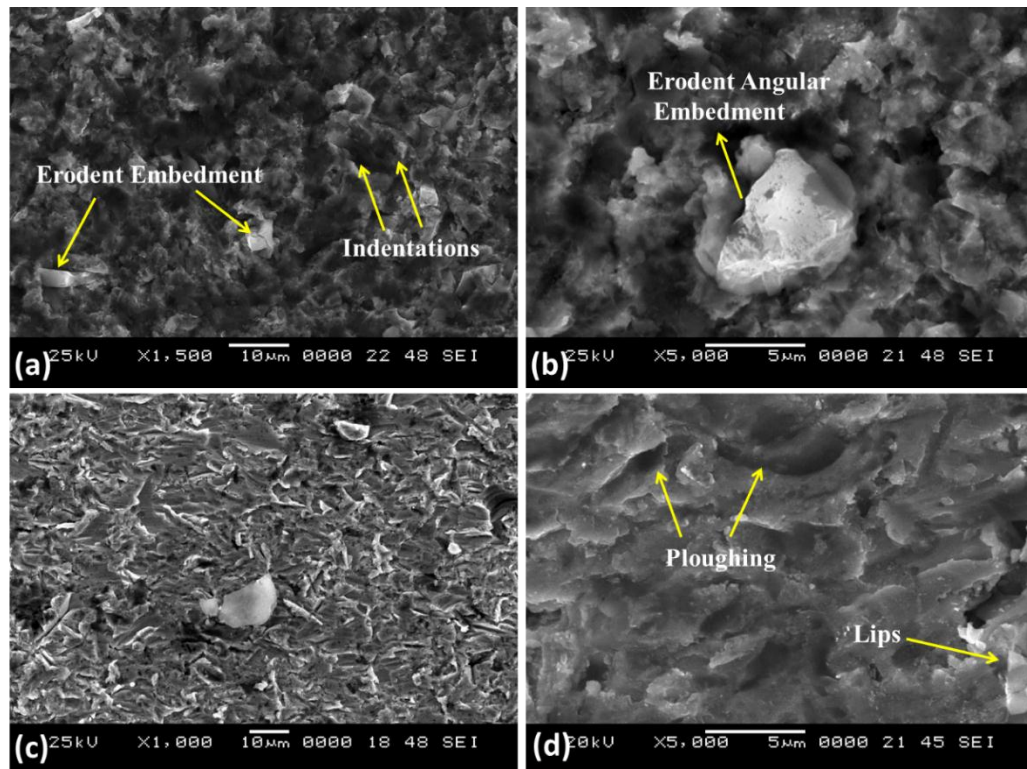


Figure 5.24 Erosion surface morphology of Superni 76 at (a, b) 90° and (c, d) 30° impact angle.

The erosion morphology of Superni 76 at 90° and 30° impact angles are shown in Figure 5.24. At 90° impact angle, indentations are observed in softer matrix region with ridges around the indentations. It is observed from Figure 5.24 that embedment of angular

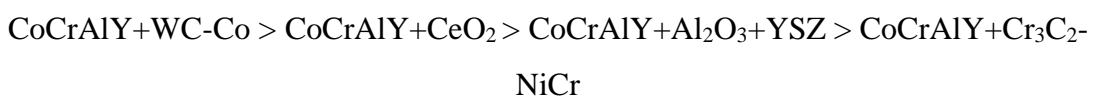
erodent is found to be severe. The repetitive impact of erodent on the embedded erodent particles resulting in brittle fracture and this phenomenon at region 'A' in Figure 5.24a.

At 30° impact angle severe ploughing and micro cutting are observed resulting in significant material removal. As a result of this the material removal takes place in the form of platelets. Cracks, craters and chipping are not observed on the eroded surface which indicates the supeni 76 undergone completely ductile erosion mechanism. Hence the erodent embedment on the target surface is observed in both erosion impact angle. The embedment of erodent due to high ductile nature of target surface and detachment of the same erodent by brittle fracture due to repetitive impact of following erodent particles is the main reason for immense variation in erosion rate, when erosion is validated by weight loss method. This is observed from Figure 5.3.

### **5.8 Comparative discussion of erosion of coatings**

The erosion behavior of the substrate and coatings are evaluated with respect to the total volume loss occurred during erosion. The erosion volume loss of substrate and coatings at 90° and 30° impact angle are represented in the form of a bar chart in Figure 5.25. From Figure 5.25 it is observed that the substrate and coatings have experienced higher volume loss at 30° impact angle as compared to 90° indicating that ductile erosion mechanism is found to be prominent (Sidhu et al. 2007B). All the coatings have shown better erosion resistance than the substrate.

Based on the erosion volume loss data under erosion test conditions it can be inferred that the CoCrAlY+WC-Co coating provides the highest erosion resistance at both impact angles whereas the CoCrAlY+Cr<sub>3</sub>C<sub>2</sub>-NiCr coating indicates the least resistance to the erosion at elevated temperature of 600°C. The explanation of two oxides reinforced coatings and two carbides reinforced coatings are discussed separately and compared in the following section. The relative solid particle erosion resistance of the various coatings in the present study can be arranged in the following sequence:



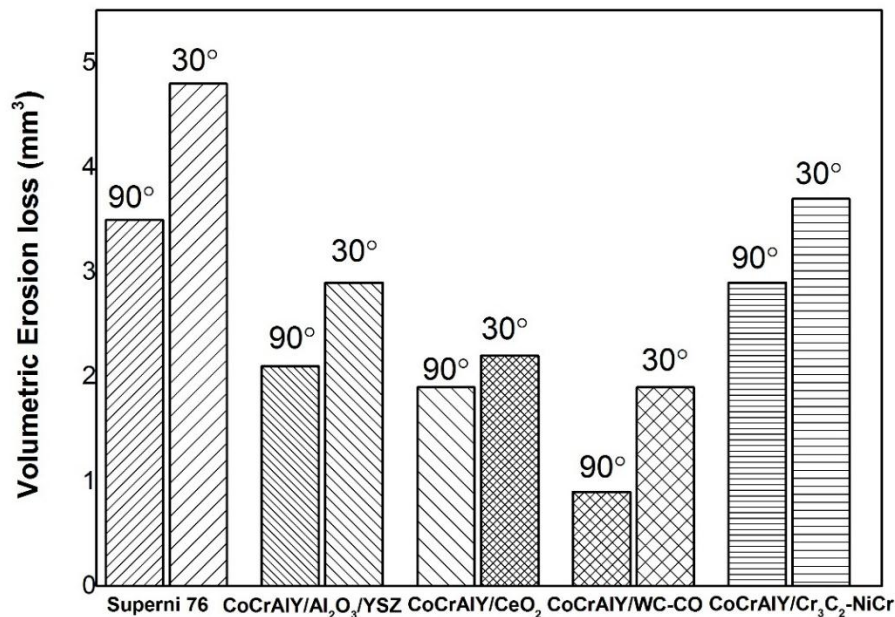


Figure 5.25 Bar chart illustrating erosion volume loss of substrate and coatings at 90° and 30° impact angles.

For high temperature erosion conditions, the samples are kept in the erosion test rig for about 10-15 min to reach the set temperature. During this period the specimens undergo oxidation forming oxide scale on the surface. During the initial stages of erosion test the oxide scale undergoes brittle fracture and material eroded is more of the oxide fragments. Later the underneath actual coating material contributes towards erosion resistance. This occurs for all the metallic coating compositions subjected to high temperature erosion.

The erosion resistance of CoCrAlY+Al<sub>2</sub>O<sub>3</sub>+YSZ coating at 600°C is found to be 40% and 39.5% higher than Superni 76 alloy at 90° and 30° impact angle respectively. Whereas, the CoCrAlY+CeO<sub>2</sub> coating shows 45.7% and 54.1% higher erosion resistance than Superni 76 at 90° and 30° impact angle respectively. From the above discussion it is observed that the CoCrAlY+CeO<sub>2</sub> coating exhibits higher erosion resistance than CoCrAlY+Al<sub>2</sub>O<sub>3</sub>+YSZ coating i.e. 12.4% and 26.9% at 90° and 30° impact angle respectively. In both coatings indentations, craters, ploughing, lips and micro cutting features are observed at the erosion region showing dominant ductile erosion mechanism. The Al<sub>2</sub>O<sub>3</sub> and YSZ reinforcements restrict the erosion impact during the initial erosion cycles and the repetitive impact erodent leads to the brittle

fracture which leads to the formation of craters at 90°. In case of CoCrAlY+CeO<sub>2</sub> coating, the surface active nature of CeO<sub>2</sub> reinforcement and its dispersion along the splat boundaries of coating material on solidification contributes to grain refinement effect (Kamal et al. 2010) (Long et al. 2014). This results in higher adhesion strength and fracture toughness of CoCrAlY+CeO<sub>2</sub> coating as compared to CoCrAlY+Al<sub>2</sub>O<sub>3</sub>+YSZ coating. Erosion of CoCrAlY+Al<sub>2</sub>O<sub>3</sub>+YSZ coating at 30° impact angle shows the presence of craters formed due to the hard phase (Al<sub>2</sub>O<sub>3</sub>) pull out which results in higher erosion volume loss. But this is not observed in case of CoCrAlY+CeO<sub>2</sub> coating due refined coating structure, smaller particle size of CeO<sub>2</sub> reinforcement and more importantly the lesser reinforcement percentage.

The erosion resistance of CoCrAlY+WC-Co coating at 600°C is found to be 74.2% and 56.2% higher than Superni 76 alloy at 90° and 30° impact angle respectively. Whereas, the CoCrAlY+Cr<sub>3</sub>C<sub>2</sub>-NiCr coating shows 17.1% and 22.9% higher erosion resistance than Superni 76 at 90° and 30° impact angle respectively.

In case of carbides reinforced coatings, it is observed that the CoCrAlY+WC-Co coating exhibits higher erosion resistance than CoCrAlY+Cr<sub>3</sub>C<sub>2</sub>-NiCr coating i.e. 76.9% and 59.2% at 90° and 30° impact angle respectively. Both the carbide reinforced coatings exhibit a combination of ductile and brittle erosion mechanism. In case of CoCrAlY+WC-Co coating material removal takes place by indentations, ploughing and lips indicating dominant ductile erosion mechanism with unusual cracks on the coating surface. Whereas in case of CoCrAlY+Cr<sub>3</sub>C<sub>2</sub>-NiCr coating the severe cracks, craters and chipping features are observed on the eroded surface indicating the brittle erosion behaviour at both the impact angle in CoCrAlY+Cr<sub>3</sub>C<sub>2</sub>-NiCr coating. Carbides undergo dissolution within the metallic binder during coating process due to high processing temperature. Dissolution of these carbides leads to embrittlement (Murthy et al. 2001) (Mathapati et al. 2017). Accordingly Cr<sub>3</sub>C<sub>2</sub> (1895 °C) undergoes substantial dissolution with metallic binder as compared to WC (2870 °C) due to its lower melting point. Thus resulting in severe material loss for the coating containing Cr<sub>3</sub>C<sub>2</sub>-NiCr attributed to lower erosion resistance. It is also observed from the Figure 5.17 and Figure 5.21 that peripheral deformation by erodent impact is more localised within the impact zone in CoCrAlY+WC-Co coating, but in CoCrAlY+Cr<sub>3</sub>C<sub>2</sub>-NiCr coating

deformation is widely diverges from the impact zone. Higher ductility nature of CoCrAlY metallic matrix could provide adequate strain before the fracture of coating material. The embedment of erodent particles within metallic matrix may also result in an increase in the erosion resistance by protecting the underlying material which is observed in CoCrAlY+WC-Co coating. A certain amount of impact energy is required before they are extricated from the coating surface.

From the above discussion it can be inferred that high temperature erosion is a combination of simultaneous building up of material by oxidation and removal of material by erosion process. Surface oxides are formed on the coating surface depending on material, temperature and the time of exposure. Hence this can be termed as oxidation modified erosion process and in the present investigation it is observed that erosion is slightly dominant over the oxidation process by removing surface oxide scale during the initial cycles.

**THIS PAGE IS LEFT BLANK.**

## 6 HOT CORROSION

The cyclic hot corrosion studies are conducted by thermogravimetric technique in  $\text{Na}_2\text{SO}_4$ -60%  $\text{V}_2\text{O}_5$  salt environment at  $700^\circ\text{C}$  for 50 cycles. The reaction rate and kinetics have been studied by means of thermogravimetry technique. The identification and structural investigation of reaction products of the corroded specimens are made by means of the XRD and SEM/EDAX techniques. The results are compiled in different sections of this chapter to evaluate the performance of each coating.

### 6.1 CoCrAlY+Al<sub>2</sub>O<sub>3</sub>+YSZ coating

#### 6.1.1 Thermogravimetric studies

The cumulative weight gain ( $\text{mg}/\text{cm}^2$ ) plots of CoCrAlY+Al<sub>2</sub>O<sub>3</sub>+YSZ coatings vs. number of cycles in Figure 6.1. Each cycle is of 1 hour duration and samples were weighed after each cycle. The overall weight gain after 50 cycles of hot corrosion of the CoCrAlY+Al<sub>2</sub>O<sub>3</sub>+YSZ coated MDN 321 and Superni 76 alloys are 2.38 and 2.27  $\text{mg}/\text{cm}^2$ , respectively. Evidently, both the coated alloys showed minimal weight gain difference.

The initial weight gain of the coated samples is linear in nature and after first 10 cycles the weight gain rate gradually reduced and reached steady state. The reduction in weight gain rate or steady state is due to development of protective oxide layer on the coating surface. The higher weight gain rate during the initial cycles is due to the rapid oxidation of active elements. Once the stable oxide layer is formed the weight gain rate is gradually reduced and approaches steady state conditions. Both the coated alloys shows nearly parabolic nature of weight gain indicating the presence of stable protective oxide scale at the surface. The weight loss observed in some cycles is attributed to the sputtering of oxide flakes due to the thermal stress produced during cyclic cooling.

The weight gain square ( $\text{mg}^2/\text{cm}^4$ ) data plotted as a function of time to examine the corrosion kinetics is shown in Figure 6.2. The parabolic rate constant ( $K_p$  in  $10^{-10} \text{g}^2\text{cm}^{-4}\text{s}^{-1}$ ) value of coated MDN 321 and Superni 76 alloys are 0.43 and 0.39 respectively. Similar observations have also been made earlier and the minor deviation of  $K_p$  values are attributed to the formation and rapid growth of inhomogeneous oxides and their dissolution due to the fluxing action of molten salt (Somasundaram, Ph.D thesis 2015).

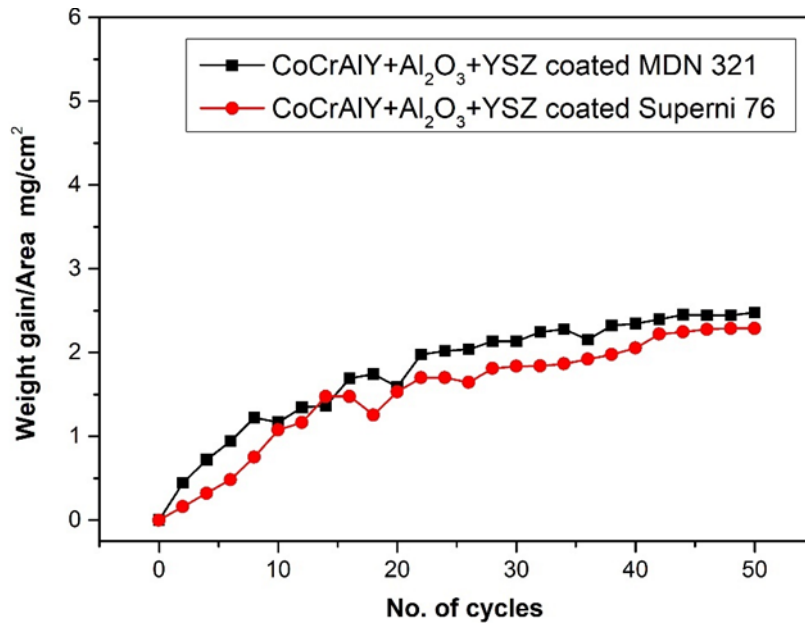


Figure 6.1 Weight gain vs. number of cycles plot of CoCrAlY+Al<sub>2</sub>O<sub>3</sub>+YSZ coated alloys subjected to hot corrosion.

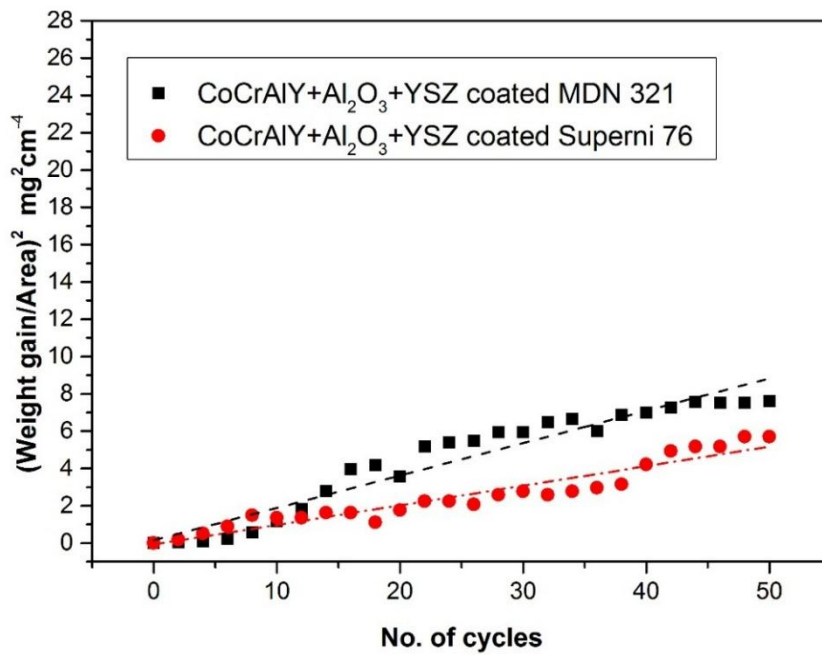


Figure 6.2 (Weight gain/area)<sup>2</sup> vs. number of cycles plot of CoCrAlY+Al<sub>2</sub>O<sub>3</sub>+YSZ coated alloys subjected to hot corrosion.

### 6.1.2 X-RAY diffraction analysis

XRD patterns of hot corroded CoCrAlY+Al<sub>2</sub>O<sub>3</sub>+YSZ coated alloys exposed to salt environment at 700 °C are shown in Figure 6.3. The major peaks in coated alloys correspond to CoO, Cr<sub>2</sub>O<sub>3</sub> and CoAl<sub>2</sub>O<sub>4</sub>, while the minor peaks indexed to αAl<sub>2</sub>O<sub>3</sub>,

AlCo and  $\text{CoCr}_2\text{O}_4$ ,  $\text{AlVO}_4$ ,  $\text{CrVO}_4$  and  $\text{CoSO}_4$ . The vanadates and sulfates formed by the dissolution of metal oxides with molten salt. The major elements of substrates such as Fe or Ni are not observed on coating surface indicating the absence of substrate influence on the formation of surface oxide scale. Almost all the phases/peaks observed in both the coated alloys are similar.

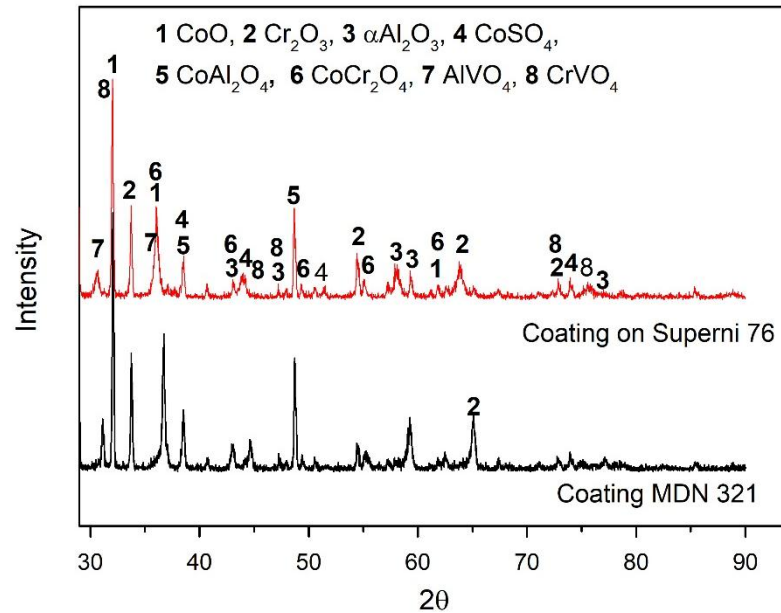


Figure 6.3 XRD patterns for CoCrAlY+Al<sub>2</sub>O<sub>3</sub>+YSZ coated alloys subjected to hot corrosion.

### 6.1.3 Surface SEM and EDS analysis

The surface morphology of corroded CoCrAlY+Al<sub>2</sub>O<sub>3</sub>+YSZ coatings on MDN 321 and Superni76 is shown in Figure 6.4 respectively. The continuous closely packed globular structure has appeared throughout the corroded coating surface in both the cases. EDS analysis of region 'A' in Figure 6.4a and b shows the major elements as O, Co and Cr with minor elements such as Al, Na, S and V salts. The region 'B' consists of O, Cr and Co as major element with Al and V salt as minor elements. At this region the Cr content is higher which may be due to the oxidation of respective splat existing at the region 'B'. Thus referring to the EDS analysis at different points, the globular structure is a combination of oxides of active elements such as Co, Cr, Al and their spinels with some salts which is evident from the surface XRD analysis of corroded coatings (Figure 6.3).

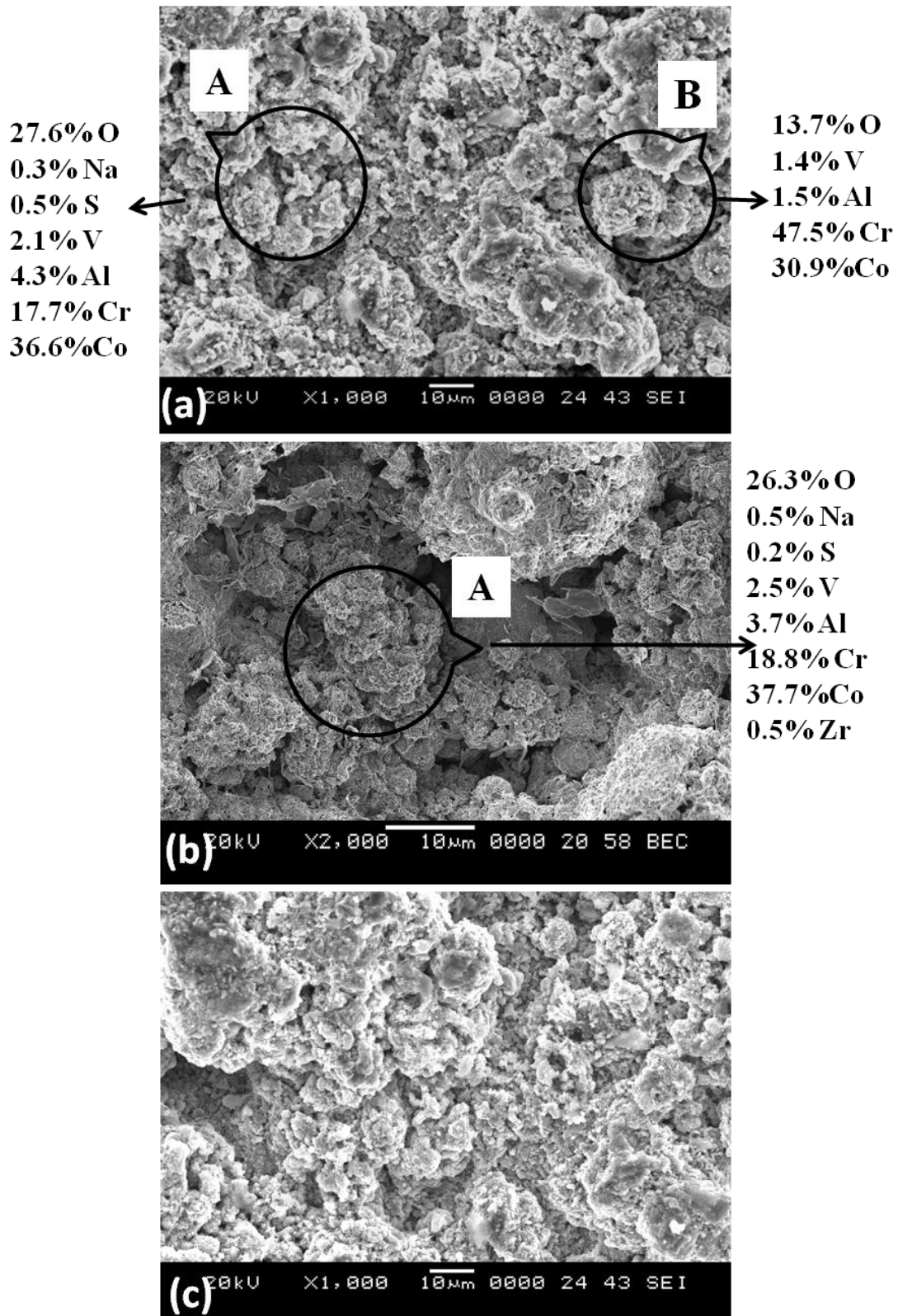


Figure 6.4 Surface morphology of hot corroded CoCrAlY+Al<sub>2</sub>O<sub>3</sub>+YSZ coatings on MDN 321(a, b) and Superni76 (c).

### 6.1.4 Cross sectional and elemental mapping

The cross section of the hot corroded coating is shown in Figure 6.5a and b. The Figure 6.5a shows thin continuous dense oxide scale at the coating surface and the scale thickness is in the range of 12-15µm. Elemental composition at various locations of the cross section is analysed by point EDS analysis (Figure 6.5b) and reported in Table 6.1. EDS of upper oxide scale at region 1 is dominant in Co, Cr, Al and O with V and S salts. The presence of small amount of O at the at the splat boundaries is observed below the coating surface which is due to the oxidation of coating powders during the coating process due to longer in flight time. The elemental analysis along the cross section elucidates that O rich Cr, Co, Al and other salts are observed only at the coating surface indicating the protective oxide scale acts as barrier.

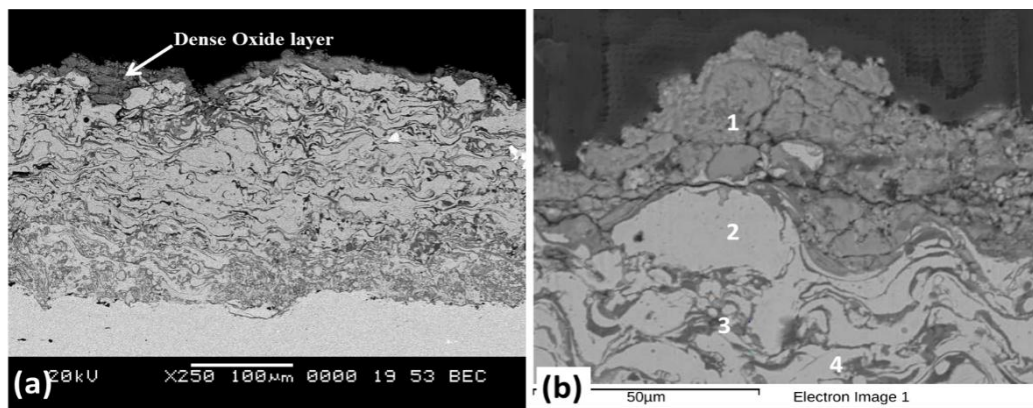


Figure 6.5 Corroded coating cross section and EDS point analysis (wt. %) of the CoCrAlY+Al<sub>2</sub>O<sub>3</sub>+YSZ coating.

Table 6.1 Point EDS of CoCrAlY+Al<sub>2</sub>O<sub>3</sub>+YSZ coating cross section in wt. %.

Elements (wt%)	Region 1	Region 2	Region 3	Region 4
O	26.4	-	7.9	5
Al	18.8	5.6	10.1	6
S	0.8	-	-	-
V	2.1	-	-	-
Na	3.5			
Cr	3.6	11.2	18.9	14.5
Co	37.6	82.1	46.7	72.1

X-ray mapping of coating cross section depicting the elemental distribution is shown in Figure 6.6. The presence of rich oxygen layer is observed at the surface of the coating and the distribution of  $\text{Al}_2\text{O}_3$  and YSZ reinforcements has appeared as white spots in Al and Zr mapping. The distribution of oxygen observed throughout the coating cross section is probably due to the intersplat oxidation.

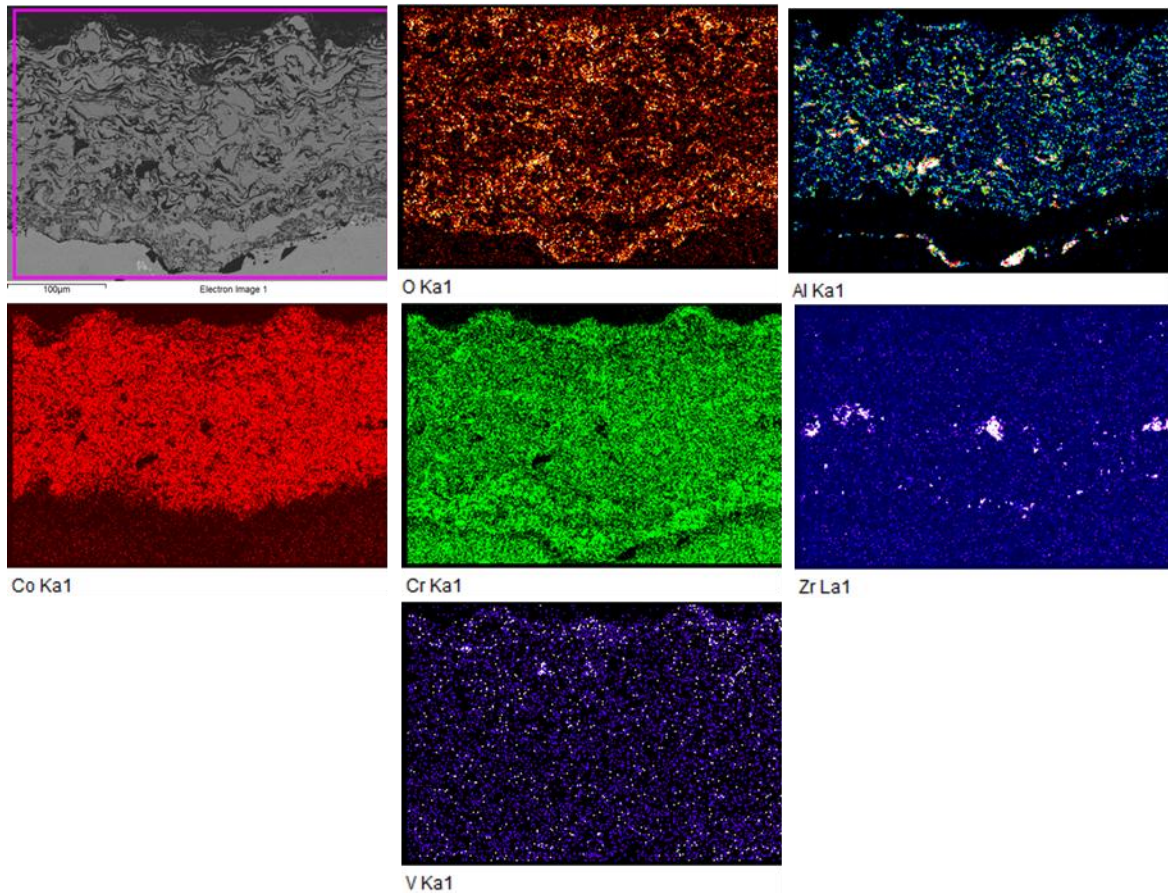


Figure 6.6 BSEI and elemental X-ray mapping along the cross-section of the  $\text{CoCrAlY}+\text{Al}_2\text{O}_3+\text{YSZ}$  coating subjected to hot corrosion.

The upper scale is predominant in Co, Cr, Al, O and corrosion salts. Outward diffusion of Co and Cr from the coating might have resulted in formation of  $\text{CoCr}_2\text{O}_4$  with subsequent corrosion cycles. The presence of  $\text{Al}_2\text{O}_3$  reinforcement in the matrix and Al rich sub layer as bright white colour underneath the oxide scale is observed from the Al mapping. The vanadium salt appeared only at the outer layer of the surface implying the restriction of corrosive element inside the coating. The black phase present along the coating substrate interface is rich in aluminium and oxygen, and therefore, it may

be inclusion of the alumina particles possibly embedded during the grit blasting of the substrate surface before plasma spraying and also would have induced during polishing of specimens.

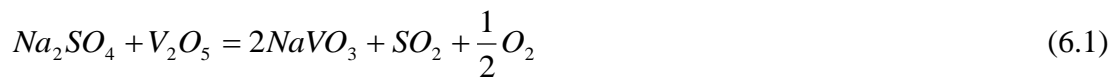
### 6.1.5 Discussion

The weight gain after 50 cycles of exposure of the CoCrAlY+Al<sub>2</sub>O<sub>3</sub>+YSZ coated alloys are found to be 70% and 65% lesser weight gain as compared to uncoated MDN 321 and Superni 76 substrates respectively. The parabolic rate constant ( $K_p$ ) value decreases for both the coated alloys in comparison to MDN 321 and Superni 76 substrates and therefore, it can be inferred that the necessary protection has been provided by the plasma sprayed CoCrAlY+Al<sub>2</sub>O<sub>3</sub>+YSZ coating to the substrates. It is observed from the Figure 6.1 showing surface morphology of corrode coating comprises of closely packed continuous globular structure. Cross section of corroded coating shows the thin, dense well adhered oxide scale on the coating surface. These are the characteristic features of protective oxides on the coating surface.

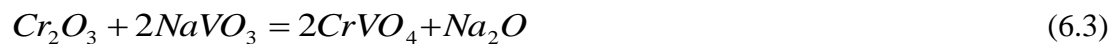
The high temperature exposure leads to the preferential oxidation of active elements of the coating and oxidized phases of these coating elements is observed from the XRD analysis on the surface of the corroded CoCrAlY+Al<sub>2</sub>O<sub>3</sub>+YSZ coating (Figure 6.3) i.e. CoO, Cr<sub>2</sub>O<sub>3</sub>,  $\alpha$ -Al<sub>2</sub>O<sub>3</sub> and there spinels on the top scale. As Al<sub>2</sub>O<sub>3</sub> has a high melting point and stability without showing phase transition at high temperature due to its high chemical neutrality, low solubility in molten salt and oxygen diffusion rate (Wang et al. 2016).  $\alpha$ -Al<sub>2</sub>O<sub>3</sub> is the stable phase shows slow-scale growth kinetics during the oxidation (Zhu et al. 2013). The CoO, Cr<sub>2</sub>O<sub>3</sub> and Al<sub>2</sub>O<sub>3</sub> are the protective phases that are formed during the early stage of corrosion. Later with the subsequent hot corrosion cycles the nucleation of these Cr<sub>2</sub>O<sub>3</sub> and Al<sub>2</sub>O<sub>3</sub> with CoO will result in the development of CoCr<sub>2</sub>O<sub>4</sub> and CoAl<sub>2</sub>O<sub>4</sub> spinel oxides. The presence of phases CoO, Cr<sub>2</sub>O<sub>3</sub>, CoCr<sub>2</sub>O<sub>4</sub> and CoAl<sub>2</sub>O<sub>4</sub> as indexed by XRD analysis and presence oxygen rich Co, Cr, and Al elements by EDS is in accordance with the studies of Singh et al. (2016). The protection shown by this coating by steady state weight gain may be due to the formation of Cr<sub>2</sub>O<sub>3</sub>,  $\alpha$ -Al<sub>2</sub>O<sub>3</sub> and there spinels. These spinel oxides will have lower diffusion coefficient than the parent oxide (Zhu et al. 2013). (Luthra and LeBlanc 1987) proposed that the formation of spinels might stop the diffusion activities through the CoO, which in turn

suppresses the further formation of this oxide. The increase in the growth of  $\text{CoCr}_2\text{O}_4$  and  $\text{Cr}_2\text{O}_3$  in competition with  $\text{CoO}$  formation increases the corrosion resistance of alloys.  $\text{Cr}_2\text{O}_3$ ,  $\text{CoCr}_2\text{O}_4$  and  $\text{CoAl}_2\text{O}_4$  are protective oxides, providing the necessary protection against penetration of corrosive species into the coating. Similar observations are reported by Zhang et al. (2016) and Somasundaram et al. (2014) during the hot corrosion studies of Co-based coatings.

From the X-ray mapping it is observed that the presence of salts on the outer most surface implies the surface oxide scale acts as a diffusion barrier to the inward diffusion of the corrosive species (Figure 6.5). The EDS analysis along the cross section also confirms the distribution of Na and V on the uppermost oxide scale. And, hence, the acidic fluxing by  $\text{Na}_2\text{SO}_4$ -60%  $\text{V}_2\text{O}_5$  mixture may be expected. Based on the available thermodynamic data,  $\text{Na}_2\text{SO}_4$  can react with  $\text{V}_2\text{O}_5$  to increase the acidity of melt by the formation of vanadates  $\text{NaVO}_3$  (melting point  $610^\circ\text{C}$ ) as per following reaction (Kolts et al.1972).



This  $\text{NaVO}_3$  acts as a catalyst and the acidic dissolution of  $\text{CoO}$ ,  $\text{Al}_2\text{O}_3$ , and  $\text{Cr}_2\text{O}_3$  probably might have occurred according to the reactions (Longa et al. 1996) (Hwang et al. 1989):



These dissolution reactions could have caused breakdown of the initially formed oxide film on the coating surface. The XRD and EDS results also corroborated the formation of these metal vanadates which are concentrated mainly in the top scale.

In this coating after corrosion,  $\text{YVO}_4$  which is a severe corrosion product in presence of  $\text{Na}_2\text{SO}_4$ -60%  $\text{V}_2\text{O}_5$  salt environment is not indexed in XRD analysis. Afrasiabi et al. (2008) described that the formation of  $\text{YVO}_4$  crystals having rod shape morphology is responsible for the degradation of  $\text{YSZ}+40\%\text{Al}_2\text{O}_3$  coating during hot corrosion. The higher percentage of  $\text{YSZ}$  was more prone to the formation of  $\text{YVO}_4$ . But, in

CoCrAlY+Al<sub>2</sub>O<sub>3</sub>+YSZ coating the finely dispersed Al<sub>2</sub>O<sub>3</sub> in Co-matrix would also restrict the direct contact of V<sub>2</sub>O<sub>5</sub> salt with YSZ, formation of YVO<sub>4</sub> crystals is very insignificant.

## 6.2 CoCrAlY+CeO<sub>2</sub> coating

### 6.2.1 Thermogravimetric studies

The cumulative weight gain (mg/cm<sup>2</sup>) plots of CoCrAlY+CeO<sub>2</sub> coatings as a function of time expressed in number of cycles are shown in Figure 6.7. The overall weight gain after 50 cycles of hot corrosion of the CoCrAlY+CeO<sub>2</sub> coated MDN 321 and Superni 76 alloys are 4.81 and 4.59 mg/cm<sup>2</sup>, respectively. The weight gain values of both the coated alloys are very close to each other indicating the absence of substrate influence on developing the surface oxide scale for corrosion protection. Drastic weight gain is observed during the initial cycles and further the curve follows linear weight gain nature throughout the subsequent hot corrosion cycles.

The weight gain square (mg<sup>2</sup>/cm<sup>4</sup>) data plotted against the time to examine the corrosion kinetics and shown in Figure 6.8. The parabolic rate constant (K<sub>p</sub> in 10<sup>-10</sup> g<sup>2</sup>cm<sup>-4</sup>s<sup>-1</sup>) value of coated MDN 321 and Superni 76 alloys is 1.16 and 1.10 respectively.

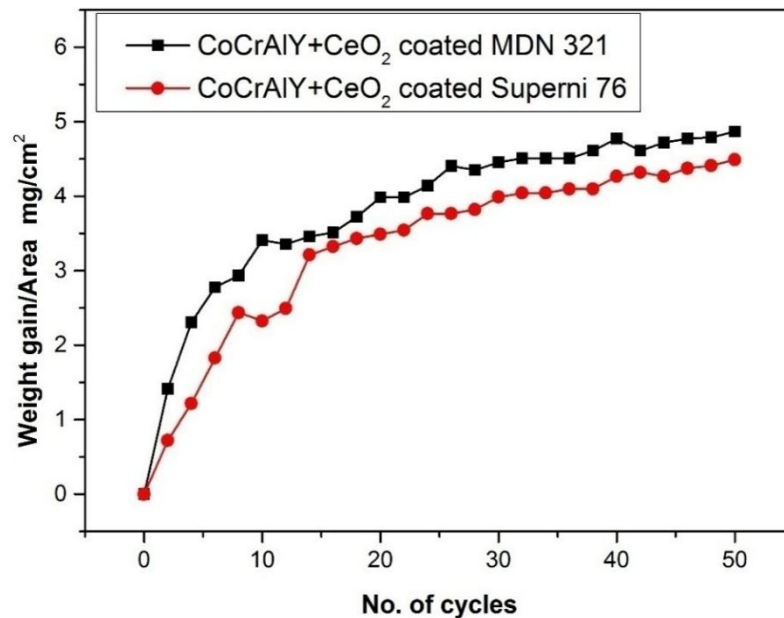


Figure 6.7 Weight gain vs. number of cycles plot of CoCrAlY+CeO<sub>2</sub> coated alloys subjected to hot corrosion.

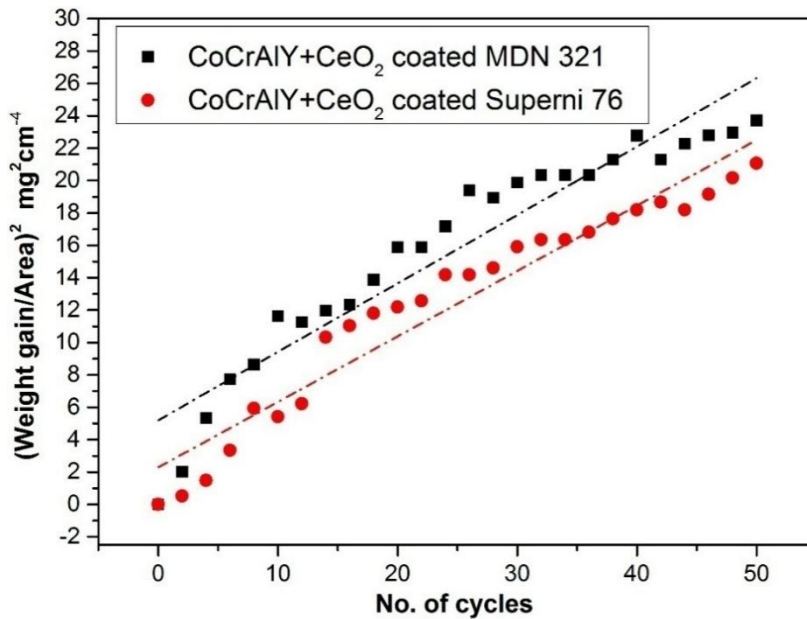


Figure 6.8  $(\text{Weight gain/area})^2$  vs. number of cycles plot of CoCrAlY+CeO<sub>2</sub>coated alloys subjected to hot corrosion.

### 6.2.2 X-ray diffraction analysis

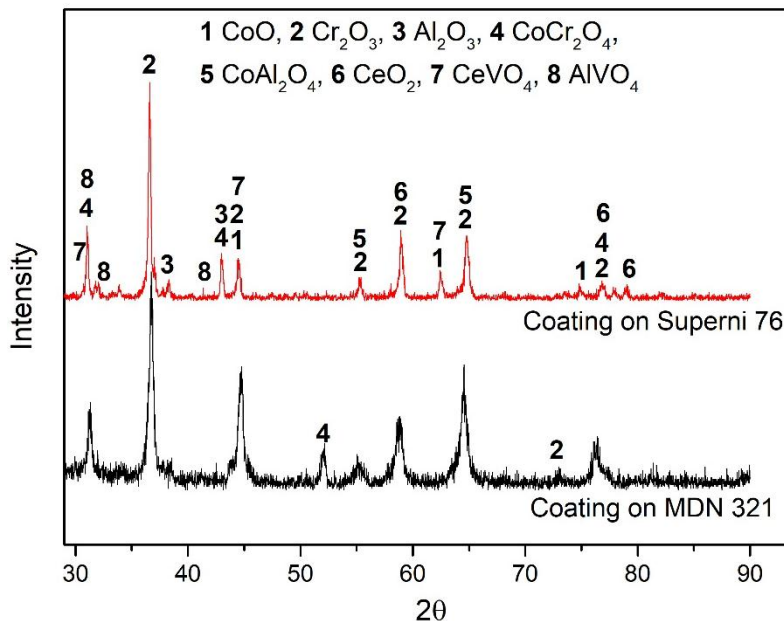


Figure 6.9 XRD patterns for CoCrAlY+CeO<sub>2</sub> coated alloys subjected to hot corrosion.

XRD patterns of hot corroded CoCrAlY+CeO<sub>2</sub> coated alloys exposed to salt environment at 700 °C are shown in Figure 6.9. The major peaks in coated alloys indexed to Cr<sub>2</sub>O<sub>3</sub> whereas all the other phases such as CoO, Al<sub>2</sub>O<sub>3</sub>, V<sub>2</sub>O<sub>5</sub>, CoAl<sub>2</sub>O<sub>4</sub>, CoCr<sub>2</sub>O<sub>4</sub>, AlVO<sub>4</sub> and CeVO<sub>4</sub> indexed to intermediate/minor peaks. The major phases

observed in both the coated alloys are similar and elements of substrate such as Fe or Ni were not found in corroded coating surface.

### **6.2.3 Surface SEM and EDS analysis**

The surface morphology of corroded CoCrAlY+CeO<sub>2</sub> coatings on MDN 321 and Superni76is shown in Figure 6.10a and c respectively. The continuous closely packed globular structure and dark irregular crystals are observed on the corroded coating surface. EDS analysis of region 'A' and 'C' in Figure 6.10 showed the dominant presence of O, Co and Cr with small amount of Al and Na, S, V salts. Short rod like structure represents the V<sub>2</sub>O<sub>5</sub> salt. Figure 6.10b shows the magnified image of irregular crystals developed on the coating surface. The EDS of irregular crystals referred as region 'B' has major O, Ce and V with small amount of Al which is an indication of presence of CeVO<sub>4</sub>. The presence of oxides of Co, Cr, Al and its spinels and also the corrosion product CeVO<sub>4</sub> is also evident from the XRD analysis of corroded coatings.

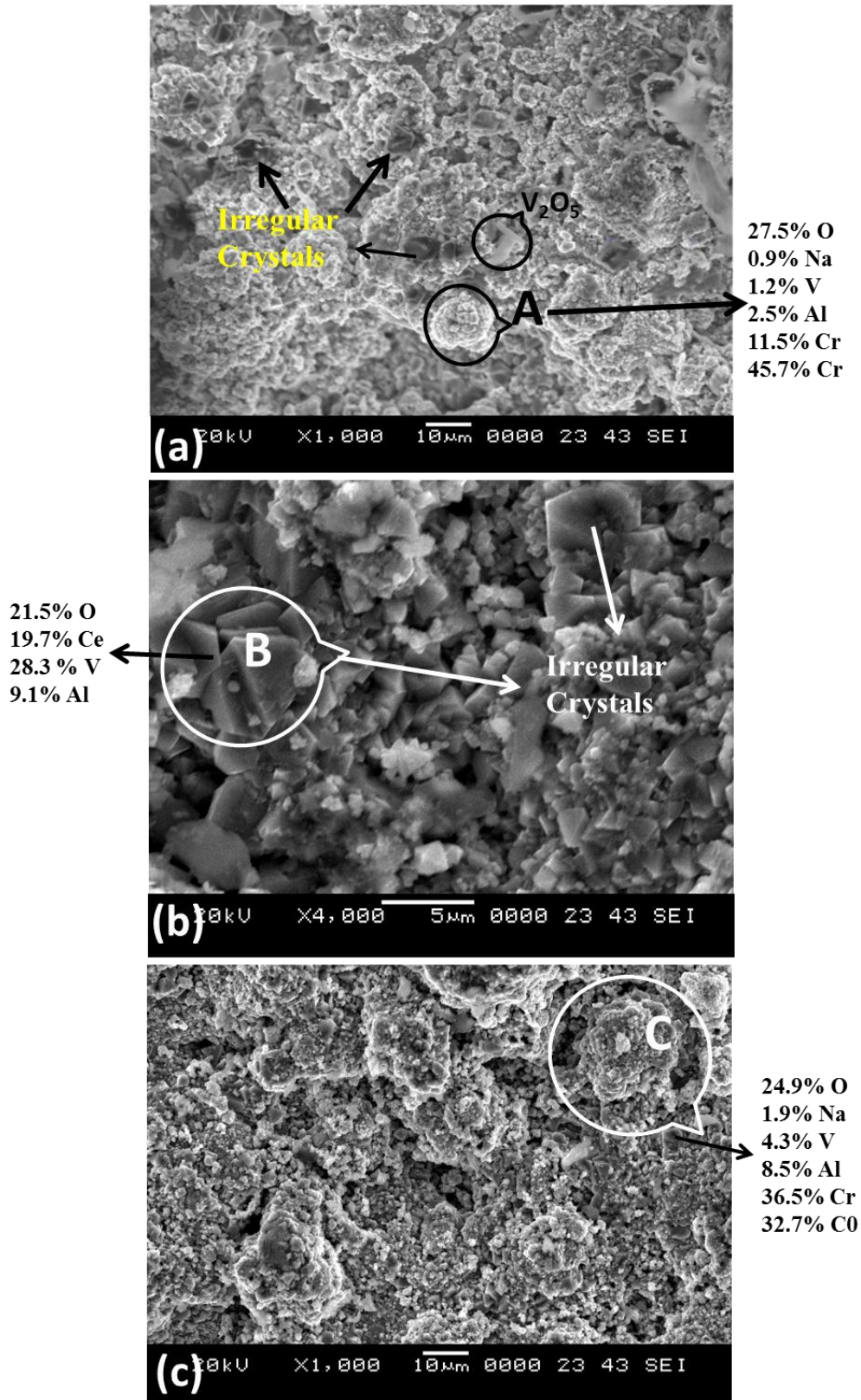


Figure 6.10 Surface morphology of hot corroded CoCrAlY+CeO<sub>2</sub> coatings on (a) MDN 321 and (b) Superni76.

### 6.2.4 Cross sectional and elemental mapping

Oxide scale growth of the corroded coating is represented by coated cross section and shown in Figure 6.11. The Figure 6.11a shows thick, delaminated oxide scale ranging between 37-43  $\mu\text{m}$  and many cracks are observed in the oxide scale. The thick oxide scale delaminating from the coating surface and cracks proceeding into the coating along the splat boundaries is observed in Figure 6.11a. The elemental composition at various location of the cross section is analysed by point EDS analysis (Figure 6.11b) and reported in Table 6.2. The upper oxide scale at region 1 is dominant in Co, Cr and O with Na and V salts. However, at region 2 the presence of higher amount of O and V as compared to region 1 indicates that corrosion species entered into the coating. Higher Co and Cr elements are seen at region 3 where the EDS is analysed at only one bigger splat.

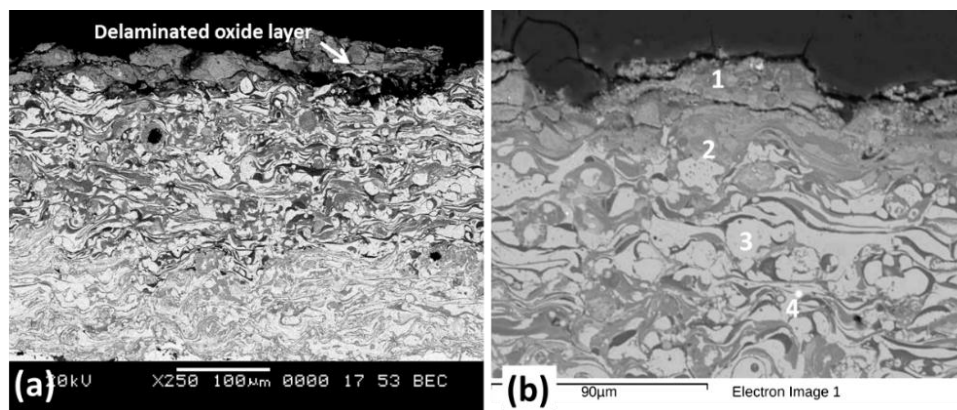


Figure 6.11 Corroded coating cross section and EDS point analysis (wt. %) of the CoCrAlY+CeO<sub>2</sub> coating.

Table 6.2 Point EDS of CoCrAlY+CeO<sub>2</sub> coating along the cross section in wt. %.

Elements (wt%)	Region 1	Region 2	Region 3	Region 4
O	18.8	27.5	1.1	10.5
Na	1.4	-	-	-
Al	1.4	1.9	-	11.8
V	2.5	2.7	-	-
Cr	4.5	10.8	26.4	5.6
Co	63.4	48.5	72	62.7
Ce	0.9	-	-	-

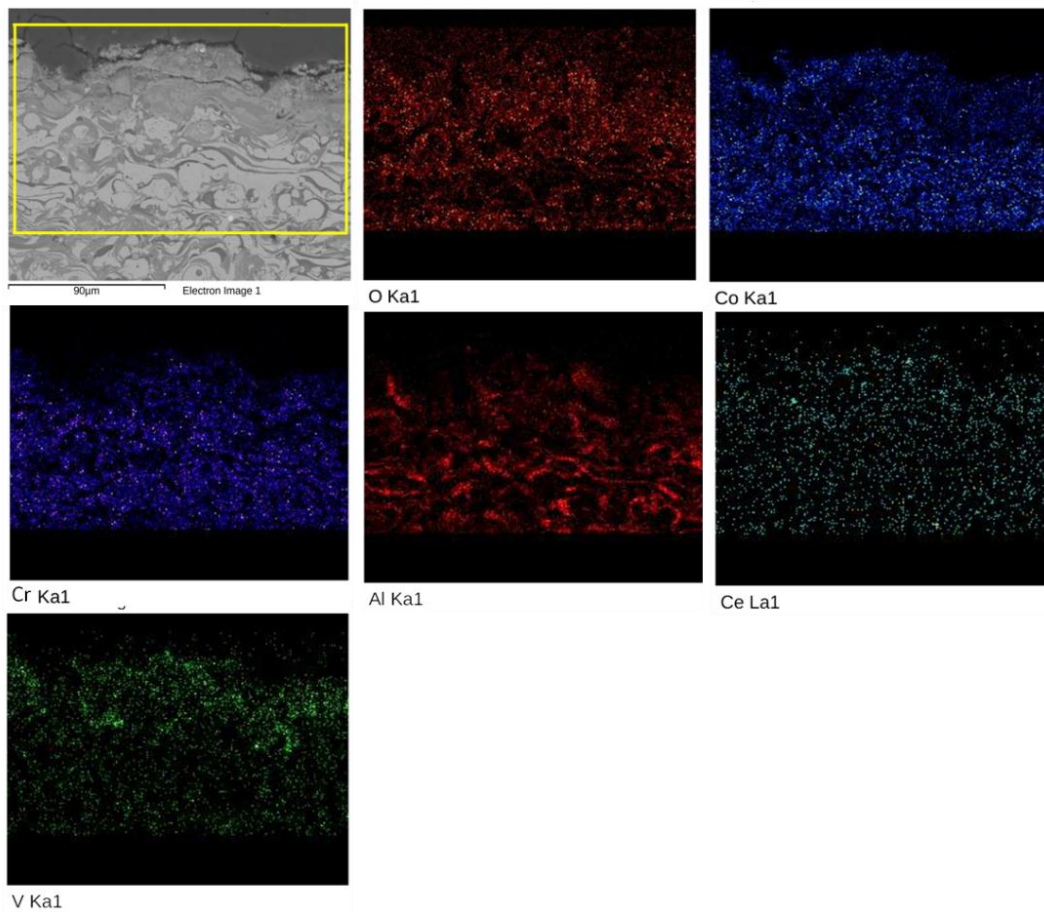


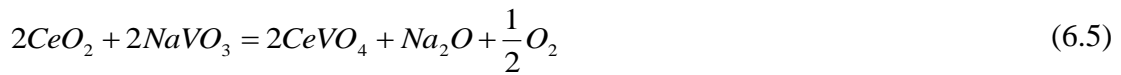
Figure 6.12 BSEI and elemental X-ray mapping along the cross-section of the CoCrAlY+CeO<sub>2</sub> coating subjected to hot corrosion.

X-ray mapping of coating cross section showing the elemental distribution is represented in Figure 6.12. Throughout the coating presence of oxygen is observed along the splats in the corroded coating. The upper scale is predominant in Co, Cr and V, whereas the O is located through the coating surface. The Al is not prominent at the coating surface. The presence of Ce and V is prominent at the outer surface might have resulted in formation of CeVO<sub>4</sub> with subsequent corrosion cycles. This corrosion product would be responsible for coating degradation.

### 6.2.5 Discussion

The observations on the surface morphology of the corroded coatings in Figure 6.10 shows the continuous globular structure with dark irregular crystals on the corroded surface and superficial cracks have been observed on the coating surface. The backscattered image across the cross section in Figure 6.11 shows that the oxide scale

formed on the surface of the corroded coating is delaminated from the coating surface and cracks in the coating cross section have also been observed. The XRD analysis in Figure 6.9 shows the dominant presence of protective Cr<sub>2</sub>O<sub>3</sub> and spinels such as CoCr<sub>2</sub>O<sub>4</sub> and CoAl<sub>2</sub>O<sub>4</sub> which are favorable for corrosion protection. During high temperature exposure the reaction between Na<sub>2</sub>SO<sub>4</sub> and V<sub>2</sub>O<sub>5</sub> resulted in the formation of NaVO<sub>3</sub> (equation 6.4) having melting point of 610° C (Yin et al. 2016). The acidic fluxing of the reinforced CeO<sub>2</sub> by the eutectic molten salt mixture during the corrosion cycles resulted in the growth of CeVO<sub>4</sub> irregular crystals (Figure 6.10b). On the other hand, Jones et al. (1986) and Nejati et al. (2014) reported destabilization of CSZ and pure CeO<sub>2</sub> by molten NaVO<sub>3</sub> or V<sub>2</sub>O<sub>5</sub> to form reaction corrosion product CeVO<sub>4</sub>. The possible reaction is in the equation 6.5.



The reaction between the coating elements and molten salts will result in the formation of corrosion products. The corrosion product CeVO<sub>4</sub> is accompanied by a destructive volume expansion resulting in outward growth in the form of irregular crystals and leads to the stresses on surrounding splats/oxide scale. Later, the molten salt infiltrates into the coating through the cracks and enhances the corrosion rate. This further leads to delamination of outer oxide layer and degradation of coating material. The presence of V inside the coating is observed in the mapping (Figure 6.12) which further leads to delamination of outer oxide layer and degradation of coating material. The reaction of active elements of the coating with the salt is not observed in XRD analysis, hence the stress developed by other hot corrosion products is not considered.

Similar observations was reported by Nejati et al. (2014) and Ahmadi-Pidani et al. (2014) that the growth of CeVO<sub>4</sub> and YVO<sub>4</sub> irregular crystals as corrosion products is responsible for the development crack on Ce and Y stabilized thermal barrier coatings. Afrasiabi and Kobayashi (2013) reported that these hot corrosion products as irregular crystals exhibit compressive stresses on the surrounding splats leading to crack resulting in accelerated corrosion.

The major steps involved in the failure of CoCrAlY+CeO<sub>2</sub> coating:

- i. Reaction of molten eutectic salt NaVO<sub>3</sub> and NaVO<sub>3</sub>-V<sub>2</sub>O<sub>5</sub> mixture with reinforcement CeO<sub>2</sub> resulting in the formation of CeVO<sub>4</sub> irregular crystals.
- ii. Growth of hot corrosion product CeVO<sub>4</sub> caused additional stresses and superficial cracks on the coating.
- iii. Infiltration of molten salt into the coating through the cracks and delamination of protective oxide scale.
- iv. Progress of superficial cracks in cyclic hot corrosion condition due to addition thermal stresses.

The CeO<sub>2</sub> particles get distributed along the splat boundaries during the coating the coating process due to their surface active nature (He et al. 2014). During hot corrosion condition the molten salt makes an attempt to enter into the coating through splat boundaries. This result in substantial reaction between molten salt and CeO<sub>2</sub> leads to the formation of severe corrosion product which diminishes the protective oxide scale and progresses the corrosion rate.

### **6.3 CoCrAlY+WC-Co coating**

#### **6.3.1 Thermogravimetric studies**

The cumulative weight gain (mg/cm<sup>2</sup>) plots of CoCrAlY+WC-Co coatings as a function of time expressed in number of cycles are shown in Figure 6.13. The overall weight gain after 50 cycles of hot corrosion of the CoCrAlY+WC-Co coated MDN 321 and Superni 76 alloys are 3.2 and 3.12 mg/cm<sup>2</sup>, respectively. The weight gain values of both the coated alloys are very close to each other referring the absence of substrate influence on the growth surface oxide for corrosion protection. Linear weight gain is observed in initial cycles and further experience steady state weight gain nature with the subsequent hot corrosion cycles throughout the corrosion cycles. Drastic weight gain during initial corrosion cycles because there is no dense and protective oxide film formed on the coating surface yet, and the reaction of oxidation is violent on the surface which is exposed to corrosive medium.

The weight gain square (mg<sup>2</sup>/cm<sup>4</sup>) data plotted against the time to examine the corrosion kinetics and shown in Figure 6.14. The parabolic rate constant (K<sub>p</sub> in 10<sup>-10</sup> g<sup>2</sup>cm<sup>-4</sup>s<sup>-1</sup>) value of coated MDN 321 and Superni 76 alloys is 0.65 and 0.62 respectively.

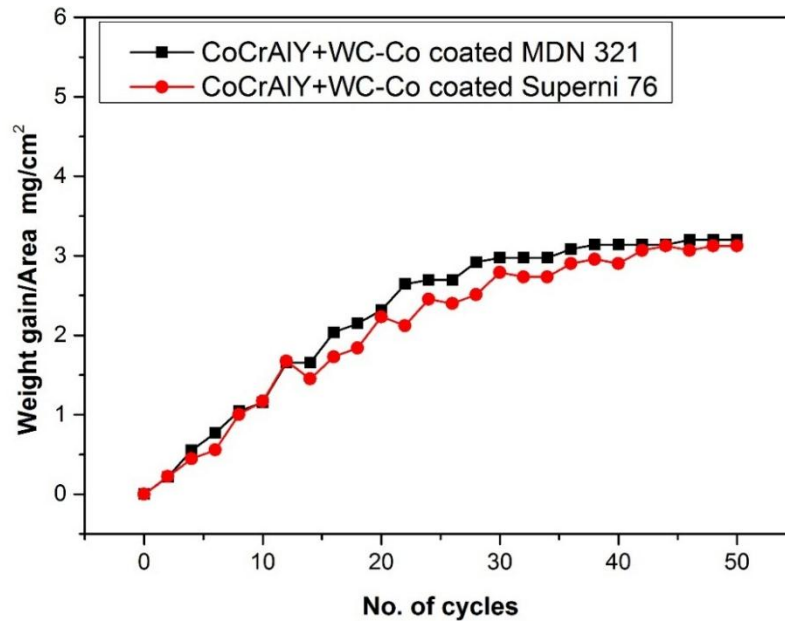


Figure 6.13 Weight gain vs. number of cycles plot of CoCrAlY+WC-Co coated alloys subjected to hot corrosion.

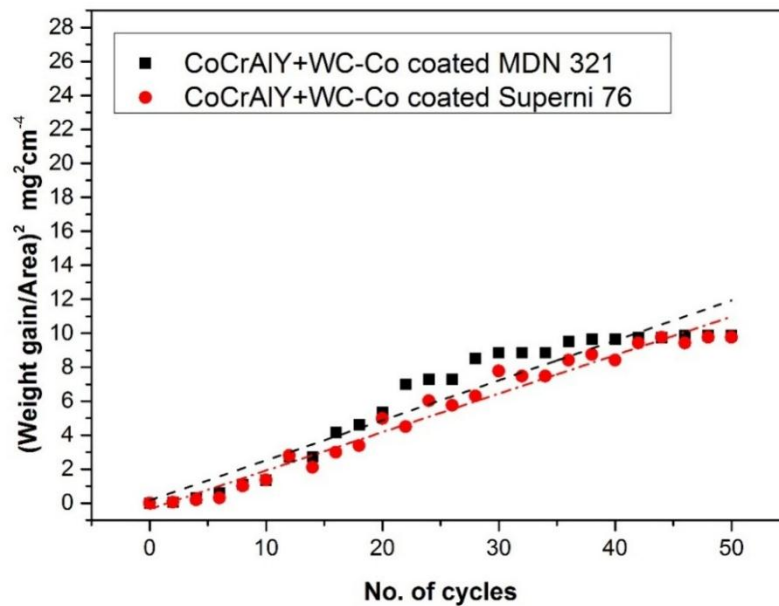


Figure 6.14  $(\text{Weight gain/area})^2$  vs. number of cycles plot of CoCrAlY+WC-Co coated alloys subjected to hot corrosion.

### 6.3.2 X-Ray diffraction analysis

XRD patterns of hot corroded CoCrAlY+WC-Co coated alloys exposed to salt environment at 700 °C are shown in Figure 6.15. The major peaks correspond to CoO, Cr<sub>2</sub>O<sub>3</sub> and CoWO<sub>4</sub> with the intermediate peaks indicating WO<sub>3</sub>, CoCr<sub>2</sub>O<sub>4</sub> and CoSO<sub>4</sub>.

Low intensity peaks represents  $\text{Al}_2\text{O}_3$  and  $\text{CrVO}_4$ . The phases observed on the surface of both the coated alloys are similar.

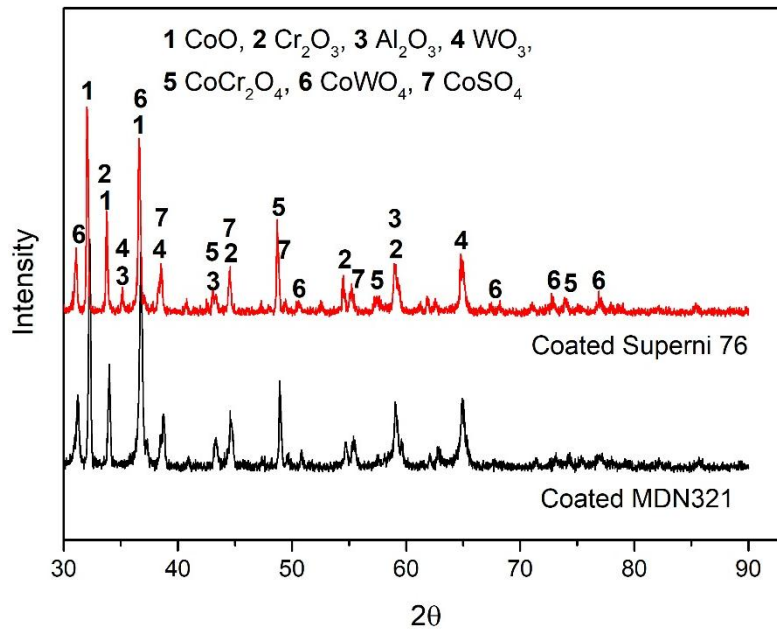


Figure 6.15 XRD patterns for CoCrAlY+WC-Co coated alloys subjected to hot corrosion.

### 6.3.3 Surface SEM and EDS analysis

The surface morphology of corroded CoCrAlY+WC-Co coatings is shown in Figure 6.16. Figure 6.16a shows the globular structure with light grey patches and Figure 6.16b shows dark grey continuous smooth layer is appeared throughout the corroded surface. EDS analysis on globular structure at region 'A' in Figure 6.16a showed the dominant presence of Co, Cr, and O which may indicate the presence of spinel oxide of  $\text{CoCr}_2\text{O}_4$  as a result of accelerated oxidation. Region 'B' showing light grey patches are rich in salt species of Na, S salts along with O and moderate amount of Co, WC and V salt. In Figure 6.16b, region 'A' shows the major constituents of Co, S and O with traces of Cr, whereas the continuous dark grey smooth layer marked as 'B' is observed to be major constituents of Co, W and O with traces of Cr and C, the presence these elements probably indicated the presence of  $\text{CoWO}_4$ . The phases such as  $\text{CoO}$ ,  $\text{Cr}_2\text{O}_3$ ,  $\text{CoWO}_4$ ,  $\text{CoSO}_4$  and  $\text{CoCr}_2\text{O}_4$  estimated from the EDS analysis are observed in the surface XRD analysis of corroded coatings.

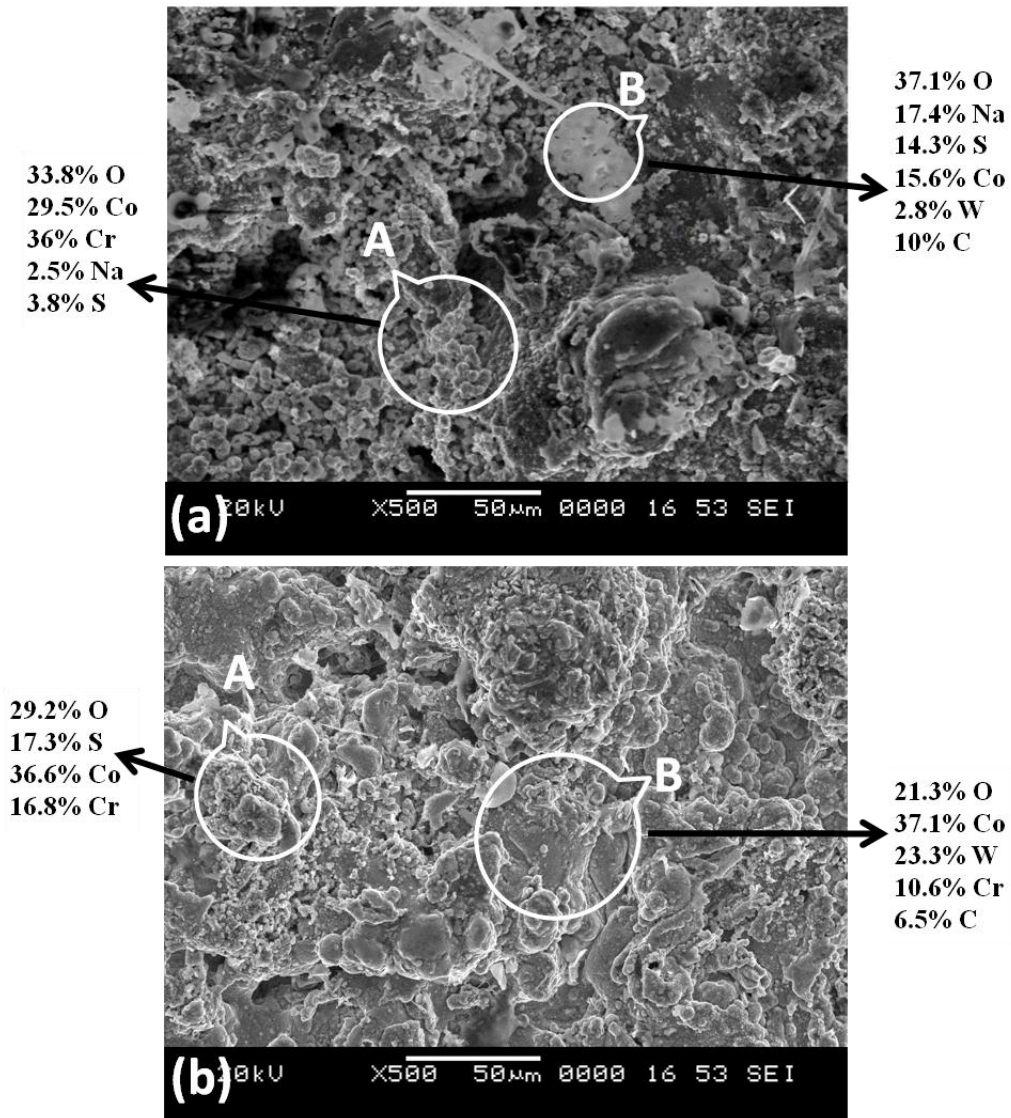


Figure 6.16 Surface morphology of hot corroded CoCrAlY+WC-Co coatings on (a) MDN 321 and (b) Superni76.

### 6.3.4 Cross sectional and elemental mapping

Oxide scale growth of the corroded coating is represented by cross section coatings and is shown in Figure 6.17. The Figure 6.17a shows continuous, thin, compact, well adherent, no spallation of scale and cracks have been observed after exposed to corrosion thermo cycles. The oxide scale ranges between 10-16 μm. The elemental composition at various location of the cross section is analysed by EDS point analysis (Figure 6.17b) and reported in Table 6.3. EDS of upper oxide scale referred as region 1 dominant in Co, Cr and O with considerable amount of WC and negligible amount of Na and V salts. In region 2, the O percentage is reduced while the elemental percentage

of remaining elements is closer to region 1. Region 3 is rich in W and O percentage is negligible inside the coating surface, indicating resistance offered by coating.

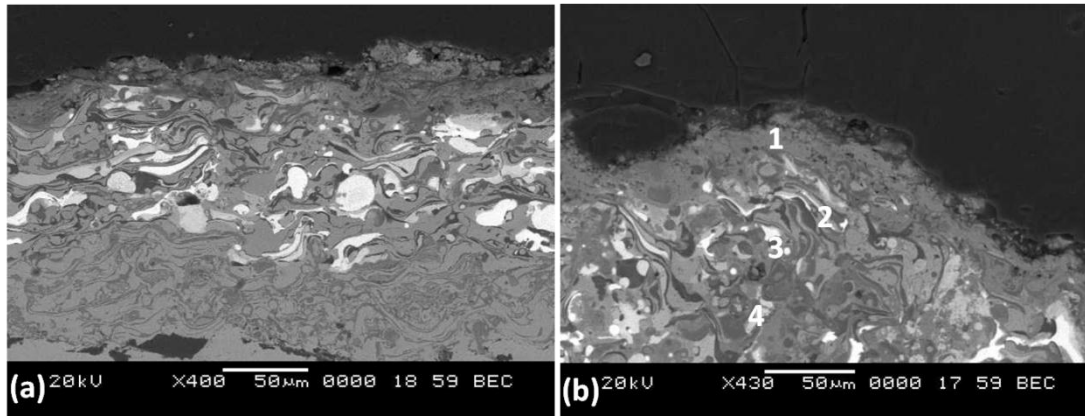


Figure 6.17 Corroded coating cross section and EDS point analysis (wt. %) of the CoCrAlY+WC-Co coating.

Table 6.3 Point EDS of CoCrAlY+WC-Co coating along the cross section in wt. %.

Elements (wt%)	Region 1	Region 2	Region 3	Region 4
O	22.1	12.8	2.1	2.6
Na	0.2	-	-	-
Al	5	10.7	0.6	8.1
V	1	-	-	-
Cr	5.7	10.6	12.3	12.1
Co	55.1	40.3	11.7	42.4
W	2.1	2.4	41.4	13.4
C	8.3	9.1	14.7	5.4

X-ray mapping of coating cross section is shown in Figure 6.18. The presence of oxygen rich layer at the coating surface is observed in the corroded coating. The distribution of Co, Cr, W and O are observed as major elements on the upper most scale of the coating. The salts distributions are observed only at the coating surface. Al distribution is observed below the oxide scale and only traces of Al are observed on the upper oxide scale. The presence of Co, Cr, W and O is prominent at the outer surface might have resulted in formation of  $\text{CoWO}_4$ ,  $\text{CoCr}_2\text{O}_4$  with subsequent corrosion cycles.

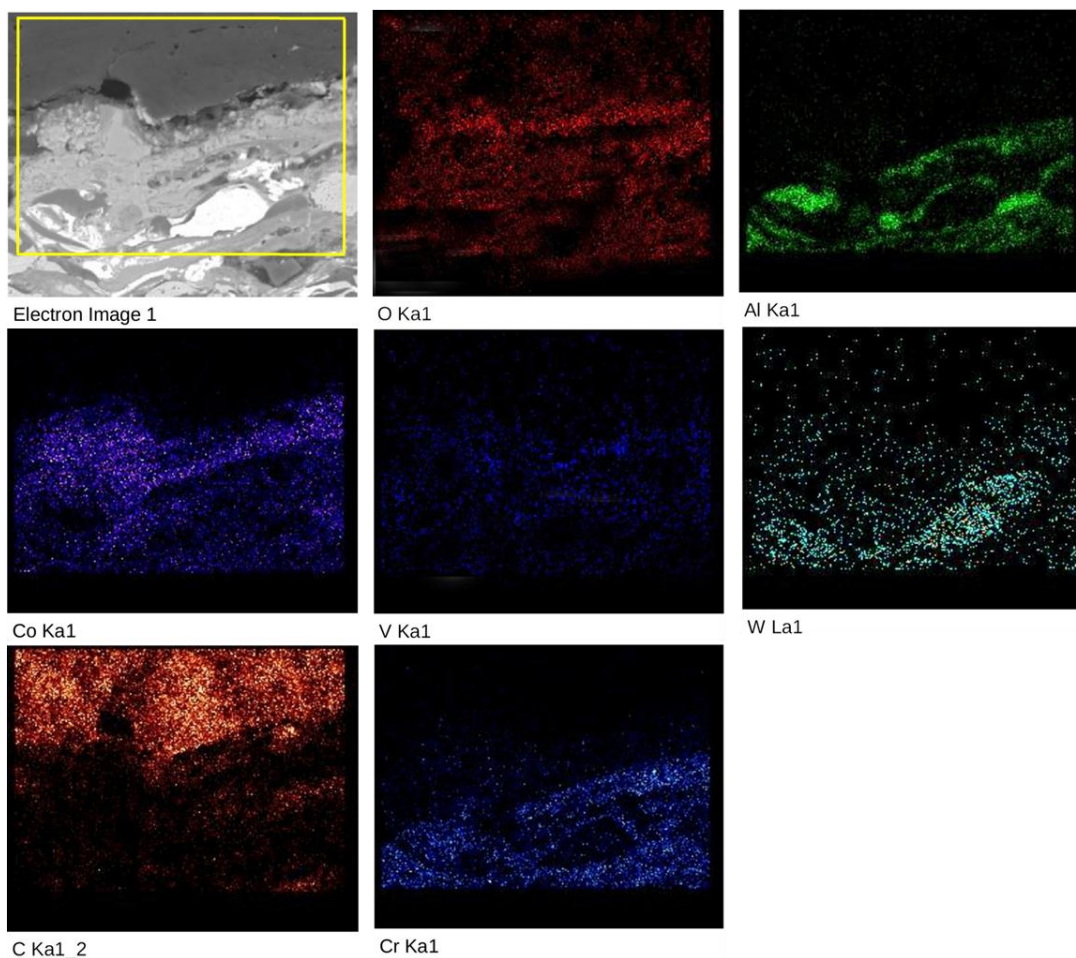


Figure 6.18 BSEI and elemental X-ray mapping along the cross-section of the CoCrAlY+WC-Co coating subjected to hot corrosion.

### 6.3.5 Discussion

After 50 cycles of exposure to  $\text{Na}_2\text{SO}_4$ -60%  $\text{V}_2\text{O}_5$  molten salt environment at  $700^\circ\text{C}$  the overall weight gain of CoCrAlY+WC-Co coated MDN 321 and Superni 76 alloys are 3.20 and 3.12  $\text{mg}/\text{cm}^2$ , respectively. Both the coated alloys showed minimal weight gain difference.

The morphology of the corroded coating surface is shown in Figure 6.16 and it is observed that the oxide scale formed comprises of predominantly dominant continuous dark grey smooth layer along with globular structure and light grey patches. A continuous, thin, non-porous and well adhered oxide scale is evident from the back scattered electron image (Figure 6.17) taken along the cross section of corroded coating. The XRD analysis of the corroded coating surface shows the presence of  $\text{CoO}$ ,  $\text{Cr}_2\text{O}_3$ ,  $\text{CoWO}_4$ ,  $\text{CoCr}_2\text{O}_4$ ,  $\text{CoSO}_4$ ,  $\text{Al}_2\text{O}_3$ ,  $\text{WO}_3$  and  $\text{CrVO}_4$ . It is observed from the EDS and

XRD analysis that the dominant phases formed on the coating surface are  $\text{CoWO}_4$ ,  $\text{CoO}$  and  $\text{CoSO}_4$ .

At the inception stage of hot corrosion, the interaction of atmospheric oxygen ions with the coating material is interrupted by the molten salt layer on the surface of the coating and active elements in the utilize oxygen ions from  $\text{SO}_4$  to form metal oxides. The tungsten has greater affinity to oxygen at temperatures of  $400^\circ\text{C}$  and above. It utilizes the oxide ions from the salt layer next to coating to form  $\text{WO}_3$  during the early stages of hot corrosion as per the reaction is shown in equation 6.6 (Espevik et al. 1980). This reduces the activity of oxide ion in salt consequently increasing the activity of the salt resulting in acidic fluxing of metal oxides. Generally, the acidic fluxing action is predominant in tungsten rich region of the coating, since the activity of  $\text{WO}_3$  under the given condition is substantially higher.



The  $\text{WO}_3$  will form tungsten localised regions, as the hot corrosion progresses the Co and Cr in the coating get oxidized (equation 6.7 and 6.8). As the corrosion cycle progresses the Co which is a major phase in the coating gets oxidised to  $\text{CoO}$  and react with active sulfur to form  $\text{CoSO}_4$  sulfate (equation 6.9). These sulfates are known to be more aggressive only in molten state. The melting temperature of  $\text{CoSO}_4$  being  $735^\circ\text{C}$ , which is higher than corrosion test temperature.  $\text{CoSO}_4$  is stable at testing temperature and not playing active role in inducing hot corrosion.



XRD analysis on the external surface of corroded coatings confirmed the presence of  $\text{CoO}$ ,  $\text{Cr}_2\text{O}_3$  and its spinel as a major phase. The nucleation of  $\text{CoO}$  and  $\text{Cr}_2\text{O}_3$  resulting in the formation of spinel oxide  $\text{CoCr}_2\text{O}_4$ .

Somasundaram et al. (2014) have reported protrusion on the tungsten rich surface and it is considered as an evidence for acidic fluxing due to heavily localised attack of salt.

The similar fluxing observations have been reported by Gurappa (1999) and Wang and Lin (2002) based on their studies on hot corrosion behaviour of superalloys containing tungsten. In the present study since the protrusion like structure has not appeared on the corroded coating surface, it may be considered that acidic fluxing is not predominant.

Further the nucleation of  $\text{WO}_3$  and  $\text{CoO}$  resulted in the formation of  $\text{CoWO}_4$  spinel oxide and it is observed in XRD analysis as a strong phase and appeared as dominant continuous dark grey smooth layer as observed from EDS analysis. The presence of  $\text{CoWO}_4$  spinel oxide as strong phase suppresses inward oxygen diffusion, since it provides less porosity and more passivation effect against the entry of molten salt. While  $\text{WO}_3$  possess porous structure. Similar observations are reported by Jafari et al. (2013) and (Singh et al. 2016). The presence of  $\text{CoWO}_4$  as a strong phase with corrosion protective  $\text{Cr}_2\text{O}_3$  and its spinel oxide  $\text{CoCr}_2\text{O}_4$  have contributed to corrosion resistance of coatings. The spinel of Co and Cr oxides ( $\text{CoCr}_2\text{O}_4$ ) have much smaller diffusion coefficients of the cations and anions than those in their parent oxides, hence helps to develop corrosion resistance (Chatterjee et al. 2001). Ul-Hamid, (2003) reported that the presence of  $\text{Cr}_2\text{O}_3$  and  $\text{NiCr}_2\text{O}_4$  within the scale would restrict diffusion through it and lower the scaling rate which provides the necessary corrosion resistance.

## **6.4 CoCrAlY+Cr<sub>3</sub>C<sub>2</sub>-NiCr coating**

### **6.4.1 Thermogravimetric studies**

The cumulative weight gain ( $\text{mg}/\text{cm}^2$ ) plots of CoCrAlY+Cr<sub>3</sub>C<sub>2</sub>-NiCr coatings as a function of time expressed in number of cycles are shown in Figure 6.19. The overall weight gain after 50 cycles of corroded CoCrAlY+Cr<sub>3</sub>C<sub>2</sub>-NiCr coated MDN 321 and Superni 76 alloys are 1.73 and 1.66  $\text{mg}/\text{cm}^2$ , respectively. Higher weight gain is observed in the initial stages where oxidation is predominant and the steady state weight gain is observed with subsequent corrosion cycles. After few cycles the steady state weight gain is achieved till the completion of 50 cycles which is mainly due to the formation of stable protective oxide layer. The weight gain square ( $\text{mg}^2/\text{cm}^4$ ) data plotted as a function of time to determine the corrosion kinetics is shown in Figure 6.20. The parabolic rate constant ( $K_p$  in  $10^{-10} \text{ g}^2\text{cm}^{-4}\text{s}^{-1}$ ) value of coated MDN 321 and Superni 76 alloys is 0.053 and 0.048 respectively.

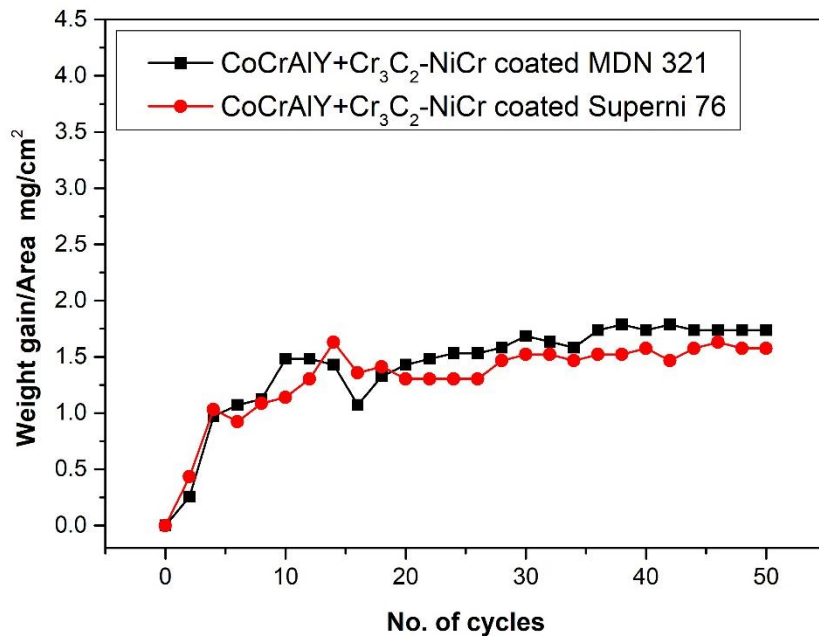


Figure 6.19 Weight gain vs. number of cycles plot of CoCrAlY+Cr<sub>3</sub>C<sub>2</sub>-NiCr coated alloys subjected to hot corrosion.

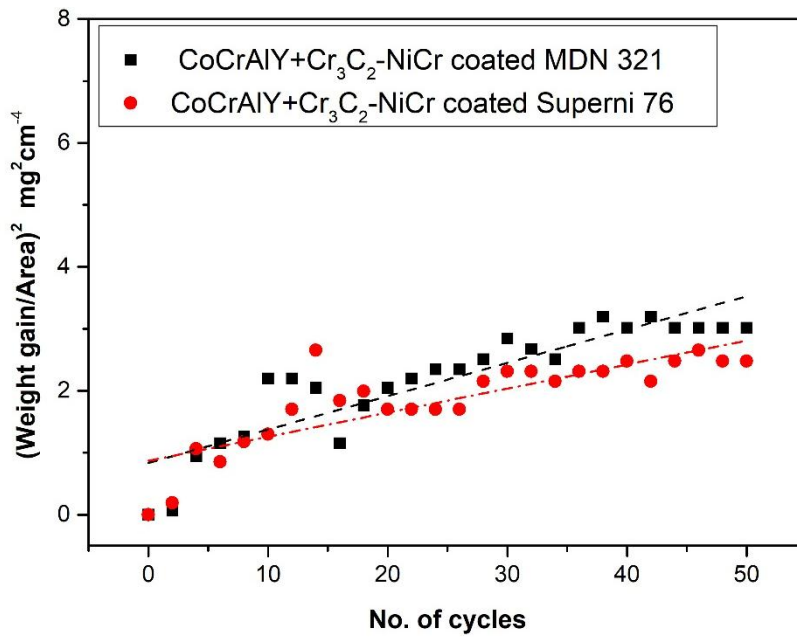


Figure 6.20 (Weight gain/area)<sup>2</sup> vs. number of cycles plot of CoCrAlY+Cr<sub>3</sub>C<sub>2</sub>-NiCr coated alloys subjected to hot corrosion.

### 6.4.2 X-Ray diffraction analysis

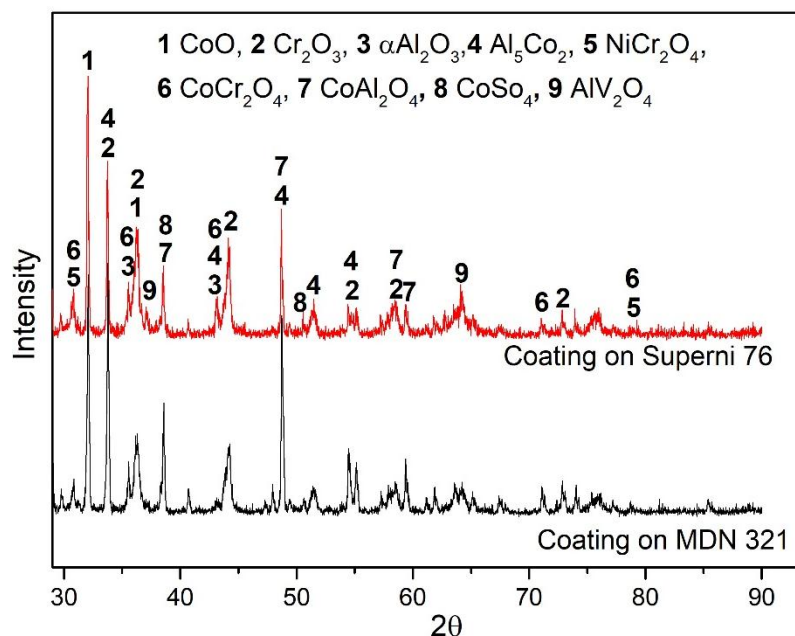


Figure 6.21 XRD patterns for CoCrAlY+Cr<sub>3</sub>C<sub>2</sub>-NiCr coated alloys subjected to hot corrosion.

XRD patterns of CoCrAlY+Cr<sub>3</sub>C<sub>2</sub>-NiCr coated alloys subjected to hot corrosion in environment at 700 °C are shown in Figure 6.21. The major peaks in coated alloys are indexed to CoO and Cr<sub>2</sub>O<sub>3</sub> while the intermediate/minor peaks indexed to  $\alpha$ Al<sub>2</sub>O<sub>3</sub>, V<sub>2</sub>O<sub>5</sub>, CoAl<sub>2</sub>O<sub>4</sub>, CoCr<sub>2</sub>O<sub>4</sub> and NiCr<sub>2</sub>O<sub>4</sub>. The presence of NiCr as binder in Cr<sub>3</sub>C<sub>2</sub> is responsible for the formation of NiCr<sub>2</sub>O<sub>4</sub> spinel oxide during the corrosion cycles. The peaks and phases obtained on both the coated alloys after subjected to corrosion are similar.

### 6.4.3 Surface SEM and EDS analysis

The surface morphology of corroded CoCrAlY+Cr<sub>3</sub>C<sub>2</sub>-NiCr coatings is shown in Figure 6.22. Surface oxide is developed due to the oxidation of each splats and it has appeared as a continuous closely packed globular structure. This structure is observed throughout the coating surface after subjected to hot corrosion. EDS analysis of point 'A' and 'C' in Figure 6.22a and b shows the dominant presence of oxides of Co, Cr and Al, indicating the formation probable phases of CoO, Cr<sub>2</sub>O<sub>3</sub>, Al<sub>2</sub>O<sub>3</sub> and the combination of these oxide as CoCr<sub>2</sub>O<sub>4</sub> and CoAl<sub>2</sub>O<sub>4</sub> spinels. The point 'B' has appreciable

composition of many major elements such as O, Co, Cr, Ni and V leading to the interpretation of presence of  $\text{NiCr}_2\text{O}_4$  and  $\text{V}_2\text{O}_5/\text{CrV}_2\text{O}_4$ . Thus the oxide scale developed on the coating surface may be the combination of  $\text{CoO}$ ,  $\text{Cr}_2\text{O}_3$ ,  $\text{Al}_2\text{O}_3$  and spinels such as  $\text{CoCr}_2\text{O}_4$ ,  $\text{CoAl}_2\text{O}_4$  and  $\text{NiCr}_2\text{O}_4$ . The presence of these phases are also confirmed by the XRD results of corroded coating.

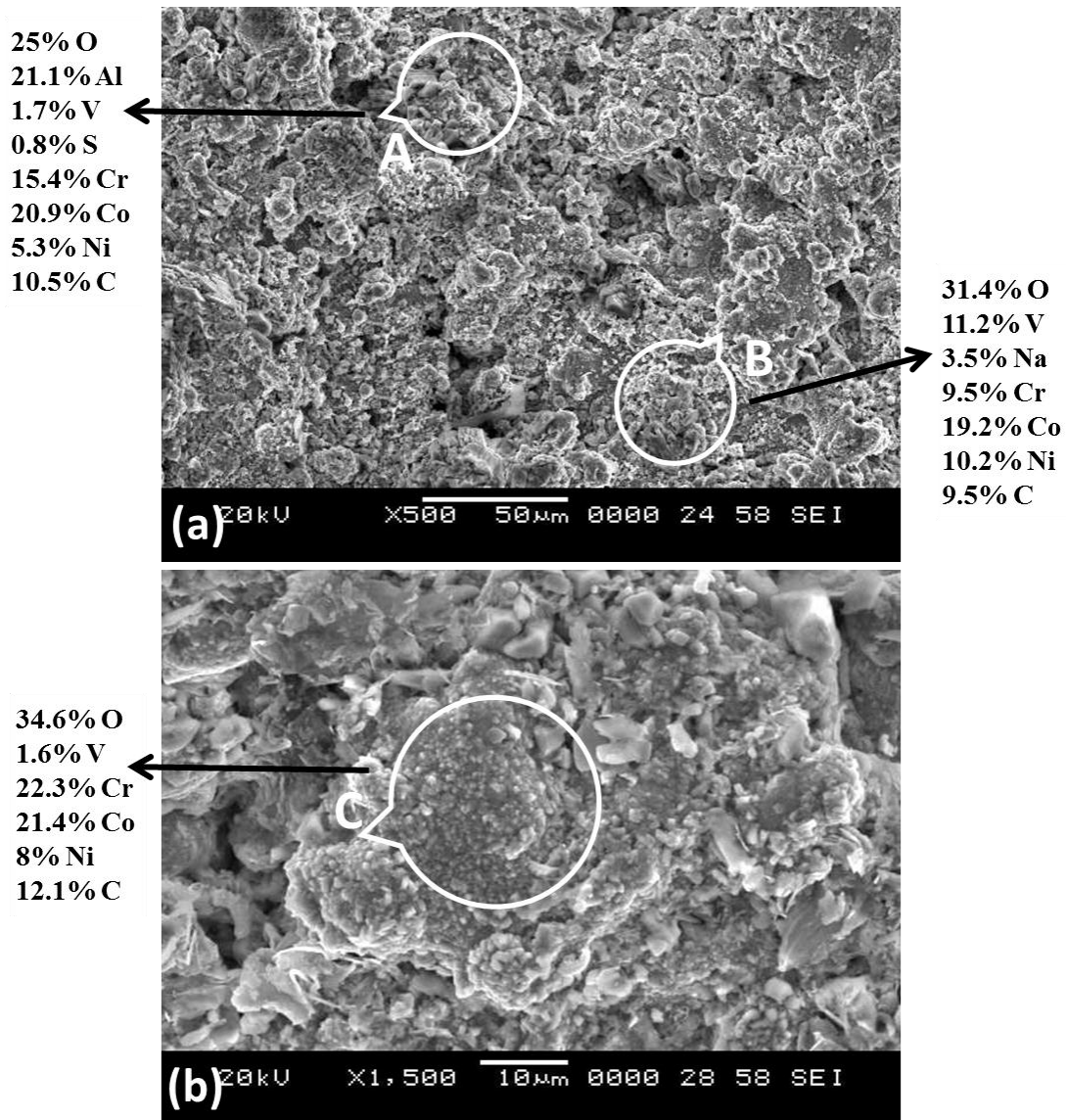


Figure 6.22 Surface morphology of corroded  $\text{CoCrAlY}+\text{Cr}_3\text{C}_2$ -NiCr coating on (a) MDN 321 and (b) Superni76.

#### 6.4.4 Cross section and elemental mapping

Figure 6.23a shows the formation of a thin oxide scale on the upper most layer of the coating surface and lamellar structure of the coating is retained below the oxide scale. This shows that the developed surface oxide scale has protected the underneath coating and more importantly the substrate alloys.

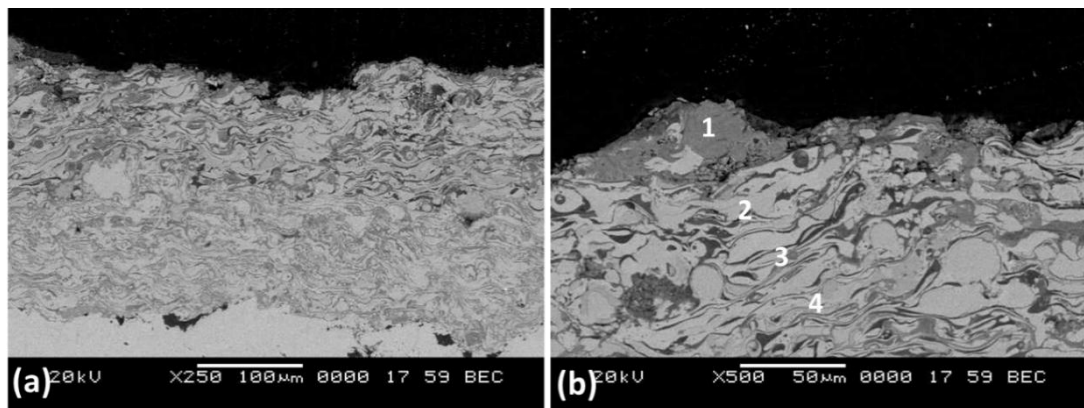


Figure 6.23 Cross section and EDS point analysis of the CoCrAlY+Cr<sub>3</sub>C<sub>2</sub>-NiCr coating subjected to hot corrosion.

Table 6.4 Point EDS of CoCrAlY+Cr<sub>3</sub>C<sub>2</sub>-NiCr coating cross section in wt. %.

Elements (wt%)	Region 1	Region 2	Region 3	Region 4
O	27.2	12.9	2.8	2.1
Na	0.2	-	-	-
V	0.9	-	-	-
Al	7	6.8	22.6	9.4
Cr	19.4	27.1	15.8	22.8
Co	22.4	23.6	32.6	32.1
Ni	20.8	24.4	19.4	15.8
C	2.1	4.8	1	2.8

The back scattered electron image of corroded coating cross section after 50 cycles in The elemental composition at various point of the oxidised coating cross section is analysed by EDS analysis (Figure 6.23b) and reported in Table 6.4. The O percentage at point '1' is higher and is gradually reduced as we move to point '4' showing that the

oxide scale acts as barrier for the corrosion species to enter into the coating. The Na and V salts are present at the upper most layer of the coating and not appeared below Point '1' leading to the evidence of oxide layer as a barrier for the entry of salts thus protecting the lower layer of coating from further degradation. The presence of small amount of O at point '4' is due to the oxide stringers at the splat boundaries that are formed during the coating process.

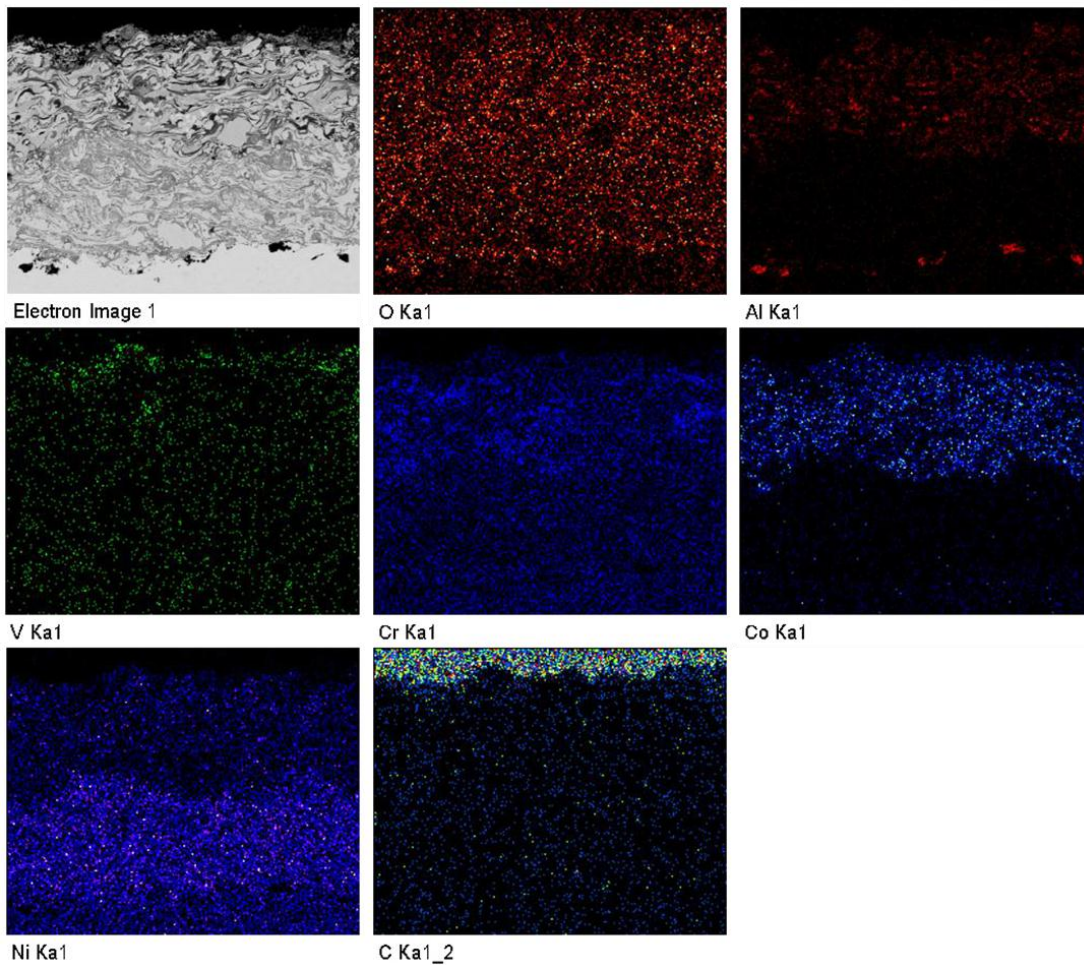


Figure 6.24 BSEI and elemental X-ray mapping along the cross-section of the CoCrAlY+Cr<sub>3</sub>C<sub>2</sub>-NiCr coating subjected to hot corrosion.

X-ray mapping (Figure 6.24) of coating cross section shows the distribution of Co, Cr Ni and O throughout the coating cross section, whereas the O distribution is denser at the coating surface indicating the presence of oxides of Co, Cr, Ni, Al and its spinels. The presence of Al is observed in the top coat and also at the interface of bond coat and substrate which is due to the embedment of alumina particles during grit blasting prior

to the coating process. Also the distribution of V and Na salts are observed only at the surface of the coating and these salts can be interpreted as the oxide layer acting as a barrier to the entry of salts. The presence of these oxides is supported by surface EDS and is strongly in agreement with the XRD analysis of oxidised coating as observed in Figure 6.21.

#### 6.4.5 Discussion

As seen in Figure 6.22, closely packed globular structure is observed throughout the corroded CoCrAlY+Cr<sub>3</sub>C<sub>2</sub>-NiCr coating surface. The coating surface XRD and EDS analysis, reveals that the oxide scale is formed by the combination of CoO, Cr<sub>2</sub>O<sub>3</sub>, Al<sub>2</sub>O<sub>3</sub> and multiple spinel oxides such as CoAl<sub>2</sub>O<sub>4</sub>, CoCr<sub>2</sub>O<sub>4</sub> and NiCr<sub>2</sub>O<sub>4</sub>. The uppermost portion of the oxide scale mainly consists of a continuous film which is found to be CoO, Cr<sub>2</sub>O<sub>3</sub> and CoCr<sub>2</sub>O<sub>4</sub>. The total Cr percentage present in coating including the Cr present in Cr<sub>3</sub>C<sub>2</sub>-NiCr reinforcement is 36%. The higher Cr content in the coating leads to the fast transformation of Cr to Cr<sub>2</sub>O<sub>3</sub> during the early stage of hot corrosion. This is attributed to the presence of Cr<sub>2</sub>O<sub>3</sub> as a dominant phase with other major CoO. The nucleation of these oxides with subsequent hot corrosion cycles would result in the formation of CoCr<sub>2</sub>O<sub>4</sub> spinel oxide which is also a major phase as observed from XRD analysis. The presence of small amount of Ni in the reinforcement is responsible for the formation of NiCr<sub>2</sub>O<sub>4</sub>. The minor phases of the mixed spinel oxides of CoAl<sub>2</sub>O<sub>4</sub> and NiCr<sub>2</sub>O<sub>4</sub> have also been identified by the XRD analysis. After sufficient number of cycles of exposure to corrosion media, the CoO formed would undergo solid state reaction with Cr<sub>2</sub>O<sub>3</sub> to form CoCr<sub>2</sub>O<sub>4</sub> spinel oxide. CoCr<sub>2</sub>O<sub>4</sub> is a protective oxide that could limit Co diffusion, thus slowing down the oxidation rate.

These surface oxides act as a barrier to the diffusion of oxygen and the corrosive species of the molten salt into underneath coating and thereby contribute for the hot corrosion resistance of CoCrAlY+Cr<sub>3</sub>C<sub>2</sub>-NiCr coating. It is also corroborated from Figure 6.23a and Figure 6.24 that the coatings have been partially oxidized and the corrosion is restricted to a depth of few microns on the surface at the end of 50 cycles of hot corrosion studies. The absence of oxygen as well as Na and V is observed in the region below the surface oxide layer. This can be further substantiated from the weight gain

(mg/cm<sup>2</sup>) data plotted as a function of time (Figure 6.20), which shows a parabolic behaviour of both the coated alloys.

In the present studies, the improvement in corrosion resistance provided by the spinels formed during the action of corrosive media can be further substantiated by the fact that few other researchers have also made similar observations. Nicholls et al. (2002) and Talboom et al. (1970) reported that in type II hot corrosion condition (650–800°C), CoCrAlY coatings containing high chromium (20-40%) could assist better corrosion resistance than NiCrAlY based coatings. Zhang et al. (2016) reported that the presence of CoCr<sub>2</sub>O<sub>4</sub> and NiCr<sub>2</sub>O<sub>4</sub> spinels on the plasma sprayed corroded CoNiCrAlY/Cr<sub>2</sub>O<sub>3</sub> coating surface could able to provide resistance against corrosion in molten salt environment. He also has suggested that spinel usually has lower diffusion coefficients of cations and anions, which is beneficial for reducing the corrosion rate (Chatterjee et al. 2001). Hence it can be inferred that the presence of sufficient/favourable amount of Cr in the coating composition and the favourable temperature attributed to the formation of Cr<sub>2</sub>O<sub>3</sub> as major oxide and its spinels with other coating elements is responsible for providing hot corrosion resistance.

## **6.5 Uncoated alloys**

### **6.5.1 Thermogravimetric studies**

The plots of cumulative weight gain (mg/cm<sup>2</sup>) as a function of time expressed in number of cycles are shown in Figure 6.25. The weight gain of MDN 321 and Superni 76 at the end of 50 cycles are found to be 9.5 and 8.1 respectively. Evidently, the MDN 321 alloy showed 15% higher weight gain during the hot corrosion as compared to Superni 76. Further, the weight gain square (mg<sup>2</sup>/cm<sup>4</sup>) data is plotted as a function of time in Figure 6.26. The plot shows linear nature for both uncoated alloys, which indicates that the oxide scale on the alloy surface is not defensive in molten salt environment. It is evident from the plot that the both alloys have shown linear behaviour with MDN 321 showing lower weight gain as compared to Superni 76. The parabolic rate constants, K<sub>p</sub> value of uncoated MDN 321 and Superni 76 are found to be 4.65 and 3.32 g<sup>2</sup> cm<sup>-4</sup> s<sup>-1</sup>, respectively. Based on the results obtained during hot corrosion for uncoated alloys in terms of total weight gain values and parabolic rate constant value

( $K_p$ ), it can be inferred that all the composite coatings are able to provide at the least of 40% higher resistance to hot corrosion than uncoated alloys.

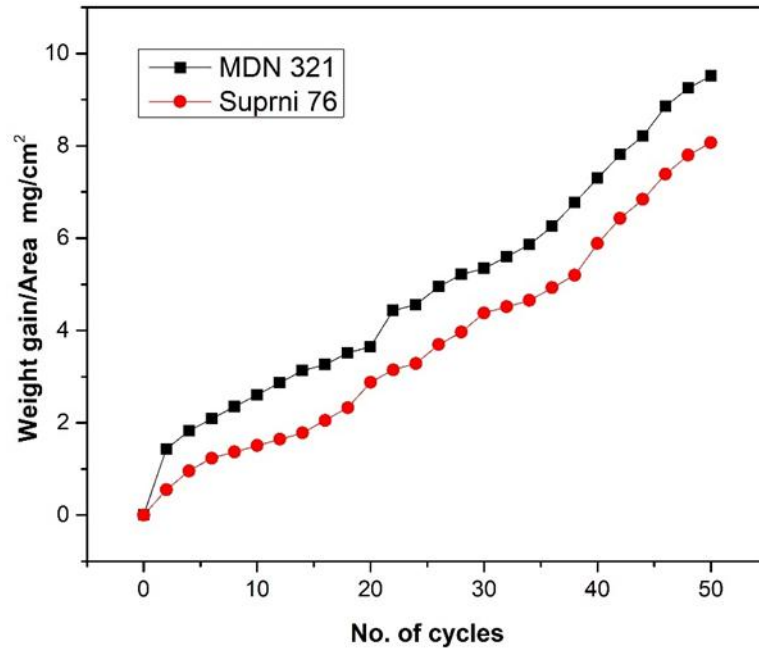


Figure 6.25 Weight gain vs. number of cycles plot of uncoated alloys subjected to hot corrosion.

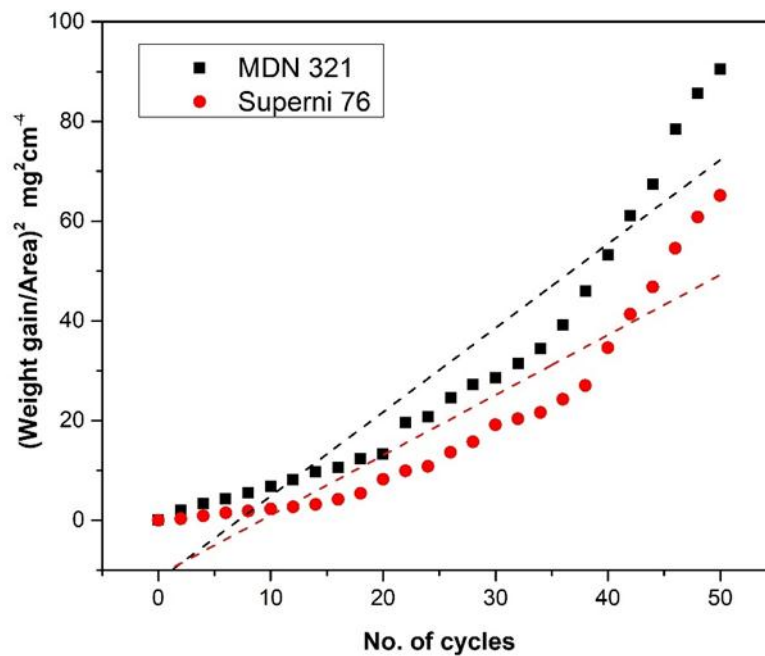


Figure 6.26  $(\text{Weight gain/area})^2$  Vs. number of cycles plot of uncoated alloys subjected to hot corrosion.

## 6.6 Comparative discussion

The total weight gain ( $\text{mg}/\text{cm}^2$ ) of uncoated and coated alloys subjected to hot corrosion in  $\text{Na}_2\text{SO}_4$ - 60%  $\text{V}_2\text{O}_5$  molten salt environment for 50 cycles at  $700^\circ\text{C}$  is shown in Figure 6.27. From the bar charts, it is observed that the weight gain of all the coated alloys are significantly lower than that of uncoated alloys in the molten salt environment showing all the coatings have performed better in terms of hot corrosion resistance than the substrate.

Based on the Weight change data it can be inferred that among the four coatings CoCrAlY+ $\text{Cr}_3\text{C}_2$ -NiCr coating has shown the highest hot corrosion resistance and CoCrAlY+ $\text{CeO}_2$  coating shows the lowest resistance to the molten salt environment. The relative hot corrosion resistance of the various coatings under study can be arranged in the following sequence:

$$\text{CoCrAlY}+\text{Cr}_3\text{C}_2\text{-NiCr} > \text{CoCrAlY}+\text{Al}_2\text{O}_3+\text{YSZ} > \text{CoCrAlY}+\text{WC-Co} > \text{CoCrAlY}+\text{CeO}_2$$

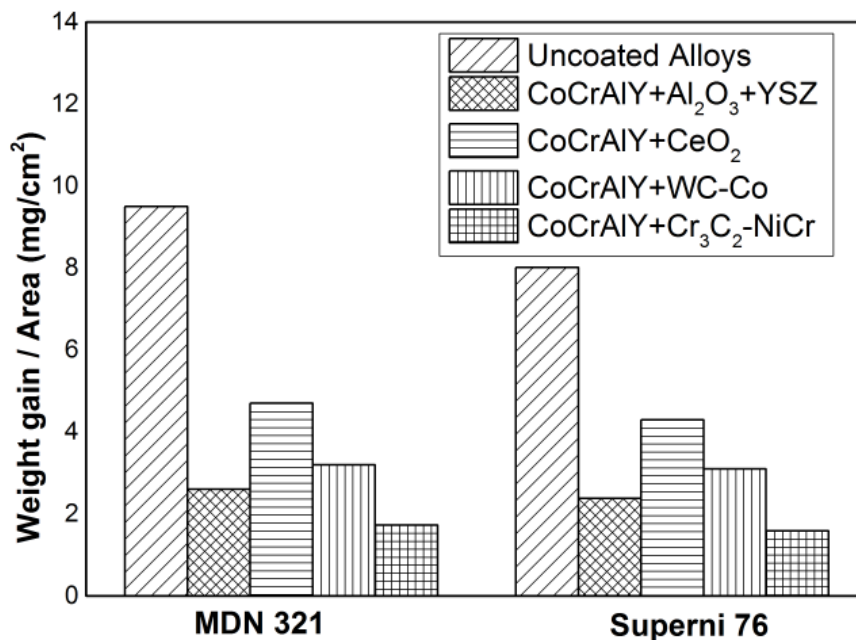


Figure 6.27 Total weight gain ( $\text{mg}/\text{cm}^2$ ) of uncoated and Plasma coated alloys subjected to hot corrosion.

The total weight gain of the CoCrAlY+Cr<sub>3</sub>C<sub>2</sub>-NiCr coated alloys are found to be 82% and 79% lesser as compared to uncoated MDN 321 and Superni 76 substrates respectively. CoCrAlY+Cr<sub>3</sub>C<sub>2</sub>-NiCr coating approximately experience 23%, 46% and 64% lesser weight gain than CoCrAlY+Al<sub>2</sub>O<sub>3</sub>+YSZ, CoCrAlY+WC-Co and CoCrAlY+CeO<sub>2</sub> coatings respectively. The superior hot corrosion resistance of CoCrAlY+Cr<sub>3</sub>C<sub>2</sub>-NiCr can be attributed to the nature of protective oxide scale developed on the surface. CoCrAlY+Cr<sub>3</sub>C<sub>2</sub>-NiCr coating contains 36 wt.% of Cr which is substantially higher than other coating compositions. The higher Cr content leads to the preferential oxidation of Cr at the early stage of corrosion to form Cr<sub>2</sub>O<sub>3</sub> as a major oxide. This resulted in the formation of CoCr<sub>2</sub>O<sub>4</sub> spinel oxide with subsequent hot corrosion cycles which is also one of the major phase observed in XRD analysis. The presence of Cr in MCrAlY coating is suggested to be up to 40% and the Cr content in present coating is closer to higher limit (Nicholls et al. 2002). This would be more beneficial for the development of protective oxide scale which is responsible for providing the superior hot corrosion resistance than the other coating and this further evident from the weight gain graph where steady state weight gain nature is obtained only after few initial cycles. The thin (8-15 μm) oxide scale is also beneficial since it undergoes less thermal stress during cyclic loading and it has better adhesion with the coating surface. The uppermost layer of the oxide scale is mainly comprised of continuous CoO, Cr<sub>2</sub>O<sub>3</sub> and their spinel oxides. The presence of NiCr<sub>2</sub>O<sub>4</sub> also plays a minor role in reducing the corrosion rate. These oxides act as barrier to the diffusion of O<sub>2</sub> and corrosive species of molten salt into the inside of coating, hence coating region beneath this oxide scale remain unoxidised. Corrosion products are confined to the outermost oxide scale.

In case of CoCrAlY+Al<sub>2</sub>O<sub>3</sub>+YSZ coated alloys, the weight gain after 50 cycles of exposure is found to be 70% and 65% lesser as compared to uncoated MDN 321 and Superni 76 substrates respectively. The thicker and denser oxide scale also initially contributes to weight gain. The CoO, Cr<sub>2</sub>O<sub>3</sub> and Al<sub>2</sub>O<sub>3</sub> are the protective phases that are formed during the early stages of corrosion. The presence of α-Al<sub>2</sub>O<sub>3</sub> as a minor phase is the thermodynamically stable phase shows slow-scale growth kinetics during the oxidation (Zhu et al. 2013). Later with the subsequent hot corrosion cycles the

nucleation of these  $\text{Cr}_2\text{O}_3$  and  $\text{Al}_2\text{O}_3$  with  $\text{CoO}$  will result in the development of  $\text{CoCr}_2\text{O}_4$  and  $\text{CoAl}_2\text{O}_4$  spinel oxides. The presence of spinels might stop the diffusion activities through the  $\text{CoO}$ , which in turn suppresses the further formation of this oxide. This is attributed to better corrosion resistance of  $\text{CoCrAlY}+\text{Al}_2\text{O}_3+\text{YSZ}$  coating by undergoing 28% and 52% lesser weight gain than other two  $\text{CoCrAlY}+\text{WC}-\text{Co}$  and  $\text{CoCrAlY}+\text{CeO}_2$  coatings respectively.

For  $\text{CoCrAlY}+\text{WC}-\text{Co}$  coated alloys, 66% and 60% lesser weight gain are observed as compared to uncoated MDN 321 and Superni 76 substrates respectively. The thick, dense, well adhered and non-porous oxide scale is observed at the cross section of the  $\text{CoCrAlY}+\text{WC}-\text{Co}$  coating. The oxide shows globular and dominant continuous smooth dark grey layer on the coating surface. From the evidence obtained from the EDS and XRD analysis, the continuous smooth dark grey layer is identified as  $\text{CoWO}_4$ . During the inception stages of hot corrosion, tungsten undergoes rapid oxidation due to its greater affinity to oxygen at temperatures above  $400^\circ\text{C}$ , this results in increasing weight gain i.e. linear weight gain nature up to 25<sup>th</sup> cycles. Later the growth of protective  $\text{CoWO}_4$  spinel oxide as a strong phase and stable  $\text{CoSO}_4$  phase as result of higher sulfur activity is a slow process. Hence the steady state weight gain is attained approximately after the 25<sup>th</sup> corrosion cycle. This is attributed to the lower corrosion resistance as compared to  $\text{CoCrAlY}+\text{Cr}_3\text{C}_2-\text{NiC}$  and  $\text{CoCrAlY}+\text{Al}_2\text{O}_3+\text{YSZ}$  coating. Also  $\text{CoCrAlY}+\text{WC}-\text{Co}$  coating experience approximately 33% lesser weight gain than  $\text{CoCrAlY}+\text{CeO}_2$  coating.

$\text{CoCrAlY}+\text{CeO}_2$  coating showed a weight gain 49% and 40% lesser than MDN 321 and Superni 76 substrates respectively. The  $\text{CoCrAlY}+\text{CeO}_2$  coating shows the least hot corrosion resistance among the other coatings due to the delaminated oxide scale. In addition superficial cracks on the coating surface were also observed. The reaction between the coating elements and molten salts due to the fluxing action will results in the formation of corrosion products. During the coating process, due their surface active nature,  $\text{CeO}_2$  particles get distributed along the splat boundaries and under hot corrosion conditions the molten salt makes an attempt to enter into the coating through splat boundaries. This results in significant reaction between molten  $\text{NaVO}_3$  and  $\text{CeO}_2$  leading to the formation of corrosion product  $\text{CeVO}_4$ . The corrosion product  $\text{CeVO}_4$  is

accompanied by a destructive volume expansion resulting in outward growth in the form of irregular crystals and leads to the stresses on surrounding splats/oxide scale. The stresses produced from the irregular crystals resulted in the development of superficial cracks on the coating surface. Later, the molten salt infiltrates into the coating through the cracks and enhances the corrosion rate. This further leads to delamination of outer oxide layer and degradation of coating material by progressive corrosion.

**THIS PAGE IS LEFT BLANK.**

## 7 OXIDATION STUDIES

This chapter describes the oxidation behaviour of Plasma sprayed CoCrAlY+Al<sub>2</sub>O<sub>3</sub>+YSZ, CoCrAlY+CeO<sub>2</sub>, CoCrAlY+WC-Co and CoCrAlY+Cr<sub>3</sub>C<sub>2</sub>-NiCr and uncoated alloys. The cyclic oxidation is conducted in air for 50 cycles at an elevated temperature of 700°C. The specimens were visually examined at the end of each cycle during the course of the study. Thermogravimetry technique is used to study the reaction rate and kinetics of the oxidation process. The identification and structural investigation of reaction products of the oxidized specimens were made by means of the XRD and SEM/EDAX techniques. The results have been compiled in different sections of the chapter to assess the performance of each coating.

### 7.1 CoCrAlY+Al<sub>2</sub>O<sub>3</sub>+YSZ coating

#### 7.1.1 Thermogravimetric studies

The cumulative weight gain (mg/cm<sup>2</sup>) plots of CoCrAlY+Al<sub>2</sub>O<sub>3</sub>+YSZ coatings as a function of time expressed in number of cycles are shown in Figure 7.1. The overall weight gain after 50 cycles of oxidation of the CoCrAlY+Al<sub>2</sub>O<sub>3</sub>+YSZ coated MDN 321 and Superni 76 alloys are 1.68 and 1.46 mg/cm<sup>2</sup>, respectively. Both the coated alloys showed minimal difference in weight gain. During initial oxidation cycles, rate of weight gain of the coated alloys was observed higher and it may be attributed to the rapid formation of oxides of active elements and oxidation at the coating splat boundaries as well as due to the penetration of the oxidizing species along the splat boundaries/open pores. However, the oxide scale on the coating subsequently becomes dense and diffusion of oxidizing species into the inner portion of the coating gets slowed down once the oxides are formed at pores and splat boundaries. This would relatively minimize the weight gain in progressive cycles which revealed that both coated alloys shows parabolic nature. The weight gain square (mg<sup>2</sup>/cm<sup>4</sup>) data plotted as a function of time to determine the oxidation kinetics is shown in Figure 7.2. The parabolic rate constant (K<sub>p</sub> in 10<sup>-10</sup> g<sup>2</sup>cm<sup>-4</sup>s<sup>-1</sup>) value of coated MDN 321 and Superni 76 alloys is 0.16 and 0.12 respectively.

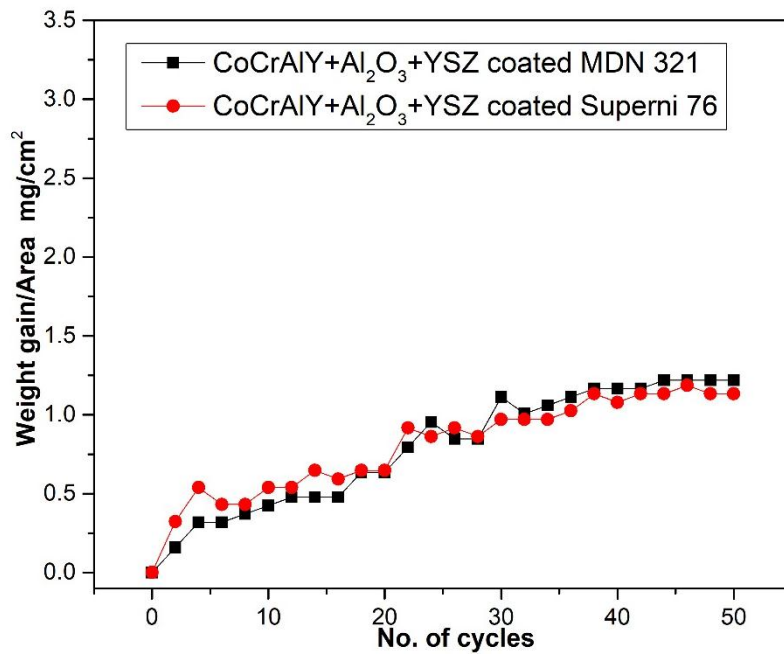


Figure 7.1 Weight gain vs. number of cycles plot of CoCrAlY+Al<sub>2</sub>O<sub>3</sub>+YSZ coated alloys subjected to oxidation.

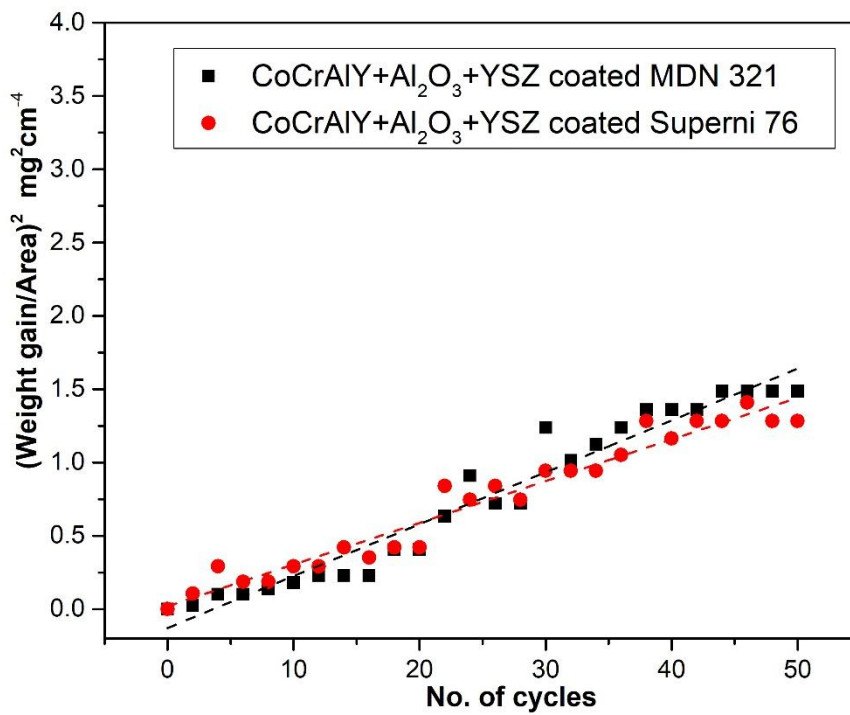


Figure 7.2 (Weight gain/area)<sup>2</sup> vs. number of cycles plot of CoCrAlY+Al<sub>2</sub>O<sub>3</sub>+YSZ coated alloys subjected to oxidation.

### 7.1.2 X-ray Diffraction Analysis

XRD patterns of oxidised CoCrAlY+Al<sub>2</sub>O<sub>3</sub>+YSZ coated alloys at 700 °C are shown in Figure 7.3. The major peaks of the oxidised coated alloys correspond to Cr<sub>2</sub>O<sub>3</sub>, CoO, CoCr<sub>2</sub>O<sub>4</sub> and CoAl<sub>2</sub>O<sub>4</sub>. The minor peaks indexed to  $\alpha$ -Al<sub>2</sub>O<sub>3</sub> and AlCo. The major phases observed in both the coated alloys are similar and no peaks of the elements of substrate alloys were found in the XRD indicating that no diffusion has occurred from the substrate.

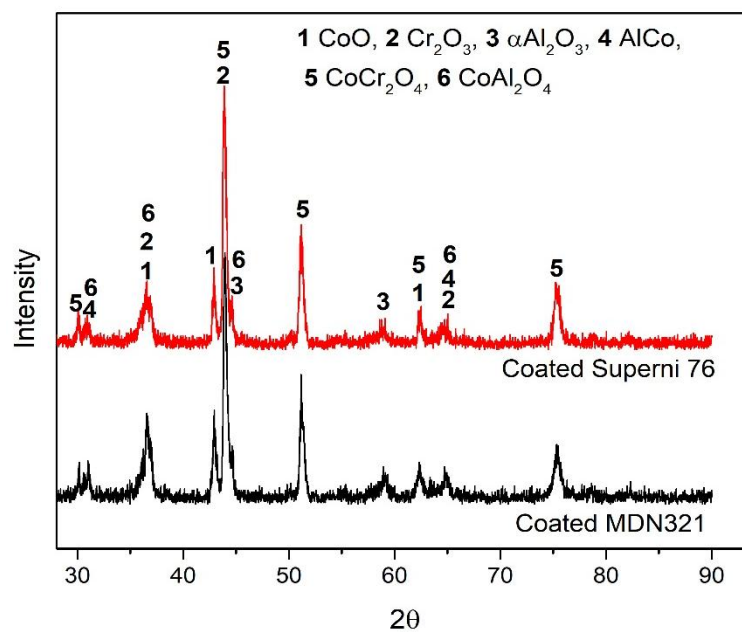


Figure 7.3 XRD patterns for CoCrAlY+Al<sub>2</sub>O<sub>3</sub>+YSZ coated alloys subjected to oxidation.

### 7.1.3 Surface SEM and EDS analysis

The surface morphology of corroded CoCrAlY+Al<sub>2</sub>O<sub>3</sub>+YSZ coatings is shown in Figure 7.4. The dark and light grey larger patches and globular structures have appeared on the oxidised surface. EDS analysis of dark grey patch marked as region 'A' in Figure 7.4a showed the dominant presence of Co with nominal O and Cr and traces of Al. The light grey layer marked as region 'B' indicates the dominant presence of O, Cr and Co with traces Al. In Figure 7.4b the region 'A' shows the presence of continuous globules which are rich in O, Cr and Co with traces of Al and Y. From the EDS results at different region it is observed that, the upper surface of the oxidized coating is the major

constituents of rich oxygen, Cr and Co elements. The presence of  $\text{Cr}_2\text{O}_3$ ,  $\text{CoO}$ ,  $\text{CoCr}_2\text{O}_4$  and  $\text{CoAl}_2\text{O}_4$  as a major phase is observed from the XRD analysis of oxidised coatings.

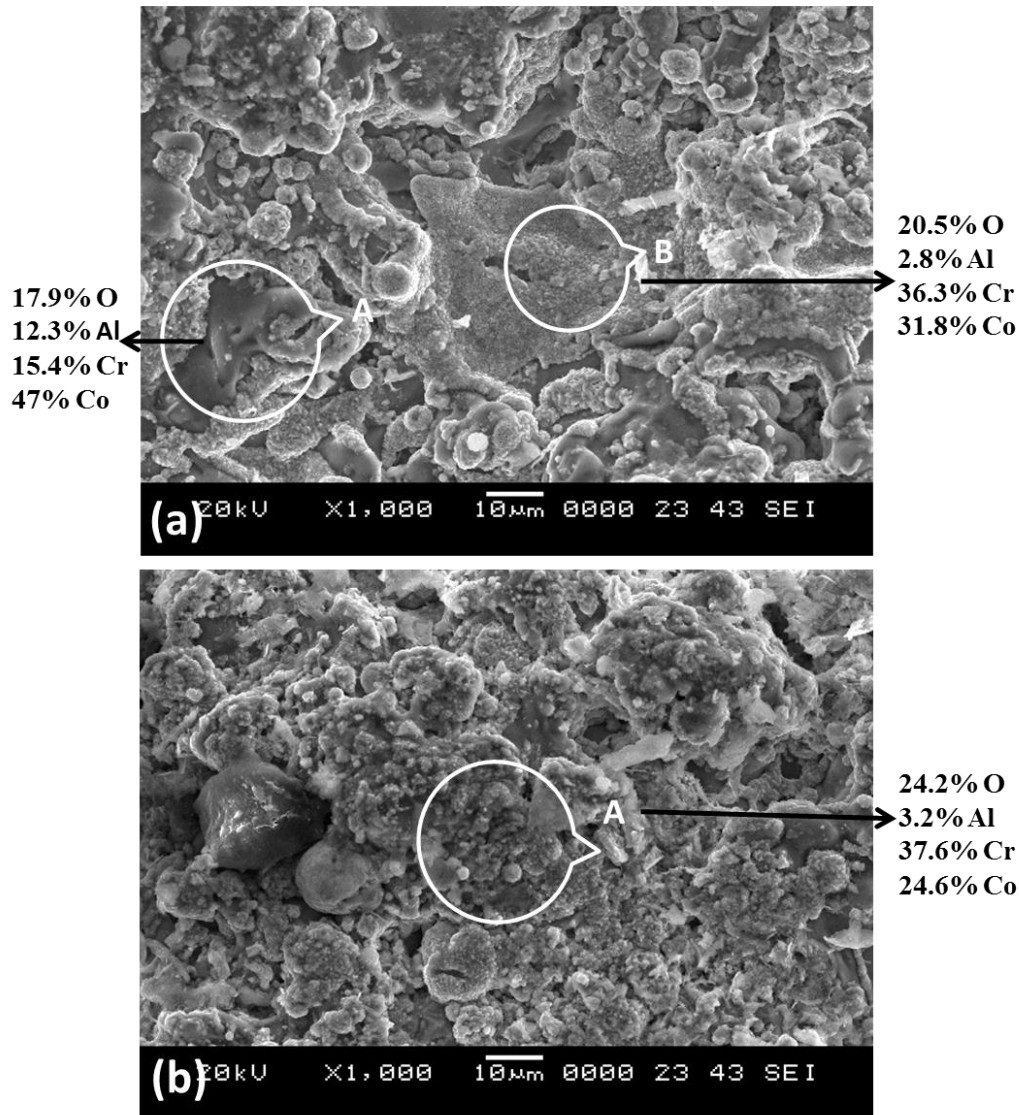


Figure 7.4 Surface morphology of oxidised  $\text{CoCrAlY}+\text{Al}_2\text{O}_3+\text{YSZ}$  coatings on (a) MDN 321 and (b) Superni76.

#### 7.1.4 Cross sectional and elemental mapping

The BSE image of coating cross section subjected to 50 cycles of oxidation is shown in Figure 7.5. The micrographs (Figure 7.5a) show that the coatings have retained their lamellar structure, with no obvious internal oxidation found on coating. Compared with the as-sprayed coating, thin and discontinuous oxide scale is observed on the coating

surface. The elemental composition at various locations of the cross section is analysed by EDS analysis (Figure 7.5b) and reported in Table 7.1.

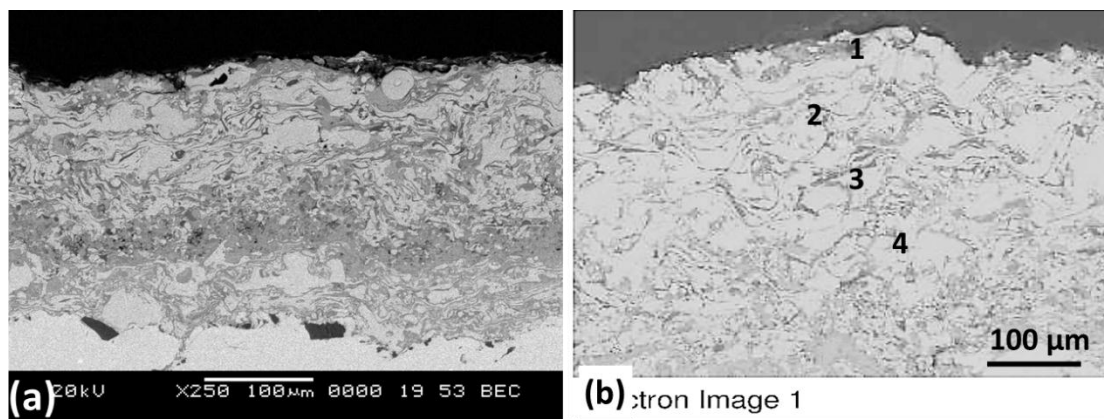


Figure 7.5 Oxidised coating cross section and EDS point analysis (wt. %) of the CoCrAlY+Al<sub>2</sub>O<sub>3</sub>+YSZ coating.

Table 7.1 Point EDS of CoCrAlY+ Al<sub>2</sub>O<sub>3</sub>+YSZ coating along the cross section in wt. %.

Elements (wt. %)	Region 1	Region 2	Region 3	Region 4
O	18.5	8.6	10	5
Al	10.8	9.7	8.1	6
Cr	47.2	18.4	17.8	14.5
Co	23.3	62.7	59.2	72.1

The cross section of oxidised coating is mainly composed of two regions, one region with light grey patches is composed of Co and Cr rich splats, while the dark grey/black region is composed of Al rich splats. The cross section EDS analysis at point 1 shows that oxide scale formed on the surface is mainly composed of O, Cr and Co along with traces of Al. Point 2 represent the Co and Cr rich splat with reduced O content. At point 3 and 4 the percentage of O shows a gradual reduction and more of Co rich splats are seen. The reduction in O percentage inside the coating indicates that oxidation has been restricted to the uppermost layer of the coating surface by the protective surface oxides of Cr and Co.

X-ray mapping of coating cross section (Figure 7.6) shows the distribution of O elements at the coating surface, but the oxide layer is not continuous throughout the

coating cross section. Consequently O is observed below the coating surface. The upper scale predominant in Cr, Co and O indicates the presence oxides of Co and Cr. The distribution of Al and Zr is also observed in coating cross section.

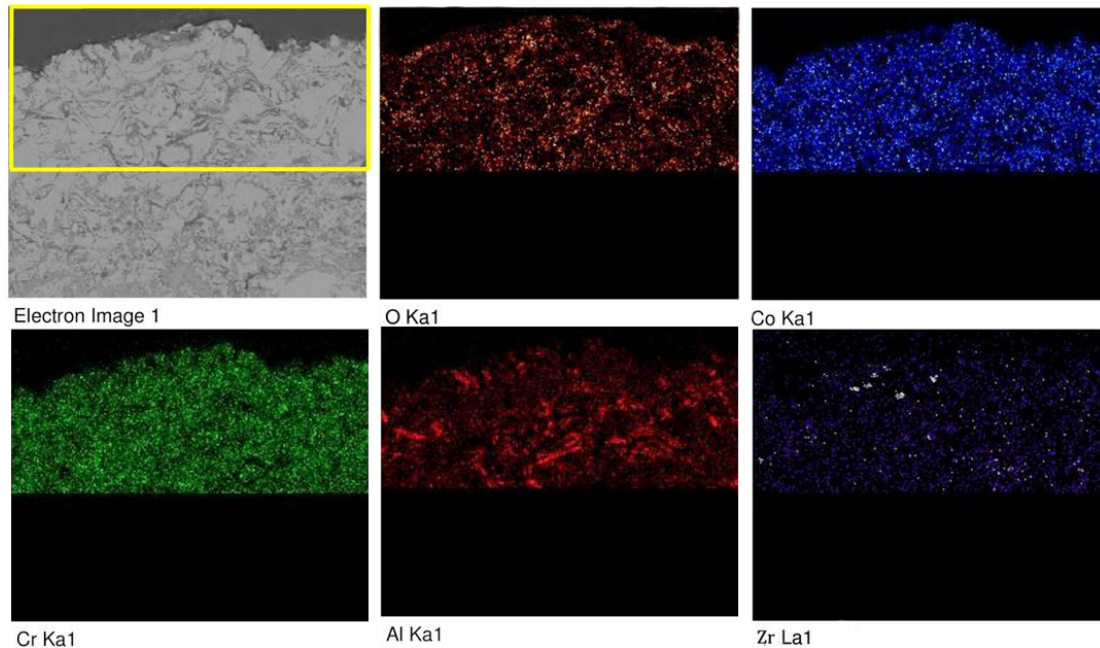


Figure 7.6 BSEI and elemental X-ray mapping along the cross-section of the CoCrAlY+Al<sub>2</sub>O<sub>3</sub>+YSZ coating subjected to oxidation.

### 7.1.5 Discussion

It is observed from the Figure 7.4 that the surface morphology of oxidised CoCrAlY+Al<sub>2</sub>O<sub>3</sub>+YSZ coating comprises of closely packed continuous globular structure. The Cross section of oxidised coating in Figure 7.5 shows the thin, dense, non-porous and well adhered oxide scale on the coating surface. These are the characteristic features of protective oxides on the coating surface.

During the initial stages of oxidation, the oxygen penetrates into the coatings through the open porosities located along the splat boundaries until all the accessible internal surfaces have been oxidized. Further Al and Cr are partially oxidized reduced the additional oxygen ingress into the coating. The distribution of thermodynamically stable  $\alpha$ -Al<sub>2</sub>O<sub>3</sub> in the coating is shows slow-scale growth kinetics during the oxidation (Zhu et al. 2013). Also the  $\alpha$ -Al<sub>2</sub>O<sub>3</sub> is a pre-oxidised phase which further will not undergo any oxidation is one of the reason for lower weight gain. Subsequently, the

oxidation phenomenon takes place only on the external surface of the coating. Cr gets oxidized to  $\text{Cr}_2\text{O}_3$  with  $\text{CoAl}_2\text{O}_4$  and  $\text{CoCr}_2\text{O}_4$  spinels which further retards the oxide growth and results in a lower oxide scale thickness as observed in the present study. (Sidhu and Prakash 2006A), (Singh et al. 2005), Niranatlumpon et al. (2000), also reported the internal oxidation via open pores during the early stages of oxidation for thermal-sprayed MCrAlY coating substantiating the observations in the present work.

The XRD analysis of oxidized surface reveals presence of  $\text{Cr}_2\text{O}_3$ ,  $\text{CoCr}_2\text{O}_4$  and  $\text{CoAl}_2\text{O}_4$  as the major phases which are thermodynamically stable, having close-packed globular structure. Particularly  $\text{Cr}_2\text{O}_3$  is one of the most protective oxide below  $850^\circ\text{C}$  (D. Seo et al. 2008). Further EDS analysis and X-ray mapping confirmed the presence of thin oxide rich layer on the coating surface with the oxides of Cr, Co and Al. The solid state reaction or nucleation between initially grown  $\text{CoO}$  and  $\text{Cr}_2\text{O}_3$  might have resulted in  $\text{CoCr}_2\text{O}_4$ . Temperatures below  $900^\circ\text{C}$  are favourable for the formation of Cr dominant  $\text{CoCr}_2\text{O}_4$  spinel (Yuan et al. 2015). However, some Co may easily get oxidized and form  $\text{CoO}$ , which is may not be a favourable oxide. During the early stages of oxidation, the  $\text{CoO}$  and the reinforced  $\alpha\text{-Al}_2\text{O}_3$  might have undergone the nucleation to form  $\text{CoAl}_2\text{O}_4$ . However, with the subsequent oxidation cycles the readily oxidised  $\text{Cr}_2\text{O}_3$  and transformation to parent oxides to its spinel oxide  $\text{CoAl}_2\text{O}_4$  by nucleation could suppress the formation further possible oxide ( $\text{CoO}$ ).

The free energy of formation of oxide, affinity to oxygen and flattened structure of the plasma coatings are the governing factors in selective oxidation. The Aluminum ( $\Delta G^\circ = -925 \text{ kJ mol}^{-1}$  at  $700^\circ\text{C}$ ) in the coating oxidizes before Cr ( $\Delta G^\circ = -580 \text{ kJ mol}^{-1}$ ) and Co ( $\Delta G^\circ = -325 \text{ kJ mol}^{-1}$ ) due to relatively high negative free energy of formation of oxide as referred by Ellingham diagram. During the early stages of oxidation, Al as most active element is oxidised to  $\text{Al}_2\text{O}_3$  and Cr being one of the major element in the coating undergoes rapid oxidation to form  $\text{Cr}_2\text{O}_3$ . The highly oxidised  $\text{Cr}_2\text{O}_3$  and the spinel oxides formed by solid state reaction would overlap the early oxidised  $\text{Al}_2\text{O}_3$  and as a result the XRD analysis shows  $\text{Al}_2\text{O}_3$  in the minor peaks. Hence the protected against oxidation for coating could be provided by uppermost  $\text{Cr}_2\text{O}_3$ ,  $\text{CoAl}_2\text{O}_4$ ,  $\text{CoCr}_2\text{O}_4$  and underneath  $\text{Al}_2\text{O}_3$ .

## 7.2 CoCrAlY+CeO<sub>2</sub> coating

### 7.2.1 Thermogravimetric studies

The cumulative weight gain ( $\text{mg}/\text{cm}^2$ ) plots of CoCrAlY+CeO<sub>2</sub> coatings as a function of number of cycles are shown in Figure 7.7. The overall weight gain of 2.35 and 2.60  $\text{mg}/\text{cm}^2$  is observed for coated MDN 321 and Superni 76 alloys respectively after 50 cycles of oxidation. The parabolic weight gain nature of the coated alloys indicates the growth of protective oxide scale. The weight loss observed in some cycles is attributed to the sputtering of oxides due to thermal stress produced during cyclic conditions. The weight gain square ( $\text{mg}^2/\text{cm}^4$ ) data plotted as a function of time to determine the oxidation kinetics is shown in Figure 7.8. The parabolic rate constant ( $K_p$  in  $10^{-10} \text{ g}^2\text{cm}^{-4}\text{s}^{-1}$ ) value of coated MDN 321 and Superni 76 alloys is 0.31 and 0.35 respectively.

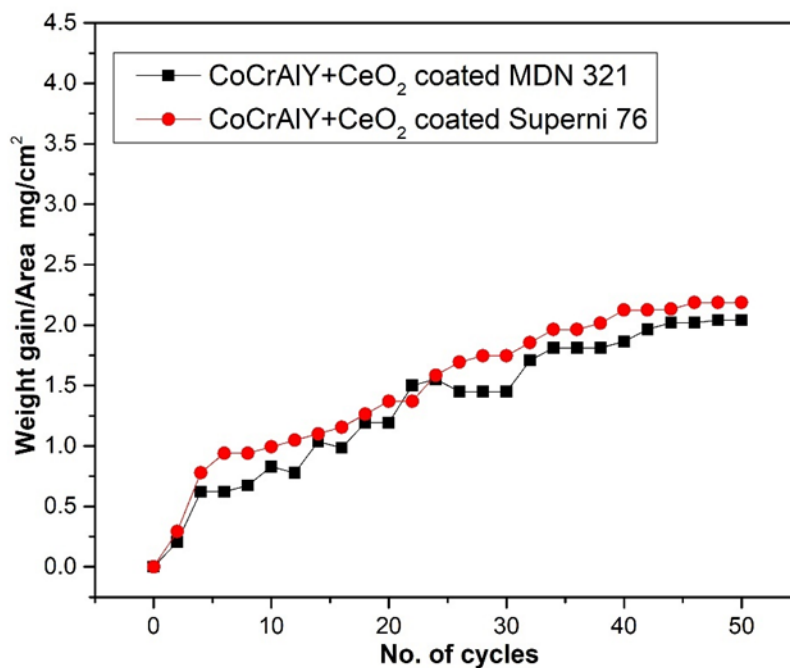


Figure 7.7 Weight gain vs. number of cycles plot of CoCrAlY+CeO<sub>2</sub> coated alloys subjected to oxidation.

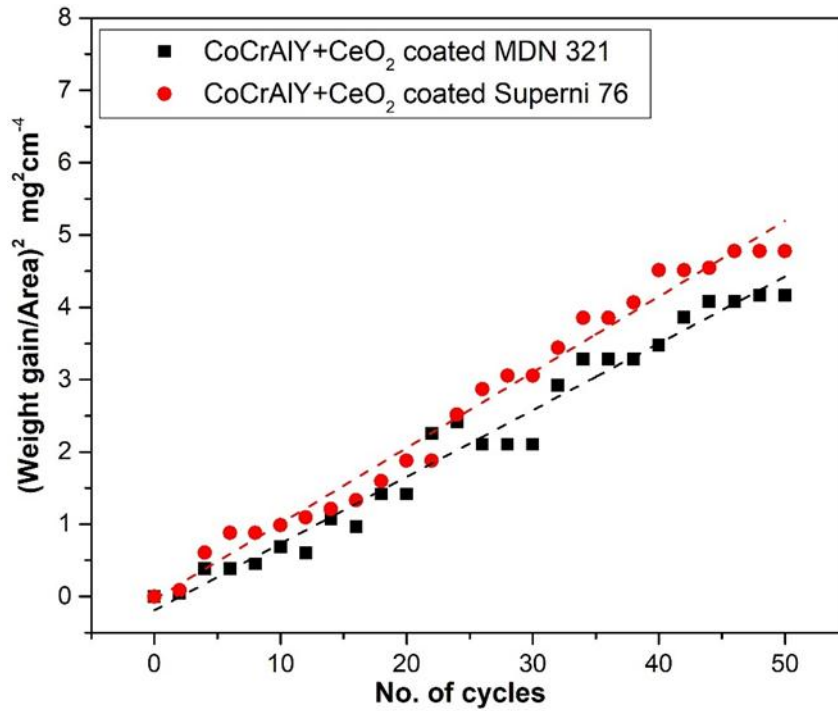


Figure 7.8 (Weight gain/area)<sup>2</sup> vs. number of cycles plot of CoCrAlY+CeO<sub>2</sub> coated alloys subjected to oxidation.

### 7.2.2 X-ray diffraction analysis

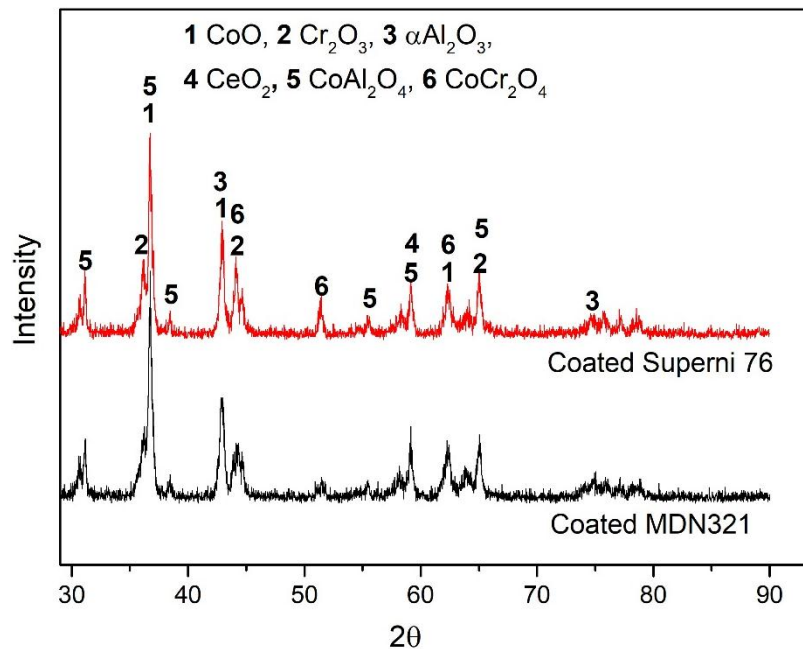


Figure 7.9 XRD patterns for CoCrAlY+CeO<sub>2</sub> coated alloys subjected to oxidation. XRD patterns of oxidised CoCrAlY+CeO<sub>2</sub> coated alloys at 700 °C are shown in Figure 7.9. CoO, Cr<sub>2</sub>O<sub>3</sub>, α-Al<sub>2</sub>O<sub>3</sub> and CoAl<sub>2</sub>O<sub>4</sub> are the major peaks indexed. The minor peaks

are indexed to AlCo, CeO<sub>2</sub> and CoCr<sub>2</sub>O<sub>4</sub>. The major phases observed in both the coated alloys are similar.

### 7.2.3 Surface SEM and EDS analysis

The surface morphology of corroded CoCrAlY+CeO<sub>2</sub> coatings is shown in Figure 7.10. The oxide scale (Figure 7.10a) consists of compact granules like structure with unusual dark gray patches across the oxidized coating surface.

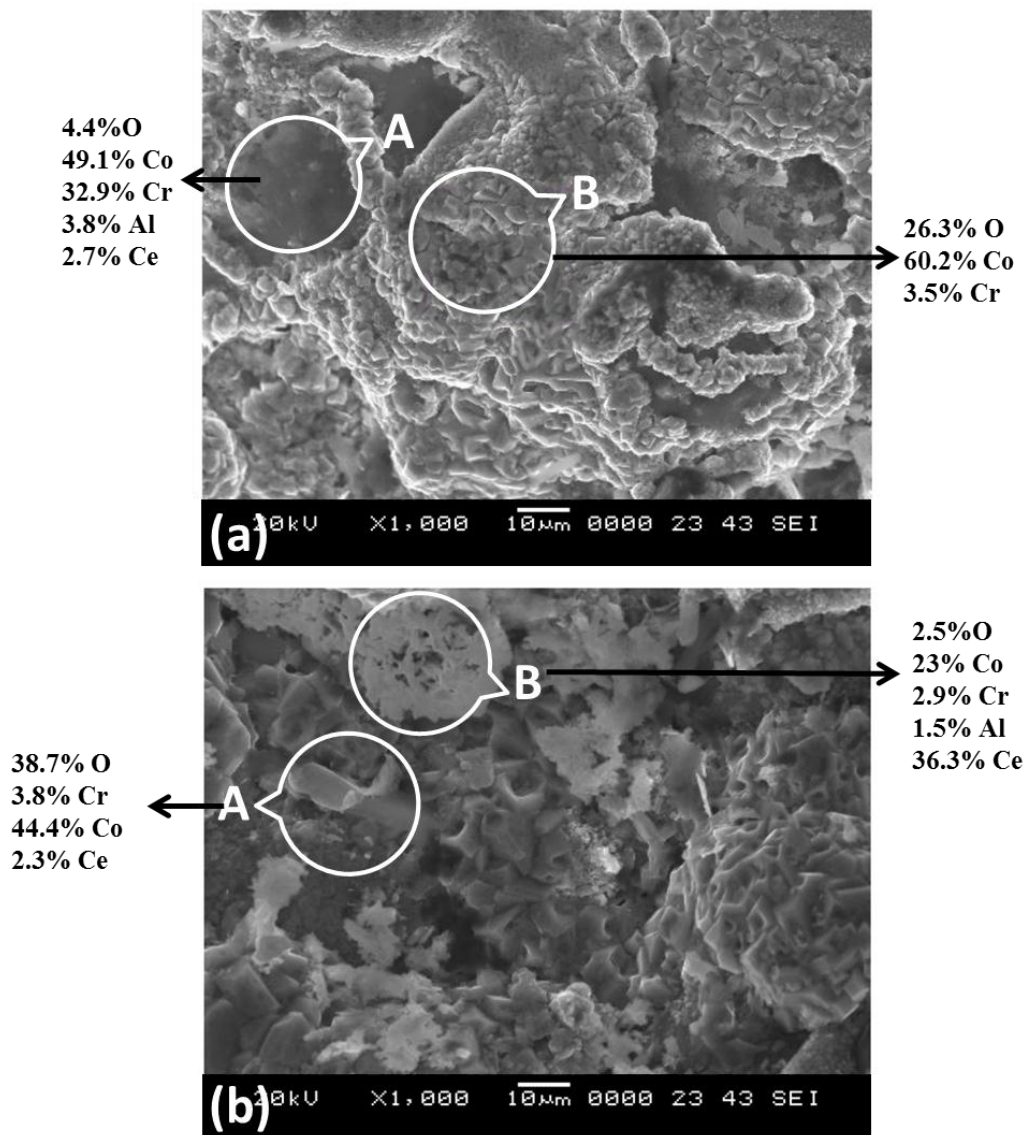


Figure 7.10 Surface morphology of oxidised CoCrAlY+CeO<sub>2</sub> coatings on (a) MDN 321 and (b) Superni76.

The EDS analysis on the dark gray patches marked as region 'A' indicates the presence of dominant Co and Cr elements with minimal amount of Al, Ce and O. The compact granular structure marked as region 'B' revealed the possible presence of O and Co as a major constituent with minor Cr content. In Figure 7.10b granular structure is referred as region 'A' and light grey as region 'B'. EDS of region 'A' consists of complex mixed oxides of Co, Cr and Ce, while region 'B' is rich in Ce and O with small amount of Co, Cr and Al. From the above discussion it can be inferred that, most of the oxidised CoCrAlY+CeO<sub>2</sub> coatings surface covered with compact granular structure with unusual dark gray patches indicating the presence of mixed oxides of Co and Cr.

#### **7.2.4 Cross Section and Elemental mapping**

Figure 7.5 shows the BSE image of coating cross section after 50 cycles of oxidation. The micrographs (Figure 7.5a) shows that the coating has maintained lamellar structure, with no obvious microstructure defects in topcoat-bondcoat interface region. Also thin, uneven oxide scale is observed at the coating surface. EDS analysis at various locations (Figure 7.11b) of the cross section for elemental composition is reported in Table 7.2. The oxidised coating is composed of dark and light grey splats. The light grey patches composed of Co and Cr rich splats, while the dark grey/black region composed of Al rich splats. The EDS analysis at point '1' shows that oxide scale on the coating surface is mainly composed of oxides of Cr and Co with small amount of Al. At point '2' composed Co and O as major constituent with moderate amount of Cr, Al and Ce. The O content reduced gradually in point '3' and '4' as the EDS analysis is done deep inside the coating. The reduction in O percentage inside the coating indicates that oxidation has been restricted to the uppermost layer of the coating surface by the protective surface oxides of Cr, CO and their spinel. Point '4' composed of major Ce and Co elements.

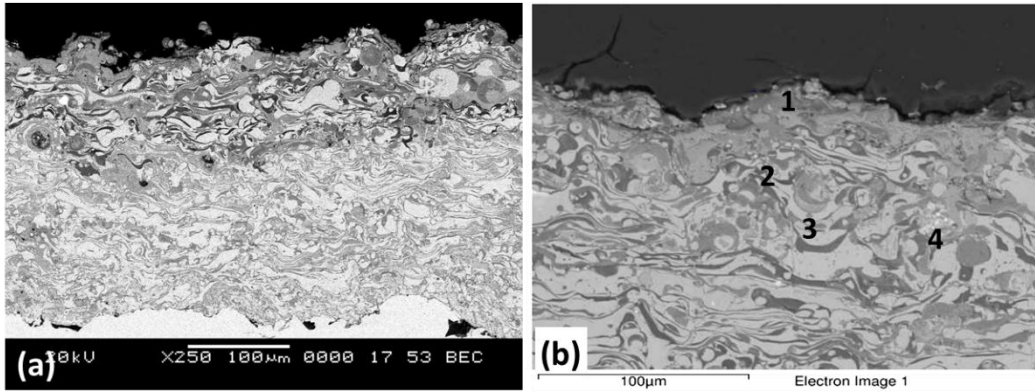


Figure 7.11 Oxidised coating cross section and EDS point analysis (wt. %) of the CoCrAlY+CeO<sub>2</sub> coating.

Table 7.2 Point EDS of CoCrAlY+CeO<sub>2</sub> coating along the cross section in wt. %.

Elements (wt%)	Region 1	Region 2	Region 3	Region 4
O	23.4	20.5	11	11.3
Al	2.5	9.5	7.2	10.9
Cr	14.5	13.5	12.7	17.1
Co	50.2	47.2	61	29.1
Ce	-	7.7	1.7	28.4

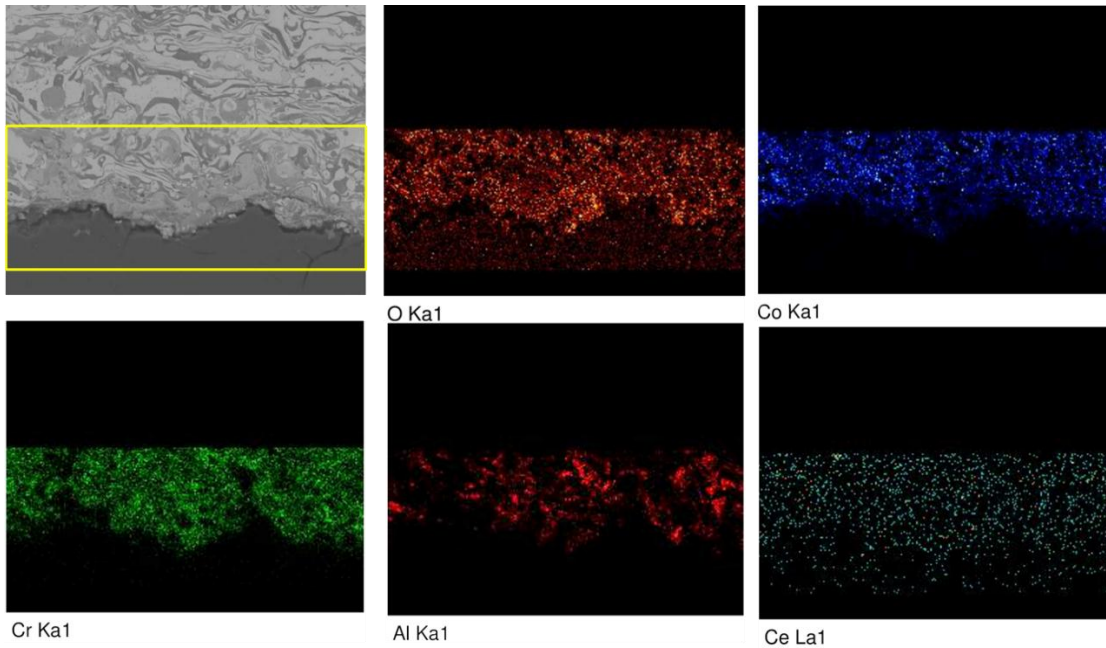


Figure 7.12 BSEI and elemental X-ray mapping along the cross-section of the CoCrAlY+CeO<sub>2</sub> coating subjected to oxidation.

### 7.2.5 Discussion

The observations on the surface morphology of the oxidised coatings in Figure 7.10 shows the dominant granules like structure with smooth grey patches and light grey patches. From EDS analysis the granules like structure are observed to be dominant oxides of Co and the smooth grey patches are identified as least oxidised splats. The light grey patches/layer are identified as Ce rich region. The backscattered image across the coating cross section in Figure 7.11 shows that the thin, nonporous and well adhered oxide scale formed on the surface of the oxidised coating. Earlier research have reported that the addition of low levels of oxygen reactive elements such as rare earths to alloys would reduce oxidation rates under high temperature oxidising atmospheres and can enhance oxide scale adhesion (Ramanathan, 1993). The XRD analysis in Figure 7.9 shows the dominant presence of CoO, Cr<sub>2</sub>O<sub>3</sub>, AlCo, CeO<sub>2</sub> and spinels such as CoCr<sub>2</sub>O<sub>4</sub> and CoAl<sub>2</sub>O<sub>4</sub>.

The CeO<sub>2</sub> as a rare earth oxide having surface active nature segregates along the splat boundaries which results in fine splats and better bonding between splats. Mapping of CoCrAlY+CeO<sub>2</sub> coating cross section (Figure 7.12) shows the distribution of O and Ce throughout the coating thickness. During the early stages of oxidation, Co, Cr and Al get oxidised resulting in the formation of CoO and Cr<sub>2</sub>O<sub>3</sub>, thus forming an oxide scale on the coating surface. With subsequent oxidation cycles CeO<sub>2</sub> first segregate to metal-scale interface by dissolution, later enters the gas/scale interface through the scale-grain boundaries. Based on mapping results, probably the sufficient amount of CeO<sub>2</sub> segregate at the grain boundaries of oxide scale, thus Ce ions blocks the outward diffusion of Co and inward diffusion of oxygen. From the above discussion, it can be inferred that CeO<sub>2</sub> particles in the Co based coating blocks the outward diffusion of Co and changes the oxidation growth mechanism, which causes a reduction of scaling rate. Zhang et al. (2013) have reported that the inward oxygen diffusion is several orders of magnitude lower than the outward Co diffusion at 800°C.

Mahesh et al. (2010) have also observed that the formation of aluminium oxide, chromium oxide, nickel oxide and spinel of nickel and chromium has provided better protection to the substrate superalloys. The addition of Ce oxides improve the oxidation resistance of base alloys under isothermal or cyclic conditions through the following

effects: selective oxidation of Cr and the formation of a continuous, fine-grained  $\text{Cr}_2\text{O}_3$  scale, enhancement of alloy oxide adhesion, and reduction of the growth rate of the oxide scale through a change in transport mechanism. The strengthening mechanism of  $\text{CeO}_2$  reinforcement by Zhou and Ouyang (2017), that the inter-locking interactions towards cracking grain boundaries defects by the precipitated Ce-rich phase resulted in the recombination of cracking oxide boundaries and structural densification during oxidation at  $1000^\circ\text{C}$  in air.

### 7.3 CoCrAlY+WC-Co coating

#### 7.3.1 Thermogravimetric studies

The cumulative weight gain ( $\text{mg}/\text{cm}^2$ ) plots of CoCrAlY+WC-Co coatings are shown in Figure 7.13. The overall weight gain of coated MDN 321 and Superni 76 alloys after 50 cycles of oxidation are 2.97 and  $3.20 \text{ mg}/\text{cm}^2$ , respectively. During the initial oxidation cycles weight gain is relatively higher and as the oxidation proceeds linear weight gain is observed. The weight loss observed in some cycles is attributed to the sputtering of oxides due to thermal stress produced during cyclic condition. The weight gain square ( $\text{mg}^2/\text{cm}^4$ ) data plotted as a function of time to determine the oxidation kinetics is shown in Figure 7.14. The parabolic rate constant ( $K_p$  in  $10^{-10} \text{ g}^2\text{cm}^{-4}\text{s}^{-1}$ ) value of coated MDN 321 and Superni 76 alloys is 0.41 and 0.50 respectively. Both the coated alloys show linear weight gain nature.

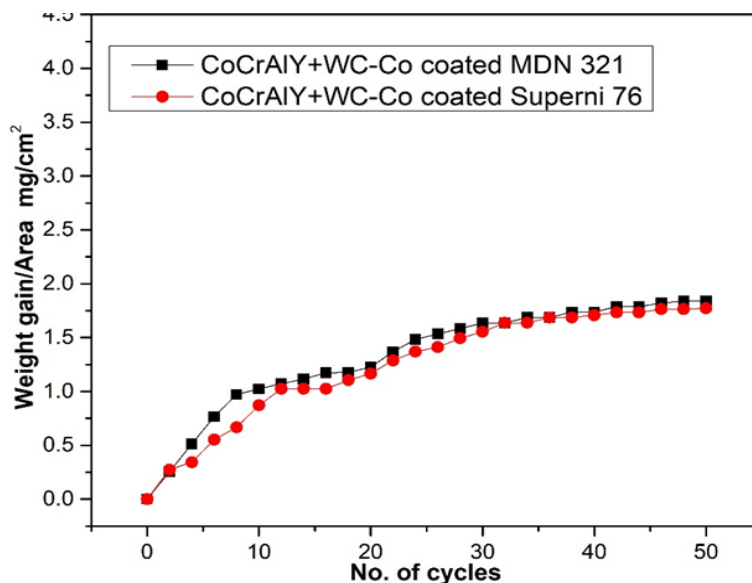


Figure 7.13 Weight gain vs. number of cycles plot of CoCrAlY+WC-Co coated alloys subjected to oxidation.

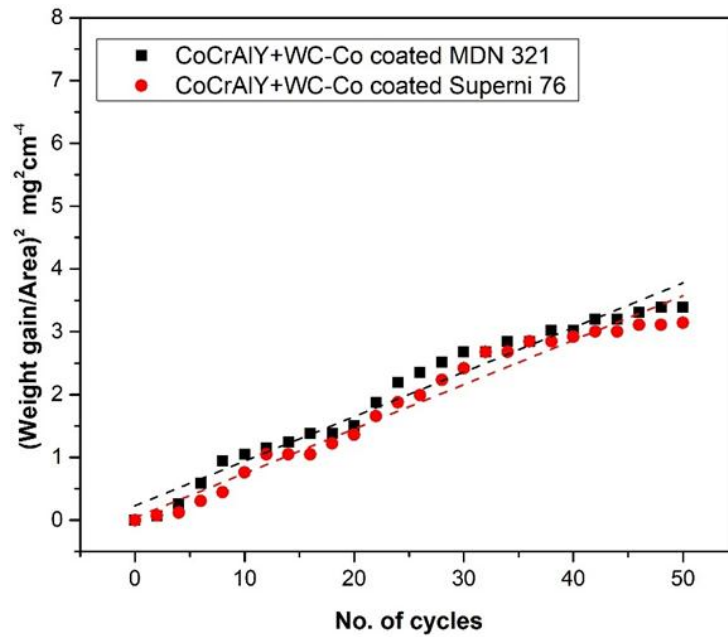


Figure 7.14  $(\text{Weight gain/area})^2$  vs. number of cycles plot of CoCrAlY+WC-Co coated alloys subjected to oxidation.

### 7.3.2 X-ray diffraction analysis

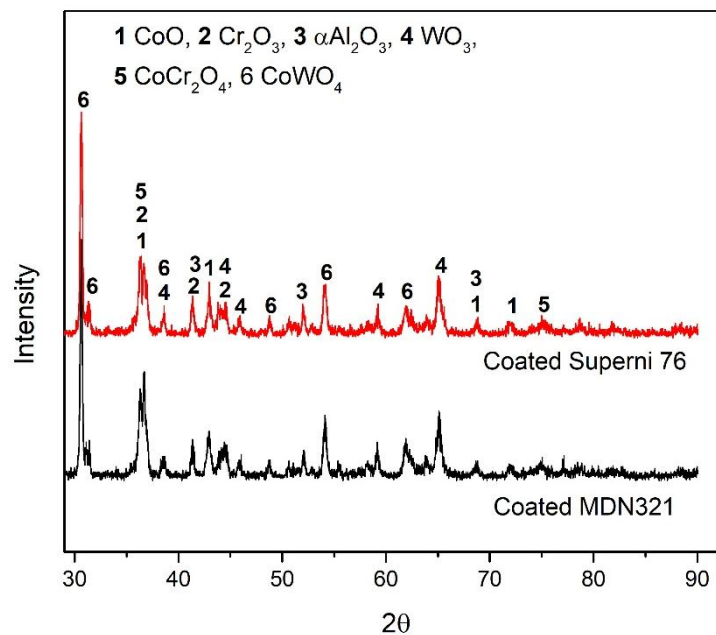


Figure 7.15 XRD patterns for CoCrAlY+WC-Co coated alloys subjected to oxidation.

XRD patterns of oxidised CoCrAlY+WC-Co coated alloys at 700 °C are shown in Figure 7.15. The major peaks correspond to  $\text{CoWO}_4$  while the intermediate peaks are indexed to  $\text{CoO}$ ,  $\text{Cr}_2\text{O}_3$  and  $\text{CoCr}_2\text{O}_4$ . However many number of minor peaks are indexed to  $\text{WO}_3$ .

### 7.3.3 Surface SEM and EDS analysis

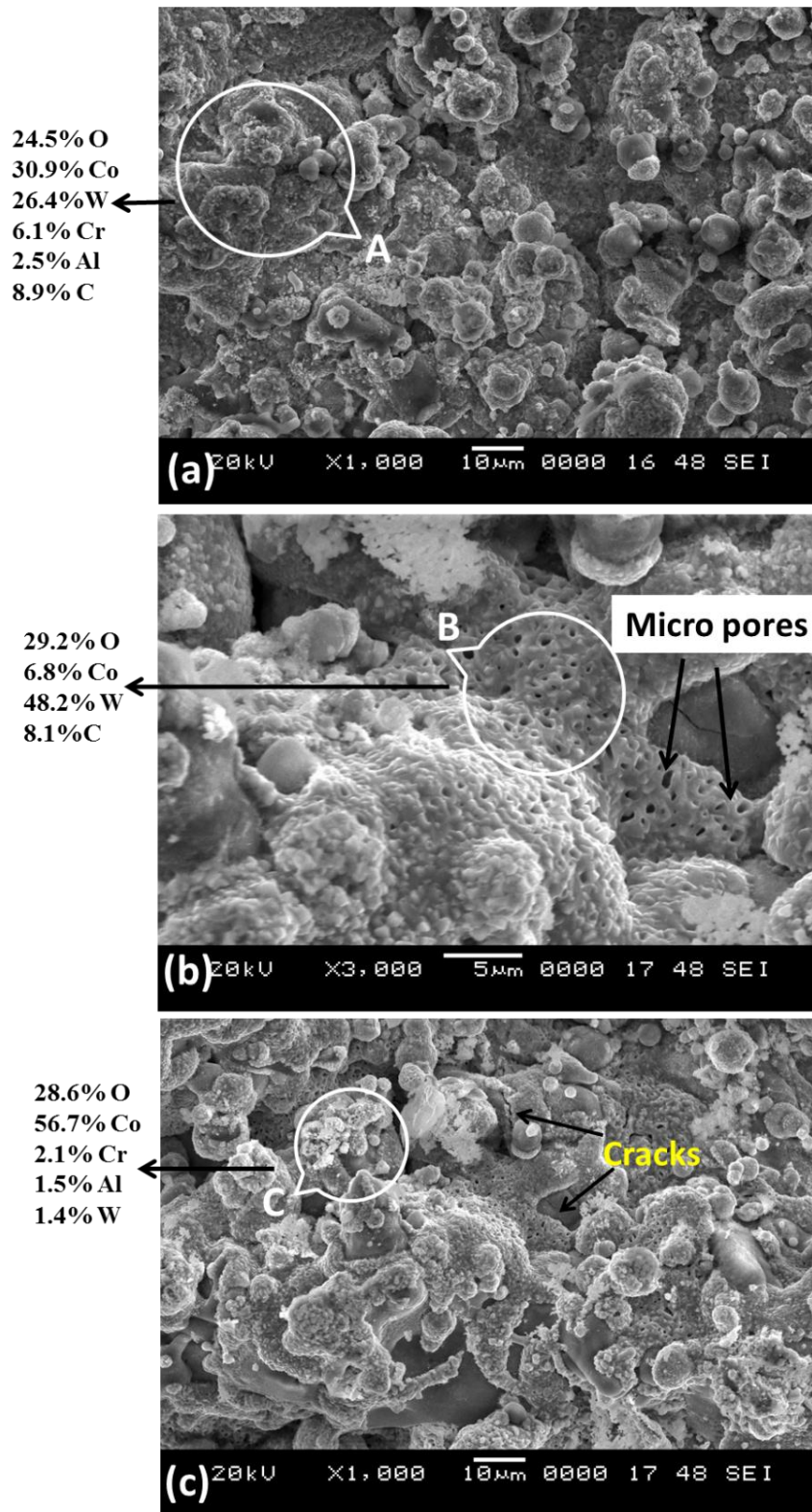


Figure 7.16 Surface morphology of oxidised CoCrAlY+WC-Co coatings on (a) MDN 321 and (b) Superni76.

The surface morphology of corroded CoCrAlY+WC-Co coatings is shown in Figure 7.16. The oxide scale shows the existence of combination of globular and micro-porous (sponge) structure with superficial cracks. The EDS analysis revealed the presence Co, Cr and W rich oxides in globular structure, while the sponge like structure (Figure 7.16b) indexed the presence of W rich oxides which may be tungsten-trioxide ( $WO_3$ ). Also referring to Figure 7.16c the superficial cracks appeared on the micro-pores defective oxide scale. From the above discussion it can be inferred that, the oxidised CoCrAlY+WC-Co coatings surface covered with continuous globular structure with defective oxide scale having micro porous and crack at some regions.

#### **7.3.4 Cross Section and Elemental mapping**

The BSE image of coating cross section after 50 cycles of oxidation is shown in Figure 7.17. The micrographs (Figure 7.17a) show that the coating maintained lamellar structure, with few dispersed pores. The elemental composition at various locations of the cross section is analysed by EDS analysis (Figure 7.17b) and reported in **Error! Reference source not found.** The oxidised coating cross section is composed of 4 different phases, i.e. white, light grey, dark grey and black splats. The white region is W rich splat, Co and Cr rich splats are observed in grey region, while the dark grey region is composed of Al rich splats the black region is composed of C. The EDS analysis at point 1 shows that oxide scale on the coating surface is mainly composed of oxides of Cr and Co with moderate amount of WC and Al. The point 2 composed of WC as major constituent with moderate amount Co and very less O content. The O content reduced gradually from point 3 to 4 indicating that O has not entered inside the coating. The reduction in O percentage inside the coating indicates that oxidation has been restricted to the uppermost layer of the coating surface by the protective surface oxides of Cr, CO and their spinels. Point 4 composed of moderate amount of Al and Co.

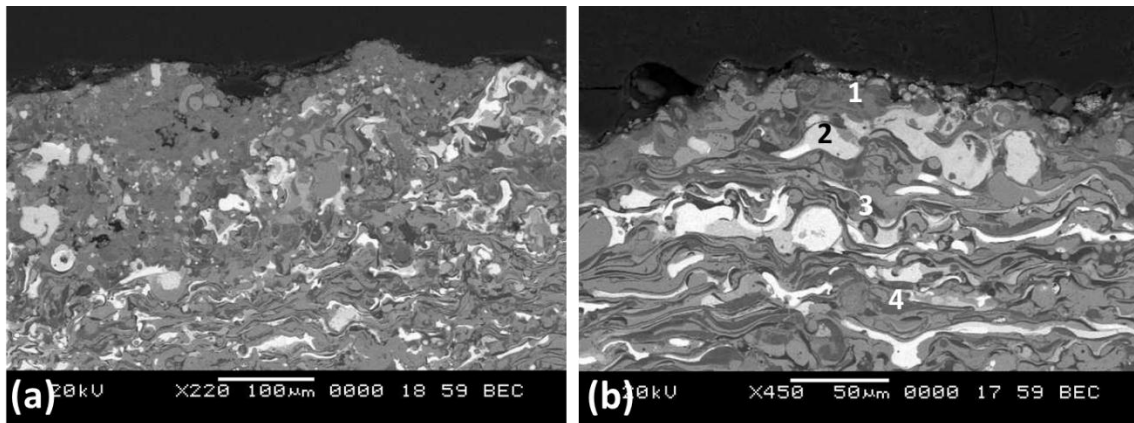


Figure 7.17 Oxidised coating cross section and EDS point analysis (wt. %) of the CoCrAlY+WC-Co coating.

Table 7.3 Point EDS of CoCrAlY+WC-Co coating along the cross section in wt. %.

Elements (wt%)	Region 1	Region 2	Region 3	Region 4
O	18.9	3.6	12	6.1
Al	5.3	-	5.9	26.8
Cr	11.1	1.5	10.1	17
Co	36.7	11.6	36.7	24.6
W	7	36.9	0.3	3.6
C	7	34.6	0.7	2.7

X-ray mapping (Figure 7.18) of coating cross section shows that the oxygen is distributed along the coating cross section. The oxide scale consist of dominant O, Co, W and Cr which is in agreement with the phases ( $\text{CoWO}_4$ ,  $\text{CoO}$ ,  $\text{Cr}_2\text{O}_3$  and  $\text{CoCr}_2\text{O}_4$ ) obtained as a major phase in XRD analysis. At some regions the distribution of Al and O is also observed due to which  $\text{Al}_2\text{O}_3$  is identified with minor peaks. From the above discussion it can be inferred that the oxide layer on CoCrAlY+WC-Co coating is the combination individual Co, Cr and W oxide and their spinels with the presence of micro porous and cracks at some points, resulting in higher weight gain during oxidation cycles.

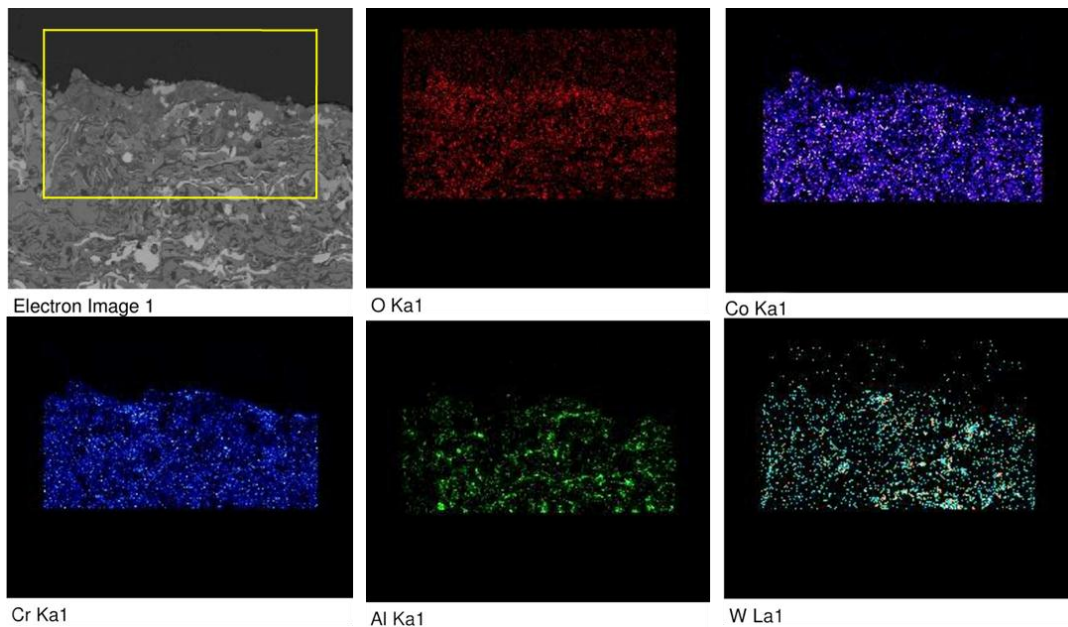


Figure 7.18 BSEI and elemental X-ray mapping along the cross-section of the CoCrAlY+WC-Co coating subjected to oxidation.

### 7.3.5 Discussion

The surface morphology of the oxidised coatings in Figure 7.16 shows the existence of combination of dominant globular and sponge (micro porous like structure) with superficial cracks. The EDS results reveals that globular structure is the constituents of dominant O, Co, W and Cr with traces of, C and Al. The back scattered image at the cross section in Figure 7.11 shows dense, well adhered oxide scale formed on the surface of the oxidised coating with unusual pores underneath the coating surface.

During high temperature exposure, the active elements of the coating such as W, Cr, Al and Co undergo rapid oxidation to form  $WO_3$ ,  $Cr_2O_3$ ,  $CoO$  and  $Al_2O_3$ . Further the nucleation of  $WO_3$  and  $CoO$  resulted in the formation of  $CoWO_4$  spinel oxide and it is observed in XRD analysis as a strong phase. The presence of  $CoWO_4$  spinel oxide as strong phase suppresses inward oxygen diffusion, since it provides less porosity and more passivation effect against the entry of molten salt. Similarly, Jafari et al. (2016) and (Singh et al. 2016) have been reported that the presence  $Cr_2O_3$ ,  $CoWO_4$  and  $CoCr_2O_4$  as a strong phase during oxidation studies of W based coatings. Also in the present study  $Cr_2O_3$  and  $CoCr_2O_4$  are observed as major phase with  $CoWO_4$ . The presence of dense, well adhered oxide scale has been observed in Figure 7.17. However,

WO<sub>3</sub> possess porous structure as observed from the EDS analysis done at region ‘B’ in Figure 7.16b. One of the reason for weight gain during oxidation cycles could be that the oxygen enters into the coating through these pores and the oxidation of underneath coating material occurs. Even though the CoCrAlY+WC-Co coating having protective oxide layer of CoWO<sub>4</sub>, Cr<sub>2</sub>O<sub>3</sub> and CoCr<sub>2</sub>O<sub>4</sub>, the presence of porous WO<sub>3</sub> oxide at some regions may to be detrimental for oxidation resistance.

## 7.4 CoCrAlY+Cr<sub>3</sub>C<sub>2</sub>-NiCr Coating

### 7.4.1 Thermogravimetric studies

Figure 7.19 shows the cumulative weight gain (mg/cm<sup>2</sup>) plots of CoCrAlY+Cr<sub>3</sub>C<sub>2</sub>-NiCr coatings. The overall weight gain for coated MDN 321 and Superni 76 alloys are 1.65 and 1.69 mg/cm<sup>2</sup>, respectively. In some cycles weight loss is observed and this attributed to the sputtering of oxides due to thermal stress produced during cyclic oxidation. The weight gain square (mg<sup>2</sup>/cm<sup>4</sup>) data plotted as a function of time to determine the oxidation kinetics is shown in Figure 7.8. The parabolic rate constant (Kp in 10<sup>-10</sup> g<sup>2</sup>cm<sup>-4</sup>s<sup>-1</sup>) value of coated MDN 321 and Superni 76 alloys is 0.44 and 0.38 respectively.

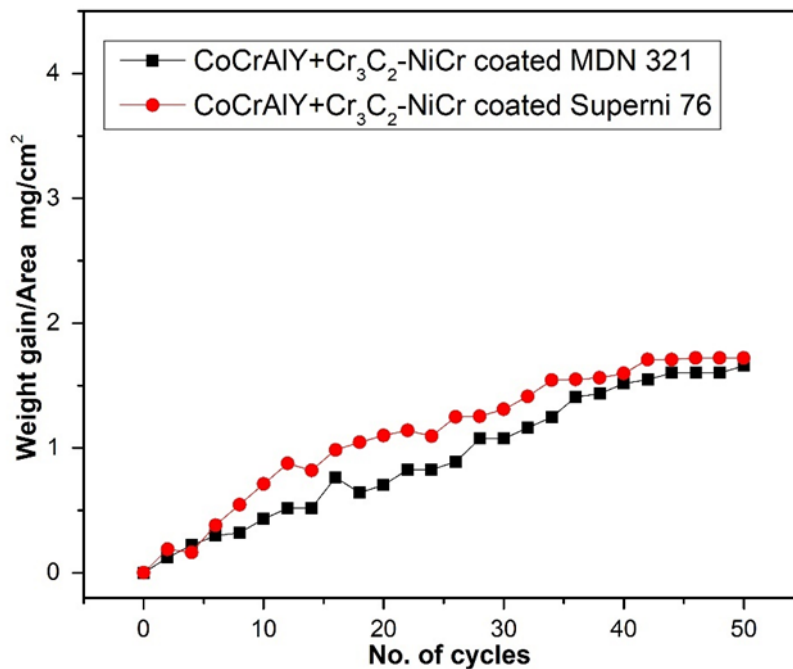


Figure 7.19 Weight gain vs. number of cycles plot of CoCrAlY+Cr<sub>3</sub>C<sub>2</sub>-NiCr coated alloys subjected to oxidation.

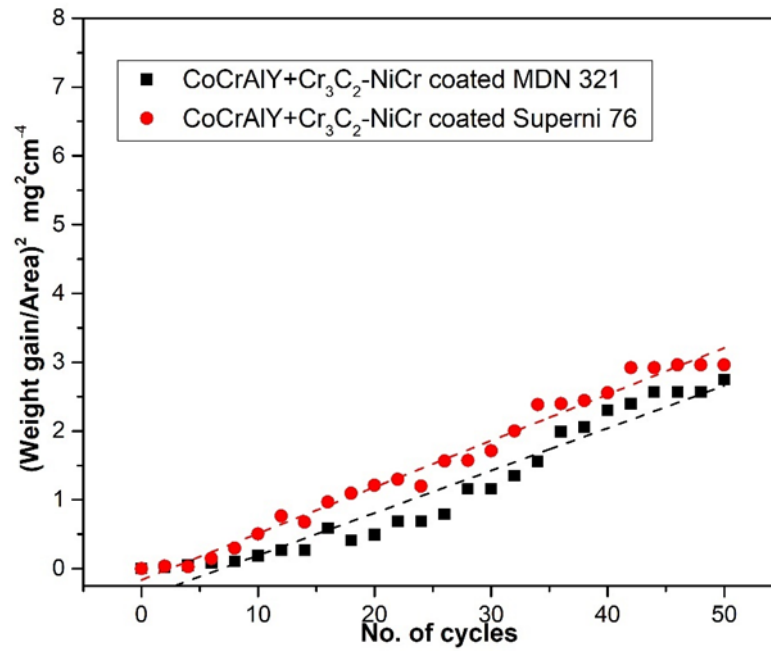


Figure 7.20  $(\text{Weight gain/area})^2$  vs. number of cycles plot of CoCrAlY+Cr<sub>3</sub>C<sub>2</sub>-NiCr coated alloys subjected to oxidation.

#### 7.4.2 X-ray Diffraction Analysis

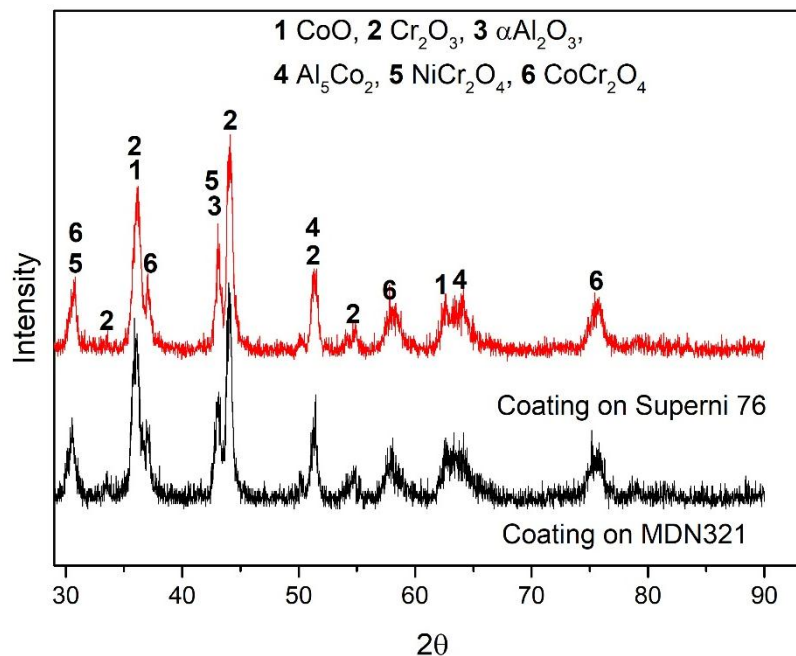


Figure 7.21 XRD patterns for CoCrAlY+Cr<sub>3</sub>C<sub>2</sub>-NiCr coated alloys subjected to oxidation.

In case of CoCrAlY+Cr<sub>3</sub>C<sub>2</sub>-NiCr coated alloys the XRD patterns shown in Figure 7.21, CoO, Cr<sub>2</sub>O<sub>3</sub>, αAl<sub>2</sub>O<sub>3</sub> and NiCr<sub>2</sub>O<sub>4</sub> are the major peaks whereas the intermediate peak are indexed to CoCr<sub>2</sub>O<sub>4</sub> and Al<sub>5</sub>Co<sub>2</sub>.

### 7.4.3 Surface SEM and EDS analysis

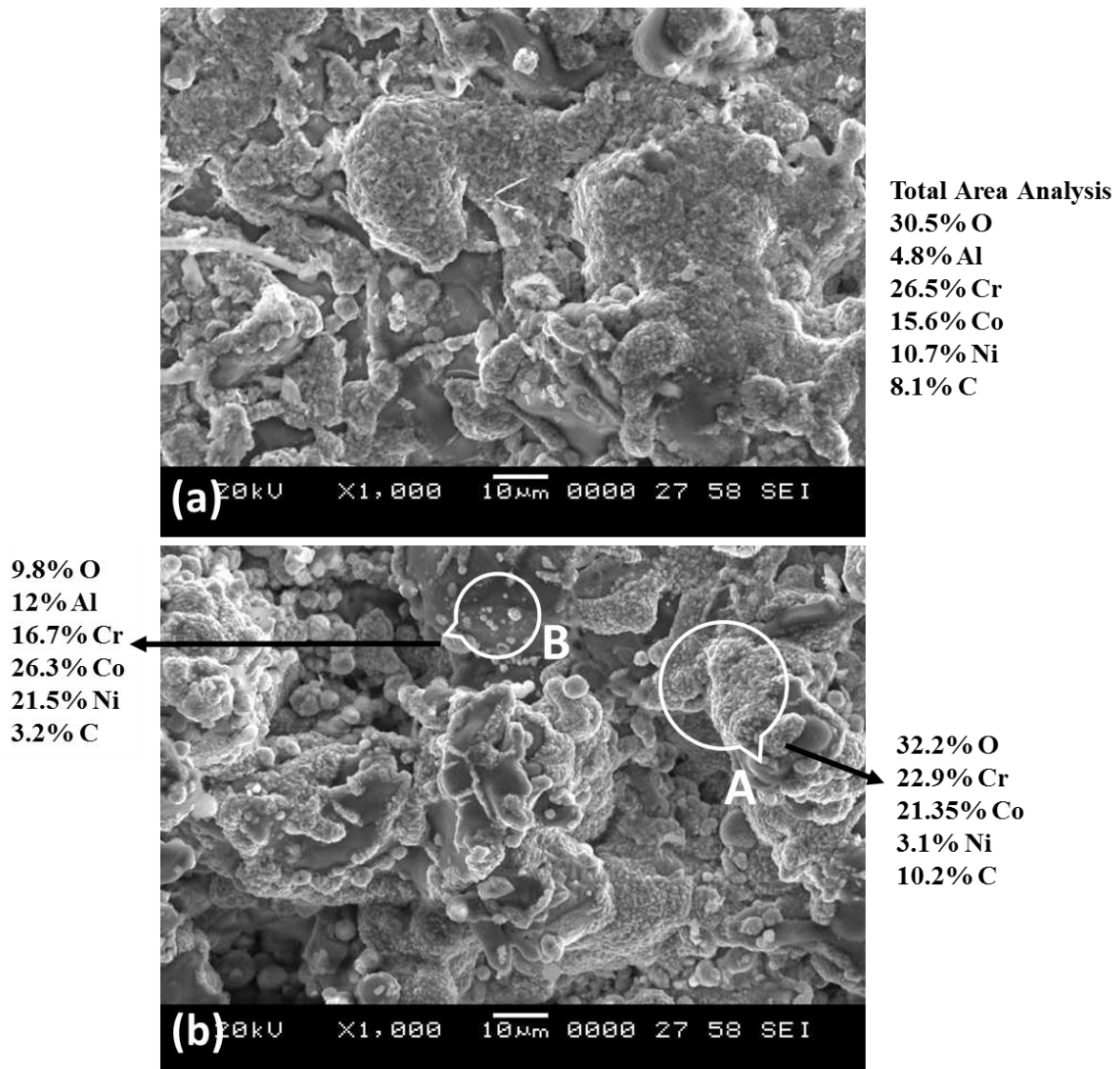


Figure 7.22 Surface morphology of oxidised CoCrAlY+Cr<sub>3</sub>C<sub>2</sub>-NiCr coating on (a) MDN 321 and (b) Superni 76.

The surface morphology of oxidised CoCrAlY+Cr<sub>3</sub>C<sub>2</sub>-NiCr coating is shown in Figure 7.22. The surface oxide scale (Figure 7.22a) consist of globular structure with patches of dispersed unusual dark gray regions across the oxidized coating surface. The EDS analysis of total surface area of Figure 7.22a shows the presence of dominant Cr and O

as major constituents with Co and Ni. Referring to magnified image in Figure 7.22b the globular structure marked as ‘A’ is the major constituent of O, Cr and Co which indicates the presence of oxides of Cr and Co. Grey patches marked as ‘B’ is the major constituents of Co and Ni with Al and O which may indicate the presence of oxides of oxides Co and Ni. The oxide scale developed on the coating surface is the combination of compact globular structure and some grey patches. The presence of oxides of Co, Cr, Al and its spinels is also evident from the XRD analysis of coating surface (Figure 7.21).

#### 7.4.4 Cross Section and Elemental mapping

The BSE image of oxidised coating cross section after 50 cycles is shown in Figure 7.17. The elemental composition at various location of the oxidised coating cross section is analysed by EDS analysis (Figure 7.23b) and reported in Table 7.4. The O percentage at point ‘1’ is higher and O percentage is gradually reduced point ‘1’ to ‘4’ indicating that oxide scale acts as barrier for the oxide species to enter into the coating. Point ‘4’ shows the Cr, C and Ni as major constituent and the presence of small amount of O is due to the presence of oxide stringers at the splat boundaries.

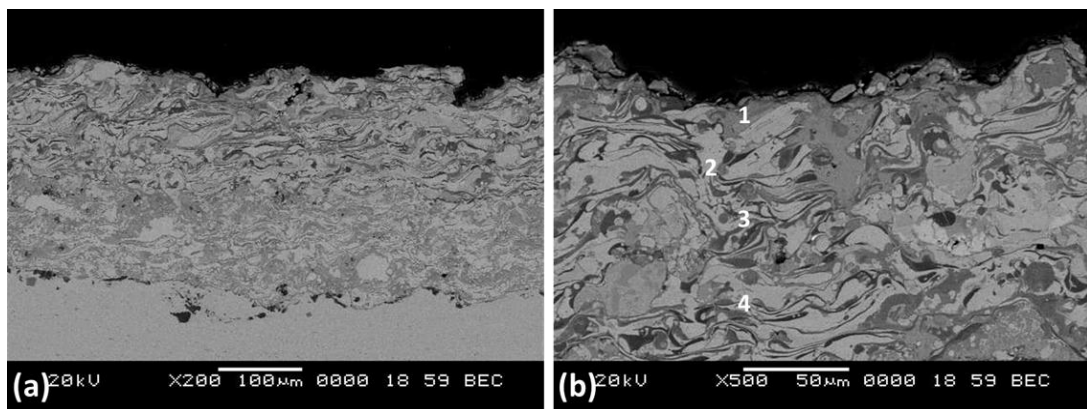


Figure 7.23 Oxidised coating cross section and EDS point analysis (wt. %) of the CoCrAlY+Cr<sub>3</sub>C<sub>2</sub>-NiCr coating.

Table 7.4 Point EDS of CoCrAlY+Cr<sub>3</sub>C<sub>2</sub>-NiCr coating cross section in wt. %.

Elements (wt%)	Region 1	Region 2	Region 3	Region 4
O	25.5	14.1	11.2	5.1
Al	7.5	8	15.2	2.5
Cr	24.6	29.5	19.2	38.2
Co	15.8	19.5	25.6	4.6
Ni	18.3	21.2	-	23.6
C	8	7.7	-	8.5

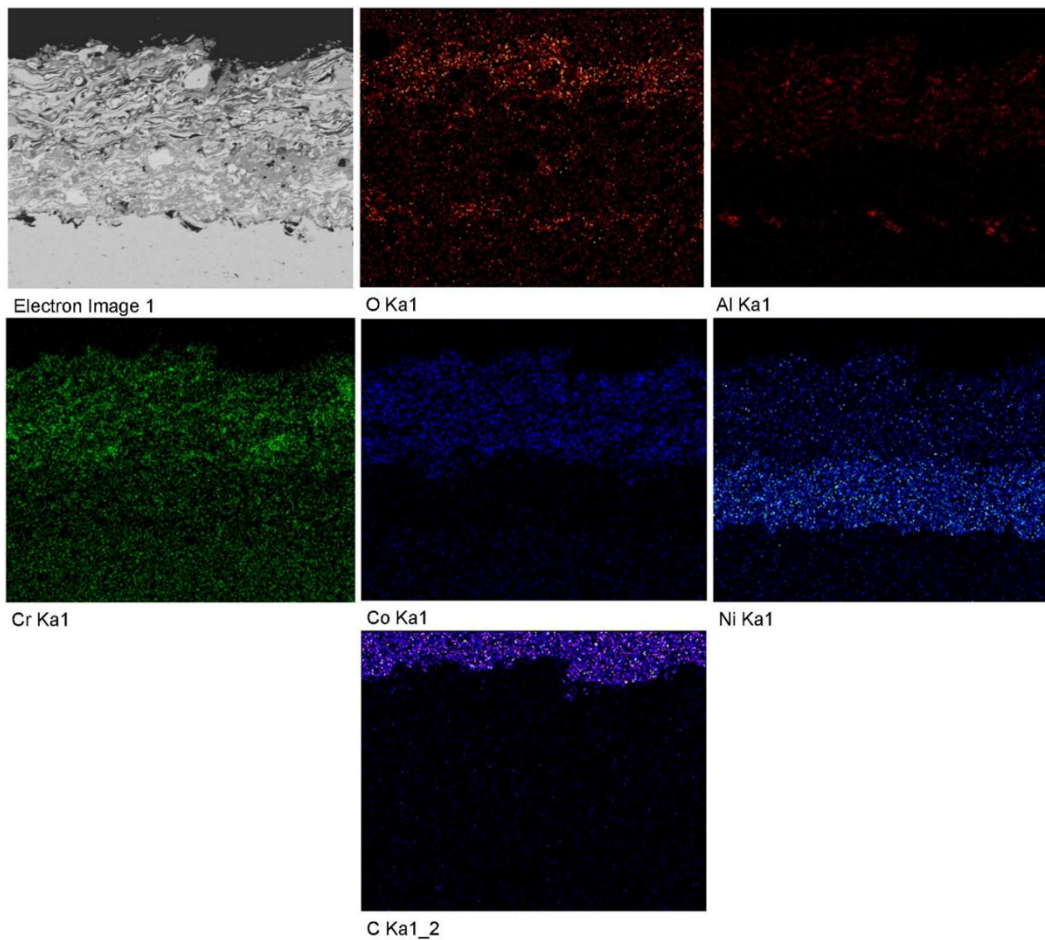


Figure 7.24 BSEI and elemental X-ray mapping along the cross-section of the CoCrAlY+Cr<sub>3</sub>C<sub>2</sub>-NiCr coating subjected to oxidation.

X-ray mapping (Figure 7.24) of coating cross section shows the oxygen rich layer at the coating surface. The distribution of Co, Cr and Ni elements in the oxide rich scale

is observed which indicating the presence of oxides of Co, Cr, Ni and its spinels. The presence of these oxides are supported by surface EDS and strongly in agreement with the XRD analysis of oxidised coating as observed in Figure 7.21. The distribution of Al is observed throughout the coating cross section is observed.

#### 7.4.5 Discussion

From the Figure 7.22 closely packed globular structure with dark grey least oxidised grey patches are observed throughout the oxidised CoCrAlY+Cr<sub>3</sub>C<sub>2</sub>-NiCr coating surface. The coating surface XRD and EDS analysis, reveals that the oxide scale is formed by the combination of CoO, Cr<sub>2</sub>O<sub>3</sub>,  $\alpha$ -Al<sub>2</sub>O<sub>3</sub> and multiple spinel oxides such as CoCr<sub>2</sub>O<sub>4</sub> and NiCr<sub>2</sub>O<sub>4</sub>. The uppermost portion of the oxide scale mainly consists of a continuous film which is found to be Cr<sub>2</sub>O<sub>3</sub>, NiCr<sub>2</sub>O<sub>4</sub> and CoCr<sub>2</sub>O<sub>4</sub>. The total Cr percentage present in coating including the Cr present in Cr<sub>3</sub>C<sub>2</sub>-NiCr reinforcement is 36%. The higher Cr content in the coating leads to the fast transformation of Cr to Cr<sub>2</sub>O<sub>3</sub> during the early stage of hot corrosion. This is attributed to the presence of Cr<sub>2</sub>O<sub>3</sub> as a dominant phase (Figure 7.21). Cr<sub>2</sub>O<sub>3</sub> provides resistance against oxidation and corrosion by restricting the inward diffusion of oxygen below the temperatures of 800°C. Above 800°C temperature the Cr<sub>2</sub>O<sub>3</sub> starts to evaporate and form volatile chromium oxide (CrO<sub>3</sub>) which is not beneficial to resist oxidation (Seo et al. 2008). The CoCr<sub>2</sub>O<sub>4</sub> spinel oxide which is also a major phase as observed from XRD analysis due to nucleation of CoO and Cr<sub>2</sub>O<sub>3</sub>. The presence of small amount of Ni in Cr<sub>3</sub>C<sub>2</sub>-NiCr reinforcement oxidised to NiO and nucleation of NiO and Cr<sub>2</sub>O<sub>3</sub> results in the formation of NiCr<sub>2</sub>O<sub>4</sub>. The spinel oxides NiCr<sub>2</sub>O<sub>4</sub> have also been identified by the XRD analysis. NiCr<sub>2</sub>O<sub>4</sub> and CoCr<sub>2</sub>O<sub>4</sub> is a protective oxide that could limit the outward diffusion of Co, thus slowing down the oxidation rate.

The surface oxides Cr<sub>2</sub>O<sub>3</sub>, NiCr<sub>2</sub>O<sub>4</sub> and CoCr<sub>2</sub>O<sub>4</sub> act as a barrier to the diffusion of oxygen thereby contribute for the oxidation resistance of CoCrAlY+Cr<sub>3</sub>C<sub>2</sub>-NiCr coating. It is also corroborated from Figure 7.24 that the coatings have been oxidized and the oxidation is restricted to a depth of few microns on the surface at the end of 50 cycles of hot corrosion studies. This can be substantiated from the weight gain (mg/cm<sup>2</sup>) data plotted as a function of time (Figure 7.19), which shows a parabolic behaviour of both the coated alloys.

From the above discussion and the reference reported it can be inferred that the oxidation resistance is mainly provided by  $\text{Cr}_2\text{O}_3$ ,  $\text{NiCr}_2\text{O}_4$  and  $\text{CoCr}_2\text{O}_4$  spinels formed during the action of oxidation. Few researchers like Yuan et al. (2015), Zhang et al. (2016) and Sidhu et al. (2006B) reported that the presence of  $\text{CoCr}_2\text{O}_4$  and  $\text{NiCr}_2\text{O}_4$  spinels on the plasma sprayed corroded  $\text{CoNiCrAlY/Cr}_2\text{O}_3$  coating surface have improved resistance against oxidising environment. Chatterjee et al. (2001) suggested that spinel usually has lower diffusion coefficients of cations and anions, which is beneficial for reducing the oxidation rate. Hence it can be inferred that the presence of sufficient/favourable amount of Cr and temperature attributed to the formation of  $\text{Cr}_2\text{O}_3$  as major oxide and its spinels is responsible for providing oxidation resistance.

## **7.5 Uncoated alloys**

### **7.5.1 Thermo gravimetric studies**

The plots of cumulative weight gain ( $\text{mg}/\text{cm}^2$ ) to number of cycles are shown in Figure 7.25. The total weight gain for MDN 321 is 1.68 and for Superni 76 is 1.31  $\text{mg}/\text{cm}^2$ . MDN 321 showed 22% higher weight gain as compared to Superni 76. Further, the weight gain square ( $\text{mg}^2/\text{cm}^4$ ) data is plotted as a function of time (Figure 6.26 ) to determine the parabolic rate constants,  $K_p$ . The corresponding values for MDN 321 and Superni 76 are found to be 0.09 and 0.08  $\text{g}^2 \text{cm}^{-4} \text{s}^{-1}$ , respectively. The plot shows that MDN 321 shows drastic weight gain during the initial cycles and attain steady state weight gain i.e. parabolic nature at the early stage of oxidation. The rate of weight gain of MDN 321 increase after the 30<sup>th</sup> cycle. Superni 76 shows steady state weight gain up to 25<sup>th</sup> cycle, later the weight gain rate drastically increased up to last 50<sup>th</sup> cycles. The change in weight gain nature from parabolic to linear can be called a para-linear nature. In general, the para-linear weight gain nature is observed as the oxide layer formed during the initial cycles protects the underneath material from further oxidation. The weight gain is steady until the oxide layer becomes weak where again para-linear weight gain step is observed i.e. destruction and simultaneous formation of superficial regions of the protective layer. Similar observation have been reported by during the oxidation of IN-657 alloy at 725°C (Otero and Pardo 1992).

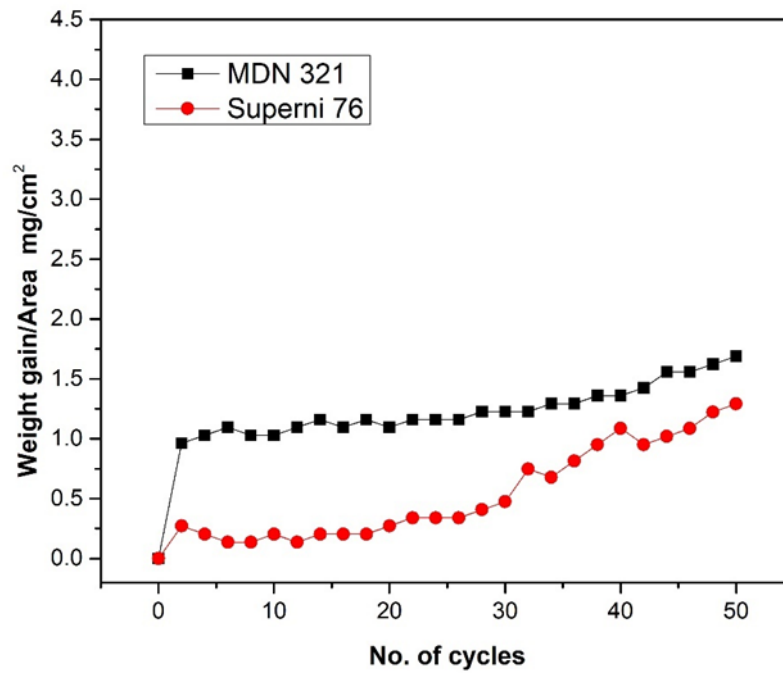


Figure 7.25 Weight gain vs. number of cycles plot of uncoated alloys subjected to oxidation for 50 cycles in air environment at 700°C.

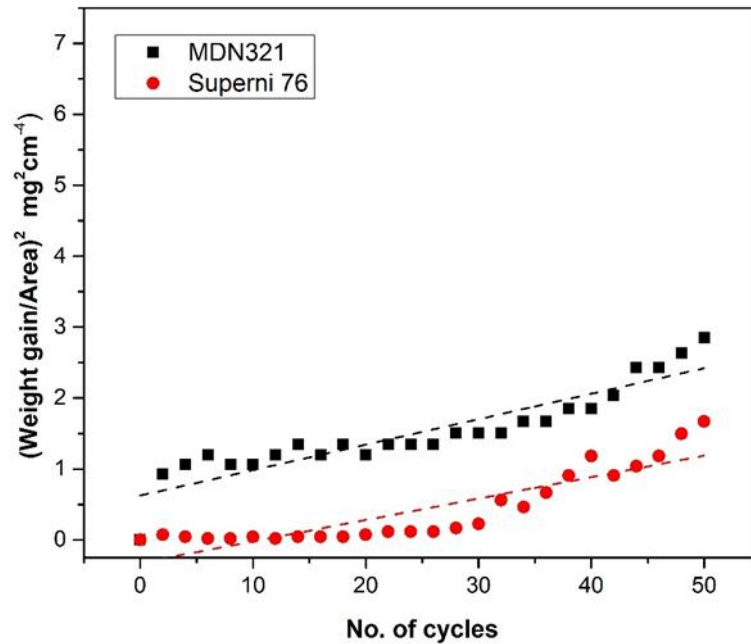


Figure 7.26 (Weight gain/area)<sup>2</sup> vs. number of cycles plot of uncoated alloys subjected to oxidation for 50 cycles in air environment at 700°C.

## 7.6 Comparative Discussion

The total weight gain ( $\text{mg}/\text{cm}^2$ ) of uncoated and coated alloys subjected to oxidation in still air for 50 cycles at  $700^\circ\text{C}$  is shown in Figure 7.27. CoCrAlY+Al<sub>2</sub>O<sub>3</sub>+YSZ coated alloys showed considerably lower weight gains than other coated and also uncoated substrates. CoCrAlY+CeO<sub>2</sub>, CoCrAlY+WC-Co and CoCrAlY+Cr<sub>3</sub>C<sub>2</sub>-NiCr coated alloys showed higher weight gain as compared to MDN 321 and Superni 76 uncoated alloys. All the coatings have experienced parabolic weight gain nature during oxidation cycles. Based on the thermogravimetric data, the relative oxidation resistance of the various coatings are shown in the following sequence and discussed in the same order:

$$\text{CoCrAlY+Al}_2\text{O}_3\text{+YSZ} > \text{CoCrAlY+Cr}_3\text{C}_2\text{-NiCr} > \text{CoCrAlY+WC-Co} > \text{CoCrAlY+CeO}_2$$

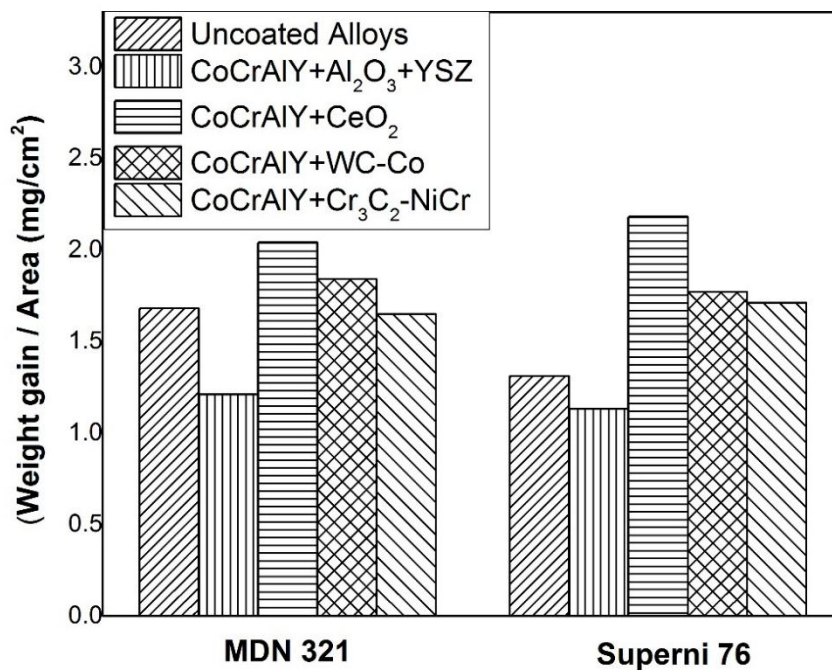


Figure 7.27 Total weight gain ( $\text{mg}/\text{cm}^2$ ) of uncoated and Plasma coated alloys subjected to oxidation.

Considering the upper limit of total weight gain of coatings on two substrates, CoCrAlY+Al<sub>2</sub>O<sub>3</sub>+YSZ coating approximately experience 29%, 8% , 28%, 34% and 44% lesser weight gain than MDN 321, Superni 76, CoCrAlY+Cr<sub>3</sub>C<sub>2</sub>-NiCr, CoCrAlY+WC-Co and CoCrAlY+CeO<sub>2</sub> coatings respectively. The major phases

observed on coatings on both the substrate are same and the major substrate elements are not identified on oxidised coatings surface shows the absence of substrate effect on growth of oxide scale.

In case of CoCrAlY+Al<sub>2</sub>O<sub>3</sub>+YSZ coating, the presence of thermodynamically stable  $\alpha$ -Al<sub>2</sub>O<sub>3</sub> in the coating is responsible for slow-scale growth kinetics during the oxidation. Further the formation of Cr<sub>2</sub>O<sub>3</sub>, CoCr<sub>2</sub>O<sub>4</sub> and CoAl<sub>2</sub>O<sub>4</sub> suppress the formation of possible metal oxides (CoO) by restricting the inward diffusion of oxygen into the coating.

In CoCrAlY+Cr<sub>3</sub>C<sub>2</sub>-NiCr coating, the total Cr percentage present in coating including the Cr present in Cr<sub>3</sub>C<sub>2</sub>-NiCr reinforcement is 36%. The rapid oxidation of Cr and other active elements during the early stage of oxidation causes higher weight gain as compared to CoCrAlY+Al<sub>2</sub>O<sub>3</sub>+YSZ coating. Later the growth of dominant Cr<sub>2</sub>O<sub>3</sub> and CoCr<sub>2</sub>O<sub>4</sub> provides oxidation resistance which is responsible for steady state weight gain nature.

During high temperature exposure of CoCrAlY+WC-Co coating, the active elements of the coating such as W, Cr, Al and Co have undergone oxidation to form WO<sub>3</sub>, Cr<sub>2</sub>O<sub>3</sub>, CoO and Al<sub>2</sub>O<sub>3</sub>. With subsequent oxidation cycles formation of CoWO<sub>4</sub> as a strong phase with Cr<sub>2</sub>O<sub>3</sub> and CoCr<sub>2</sub>O<sub>4</sub> forms a dense, non-porous oxide scale which provide oxidation resistance. The WO<sub>3</sub> seen as a porous structure which allows the inward diffusion of oxygen until it transforms into CoWO<sub>4</sub>.

In case of CoCrAlY+CeO<sub>2</sub> coating, the oxidation of active elements Co, Cr and Al resulting in the formation of oxide scale on the coating surface. CeO<sub>2</sub> segregate at the grain boundaries of oxide scale, Ce ions blocks the outward diffusion of Co and results in scale growth controlled primarily by inward diffusion of oxygen. However, the segregation of CeO<sub>2</sub> occurs at slow rate. The continuous oxidation of other active elements of coatings until the blocking of the outward and inward diffusion by Ce ions results in higher weight gain than the other coatings.

Based on the thermogravimetric data it is observed that MDN 321 and Superni 76 uncoated alloys have shown lesser weight gain than CoCrAlY+Cr<sub>3</sub>C<sub>2</sub>-NiCr,

CoCrAlY+WC-Co and CoCrAlY+CeO<sub>2</sub> coatings. However, all these coatings exhibited parabolic weight gain nature, indicating presence of protective oxide scale on coating surface. The higher weight gain of coatings during the early stages of oxidation is due to the oxygen penetration into the coatings through the open porosity located along the splat boundaries until all the accessible internal surfaces have been oxidized. Whereas uncoated alloys shows slightly para-linear weight gain by changing the weight gain nature from steady state to linear condition.

## CONCLUSIONS

In the present study cobalt based composite coatings with oxides and carbides as reinforcements are successfully developed using plasma spray technique on MDN 321 and Superni 76 substrates. The performance of these composite coatings under high temperature erosion, oxidation and hot corrosion environment have been evaluated in the present study. The salient conclusions resulting from the present investigations are enlisted as follows:

- Plasma spray process has been used successfully to deposit CoCrAlY+Al<sub>2</sub>O<sub>3</sub>+YSZ, CoCrAlY+CeO<sub>2</sub>, CoCrAlY+WC-Co and CoCrAlY+Cr<sub>3</sub>C<sub>2</sub>-NiCr on MDN 321 and Superni 76 substrates. Under the given set of spray parameters, seemingly dense flattened laminar structured coating with thickness in the desired range of 273-298 μm and porosity levels of less than 6.2% has been achieved.
- All the coatings have retained the phases observed in composite feed stock powder and have not undergone significant phase transformation. Oxidation, decomposition and decarburization of the coating powder are found to be negligible under chosen plasma spray parameters. During spraying the phases formed as a result of oxidation of Al and decarburization of WC and Cr<sub>3</sub>C<sub>2</sub> carbides are indexed to minor peaks.
- CoCrAlY+WC-Co coating exhibited superior hardness of 384±35 HV and fracture toughness of 14.3±3.5 MPa m<sup>1/2</sup> due to higher carbide retention and higher cohesive strength accompanied with lower porosity.
- CoCrAlY+CeO<sub>2</sub> showed higher bond strength of 15.6±2.2 MPa and least porosity of 4.6±0.3% which is attributed to refinement of splats induced by the CeO<sub>2</sub> reinforcement and its segregation along the splat boundaries. During the bond strength test, the fracture has occurred between the coating-substrate interface, which implies good cohesion strength between the splats.

### *Solid Particle Erosion Studies*

- All the coatings have shown higher erosion resistance than Superni 76 alloy at both 90° and 30° impact angle. Relative solid particle erosion resistance of the various coatings under the present investigation is arranged in the following sequence:

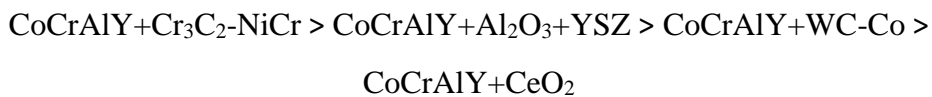
CoCrAlY+WC-Co > CoCrAlY+CeO<sub>2</sub> > CoCrAlY+Al<sub>2</sub>O<sub>3</sub>+YSZ > CoCrAlY+Cr<sub>3</sub>C<sub>2</sub>-NiCr

- The superior erosion resistance of the CoCrAlY+WC-Co coating is attributed to the higher hardness, fracture toughness and higher carbide retention or lower carbide dissolution on account of its high melting point. The coating experienced combination of ductile and brittle modes of material removal. The morphology of the eroded surface point out indentations, ridges, ploughing marks, lips formation in matrix. Craters, cracks and carbide particle pull-out prevailing erosion mechanism. WC provides the shielding effect to Co-matrix by restricting the material removal and deformation during erodent impact.
- The better erosion resistance of CoCrAlY+CeO<sub>2</sub> coating is due to the surface active nature of CeO<sub>2</sub> reinforcement and its dispersion along the splat boundaries of coating material on solidification contributes to coating refinement and better cohesion of the reinforcement with the Co matrix. The coating has also exhibited good fracture toughness and least porosity.
- The CoCrAlY+Al<sub>2</sub>O<sub>3</sub>+YSZ coating showed lower erosion resistance due to the formation of craters by brittle fracture and pull out of reinforcements. The least fracture toughness and higher porosity in this coating is responsible for the higher volume loss and cracks formation is the initiation stage of brittle fracture.
- The Cr<sub>3</sub>C<sub>2</sub> undergoes significant dissolution with metallic Co-matrix during spraying due to its lower melting point resulting in embrittlement of coating splats on solidification. The embrittlement leads to severe brittle fracture in the form of cracks, craters and chipping, resulting in least erosion resistance.
- Ductile erosion mechanism is dominant for all coatings. The higher erosion resistance observed at 90° impact angle is attributed to the ability of ductile material to absorb impact energy by deformation. Highly ductile material

softens at high temperature which is detrimental for erosion resistance. The presence of hard phases in the ductile matrix is beneficial for erosion resistance.

### *Hot corrosion studies*

- The cumulative weight gain for all the plasma coated alloys are significantly lower than that of uncoated alloys subjected to hot corrosion in Na<sub>2</sub>SO<sub>4</sub>-60% V<sub>2</sub>O<sub>5</sub> molten salt environment for 50 cycles at 700°C. Uncoated alloys suffered from cracking and intense spalling of oxide scale which might be responsible for higher corrosion rate.
- All the coatings exhibited significantly higher hot corrosion resistance than that of MDN 321 and Superni 76 alloys by showing lower weight gain and lower parabolic rate constant value (K<sub>p</sub>). The substrate alloys have experienced linear weight gain nature due to the formation of weak oxides and intense spalling of oxide scale during cyclic loading.
- Based on the thermogravimetric data, the relative hot corrosion resistance of the various coatings is arranged in the following sequence:



All the coatings exhibit characteristic thick protective oxide scale, composed of oxides and spinel oxides of the active elements of the coating and imparted resistance to the hot corrosion in the given molten salt environment.

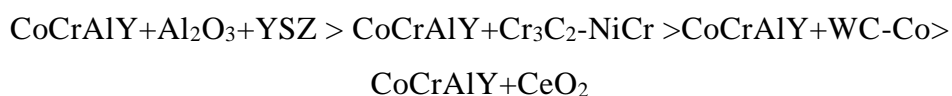
- The CoCrAlY+Cr<sub>3</sub>C<sub>2</sub>-NiCr coatings have shown 82% and 79% higher hot corrosion resistance as compared to uncoated MDN 321 and Superni 76 substrates respectively. The hot corrosion resistance of CoCrAlY+Cr<sub>3</sub>C<sub>2</sub>-NiCr coating is 23%, 46% and 64% higher than CoCrAlY+Al<sub>2</sub>O<sub>3</sub>+YSZ, CoCrAlY+WC-Co and CoCrAlY+CeO<sub>2</sub> coatings respectively. The superior hot corrosion resistance of CoCrAlY+Cr<sub>3</sub>C<sub>2</sub>-NiCr coating is due to the presence of 36 wt. % of Cr which is substantially higher than other coating compositions.
- The higher Cr content leads to the preferential oxidation of Cr at the early stage of corrosion to form Cr<sub>2</sub>O<sub>3</sub> as a major oxide. This resulted in the formation of CoCr<sub>2</sub>O<sub>4</sub> spinel oxide with subsequent hot corrosion cycles. The Cr<sub>2</sub>O<sub>3</sub> and

CoCr<sub>2</sub>O<sub>4</sub> oxide layer have lower solubility for corrosive salt melts and oxygen and hence provide hot corrosion resistance. The coating region beneath surface oxide scale remains unoxidised.

- The presence of thermodynamically stable metal oxide of  $\alpha$ -Al<sub>2</sub>O<sub>3</sub> in the CoCrAlY+Al<sub>2</sub>O<sub>3</sub>+YSZ coating shows slow-scale growth kinetics during initial hot corrosion cycles. With the subsequent hot corrosion cycles, formation of Cr<sub>2</sub>O<sub>3</sub>, CoCr<sub>2</sub>O<sub>4</sub> and CoAl<sub>2</sub>O<sub>4</sub> spinels might stop the inward diffusion of oxygen. CoCrAlY+Al<sub>2</sub>O<sub>3</sub>+YSZ coating has provided 28% and 52% lesser weight gain than CoCrAlY+WC-Co and CoCrAlY+CeO<sub>2</sub> coatings respectively.
- In CoCrAlY+WC-Co coating, tungsten seems to have undergone rapid oxidation due to its greater affinity to oxygen at temperatures above 400°C. Simultaneously, the oxidation of active elements of coating resulted in the formation of dense, non-porous, well adhered oxide scale of Cr<sub>2</sub>O<sub>3</sub>, CoO and Al<sub>2</sub>O<sub>3</sub>, leading to the parabolic corrosion kinetics. The formation of high melting temperature CoSO<sub>4</sub> phase as result of sulfur activity appears to have proved beneficial for reducing the corrosion rate.
- The lower hot corrosion resistance of CoCrAlY+CeO<sub>2</sub> coating is attributed to formation of corrosion product of CeVO<sub>4</sub>. The outward growth of CeVO<sub>4</sub> in the form of irregular crystals is accompanied by a volume expansion developing stresses on surrounding splats/oxide scale leading to cracks in the protective oxide scale.

### ***Oxidation studies***

- CoCrAlY+Al<sub>2</sub>O<sub>3</sub>+YSZ coatings exhibited higher oxidation resistance than other coatings and uncoated alloys. CoCrAlY+CeO<sub>2</sub>, CoCrAlY+WC-Co, and CoCrAlY+Cr<sub>3</sub>C<sub>2</sub>-NiCr coated alloys showed lower oxidation resistance as compared to MDN 321 and Superni 76 alloys by showing higher weight gain. Based on the thermogravimetric data, the relative oxidation resistance of the various coatings is arranged in the following sequence:



- The protection offered by CoCrAlY+Al<sub>2</sub>O<sub>3</sub>+YSZ coatings can be attributed to the oxide layer of Al<sub>2</sub>O<sub>3</sub>, Cr<sub>2</sub>O<sub>3</sub> and CoCr<sub>2</sub>O<sub>4</sub> formed on the outermost surface,

resulting in slow scale growth kinetics during oxidation. The preferential oxidation of Al and Cr along the cobalt rich splat boundary blocks the transport of oxygen into the coating through pores and voids, thereby making the oxidation rate to reach steady state.

- Analogous to the hot corrosion studies, CoCrAlY+Cr<sub>3</sub>C<sub>2</sub>-NiCr coating having the higher Cr content than the other coatings leads to the fast transformation of Cr to Cr<sub>2</sub>O<sub>3</sub> during the early stage of oxidation. The Cr<sub>2</sub>O<sub>3</sub> with spinel oxides of CoCr<sub>2</sub>O<sub>4</sub> and NiCr<sub>2</sub>O<sub>4</sub> as a thin oxide layer could limit the inward diffusion of oxygen there by slowing down the oxidation rate.
- The higher weight gain of CoCrAlY+WC-Co coating is due to rapid oxidation of W into WO<sub>3</sub>, seen as a porous structure which allows the inward diffusion of oxygen until it transforms into CoWO<sub>4</sub>. With subsequent oxidation cycles formation of dense, non-porous oxide scale Cr<sub>2</sub>O<sub>3</sub>, CoO and Al<sub>2</sub>O<sub>3</sub> provide oxidation resistance.

Based on the findings of the present study, CoCrAlY+Al<sub>2</sub>O<sub>3</sub>+YSZ and CoCrAlY+Cr<sub>3</sub>C<sub>2</sub>-NiCr coatings show superior performance in oxidation and hot corrosion environment and the erosion resistance of CoCrAlY+WC-Co and CoCrAlY+CeO<sub>2</sub> coatings are appreciable. The detailed study of properties of these coating and their behaviour in various environments can be a guide to the end users to select appropriate coatings based on requirements.

**THIS PAGE IS LEFT BLANK.**

## REFERENCES

- Afrasiabi, A., and Kobayashi, A. (2013). "Hot corrosion control in plasma sprayed YSZ coating by alumina layer with evaluation of microstructure and nanoindentation data (H, E)." *Vacuum*, 88(1), 103–107.
- Afrasiabi, A., Saremi, M., and Kobayashi, A. (2008). "A comparative study on hot corrosion resistance of three types of thermal barrier coatings: YSZ, YSZ+Al<sub>2</sub>O<sub>3</sub> and YSZ/ Al<sub>2</sub>O<sub>3</sub>." *Materials Science and Engineering A*, 478(1–2), 264–269.
- Ahmadi-Pidani, R., Shoja-Razavi, R., Mozafarinia, R., and Jamali, H. (2014). "Improving the hot corrosion resistance of plasma sprayed ceria-yttria stabilized zirconia thermal barrier coatings by laser surface treatment." *Materials and Design*, 57, 336–341.
- Amaya, C., Aperador, W., Caicedo, J. C., Espinoza-Beltrán, F. J., Muñoz-Saldaña, J., Zambrano, G., and Prieto, P. (2009). "Corrosion study of Alumina/Yttria-Stabilized Zirconia (Al<sub>2</sub>O<sub>3</sub>/YSZ) nanostructured Thermal Barrier Coatings (TBC) exposed to high temperature treatment." *Corrosion Science*, 51(12), 2994–2999.
- Baiamonte, L., Marra, F., Gazzola, S., Giovanetto, P., Bartuli, C., Valente, T., and Pulci, G. (2016). "Thermal sprayed coatings for hot corrosion protection of exhaust valves in naval diesel engines." *Surface and Coatings Technology*, 295, 78–87.
- Batchelor, A.W., Lam, L.N. and Chandrasekaran, M, (2003), "Ch. 6: Discrete Coatings," in 'Materials Degradation and its Control by Surface Engineering,' 2<sup>nd</sup> Edition, Imperial College Press.
- Berger, Z., and Livshitz, M. (2015). "The Structure and Properties of Hypervelocity Oxy-Fuel (HVOF) Sprayed Coatings." 179–186.
- Birks, N. and Meier, G. H. (1983). "Introduction to High Temperature Oxidation of Metals." Edward Arnold, London.
- Bluni, S.T. and Mardar, A.R., (1996), "Effects of Thermal Spray Coating Composition and Microstructure on Coating Response and Substrate Protection at High Temperatures," *Corrosion*, Vol. 52, No. 3, pp. 213-218.
- Bobzin, K., Schläfer, T., Richardt, K., and Brühl, M. (2008). "Development of oxide dispersion strengthened MCrAlY coatings." *Journal of Thermal Spray Technology*, 17(5–6), 853–857.
- Bolelli, G., Hulka, I., Koivuluoto, H., Lusvarghi, L., Milanti, A., Niemi, K., and Vuoristo, P. (2014A). "Properties of WC–FeCrAl coatings manufactured by different high velocity thermal spray processes." *Surface and Coatings Technology*, 247, 74–89.

Bolelli, G., Börner, T., Milanti, A., Lusvarghi, L., Laurila, J., Koivuluoto, H., Niemi, K., and Vuoristo, P. (2014B). "Surface and Coatings Technology Tribological behavior of HVOF- and HVAF-sprayed composite coatings based on Fe-Alloy + WC – 12 % Co." 248, 104–112.

Bolelli, G., Candeli, A., Lusvarghi, L., Ravaux, A., Cazes, K., Denoirjean, A., and Valette, S. (2015). "Tribology of NiCrAlY+Al<sub>2</sub>O<sub>3</sub> composite coatings by plasma spraying with hybrid feeding of dry powder+suspension." *Wear*, 344–345, 69–85.

Bornstein, N.S., DeCrescente, M.A., Roth, H.A. (1975). "Effect of vanadium and sodium on the accelerated oxidation of nickel base alloys." International conference on gas turbine in the marine (MCIC) Columbus, USA, 115-148.

Burakowski, T. and Wierzchon, T., (1999), "Surface Engineering of Metals, Principles, Equipment, Technology." CRC Press, N. W., Boca Raton, Florida

Chatha, S. S., Sidhu, H. S., and Sidhu, B. S. (2012). "High temperature hot corrosion behaviour of NiCr and Cr<sub>3</sub>C<sub>2</sub>-NiCr coatings on T91 boiler steel in an aggressive environment at 750°C." *Surface and Coatings Technology*, 206(19–20), 3839–3850.

Chatterjee, U. K., Bose, S. K., and Roy, S. K. (2001). *Environmental Degradation of Metals: Corrosion Technology Series/14*. CRC Press.

Davis, J.R., (2001). "Surface engineering for corrosion and wear resistance." ASM International, Materials park, OH, 61-62.

Dong, S., Song, B., Hansz, B., Liao, H., and Coddet, C. (2012). "Improvement of adhesion of plasma-sprayed Al<sub>2</sub>O<sub>3</sub> coatings by using dry-ice blasting." *Materials Letters*, Elsevier B.V., 66(1), 289–291.

Doychak, J., (1995). "Oxidation behaviour of high-temperature intermetallics." in intermetallic compounds, principles and practice, Principles, Eds. Westbrook, J.H. and Fleischer, F.L., Pub. John Wiley and Sons Ltd., England.

Eliasz, N., Shemesh, G., and Latanision, R. M. (2002). "Hot corrosion in gas turbine components." *Engineering Failure Analysis*, 9(1), 31–43.

Espevik, S., Rapp, R. A., Daniel, P. L., and Hirth, J. P. (1980). "Oxidation of Ni-Cr-W ternary alloys." *Oxidation of Metals*, 14(2), 85–108.

Evans, H. E. and Taylor, M. P., (2001), "Diffusion Cells and Chemical Failure of MCrAlY Bond Coats in Thermal-Barrier Coating Systems," *Oxidation of Metals*, 55(1-2), 17-34.

Fauchais, P, Vardelle, A. and, Dussoubs, B., (2001). "Quo Vadis Thermal Spray." *Journal of Thermal Spray Technology*, 10(1), 44-46.

Fauchais, P. (2004). "Understanding plasma spraying." *Journal of Physics D: Applied Physics*, 37(9), R86.

- Finnie, I. (1960). "Erosion of surfaces by solid particles." *Wear*, 3(2), 87–103.
- Finnie, I., Levi, A.V. and Mcfadden, D.H. (1979). "The fundamental mechanisms of the erosive wear of ductile metals by solid particles." ASTM STP 664 Erosion: prevention and useful applications.
- Goebel, J. A., and Pettit, F. S. (1970). "Na<sub>2</sub>SO<sub>4</sub>-induced accelerated oxidation (hot corrosion) of nickel." *Metallurgical Transactions*, 1(7), 1943–1954.
- Goward, G. W. (1998). "Progress in coatings for gas turbine airfoils." 109, 73–79.
- Grewal, H. S., Singh, H., and Agrawal, A. (2013). "Microstructural and mechanical characterization of thermal sprayed nickel – alumina composite coatings." *Surface and Coatings Technology*, 216, 78–92.
- Gurrappa, I. (1999). "Hot corrosion behavior of CM 247 LC alloy in Na<sub>2</sub>SO<sub>4</sub> and NaCl environments." *Oxidation of Metals*, 51(5-6), 353-382.
- Gurrappa, I. (2003). "Influence of alloying elements on hot corrosion of superalloys and coatings: necessity of smart coatings for gas turbine engines." *Materials Science and Technology*, 19(2), 178–183.
- Harb, J. N., and Smith, E. E. (1990). "Fireside corrosion in pc-fired boilers." *Progress in Energy and Combustion Science*, 16(3), 169–190.
- He, L., Tan, Y., Wang, X., Xu, T., and Hong, X. (2014). "Microstructure and wear properties of Al<sub>2</sub>O<sub>3</sub>-CeO<sub>2</sub>/Ni-base alloy composite coatings on aluminum alloys by plasma spray." *Applied Surface Science*, 314, 760–767.
- Heath, G.R., Heimgartner, P., Irons, G., Miller. (1997). "An assessment of thermal spray coating technologies for high temperature corrosion protection." *Material Science Forum*, 251-54, 809-816.
- Hidalgo, V. H., Varela, F. J. B., and Mene, A. C. (2001). "A comparative study of high-temperature erosion wear of plasma- sprayed NiCrBSiFe and WC-NiCrBSiFe coatings under simulated coal-fired boiler conditions." *Tribology International*, 34, 161–169.
- Hutchings, I.M. (1974). "The erosion of ductile metals by solid particles." PhD. Dissertation, University of Cambridge, 45–52.
- Hwang, Y. S. and Rapp, R. A., (1989), "Thermochemistry and Solubilities of Oxides in Sodium Sulfate-Vanadate Solutions," *Corrosion*, 45, 933-937.
- Irisawa, T., and Matsumoto, H. (2006). "Thermal shock resistance and adhesion strength of plasma-sprayed alumina coating on cast iron." *Thin Solid Films*, 509, 141–144.
- Islam, M. A., and Farhat, Z. N. (2014). "Effect of impact angle and velocity on erosion of API X42 pipeline steel under high abrasive feed rate." *Wear*, 311(1–2), 180–190.

- Ivosevic, M., Knight, R., Kalidindi, S. R., Palmese, G. R., and Sutter, J. K. (2006). "Solid particle erosion resistance of thermally sprayed functionally graded coatings for polymer matrix composites." *Surface and Coatings Technology*, 200, 5145–5151.
- Jafari, M., Enayati, M. H., Salehi, M., Nahvi, S. M., and Park, C. G. (2013). "Comparison between oxidation kinetics of HVOF sprayed WC – 12Co and WC – 10Co – 4Cr coatings." *International Journal of Refractory Metals and Hard Materials*, 41, 78–84.
- James, A. W., and Rajagopalan, S. (2014). "Gas turbines: Operating conditions, components and material requirements." *Structural Alloys for Power Plants: Operational Challenges and High-Temperature Materials*, 3–21.
- Jones, R. L., Williams, C. E., and Jones, S. R. (1986). "Reaction of Vanadium Compounds with Ceramic Oxides." *Journal of the Electrochemical Society*, 133(1), 227–230.
- Kamal, S., Jayaganthan, R., and Prakash, S. (2010). "Mechanical and microstructural characteristics of detonation gun sprayed NiCrAlY + 0.4 wt% CeO<sub>2</sub> coatings on superalloys." *Materials Chemistry and Physics*, 122(1), 262–268.
- Khajavi, M. R., and Shariat, M. H. (2004). "Failure of first stage gas turbine blades." *Engineering Failure Analysis*, 11, 589–597.
- Kim, H. J., Hwang, S. Y., Lee, C. H., and Juvanon, P. (2003). "Assessment of wear performance of flame sprayed and fused Ni-based coatings." *Surface and Coatings Technology*, 172(2–3), 262–269.
- Knotek, O., (2001), "Chapter 3: Thermal Spraying and Detonation Spray Gun Processes," in 'Handbook of Hard Coatings: Deposition Technologies, Properties and Applications,' Ed. Bunshah, R. F., Noyes Pub. Park Ridge, New Jersey, U. S. A./William Andrew Publishing, LLC, Norwich, New York, U.S.A., pp. 77-107.
- Kofstad, P. (1988). "High temperature oxidation of metals." John Wiley and Sons, Inc., New York, London, Sydney, 1, 1-50.
- Kofstad, P. K., and Hed, A. Z. (1969). "High temperature oxidation of Co-10 w/o Cr alloys. II - Oxidation kinetics." *Journal of Electrochemical Society*, 116(2), 229–234.
- Kolta, G.A., Hewaidy, L.F. and Felix N.S. (1972). "Reactions between sodium sulphate and vanadium pentoxide." *Thermochima Acta*, 4, 151-164.
- Kulu, P., and Pihl, T. (2002). "Selection criteria for wear resistant powder coatings under extreme erosive wear conditions." *Journal of thermal spray technology*, 11(4), 517-522.
- Kurz, R., and Brun, K. (2007). "Gas Turbine Tutorial-Maintenance And Operating Practices Effects On Degradation And Life by and." 173–186.

Kurz, R., Meher-homji, C., Brun, K., and Kurz, R. (2014). "43 rd Turbomachinery and 30 th Pump Users Symposia ( Pump and Turbo 2014)" September 23-25 , 2014 | Houston , TX | pumpturbo . tamu . edu.

Lawson, S. A., and Thole, K. A. (2017). "Simulations of Multiphase Particle Deposition on Endwall Film-Cooling Holes in Transverse Trenches." 134, 1–10.

Levy, A. V. (1986). "The platelet mechanism of erosion of ductile metals." *Wear*, 108(1), 1–21.

Levy, A., and Sa, C. A. U. (1991). "The effect of erodent erosion of metals particle characteristics on the." 151, 381–390.

Li, S., Langlade, C., Fayeulle, S., and Trkheux, D. (1998). "Influence of the microstructure of plasma deposited MCrAlY their tribological behaviour." *Surface and Coatings Technology*, 101, 7–11.

Liebhart, M and Levy, A. (1991). "The effect of erodent particle characteristics erosion of metals" *Wear*, 151, 381-390.

Long, H., Yefa, T., and Hua, T. (2014). "Microstructure and Tribological Properties of WC-CeO<sub>2</sub> / Ni- base Alloy Composite Coatings." *Rare Metal Materials and Engineering*, 43(4), 823–829.

Longa-Nava, Y., Zhang, Y. S., Takemoto, M. and Rapp, R. A., (1996). "Hot Corrosion of Nickel-Chromium and Nickel-Chromium-Aluminum Thermal-Spray Coatings by Sodium Sulfate-Sodium Metavanadate Salt." *Corrosion*, 52, 680-689.

Luthra, K. L., and LeBlanc, O. H. (1987). "Low Temperature Hot Corrosion of Co-Cr-AI Alloys." *Materials Science and Engineering*, 87, 329–335.

Macwan, A., Marr, M., Kesler, O., and Chen, D. L. (2015). "Microstructure, hardness and fracture toughness of suspension plasma sprayed yttria-stabilized zirconia electrolytes on stainless steel substrates." *Thin Solid Films*, 584, 23–28.

Mahesh, R. A., Jayaganthan, R., and Prakash, S. (2010). "A study on the oxidation behavior of HVOF sprayed NiCrAlY-0.4 wt.% CeO<sub>2</sub> coatings on superalloys at elevated temperature." *Materials Chemistry and Physics*, 119(3), 449–457.

Mathapati, M., Ramesh, M. R., and Doddamani, M. (2017). "High temperature erosion behavior of plasma sprayed NiCrAlY/WC-Co/cenosphere coating." *Surface and Coatings Technology*, 325, 98–106.

Matsukawa, C., Hayashi, S., Yakuwa, H., Kishikawa, T., Narita, T., and Ukai, S. (2011). "High-temperature carburization behaviour of HASTELLOY X in CH<sub>4</sub> gas." *Corrosion Science*, 53(10), 3131-3138.

Matthews, A., Areley, R.J. and Holiday, P. (1998). "Futures Bright for Surface Engineering." *Materials World*, 6, 346-347.

- Matthews, S., James, B., and Hyland, M. (2009). "Surface and Coatings Technology High temperature erosion of Cr<sub>3</sub>C<sub>2</sub>-NiCr thermal spray coatings — The role of phase microstructure." *Surface and Coatings Technology*, 203(9), 1144–1153.
- Miguel, J.M., Guilemany, J.M. and Vizcaino, S. (2003). "Tribological study of NiCrBSi coating obtained by different processes." *Tribology International*, 36, 181-187.
- Mishra, N. K., and Mishra, S. B. (2014). "Characterisation and oxidation of LVOF sprayed Al<sub>2</sub>O<sub>3</sub> –40%TiO<sub>2</sub> coating on supermi 601 and supermi 718 superalloys at 800 and 900°C." *Corrosion Engineering, Science and Technology*, 49(8), 705–711.
- Mishra, S. B., Chandra, K., Prakash, S., and Venkataraman, B. (2006). "Erosion performance of coatings produced by shrouded plasma spray process on a Co-based superalloy." *Surface and Coatings Technology*, 201, 1477–1487.
- Mishra, S. B., Prakash, S., and Chandra, K. (2006). "Studies on erosion behaviour of plasma sprayed coatings on a Ni-based superalloy." *Wear*, 260(4–5), 422–432.
- Movahedi, B. (2013). "Surface and Coatings Technology Fracture toughness and wear behavior of NiAl-based nanocomposite HVOF coatings." *Surface and Coatings Technology*, 235, 212–219.
- Murthy, J. K. N., Prasad, K. S., Gopinath, K., and Venkataraman, B. (2010). "Surface and Coatings Technology Characterisation of HVOF sprayed Cr<sub>3</sub>C<sub>2</sub>-50 ( Ni20Cr ) coating and the influence of binder properties on solid particle erosion behaviour." *Surface and Coatings Technology*, 204(24), 3975–3985.
- National Materials Advisory Board. (1996). "Coatings for High-Temperature Structural Materials: Trends and Opportunities," National Academy Press Washington D.C., <http://www.nap.edu/openbook/0309053811/html>, 1-85.
- Nejati, M., Rahimipour, M. R., and Mobasherpour, I. (2014). "Evaluation of hot corrosion behavior of CSZ, CSZ/micro Al<sub>2</sub>O<sub>3</sub> and CSZ/nano Al<sub>2</sub>O<sub>3</sub> plasma sprayed thermal barrier coatings." *Ceramics International*, 40(3), 4579–4590.
- Nicholls, J. R. (2000). "Designing Oxidation-Resistant Coatings." *JOM*, 52(1), 28-35.
- Nicholls, J. R., Simms, N. J., Chan, W. Y., and Evans, H. E. (2002). "Smart overlay coatings-concept and practice." *Surface and Coatings Technology*, 149(2), 236–244.
- Niranatlumpong, P., Ponton, C. B., and Evans, H. E. (2000). "The failure of protective oxides on plasma-sprayed NiCrAlY overlay coatings." *Oxidation of Metals*, 53(3-4), 241-258.

Nithin, H. S., Desai, V., and Ramesh, M. R. (2017A). "An Investigation on High Temperature Erosion Behaviour of Plasma Sprayed CoCrAlY/Al<sub>2</sub>O<sub>3</sub>/YSZ on Fe and Ni Based Alloys." *Pertanika Journal of Science and Technology*, 25(2) 397-406.

Nithin, H. S., Desai, V., and Ramesh, M. R. (2017). "Elevated Temperature Solid Particle Erosion Performance of Plasma-Sprayed Co-based Composite Coatings with Additions of Al<sub>2</sub>O<sub>3</sub> and CeO<sub>2</sub>." *Journal of Materials Engineering and Performance*, 26(11), 5251-5261.

Nkhoma, R. K. C., Siyasiya, C. W., and Stumpf, W. E. (2014). "Hot workability of AISI 321 and AISI 304 austenitic stainless steels." *Journal of Alloys and Compounds*, 595, 103–112.

Ogawa, K., Ito, K., Shoji, T., Seo, D. W., Tezuka, H., and Kato, H. (2006). "Effects of Ce and Si Additions to CoNiCrAlY Bond Coat Materials on Oxidation Behavior and Crack Propagation of Thermal Barrier Coatings." 15(December), 640–651.

Otero, E., and Pardo, A. (1992). "The corrosion of some superalloys ( at 1000 k ) in molten eutectic mixture 60 % V<sub>2</sub>O<sub>5</sub>-40 % Na<sub>2</sub>SO<sub>4</sub>. The influence of the oxygen and carbon residues." *Corrosion Science*, 33(11), 1747–1757.

Otero, E., Merino, M.C., Pardo, A., Biezma, M.V. and Buitrago, G. (1987). "Study on Corrosion Products of IN657 Alloy in Molten Salts." *Proc. of 10th ICMC, Madras, India*, 4, 3583-3591.

Otsuka, N., and Rapp, R. A. (1990). "Effects of Chromate and Vanadate Anions on the Hot Corrosion of Preoxidized Ni by a Thin Fused Na<sub>2</sub>SO<sub>4</sub> Film at 900°C." *Journal of Electrochemical Society*, 137(1), 53–60.

Pettit, F.S. and Meier, G.H. (1984). "Oxidation and hot corrosion of superalloys." *The Met. Soc. of AIME, Warrendale, Pennsylvania*, 651-687.

Pfender, E., (1988), "Fundamental Studies Associated with the Plasma Spray Process," *Surface and Coatings Technology*, 34, 1-14.

Puetz, P., Huang, X., Lima, R. S., Yang, Q., and Zhao, L. (2010). "Characterization of transient oxide formation on CoNiCrAlY after heat treatment in vacuum and air." *Surface and Coatings Technology*, 205(2), 647–657.

Purkayastha, S., and Dwivedi, D. K. (2013). "Abrasive and Erosive Wear Performance of Rare Earth Oxide Doped Ni/WC Coatings." *Journal of Tribology*, 136(1), 11602.

Rajendran, R. (2012). "Gas turbine coatings – An overview." *Engineering Failure Analysis*, 26, 355–369.

Ramanujam, N., and Nakamura, T. (2009). "Erosion mechanisms of thermally sprayed coatings with multiple phases." *Surface and Coatings Technology*, 204(1–2), 42–53.

- Ramesh, M. R., Prakash, S., Nath, S. K., Kumar, P., and Venkataraman, B. (2010). "Solid particle erosion of HVOF sprayed WC-Co / NiCrFeSiB coatings." *Wear*, 269(3–4), 197–205.
- Ramesh, M. R., Prakash, S., Nath, S. K., Sapra, P. K., and Krishnamurthy, N. (2011). "Evaluation of Thermocyclic Oxidation Behavior of HVOF-Sprayed NiCrFeSiB Coatings on Boiler Tube Steels." *Journal of Thermal Spray Technology*, 20, 992–1000.
- Rapp, R. A. (2002). "Hot corrosion of materials : a fluxing mechanism ?" *Corrosion Science*, 44, 209–221.
- Rapp, R. A., and Zhang, Y. S. (1994). "Hot Corrosion of Materials : Fundamental Studies." *JOM*, 47–48.
- Rodríguez, J., Martín, A., Fernández, R., and Fernández, J. E. (2003). "An experimental study of the wear performance of NiCrBSi thermal spray coatings." *Wear*, 255(7–12), 950–955.
- Ruzic, J., Vilotijevic, M., Bozic, D., and Raic, K. (2012). "Understanding plasma spraying process and characteristics of DC-arc plasma gun (PJ-100)." *Metallurgical and Materials Engineering*, 18(4), 273-282.
- Sadeghi-Fadaki, S. A., Zangeneh-Madar, K., and Valefi, Z. (2010), "The adhesion strength and indentation toughness of plasma-sprayed yttria stabilized zirconia coatings." *Surface and Coatings Technology*, 204(14), 2136-2141.
- Sampath, S., Jiang, X. Y., Matejicek, J., Leger, A. C., and Vardelle, A. (1999). "Substrate temperature effects on splat formation, microstructure development and properties of plasma sprayed coatings Part I: Case study for partially stabilized zirconia." *Materials Science and Engineering*, 272, 181–188.
- Santa, J.F., Espitia, L.A., Blanco, J.A., Romo, S.A. and Toro, A. (2009). "Slurry and cavitation erosion resistance of thermal spray coatings." *Wear*, 267, 160–167.
- Seo, D., Ogawa, K., Suzuki, Y., Ichimura, K., Shoji, T., and Murata, S. (2008). "Comparative study on oxidation behavior of selected MCrAlY coatings by elemental concentration profile analysis." *Applied Surface Science*, 255, 2581–2590.
- Seo, D., Ogawa, K., Suzuki, Y., Ichimura, K., Shoji, T., and Murata, S. (2008). "Comparative study on oxidation behavior of selected MCrAlY coatings by elemental concentration profile analysis." *Applied Surface Science*, 255, 2581–2590.
- Sharma, A., and Goel, S. K. (2016). "Erosion behaviour of WC – 10Co – 4Cr coating on 23-8-N nitronic steel by HVOF thermal spraying." *Applied Surface Science*, 370, 418–426.

Sharma, S. (2012). "Erosive Wear Study of Rare Earth-Modified HVOF-Sprayed Coatings Using Design of Experiment." *Journal of Thermal Spray Technology*, 21, 49–62.

Sheldon, G. L., and Finnie, I. (1966). "On the ductile behaviour of nominally brittle materials during erosive cutting." *Trans. ASME*, 88B, 387–392.

Sidhu, B. S., and Prakash, S. (2006A). "Performance of NiCrAlY, Ni-Cr, Stellite-6 and Ni3Al coatings in Na<sub>2</sub>SO<sub>4</sub>-60% V<sub>2</sub>O<sub>5</sub> environment at 900°C under cyclic conditions." *Surface and Coatings Technology*, 201(3–4), 1643–1654.

Sidhu, T. S., Prakash, S., and Agrawal, R. D. (2006B). "Hot corrosion resistance of high-velocity oxyfuel sprayed coatings on a nickel-base superalloy in molten salt environment." *Journal of Thermal Spray Technology*, 15(3), 387–399.

Sidhu, H. S., Sidhu, B. S., and Prakash, S. (2007A). "Hot Corrosion Behavior of HVOF Sprayed Coatings on ASTM SA213-T11 Steel." *Journal of Thermal Spray Technology*, 16, 349–354.

Sidhu, H. S., Sidhu, B. S., and Prakash, S. (2007B). "Solid particle erosion of HVOF sprayed NiCr and Stellite-6 coatings." *Surface and Coatings Technology*, 202(2), 232–238.

Sidhu, T. S., Malik, A., Prakash, S., and Agrawal, R. D. (2007C). "Oxidation and Hot Corrosion Resistance of HVOF WC-NiCrFeSiB Coating on Ni- and Fe-based Superalloys at 800°C." *Journal of Thermal Spray Technology*, 16, 844–849.

Sidky, P. S., and Hocking, M. G. (1999). "Review of inorganic coatings and coating processes for reducing wear and corrosion." *British Corrosion Journal*, 34(3), 171–183.

Simens, E., Browning, G. and Liebhafsky, H. (1955). "Corrosion." 2<sup>nd</sup> edi., John Willey and Sons, 505.

Simms, N. J., Encinas-Oropesa, A., and Nicholls, J. R. (2008). "Hot corrosion of coated and uncoated single crystal gas turbine materials." *Materials and Corrosion*, 59(6), 476–483.

Singh, H., Kaur, M., and Prakash, S. (2016). "High-Temperature Exposure Studies of HVOF-Sprayed Cr 3 C 2 -25 (NiCr)/(WC-Co) Coating." *Journal of Thermal Spray Technology*, 25(6), 1192–1207.

Singh, H., Puri, D., and Prakash, S. (2005). "Some studies on hot corrosion performance of plasma sprayed coatings on a Fe-based superalloy." *Surface and Coatings Technology*, 192(1), 27–38.

Somasundaram, B., Kadoli, R., and Ramesh, M. R. (2014). "Evaluation of Cyclic Oxidation and Hot Corrosion Behavior of HVOF-Sprayed WC-Co/NiCrAlY Coating." *Journal of Thermal Spray Technology*, 23, 1000–1008.

Somasundaram, B., (2015), "Development of HVOF coatings on boiler materials in improving resistance to hot corrosion and erosion". National Institute of Technology Karnataka, India, Ph.D. thesis.

Staia, M. H., Valente, T., Bartuli, C., Lewis, D. B., Constable, C. P., Roman, A., and Lesage, J. (2001). "Part II: tribological performance of Cr<sub>3</sub>C<sub>2</sub>-25 % NiCr reactive plasma sprayed coatings deposited at different pressures." *Surface and Coatings Technology*, 147, 563–570.

Stein, K. J., Schorr, B. S., and Marder, A. R. (1999). "Erosion of thermal spray MCr – Cr<sub>3</sub>C<sub>2</sub> cermet coatings." *Wear*, 153–159.

Stott, F. H. (1988). Principles of growth and adhesion of oxide scales, in: E. Lang (Ed.), *The Role of Active Elements in the Oxidation Behaviour of High Temperature Metals and Alloys*, Elsevier Applied Science, London.

Stringer, J. (1987). "High-temperature corrosion of superalloys." *Materials Science and Technology*, 3(7), 482–493.

Suckling, M., and Allen, C. (1995). "The design of an apparatus to test wear of boiler tubes." *Wear*, 186–187, 266–272.

Sundararajan, G. and, and Roy, M. (1997). "Solid particle erosion behaviour of metallic materials at room and elevated temperature." *Tribology International*, 30(5), 339–359.

Susila, A., Sarangan, J., Suresh, S., and Subramanian, J. S. (2015). "Erosion wear behaviour of plasma sprayed NiCrSiB / Al<sub>2</sub>O<sub>3</sub> composite coating." *Int. Journal of Refractory Metals and Hard Materials*, 52, 209–218.

Tabako, W. (1999). "Erosion resistance of superalloys and different coatings exposed to particulate flows at high temperature." *Surface and Coatings Technology*, 121, 542–547.

Tahari, M. (2015). "The effect of heat treatment and thermal spray processes on the grain growth of nanostructured composite CoNiCrAlY/YSZ powders." *Journal of Alloys and Compounds*, 646, 372–379.

Tian, Y. S., Chen, C. Z., Chen, L. X., and Huo, Q. H. (2006). "Effect of RE oxides on the microstructure of the coatings fabricated on titanium alloys by laser alloying technique." *Scripta Materialia*, 54(5), 847–852.

Tiwari and Satya Prakash, (1997). "Studies on the hot corrosion behaviour of some superalloys in Na<sub>2</sub>SO<sub>4</sub>-V<sub>2</sub>O<sub>5</sub>." *Proc. of SOLCEC*, Kalpakkam, India, paper C33, 102-107.

Tucker Jr, R. C. (1994). "Advanced thermal spray deposition techniques." *Handbook of Deposition Technologies for Films and Coatings*, 11.

- Ul-Hamid, A. (2003). "Diverse scaling behavior of the Ni–20Cr alloy." *Materials chemistry and physics*, 80(1), 135-142.
- Vashishtha, N., Khatirkar, R. K., and Sapate, S. G. (2017). "Tribology International." 105, 55–68.
- Wang, B. Q., and Shui, Z. R. (2002). "The hot erosion behavior of HVOF chromium carbide-metal cermet coatings sprayed with different powders." *Wear*, 253, 550–557.
- Wang, B., and Verstak, A. (1999). "Elevated temperature erosion of HVOF Cr<sub>3</sub>C<sub>2</sub>-TiC-NiCrMo cermet coating." *Wear*, 342–351.
- Wang, C. J., and Lin, J. S. (2002). "The oxidation of MAR M247 superalloy with Na<sub>2</sub>SO<sub>4</sub> coating." *Materials chemistry and physics*, 76(2), 123-129.
- Wang, H., Xia, W., and Jin, Y. (1996). "A study on abrasive resistance of Ni-based coatings with a WC hard phase." *Wear*, 195, 47–52.
- Wang, Y., and Chen, W. (2003). "Effect of ceria on the erosion resistance of HVOF thermal sprayed NiAl intermetallic coatings." *Journal Of Materials Science Letters*, 845–848.
- Wang, Y., Yang, Y., and Yan, M. F. (2007). "Microstructures, hardness and erosion behavior of thermal sprayed and heat treated NiAl coatings with different ceria." *Wear*, 263(1–6 SPEC. ISS.), 371–378.
- Wang, P., Deng, S., He, Y., Liu, C., and Zhnag, J. (2016). "Oxidation and hot corrosion behavior of Al<sub>2</sub>O<sub>3</sub>/YSZ coatings prepared by cathode plasma electrolytic deposition" *Corrosion Science*, 109, 13–21.
- Warnes, B. M. (2003). "Improved aluminide/MCrAlX coating systems for super alloys using CVD low activity aluminizing." *Surface and Coatings Technology*, 163, 106-111.
- Wellman, R. G., and Nicholls, J. R. (2004). "High Temperature Erosion-Oxidation Mechanisms, Maps and Models." *Wear*, 256, 907–917.
- Wensink, H., and Elwenspoek, M. C. (2002). "A closer look at the ductile – brittle transition in solid particle erosion." *Wear*, 253, 1035–1043.
- Westergård, R., Axén, N., Wiklund, U., and Hogmark, S. (2000). "An evaluation of plasma sprayed ceramic coatings by erosion, abrasion and bend testing." *Wear*, 246(1–2), 12–19.
- Wiecinski, P., Smolik, J., Garbacz, H., and Kurzydowski, K. J. (2014), "Erosion resistance of the nanostructured Cr/CrN multilayer coatings on Ti6Al4V alloy." *Vacuum*, 107, 277-283.

- Wilcox, M., Kurz, R., and Brun, K. (2012). "Technology review of modern gas turbine inlet filtration systems." *International Journal of Rotating Machinery*, 2012.
- Wright, I. G., and Gibbons, T. B. (2007). "Recent developments in gas turbine materials and technology and their implications for syngas firing." *International Journal of Hydrogen Energy*, 32(16), 3610–3621.
- Wright, I. G., and Gibbons, T. B. (2007). "Recent developments in gas turbine materials and technology and their implications for syngas firing." *International Journal of Hydrogen Energy*, 32(16), 3610–3621.
- Yamada, K., Tomono, Y., Morimoto, J., Sasaki, Y and Ohmori, A., (2002), "Hotcorrosion behavior of boiler tube materials in refuse incineration environment," *Vacuum* 65, 533-540.
- Yin, Y., Ma, W., Jin, X., Li, X., Bai, Y., and Jia, R. (2016). "Hot corrosion behavior of the  $\text{La}_2(\text{Zr}_{0.7}\text{Ce}_{0.3})_2\text{O}_7$  ceramic in molten  $\text{V}_2\text{O}_5$  and a  $\text{Na}_2\text{SO}_4+\text{V}_2\text{O}_5$  salt mixture." *Journal of Alloys and Compounds*, 689, 123–129.
- Yoshida, M., (1993), "Effect of Hot Corrosion on the Mechanical Performances of Superalloys and Coating Systems," *Corrosion Science*, 35(5-8), 1115-1124.
- Yuan, K., Lin Peng, R., Li, X. H., Johansson, S., and Wang, Y. D. (2015). "Some aspects of elemental behaviour in HVOF MCrAlY coatings in high-temperature oxidation." *Surface and Coatings Technology*, 261, 86–101.
- Zhang, T., Huang, C., Lan, H., Du, L., and Zhang, W. (2016). "Oxidation and Hot Corrosion Behavior of Plasma-Sprayed MCrAlY– $\text{Cr}_2\text{O}_3$  Coatings." *Journal of Thermal Spray Technology*, 25(6), 1208–1216.
- Zhang, Z., Wang, Z., Liang, B., and La, P. (2006). "Effects of  $\text{CeO}_2$  on friction and wear characteristics of Fe-Ni-Cr alloy coatings." *Tribology International*, 39(9), 971–978.
- Zhao, L., Parco, M., and Lugscheider, E. (2004). "Wear behaviour of  $\text{Al}_2\text{O}_3$  dispersion strengthened MCrAlY coating." *Surface and Coatings Technology*, 184(2–3), 298–306.
- Zhou, X., and Ouyang, C. (2017). "Self-healing effects by the Ce-rich precipitations on completing defective boundaries to manage microstructures and oxidation resistance of Ni- $\text{CeO}_2$  coatings." *Surface and Coatings Technology*, 315, 67–79.
- Zhu, L., Zhu, S., and Wang, F. (2013). "Applied Surface Science Hot corrosion behaviour of a Ni+CrAlYSiN composite coating in  $\text{Na}_2\text{SO}_4$ –25wt.% NaCl melt." *Applied Surface Science*, 268, 103–110.

## List of Publications and Conferences based on PhD Research Work

Sl. No.	Title of the paper	Authors (same as in paper. Underline the Scholar name)	Name of the Journal/Conference	Month, Year of Publication	Category*
1.	An investigation on high temperature erosion behaviour of Plasma sprayed CoCrAlY/Al <sub>2</sub> O <sub>3</sub> /YSZ on Fe and Ni based alloys	<u>Nithin H S</u> , Vijay Desai, Ramesh M R	Pertanika Journal of Science and Technology.	June 2016	1
2.	Elevated Temperature Solid Particle Erosion Performance of Plasma Sprayed Co-based Composite Coatings with Additions of Al <sub>2</sub> O <sub>3</sub> and CeO <sub>2</sub>	<u>Nithin H S</u> , Vijay Desai, Ramesh M R	Journal of Materials Engineering and Performance, Springer-1.331.	Sept 2017	1
3	Cyclic Oxidation and Hot Corrosion Behaviour of Plasma Sprayed CoCrAlY+WC-Co Coating on Turbine Alloys	<u>Nithin H S</u> , Vijay Desai, Ramesh M R	Journal of Failure analysis and Prevention, Springer.	May 2018 (Accepted)	1

4	Hot corrosion behaviour of refractory and rare earth oxide reinforced CoCrAlY APS coatings at 700 °C	<u>Nithin H S</u> , Vijay Desai, Ramesh M R	Transactions of the Indian Institute of Metals, Springer-0.533.	April 2018 (Accepted with major revision)	1
5	High temperature solid particle erosion behaviour of plasma sprayed CoCrAlY based composite coatings	<u>Nithin H S</u> , Vijay Desai, Ramesh M R	Materials Research Express, IOP Science-1.068.	May 2018 (Accepted with minor revision)	1
6	An investigation on high temperature erosion behaviour of Plasma sprayed CoCrAlY/Al <sub>2</sub> O <sub>3</sub> /YSZ on Fe and Ni based alloys	<u>Nithin H S</u> , Vijay Desai, Ramesh M R	International Conference on Computational Methods in Engineering and Health Sciences (ICCMEH-2015), held at University Putra Malaysia	December 2015	3
7	Cyclic Oxidation and Hot Corrosion Behaviour of Plasma Sprayed CoCrAlY/WC-Co Coating on Turbine Alloys	<u>Nithin H S</u> , Vijay Desai, Ramesh M R	44 <sup>th</sup> International Conference on Metallurgical Coatings and Thin Films (ICMCTF-2016). Held	April 2016	3

			at San Diego, CA, USA.		
8	High temperature Solid particle erosion of plasma sprayed CoCrAlY coating reinforced with WC-Co and Cr <sub>3</sub> C <sub>2</sub> -NiCr carbides.	<u>Nithin H S</u> , Vijay Desai, Ramesh M R	54 <sup>th</sup> National Metallurgists Day -70 <sup>th</sup> Annual Technical Meeting (NMD-ATM 2016), held at IIT Kanpur	November 2016	4
9	Oxidation and Hot Corrosion Behavior of Plasma Sprayed MCrAlY coating Reinforced with Chrome Carbide	<u>Nithin H S</u> , Vijay Desai, Ramesh M R	Advances in Materials & Processing: Challenges & Opportunities (AMPCO-2017), held at IIT Roorkee.	December 2017	4

\*Category:

1: Journal paper, full paper reviewed, 2: Journal paper, Abstract reviews, 3: Conference/Symposium paper, full paper reviewed, 4:Conference/Symposium paper, abstract reviewed 5: others (including papers in Workshops, NITK Research Bulletins,Short notes etc.)

**Nithin H S**

Research Scholar  
Name & Signature, with Date

**Dr. Vijay Desai**

Research Guide  
Name & Signature, with Date

**Dr. Ramesh M R**

Research Guide  
Name & Signature, with Date

## **BIO-DATA**

- 1. Name** : Nithin H S  
**2. Father's Name** : Shivegowda H S  
**3. Date of Birth** : 07<sup>th</sup> May 1989  
**4. Nationality** : Indian  
**5. Marital Status** : Married  
**6. Address** : Department of Mechanical Engineering  
National Institute of Technology Karnataka  
Surathkal, PO Srinivasnagar 575 025  
Karnataka, India.  
**7. Mobile Number** : +91 9844546475  
**8. E-mail id.** : *nithinshiv1989@gmail.com*  
**9. Educational Qualification** :

<b>Qualification</b>	<b>University/Board</b>	<b>Year of Passing</b>
Ph.D. (Mechanical Engineering)	National Institute of Technology Karnataka	Pursuing
M.Tech. (Mechanical Engineering)	Visvesvaraya Technological University, Belgaum	2012
B.E. (Automobile Engineering)	Visvesvaraya Technological University, Belgaum	2010